Synchronization in OFDM Communication Systems

Chi Wa Lam

Submitted for the Degree of
Doctor of Philosophy
from the
University of Surrey

Centre for Vision, Speech and Signal Processing
School of Electronics and Physical Sciences
University of Surrey
Guildford, Surrey GU2 7XH, U.K.

2003

BLANK IN ORIGINAL

Abstract

Orthogonal Frequency Division Multiplexing (OFDM) is one example of a multicarrier modulation scheme in which high-speed data are transmitted via multiple overlapping subcarriers. Although the subcarriers are overlapped, they are orthogonal to each other without intercarrier interference. The OFDM system is robust in multipath fading environment and is now widely used in high-speed wireless communication.

However, OFDM is sensitive to synchronization defects. Performance degradation due to synchronization defects, including symbol timing offset, phase offset, frequency offset and digital sampling clock error are studied here.

Two coarse frequency offset estimators with reference to the pilots subcarriers are proposed. The first one, pilots-power-detection algorithm, is derived based on the maximum likelihood principle and the received instantaneous power of subcarriers. Its performance, which is measured with reference to a statistical distance, depends on the pilots pattern, the total number of pilots and the transmission power of subcarriers. In addition, a comparison study between the performance of the proposed algorithm, the guard-band power detection algorithm and the maximum correlation algorithm is presented.

Secondly, a low-complexity coarse frequency estimator for the frame-based OFDM system is proposed. Data are differentially encoded on even subcarriers between the symbols of a new two-symbol frame header. The odd subcarriers are modulated with zero to facilitate the symbol timing estimation.

Finally, a case study in the DVB-T system is given which shows that the original pilots pattern is not well designed for the proposed pilots power detection algorithm. New pilots patterns with better performance are presented.

Key words: coarse frequency offset, differential modulation, DVB-T, OFDM, synchronization, pilots pattern, pilots-power detection

Email: c.lam@eim.surrey.ac.uk

WWW: http://www.eim.surrey.ac.uk/

Acknowledgements

It is a long time since I have registered as a part-time PhD student in the University of Surrey. Even with the advance in communications and convenience in flying between countries nowadays, studying towards a PhD in the UK and working in Hong Kong at the same time is far more difficult than I have expected.

I would like to take this opportunity to thank my supervisor Dr. W.J. Szajnowski for his patience, invaluable advice and guidance throughout the past five years. Without his encouragement and support, probably I would not enroll the course in the first beginning and be able to finish it on time.

I am also in debt to my friends Mrs. S.P. Tay and Mrs. Sandra Mow for their library support in helping me to locate some journal papers and books while I am pursuing my studies at home.

Finally, I would like to thank Prof. A.H.Aghvami and Dr. T.Chilton for their valuable comments and recommendations.

Contents

List of Figures

List of Tables

List of Symbols

b	Boosted power ratio
$c(k)$	The complex modulation value of the k-th subcarrier
$c(i)$	A {0,1} sequence with positions of one defined by the continual pilots pattern
$\check{c}_j(i)$	A {0,1} sequence with positions of one defined by the union of the continual pilots pattern and scattered pilots pattern of the j-th symbol, (j=0,1,2,3)
$\tilde{c}(k)$	The demodulated data of the k-th subcarrier
C_a	Computation cost of one addition operation
C_c	Computation cost of one comparison operation
C_m	Computation cost of one multiplication operation
C_{gpd}	Computation cost of the guard band power detection algorithm
C_{mc}	Computation cost of the maximum correlation algorithm
C_{ppd}	Computation cost of the pilots power detection algorithm
d	Time index of the starting position of a sliding data window
$\tilde{d}$	Estimated symbol starting position
$\mathcal{D}$	Statistical distance between the two hypothesis that either all selected subcarriers are pilots (H_1) or otherwise (H_0)
$\mathcal{D}_n$	Extension of $\mathcal{D}$ under noisy environment
f_0	Frequency of the radio frequency modulating carrier
f_d	Maximum Doppler frequency in Hz
f_k	Baseband frequency of the k-th subcarrier
g_1, g_2	Binary {0,1} sequence
$g_1^{(m_1)}$	A m-sequence with generator polynomial $x^5 + x^2 + 1$
$g_1^{(m_2)}$	A m-sequence with generator polynomial $x^7 + x^4 + 1$
$g_2^{(m)}$	A m-sequence with generator polynomial $x^5 + x^4 + x^3 + x^2 + 1$
$g_2^{(gold)}$	A Gold sequence with generator polynomial $x^{10} + x^9 + x^8 + x^6 + x^5 + x^3 + 1$
$g_2^{(golay)}$	A Golay sequence
$g_2^{(fan)}$	A binary sequence obtained by exhaustive computer search
$g_2^{(uniform)}$	A binary sequence obtained by a uniform random number generator

$g(x)$ A primitive polynomial to generate a pseudo-random sequence

h_0, h_1 Components of a two-path channel model

$h(t)$ Impulse response function of the propagation channel

$H(k)$ Frequency transfer function of the propagation channel

$\widetilde{H}(k)$ Modified channel frequency transfer function that combine $H(k)$ with the the phase offset

ICI(k) The noise component of the demodulated data of the k-th subcarrier due to intercarrier interference

J A shorthand notation for a summation

k Subcarrier index, $k = 1, 2, \ldots, N_u$

k_i Frequency index of the i-th pilot subcarrier

$\{K\}$ Pilots pattern; a set of frequency indices of pilot subcarriers

K_{cp} A set of frequency indices of the continual pilots in the DVB-T system

K_{sp} A set of frequency indices of the scattered pilots in the DVB-T system

K_{min} The smallest frequency index of the subcarriers used to transport data

K_{max} The largest frequency index of the subcarriers used to transport data

L_s The number of shifts of the data sliding window in intercarrier frequency spacing

L The total number of pilot subcarriers

M A timing metric for the estimation of the symbol timing

$\hat{m}$ The estimated starting frequency index of the shifted signal frequency spectrum

m A temporary output of the coarse frequency estimator in the units of intercarrier frequency spacing

n_p The number of pilot carriers

N The FFT/IFFT size of an OFDM system; total number of subcarriers

N_u Number of samples in the useful part of an OFDM symbol

N_g Number of samples in the guard interval of an OFDM symbol

$\mathcal{N}_{\text{ISI}}$ Noise component of the received signal due to intersymbol interference

N_v Total length of the guard band at both sides of the signal frequency spectrum

$\mathcal{N}(\mu, \sigma)$ A Gaussian density function with mean μ and standard deviation σ

$p(k)$ The demodulated data from the k-th subcarrier

$p(\theta)$ A function that converts the differential phase difference θ to either +1 or -1

r(t) Received signal in the time-domain

$\mathcal{R}$ Effective data rate of the frame-based OFDM system

$\mathcal{R}_{gg}$ Aperiodic autocorrelation function

$\mathcal{R}_{pg}(m)$ The sum of the products of the recovered data $p(k)$ at the k-th subcarrier and the sequence $g(n)$

$\mathcal{R}_s$ Raw data rate per OFDM symbol

s(t) Transmitted OFDM signal in the time-domain

s Sidelobe level ratio

S_dNR Signal-to-nose power ratio of the data subcarriers

SNR_{ICI} Signal-to-noise power ratio when data are corrupted by intercarrier interference only

T Time duration of one OFDM symbol

T_c Coherent time of the multipath channel

T_F Time duration of a frame of OFDM symbols

T_s Digital sampling period in seconds

T_g Time duration of the guard interval of an OFDM symbol

T_u Time duration of the useful part of an OFDM symbol

u_k The instantaneous power of the k-th subcarrier

u_{nk} The instantaneous power of the k-th subcarrier with additive white Gaussian noise

$u(t)$ A rectangular pulse with length equal to the symbol duration

U The set of instantaneous power of all carriers, i.e. $U = \{u_0, u_1, \ldots, u_{N-1}\}$

U_K A subset of U with subcarriers taken from a shifted pilots pattern

$\overline{U}_K(m)$ The test statistic for non-coherent estimation of the coarse frequency offset

$\overline{U}_{nk}(m)$ The test statistic used to determine the coarse frequency offset under noisy environment with additive white Gaussian noise

$U^{(\lambda)}$ A one-sided trimmed sum of a set of instantaneous power of subcarriers

w_k Modulation value for the k-th subcarrier generated from a pseudo-random binary sequence

$\mathcal{W}$ Total bandwidth occupied by the OFDM system

$\mathbf{W}$ A $N \times N$ unitary IDFT matrix

$\mathbf{W_p}$ A $N \times P$ submatrix of $\mathbf{W}$ with columns corresponding to the modulated carriers

$\mathbf{W}_\perp$ A $N \times N - P$ submatrix of $\mathbf{W}$ with columns corresponding to the virtual carriers

x_k The in-phase component of the k-th subcarrier

x_{nk} The in-phase component of the k-th subcarrier with additive white Gaussian noise

y_k The quadrature component of the k-th subcarrier

y_{nk} The quadrature component of the k-th subcarrier with additive white Gaussian noise

δ Relative frequency offset of the baseband signal with respect to the intercarrier frequency spacing

$\delta(t)$ The Dirac delta function

Δ_f Frequency difference between oscillators in the receiver and the transmitter

Δf The estimated amount of coarse frequency offset

ΔF Intercarrier frequency spacing

ϵ Relative sampling clock error with respect to the sampling period T_s

η The noise margin; difference in received power between the pilot carriers and data carriers.

λ_i The graphical distance to the center of a Gaussian distribution in the units of the standard deviation

λ The trimming level; the number of subcarriers removed in the determination of the trimmed sum of subcarriers power

$\psi(l)$ The amount of phase rotation on the useful component of the l-th subcarrier due to the fine frequency offset and the sampling clock error

$\phi(k_{2n})$ Phase difference between the k_{2n}-th subcarriers of the two adjacent symbols in the frame header

ρ_i The attenuation from scattering of the i-th path

ρ The signal-to-noise power ratio at the receiver input

σ_d Average power of the data subcarriers

σ_n Average power of the additive white Gaussian noise

σ_τ The rms delay spread of the multipath channel

σ_p Average power of the pilot subcarriers

τ Coarse frequency offset in the unit of intercarrier frequency spacing

τ_s Symbol timing offset in the unit of sample

τ_d Length of the channel impulse response function

τ_{gd} A shorthand notation of $(N_g - \tau_d + 1)$

τ_i The time delay of the i-th path measured relative to the first detectable signal arriving at the receiver at $\tau_1 = 0$.

$\overline{\tau}$ The mean excess delay that is the first moment of the power delay profile of the multipath channel

θ Phase difference in radian

φ The spectral efficiency of the OFDM system

ζ A fractional number that give the fine frequency offset in the units of intercarrier frequency spacing

Abbreviations

ACF	Autocorrelation Function
AWGN	Additive White Gaussian Noise
BRAN	Broadband Radio Access Networks
COFDM	Coded Orthogonal Frequency Division Multiplexing
CCETT	Centre Commun d'Etudes en Télédiffusion et Télécommunication
DAB	Digital Audio Broadcasting
DFT	Discrete Fourier Transform
DMT	Discrete Multitone
ETSI	The European Telecommunication Standards Institute
FFT	Fast Fourier Transform
FDM	Traditional Frequency Division Multiplexing system
GPD	Guard-band Power Detection Algorithm
GF	Galois Field
HIPERLAN	High Performance Radio Local Area Network
IEEE	The Institute of Electrical and Electronics Engineering
IFFT	Inverse Fast Fourier Transform
ICI	Intercarrier Interference
ISI	Inter-symbol Interference
MC	Maximum Correlation Algorithm
PN	Pseudo-Noise
PRBS	Pseudo-random Binary Sequence
QPSK	Quadrature Phase Shift Keying

RF	Radio Frequency
RMS	Root-Mean-Square
ROM	Read-Only Memory
OFDM	Orthogonal Frequency Division Multiplexing
SFN	Single Frequency Network
SNR	Signal-to-Noise Ratio
TPS	Transmission Parameter Signalling subcarriers
PPD	Pilots Power Detection Algorithm
QAM	Quadrature Amplitude Modulation

Summary

Orthogonal Frequency Division Multiplexing (OFDM) is a multicarrier modulation schemes. High-speed data are multiplexed onto a number of frequency carriers efficiently using Inverse Fast Fourier Transform (IFFT). Similarly, the de-multiplexing and data recovery from carriers are carried out using Fast Fourier Transform (FFT) at the receivers. Although subcarriers in OFDM are overlapped, there are no intercarrier interference and the subcarriers are orthogonal to each other. Each OFDM symbol is composed of a guard interval and an useful part. By appending a guard interval in front of each symbol, OFDM is robust in multipath fading environment. The system is now widely used in high-speed wireless communication applications such as Digital Audio Broadcasting (DAB) and Digital Video Broadcasting (DVB).

However, OFDM is sensitive to synchronization defects such as the symbol timing error, sampling clock error and frequency offset. The frequency offset error normalized by the subcarrier frequency spacing consists of an integer part (coarse frequency offset) and a fractional part (fine frequency offset). This thesis mainly works in the area of coarse frequency offset estimation.

The symbol timing error is due to the errors in locating the starting positions of the useful parts. The length of the guard interval must be longer than that of the channel impulse response in order to avoid intersymbol interference. The difference in length between the guard interval and the channel impulse response sets the maximum limit of the symbol timing error. If the symbol timing error is within this limit, there will be only an additional phase rotation on the demodulated data without intersymbol interference. On the other hand, the digital sampling clock error, phase offset and the fine frequency offset also causes phase rotation to the demodulated data. The

amount of phase rotation due to the symbol timing error and the sampling clock error increases linearly with the corresponding frequency index, while those due to the phase offset and the fine frequency error is the same to all subcarriers. Fine frequency offset not only affects the orthogonality between carriers leading to intercarrier interference, but also reduces amplitude of the received signal. Similarly, the sampling clock error causes intercarrier interference and attenuates the magnitude of the demodulated data. However, the coarse frequency offset only shifts the entire frequency spectrum of the demodulated data either up or down without causing other degradation.

Some carriers in an OFDM symbol are modulated with reference information whose transmitted values are known to the receiver and are referred as pilot subcarriers, or simply pilots. With reference to these pilots, a pilots-power-detection algorithm for coarse frequency synchronization is proposed. A test statistic based on the maximum likelihood principle and noncoherent signal processing of the received signals is derived in a Rayleigh fading channel model. It is assumed that symbol timing error and fine frequency offset have been corrected, but the channel transfer function and hence the effects of fading is still unknown to the receiver. Magnitude and phase errors are expected to occur at all frequencies. Therefore, phase modulation of pilots is disregarded and only their power is exploited for noncoherent detection. The test statistic is equal to the sum of instantaneous power of a number of frequency carriers, whose frequency indices are generated by shifting the pilots pattern. The test statistic has a χ^2 distribution and can be approximated by a Gaussian distribution for a large number of carriers. The estimation process is equivalent to sliding the known pilots pattern along all carriers. When the sliding window is at the correct position, only the pilot carriers will be selected and the test statistic will achieve the maximum value.

Alternatively, the process can be viewed as multiple binary hypotheses testing in which we want to discriminate the target hypothesis from the others. A decision has to be made that whether all carriers selected to compute the test statistic are pilots (H_1), or a combination of pilot carriers and data carriers (H_0). A statistical distance between H_1 and H_0 is defined. It corresponds to the geometric distance between the conditional means when the conditional standard deviations are used as the units of length. The sidelobe level ratio is defined as the number of pilots that are selected to calculate the

test statistic, divided by the total number of pilots available. In addition, pilots are usually transmitted at a higher power level than that of data carriers. The ratio of the average transmission power of pilots to data carriers is defined as the boosted power ratio. It has been shown that the distance decreases with increasing sidelobe level ratio and increases with boosted power ratio. However, the distance is upper bounded by the total number of pilots available and cannot be improved indefinitely by boosting the power of pilot carriers. A simple design rule on the minimum number of pilot carriers is proposed. As a rule of thumb, the total number of pilot carriers should be more than ten.

During the deviation of the coarse frequency offset estimator, it is assumed that the fine frequency offset has been estimated and corrected. It has been shown that whenever the boosted power ratio is larger than about 1.6, the amount of the residue fine frequency offset can be as large as 20% of the maximum range. This value should be larger than the residue error of any practical fine frequency estimators. In other words, the design constraint to the fine frequency offset estimator is loose.

As shown ny computer simulations in a highly frequency selective fading channel, the performance of the proposed pilots-power-detection algorithm is better than that of the maximum correlation methods and the guard-band power detection algorithm. On the other hand, the complexity of the proposed algorithm is similar to that of the guard-band power detection algorithm while the maximum correlation algorithm has the highest complexity. The major drawback of the proposed algorithm is a possible degradation of the system throughput because pilots subcarriers are not used for data transmission. However, if boosted pilots have already been used as in the DVB-T system, the application of the estimator has no effect on the data throughput.

The coarse frequency offset can also be estimated by exploiting the phase of the pilot carriers. A low-complexity coarse frequency offset estimator for a frame-based OFDM system has been proposed. The coarse frequency offset is determined by locating the maximum of the cross-correlation between the known pilots sequence and the recovered data. The data is recovered by taking differential demodulation on pairs of subcarriers between the two adjacent symbols in a new two-symbol frame header. Compared with

the conventional frame header, there is an additional guard interval between the useful parts of the two symbols.

As seen from computer simulations in two-path fading channels, the proposed algorithm is robust against the selection of the pseudo-random sequence used to generate the frame header. The performance of the new estimator is similar to those used in the conventional system. With the expenses of a minor reduction in the effective data rate and a slightly increase in the system response time, the additional guard interval improves the performance of the coarse frequency estimator. Since all symbols in the proposed OFDM system have identical structure, the complexity in hardware implementation is reduced. Another major reduction in the complexity is due to the introduction of a mapping function which convert the phase difference from a real number into a two-level integer, either 1 or -1. Then the correlation can be carried out using a combination of exclusive-nor logic gates and a simple binary adder without the needs of complex multiplier and accumulator. A block diagram illustrating the hardware architecture of the estimator is given.

The "DVB-T" is the standard for terrestrial broadcasting of digital television. It uses OFDM modulation in the physical layer definition. With different definition in the total number of subcarriers, a DVB-T can operate in either 2k mode or 8k mode. A case study in the assignment of the continual pilots in DVB-T 2k mode is presented. The continual pilots are transmitted at boosted power and are not used for data transmission. It has been shown that the frequency indices of the existing pilots pattern have a common factor three, and hence the autocorrelation function of the pilots pattern has many sidelobes and the magnitude of the sidelobes is substantially larger than unity. Due to its poor autocorrelation property, the continual pilots pattern defined in the DVB-T standard is not well designed for incoherent processing of the signals to estimate the coarse frequency offset. New pilots patterns are proposed.

On the other hand, we have also shown that the robustness of the system can be improved by using one-sided trimming to remove the strong tonal interference. An algorithm has been proposed to verify the correctness of the coarse frequency offset estimator after all synchronization errors have been removed.

The thesis is structured as follows: In Chapter 1, an introduction of OFDM is given. A brief account on the historical and recent development of OFDM, its principle, properties and a brief literature review for both the symbol timing and fine frequency estimation are presented. In Chapter 2, the effects of synchronization defects are studied. In Chapter 3, the pilots-power-detection coarse frequency estimator is derived using the maximum likelihood principle. Its properties are compared with those of the estimators using the guard-band power detection and the maximum correlation algorithms. A low-complexity coarse frequency estimator using pilots phase is proposed in Chapter 4. In Chapter 5, we will discuss the properties of the pilots pattern. Finally, the conclusions and some suggestions on future works are given in Chapter 6.

Chapter 1

Background

1.1 Introduction

The Orthogonal Frequency Division Multiplexing (OFDM) is one example of a multicarrier modulation scheme based on the discrete Fourier transform (DFT). Unlike single carrier system, data are multiplexed and transmitted on multiple overlapping radio frequency carriers instead of just one. It makes efficient use of frequency spectrum by allowing carriers to overlap and yet to remain orthogonal to each other. It is robust against multipath echoes due to its long symbol time and frequency interleaving capability. Therefore, it is being used to combat frequency selective fading in wireless applications and is widely used nowadays in high-speed wireless communication applications. However, this modulation scheme is sensitive to synchronization defects. We will describe our proposals to combat this problems in this thesis. First of all, in this chapter we will give an introduction of the OFDM and describe some conventional synchronization methods found in the literatures.

This chapter is arranged as follows. At first, we give a brief account of the historical development and recent applications of OFDM in the wireless communication standards including DVB-T, DAB, IEEE 802.11a and Hiperlan/2. Then the basic principles, advantages and disadvantages of the OFDM systems are discussed. Finally, we give a review of the conventional methods in the synchronization of OFDM systems.

1.2 Historical and Recent Development

The early applications and developments of wireless transmission using multicarriers can be dated back to 60's.

Early 60's - Frequency-division multiplexing systems have already been employed in military applications [8, 111].

1966 - The work on orthogonal multiplexing is pioneered by Chang [15]. He presented a principle of transmitting bandlimited orthogonal signals through a linear bandlimited channel without interchannel and intersymbol interferences. A general method for synthesizing the bandlimited orthogonal time functions in a limited frequency band was given.

1970 - A US patent was filed and issued in January, 1970 [80].

1971 - Weinstein and Ebert [102] suggested the usage of discrete Fourier transform as part of the modulation and demodulation processes to replace the banks of sinusoidal generators and demodulators.

1980 - Peled and Ruiz [81] solved the orthogonality problem over dispersive channels by filling the empty guard space with a cyclic extension of the OFDM symbol. This effectively simulates a channel performing cyclic convolution.

1985 - Cimini [13] provided the early results on the performance analysis of OFDM modems in mobile communication channels.

The basic idea of OFDM is to split a high-speed data stream into multiple low-speed subchannels. For a large number of subchannels, the arrays of sinusoidal generators and coherent demodulators required in a parallel system become unreasonably expensive and complex. Although the contribution by Weinstein [102] greatly reduced the system complexity and provided the basic structure of OFDM transceivers being used today, the computational requirement for real-time processing of OFDM signals was still too high for its wide acceptance in 80's.

Owing to the recent advances of digital signal processing and very large scale integrated

circuit (VLSI) technologies, the initial obstacles of OFDM implementation, such as massive complex computation and high speed memory do not exist anymore. After more than thirty years of research and development, OFDM has been widely adopted now as the standard modulation scheme to transmit high-speed data over wireless media.

It is currently used in the standards of European Digital Audio Broadcasting (DAB), Digital Video Broadcasting (DVB), High Performance Radio Local Area Network (HIPERLAN/2) and Asymmetric Digital Subscriber Services (ADSL). In a wired environment such as ADSL, the term *discrete multitone* (DMT) is more commonly used. It is a technology used to transmit high speed data over the existing twisted-pair copper telephone networks. The expected huge demand from the domestic markets in digital radios for the DAB systems and digital television sets for the DVB-T systems will drive the implementation of OFDM cost effective.

More recently, OFDM is also being studied to transmit data on powerline networks [53] and wireless asynchronous transfer mode (ATM) networks in the range of 60GHz to deliver data rates up to 155 Mbit/s [103, 104].

1.2.1 Digital Audio Broadcasting, DAB

This is the standard to broadcast digital radio. In presence of interference and multipath, only some of the carriers will be affected at any one time. Redundancy in form of channel coding can be added to correct errors arising from carriers that suffer from interference or multipath. OFDM systems that incorporate channel coding are termed Coded OFDM (COFDM) systems. DAB uses COFDM in the physical layer.

Early in the 80's, the research center France Telecom group CCETT (Centre Commun d'Etudes en Télédiffusion et Télécommunication) initiated the work on COFDM. This was developed later into the new digital audio broadcasting standard by a collaborative project, Eureka 147. The DAB standard was published in 1994 [21].

1.2.2 Digital Video Broadcasting, DVB

Digital terrestrial television has been the subject of a number of national and European cooperative research projects including [12, 66, 86, 112]:

- dTTb (digital Terrestrial Television broadcasting) by RACE (R&D in Advanced Communications Technologies in Europe)
- HD-Divine (Digital video narrowband emission) by Nordic countries
- $^{H}DTV_{T}$ (Hierarchical Digital TV Transmission) in Germany

These three projects, together with a number of other projects, have contributed to the group called DTTV-SA (Digital Terrestrial Television - Service Aspects), which was established by the DVB Technical Module (DVB-TM) in January 1994. In late 1994, the DVB User Requirements for digital terrestrial television were approved.

The original proposal was based on 6785-carrier OFDM. Because of its high complexity, an alternative system using 1696-carrier OFDM was proposed. In late 1995, the standard was finally standardized on a dual-mode system that consists of either 6817 carriers or 1705 carriers. These two operating modes are usually referred as "8k" mode or "2k" mode respectively.

In an OFDM system, the symbol duration must be the reciprocal of the intercarrier frequency spacing in order to achieve orthogonality. Since the subcarriers in the 8k system are more closely packed, the useful symbol duration in the 8k system (896 μs) is longer than those in the 2k system (224 μs). On the other hand, the maximum guard interval is usually taken to be approximately 1/4 of the useful symbol length [66] in order to obtain a reasonably useful bit-rate. Therefore, a longer guard interval can be obtained in the 8k system. In addition, signals which arrive from different transmitters, with relative time delays that are greater than the guard interval, causes interference to one another in a SFN. In conclusion, the 8k system has a longer guard interval which in turn determine the maximum transmitter distance in a SFN, the coverage area of the 8k system in the SFN is larger than those in the 2k system. In other words, although the 8k system is more complicated to be implemented, it has a better performance in the operation of a SFN.

1.2.3 HIPERLAN/2 and IEEE 802.11a

In response to growing market pressure for low-cost and high capacity radio links, the European Telecommunications Standards Institute (ETSI) has established a standardization project for Broadband Radio Access Networks (BRAN) in Spring 1997. The High Performance Radio Local Area Network (HIPERLAN/2) is one of the standards developed by this group.

The first release of the HIPERLAN/2 standard is published in April 2000 [43]. The standard specifies the air interface between broadband mobile terminals and the network, and supports data rates up to 54Mbit/s. The physical layer is based on OFDM. Each data OFDM symbol has 48 data carriers and 4 pilot carriers.

Another wireless LAN standard being developed in the 5GHz band is the IEEE802.11a. The physical layers of the two wireless LAN standards IEEE802.11a and Hiperlan/2 use OFDM scheme as modulation. On the physical layers of both standards there are only a few minor difference, but the medium access mechanisms for data transmission are quite different. The basic medium access mechanism in IEEE802.11a is a Distributed Coordinate Function (DCF) that allows for sharing of the wireless channel through the use of carrier sense multiple access with collision avoidance (CSMA/CA). On the other hand, Hiperlan/2 uses a centralized multiple access. The air-interface is based on the time-division duplex (TDD) and dynamic time division multiple access (TDMA). A performance comparison of these two radio link protocols can be found in [55].

1.2.4 Principle of OFDM

(A) Orthogonal Subcarriers

In an OFDM system, a stream of information bits is first segmented into blocks of finite length, say N. Each block of data is then simultaneously transmitted over N orthogonal frequency channels, which are specified by different subcarriers. In doing so, the high-rate data stream can be transmitted through multiple low-rate narrow-band channels. Different from the traditional frequency division multiplexing (FDM) system, in OFDM all the subchannels are overlapping in spectrum but the signals can still be received

without adjacent interference. As illustrated in Figure 1.1, the sidebands from one channel become null at the positions corresponding to the other sub-channels. The data carried by one subcarrier is independent of its adjacent subcarriers and there is no intercarrier interference.

In order to do this the carriers must be mathematically orthogonal. The receiver acts as a bank of demodulators, translating each carrier down to dc, the resulting signal then being integrated over a symbol period to recover the raw data. If the other carriers all beat down to frequencies which, in the time domain, have a whole number of cycles in the symbol period, the integration process results in zero contribution from all these other carriers. Thus, the carrier separation in an OFDM system has to be inversely proportional to the symbol period to achieve carrier orthogonality. This allows us to create a large number of orthogonal FDM channels without difficulty of building non-overlapping sub-band filters with brick wall frequency response.

(B) IFFT/FFT operations

In a single carrier system, the modulated signal of the m-th symbol over one symbol period T is given by

$$s_{m,o}(t) = x_{m,o}(t)\cos(2\pi f_o t) - y_{m,o}(t)\sin(2\pi f_o t) \qquad 0 \le t < T \qquad (1.1)$$

where f_o is the modulating carrier frequency, $x_{m,o}(t)$ and $y_{m,o}(t)$ are the in-phase and quadrature components of the q-ary complex modulating signal $c_{m,o}(t)$ respectively.

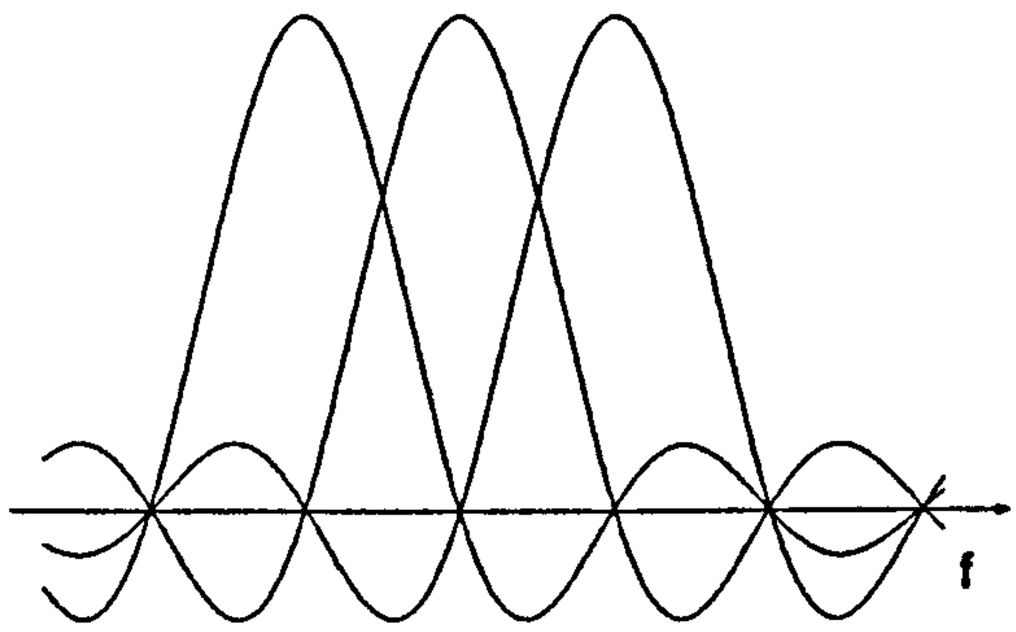

Figure 1.1: Illustration of the overlapping of OFDM subcarriers in frequency

Alternatively, $s_{m,o}(t)$ can be written as

$$s_{m,o}(t) = \mathrm{Re}\left\{c_{m,o}(t)e^{j2\pi f_o t}\right\} \qquad 0 \le t < T \qquad (1.2)$$

where $c_{m,o}(t) = x_{m,o}(t) + j\ y_{m,o}(t)$ and $\mathrm{Re}\{\cdot\}$ is the real part of the complex value inside the bracket.

Similarly the OFDM signal, which is composed of N overlapping carriers separated by ΔF in frequency, can be written as:

$$s_m(t) = \mathrm{Re}\left\{\frac{1}{N}\sum_{k=0}^{N-1} c_{m,k}(t)e^{j2\pi(f_o+f_k)t}\right\} \qquad 0 \le t < T \qquad (1.3)$$

where $k = 0 \ldots N-1$ and $f_k = k\Delta F$.

The modulating data $c_{m,k}(t)$ are constant throughout the whole symbol duration. Each data depends only on the frequency index k and the symbol index m, but independent of the time t. Therefore, $c_{m,k}(t)$ can be denoted as $c_m(k)$. Then, the continuous OFDM output signal can be represented as

$$s(t) = \mathrm{Re}\left\{\frac{e^{j2\pi f_o}}{N}\sum_{m=-\infty}^{+\infty}\sum_{k=0}^{N-1} c_m(k)e^{j2\pi f_k t}\ \cdot\ u(t-mT)\right\} \qquad (1.4)$$

where $u(t)$ is a rectangular pulse with length equal to the symbol duration, T.

$$u(t) = \begin{cases} 1 & 0 \le t < T \\ 0 & \text{otherwise} \end{cases} \qquad (1.5)$$

The demodulation process is based on the following orthogonality property:

$$\int_0^T e^{j2\pi f_{k1}t} \cdot e^{-j2\pi f_{k2}t} = \begin{cases} T & k1 = k2 \\ 0 & \text{otherwise} \end{cases} \qquad (1.6)$$

Notice that the intercarrier frequency spacing ΔF is equal to the reciprocal of the symbol duration T. That is,

$$\Delta F = \frac{1}{T} \qquad (1.7)$$

The orthogonality property will not hold if $\Delta F \neq 1/T$. The orthogonality will ensure that the receiver can separate the OFDM subcarriers without errors.

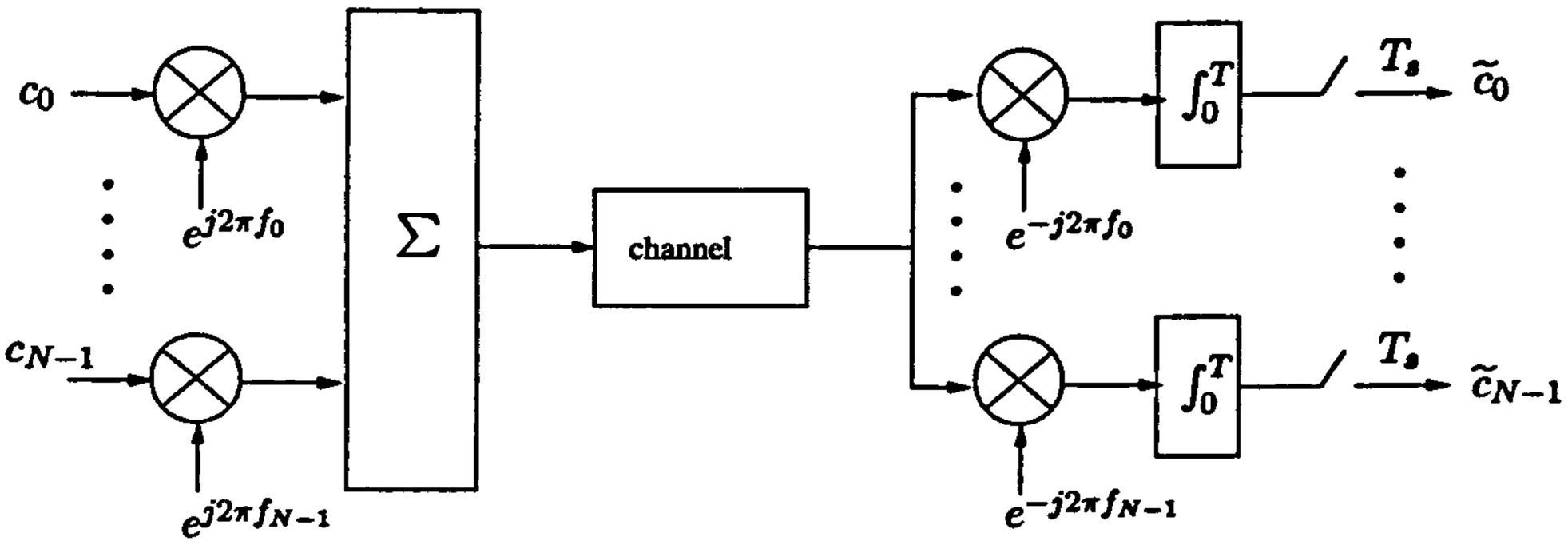

Figure 1.2: Equivalent structure of the OFDM modulator and demodulator

The OFDM system can be implemented using banks of modulators and demodulators as shown in Figure 1.2. In practice, the modulation and demodulation processes are carried out digitally. The banks of modulator and demodulator are replaced by Discrete Fourier Transform (DFT) which can be implemented either by dedicated hardware or software running on a digital signal processor.

The equivalent baseband signal of the m-th symbol is given by

$$s_m(n) = \frac{1}{N} \sum_{k=0}^{N-1} c_m(k) e^{j2\pi(\frac{k}{T})nT_s} \tag{1.8}$$

where $1/T_s$ is the digital sampling rate.

If symbol duration $= N \times$ sampling period, i.e. $T = NT_s$, we will have

$$s_m(n) = \frac{1}{N} \sum_{k=0}^{N-1} c_m(k) e^{j\frac{2\pi kn}{N}} \tag{1.9}$$

The modulated OFDM signal is generated by applying IDFT to the data $\{c_m(k)\}$. Similarly, the data can be recovered by taking DFT of the received signal $\{r_m(n)\}$ in the receiver as follows.

$$\tilde{c}_m(k) = \sum_{n=0}^{N-1} r_m(n) e^{-j\frac{2\pi kn}{N}} \tag{1.10}$$

In general, the total number of carriers N is a power of 2 so that radix-2 Fast Fourier Transform (FFT) can be used in the implementation to improve the speed of execution. An OFDM signal is generated using an inverse Fast Fourier Transform (IFFT), and the receiver uses an FFT in the demodulation process. The system block diagram of an OFDM system is shown in Figure 1.3.

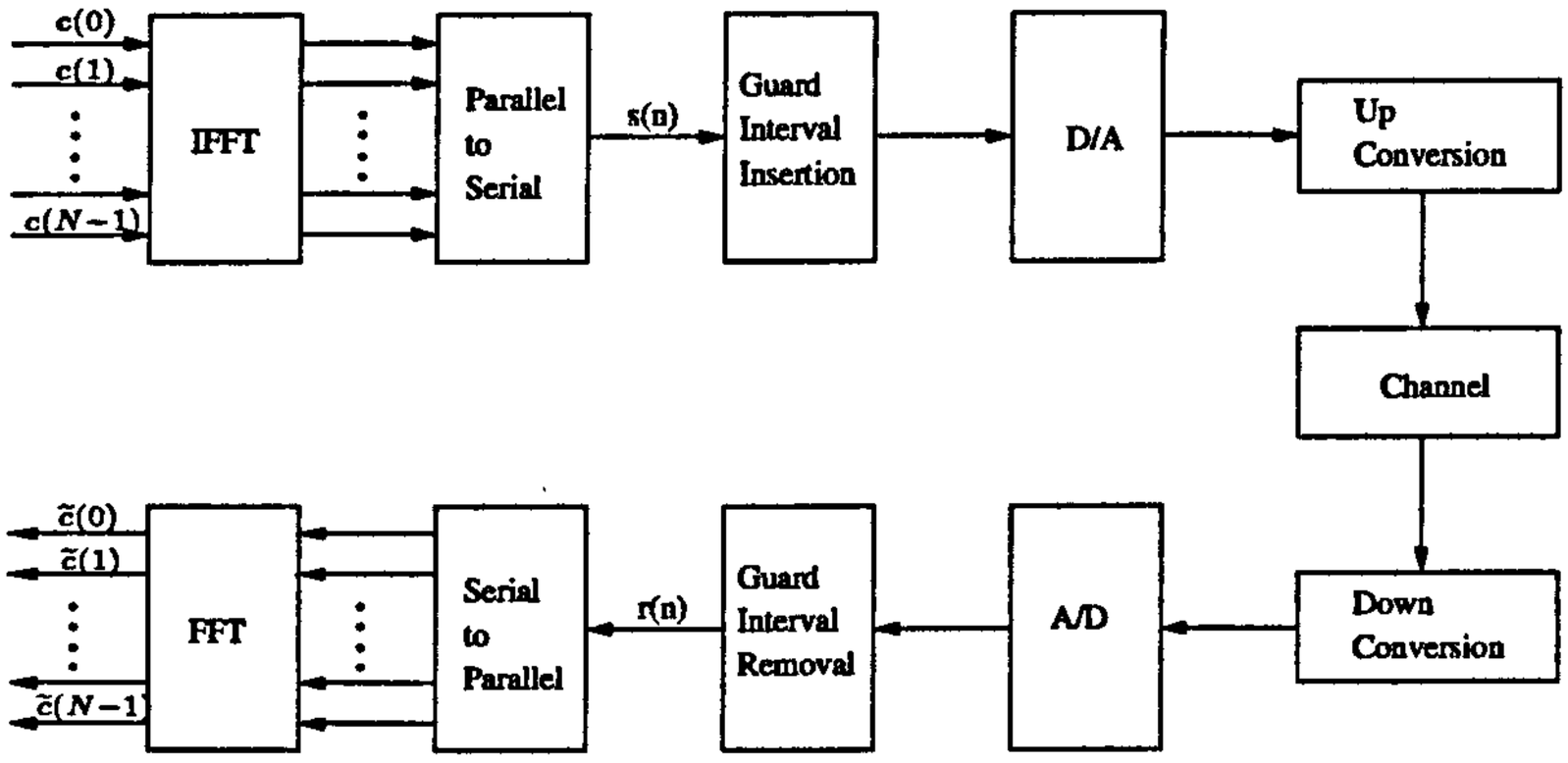

Figure 1.3: System block diagram of an OFDM system

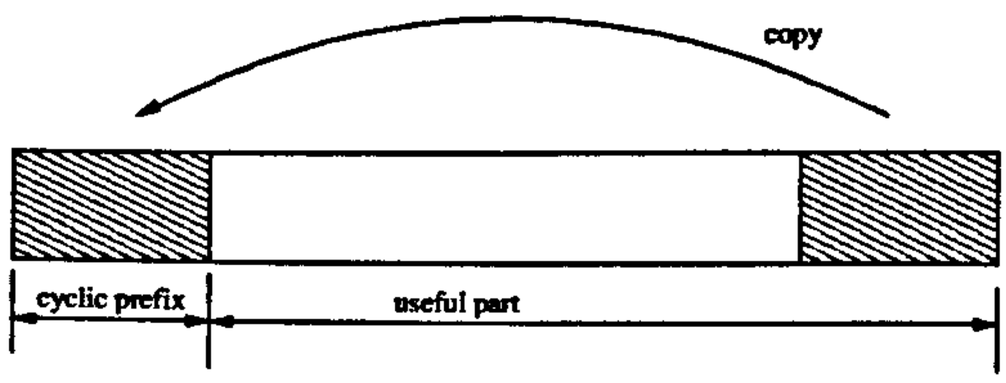

Figure 1.4: An OFDM symbol consisting of a cyclic prefix and a useful part

(C) Cyclic Prefix

A complete OFDM symbol is built up by an *useful part* generated by Equation 1.9 and a *guard interval*. A guard interval is also named as *cyclic prefix* which is the cyclic extension of the useful part and is appended at the beginning of the useful part as shown in Figure 1.4. The length of the guard interval depends on the channel characteristics and applications.

The insertion of the guard interval has two main purposes. Firstly, it helps to avoid intersymbol interference after passing through a multipath propagation channel. If multipath echoes are short compared with the total symbol period, the energy from a previous symbol should only affect few samples at the beginning of the current symbol. In other words, if the length of the guard interval is longer than that of the channel impulse response, only samples in the guard interval will be affected. Samples in the noisy guard interval will be discarded and only those taken from the useful part will be used for data demodulation. Therefore, by ensuring that the length of guard interval is

longer than that of the channel impulse response, OFDM can be free from intersymbol interference.

Secondly, the insertion of the cyclic prefix makes the OFDM system satisfy the theoretical assumption of applying the IDFT and DFT. The underlying theoretical assumption of applying DFT is that the signal is periodically repeated over an infinite time interval. The guard interval is filled up with the cyclic extension of the useful part in order to mimic a periodic signal from only one OFDM symbol. If there is error in locating the symbol starting position, the data capturing window will cover both the cyclic prefix and the useful part. The resultant observation will be a cyclic shifted version of the original data and the corresponding DFT output will only suffer additional phase shifts without distortion [77]. The cyclic prefix enables a finite OFDM symbol behaves as if it were periodic with respective to the symbol observation window and extends beyond the symbol boundary.

The major drawback of inserting the guard interval is the reduction of data throughput and power efficiency because the guard interval carries no data.

1.3 Properties of OFDM

1.3.1 Advantages of OFDM

(A) Robust in Multipath Fading Environment

In general, the maximum symbol rate of a communication system is limited by the delay spread, which is equivalent to the length of the channel impulse response. If data are transmitted at a slow rate, signals travelling through different paths will arrive at a receiver before the next symbol is transmitted. In these cases, individual symbols can be resolved easily at the receiver. However, if the transmitted data rate is further increased until the symbol period is less than the delay spread, a data symbol received at the receiver will spread into adjacent symbols causing *intersymbol interference*(ISI). Mechanisms such as channel equalization technique have to be implemented in order to combat the effects of ISI.

In an OFDM system, a guard interval is appended in front of each useful symbol. If the echoes are short compared with the total symbol period, energy from one symbol only affects the first part of the next, and that hopefully is the guard interval. In other words, if the length of the guard interval is longer than that of the channel impulse response, the effects of ISI are localized in the guard intervals leaving the main body free from ISI. In addition, each OFDM sub-channel can be treated as narrow-band channel, hence reducing the overall effect of frequency-selective fading on the data transmission.

On the other hand, a characteristic of frequency selective fading is that some frequencies are enhanced while some are attenuated. The distribution of data on multiple carriers in OFDM means that some bits will be received in error while others are received correctly. By adding adequate channel coding and frequency interleaving, corrupted data can be recovered.

In conclusion, the OFDM modulation scheme is robust in a frequency selective fading environment. This is one of the major reasons that OFDM is being selected as the modulation scheme in the latest standards in high-speed wireless communication.

(B) High Spectral Efficiency

By allowing spectral overlapping and removing guard bands between adjacent channels, which is commonly found in conventional single carrier system, OFDM systems make efficient use of frequency spectrum. The bit-rate of the OFDM system can be determined as follows.

First of all, not every subcarriers carry payload data. The sampled digital signals are bandpass filtered to avoid aliasing and to limit the transmitted signal spectrum. In real applications, the filter has a roll-off region at both ends instead of having the theoretical brick-wall shape. In order to make the filtering easier, not all the available carriers are used for transmission. *Virtual carriers* are the outer carriers at both ends that are set to zero without carrying any useful information. This leaves gaps in the spectrum which minimize the complexity of the output filter.

Suppose there are total $2N_v$ virtual carriers and N useful carriers, and the symbol duration is T seconds. If modulation schemes on all useful carriers are identical such

that the data are taken from the same q-ary constellation with 2^q points, the total bit-rate $\mathcal{R}$ of the OFDM system will be equal to

$$\mathcal{R} = \frac{(N - 2N_v)q}{T} \quad \text{bit } s^{-1} \tag{1.11}$$

When N is large, the total bandwidth $\mathcal{W}$ occupied by the N carriers is approximately equal to N/T [19]. Then, the spectral efficiency φ of an OFDM system for a constellation size of 2^q is

$$\varphi = \frac{\mathcal{R}}{\mathcal{W}} = \frac{(N - 2N_v)q}{N} \quad \text{bit } (sHz)^{-1} \tag{1.12}$$

Asymptotically, φ tends towards to q bit$(sHz)^{-1}$ when $N \gg N_v$.

(C) Low-complexity Equalizer

In a conventional single carrier system, complex multiple-tap time-domain equalizers have to be used to remove the channel effects. For a certain delay spread, the complexity of an OFDM modem versus bit rate does not grow as fast as the complexity of a single-carrier system with an equalizer. The reason is that when the bit rate is doubled, an equalizer has to be made twice as long at twice the speed, so its complexity grows quadratically with the bit rate, whereas the complexity of OFDM grows only slightly faster than linear [72].

If the bandwidth of each subcarrier is much less than the channel coherence bandwidth, a frequency-flat channel model can be assumed for each subcarrier and the equalization will be drastically simplified. The effect of the multipath channel on each subcarrier can be represented by a single valued complex number affecting the amplitude and phase of each subcarrier. Equalization can be carried out by a simple one-tap equalizer operating in the frequency domain. Pilots symbols can be used to estimate the fading channel [7, 54, 91]. Yeh [109] proposed a Frequency-Pilot-Frequency-Interpolation (FPFI) technique to estimate the channel response which is obtained via frequency interpolation of the pilots tone that are modulated with a PN sequence and are inserted into each OFDM symbol. Blind channel estimation schemes based on the second-order or high order statistics have also been proposed in [27, 71, 110].

On the other hand, equalizer is not required if data on each carrier are modulated with differential coding and the multipath environment changes slowly from symbol to symbol. This is because successive symbols will be affected by the same perturbation in the slow fading channel. The channel effects can be cancelled out by utilizing the differential demodulation.

(D) Support Single Frequency Network

In conventional systems, multiple transmitters are required to increase the radio coverage. Interference among nearby transmitters within the same network is prevented by partitioning the available frequency bandwidth into a number of frequency allocations. Nearby transmitters are each assigned with a unique frequency allocation. Frequencies can only be reused and assigned to transmitters again that are a long distance apart. This makes the network planning very complicated and difficult to manage.

However, all transmitters in an OFDM network can be operated on the same frequency. Signals coming from different transmitters appear at the receiver to be multipaths with very long delay. An OFDM system can be designed to allow relatively long delay echoes by adjusting the length of the guard interval accordingly. Therefore, the reception will be good even in the overlap zones between the transmitters provided that the transmitters radiate the same signal at the same time. This effectively increases the coverage of the network.

For example, in Eureka DAB system, the guard interval can be set to 250 μs which allows transmitters to be spaced in excess of 75 km apart before problems with interference occur [62, 96]. In other words, an OFDM system can be operated in a *Single Frequency Network* (SFN) with a number of lower power transmitters broadcasting the same material simultaneously at the same frequency. This simplifies the network planning. In addition, this re-use of the spectrum is a major saving over conventional systems which would need different frequencies in adjacent service areas.

1.3.2 Problems in Implementation

(A) High Peak-to-Average Power Ratio

OFDM is a multicarrier modulation scheme in which the time-domain envelope can be modelled as the superposition of sinusoidal functions with different frequencies and phases. The phases depend on the input data and change randomly from symbol to symbol. A high peak will appear in the time-domain envelope if these functions are added constructively, leading to a high peak-to-average power ratio.

The output power amplifier has to maintain high linearity across the entire range of input signal level. Otherwise, the signal will suffer non-linear distortion resulting in out-of-band emission that causes interference to adjacent channels [24, 112]. In order to avoid saturation and prevent clipping, the power amplifier operates with a so-call "back-off" to create headroom for the signal peaks.

There have been many studies to reduce the peak-to-average power ratio in OFDM systems. Techniques are usually based on introducing redundancy in the data stream with coding [28, 58, 69] or post-processing the time-domain OFDM signal before amplification [90, 101].

(B) Sensitive to Synchronization Errors

An OFDM system is sensitive to errors in symbol timing recovery and frequency synchronization. For this reason, synchronization has been a major research topic in OFDM systems. Upon receiving signals over the air, an OFDM receiver has to remove the RF carrier by mixing the incoming signal with local oscillator signal. Because of the Doppler frequency shift and the instability of oscillators, there will be a discrepancy in frequency between the received RF carrier of the received signal and the local signal, leading to a residual frequency error in the down-converted baseband signal. The existence of the frequency offset destroys the orthogonality among the OFDM subcarriers and leads to performance degradation. In order to maintain a signal-to-interference ratio of 20 dB or greater in an OFDM system, Cimini [13] has shown that the carrier offset should be limited to less than 4% of the intercarrier spacing.

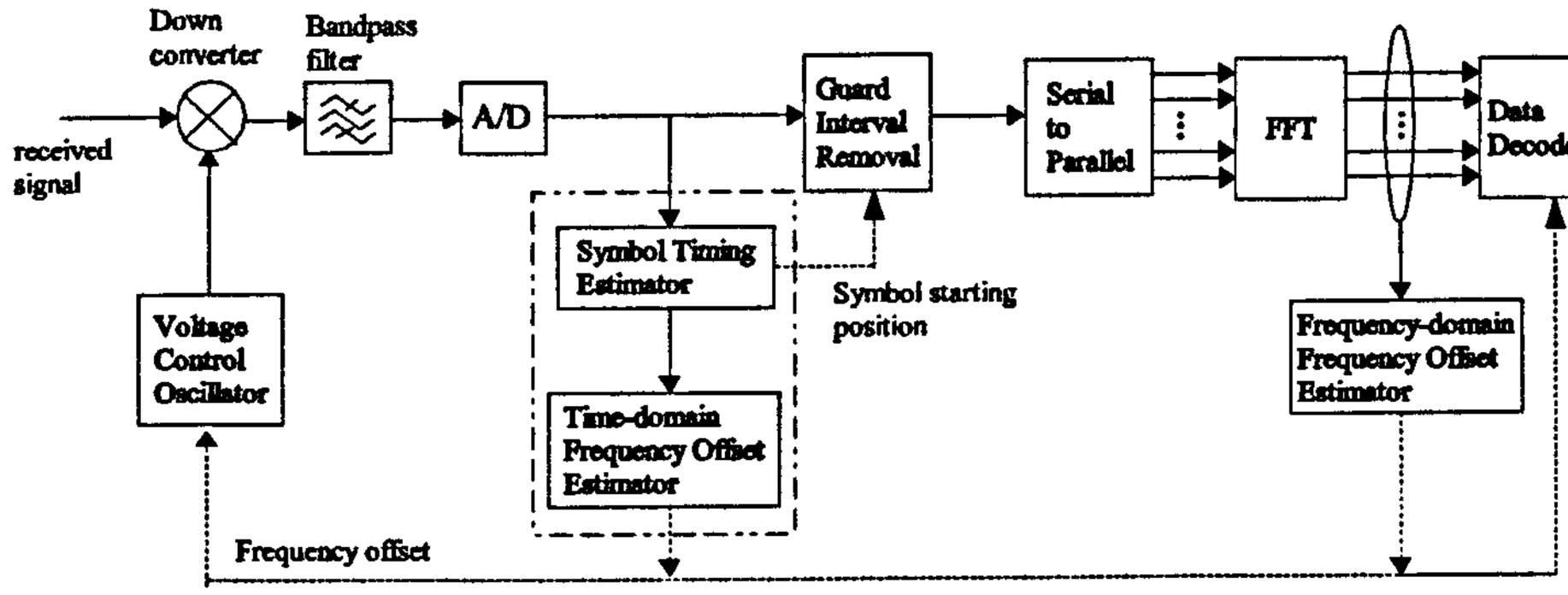

Figure 1.5: Block diagram of the arrangement of the symbol timing estimator and frequency offset estimators in an OFDM receiver

The sensitivity to frequency errors is inherent in the structure of the OFDM signal. For an OFDM system with N carriers, the frequency offset is measured with respect to the subcarrier frequency spacing, which is N times smaller than the overall signalling rate. Depending on N, the accuracy requirement in frequency recovery can be hundreds or thousands times greater than that pertaining to a single carrier system with the same overall data rate. Therefore, synchronization of the carrier frequency at the receiver must be performed very accurately. This makes OFDM systems more sensitive than single carrier systems to frequency errors.

On the other hand, symbol timing offset will cause intersymbol interference and phase rotation of demodulated data leading to errors. However, there is usually some tolerance for symbol timing errors when a cyclic prefix is used. The cyclic prefix provides a time window within which sampling may start. Timing error within this window causes only easily-correctable phase error on each carrier frequency.

Figure 1.5 shows an arrangement of the symbol timing estimator and frequency offset estimators in an OFDM receiver. The signal paths that contain the OFDM data are drawn in solid lines, while the paths that pass through the control information, including the estimated symbol timing error and the frequency offset, are drawn in broken lines. Two frequency offset estimators have been drawn in Figure 1.5. This is because the frequency offset estimation can be carried out by exploiting the redundancy of the

received OFDM signal in either time domain (pre-FFT) [5, 41, 50, 59, 65, 67, 89] or frequency domain (post-FFT) [11, 30, 68, 57, 99]. In practice, a receiver can consist of both or either one of these two types of frequency estimators. Since symbol timing and the frequency offset are usually estimated jointly, we have group the symbol timing estimator and the time-domain frequency offset estimator by broken lines. Examples of joint estimation algorithms can be found in the [4, 5, 16, 89, 106].

In the following two sections, we are going to review some of these algorithms for the symbol timing and the carrier frequency synchronization.

1.4 Symbol Timing Synchronization

A synchronization process is normally carried out in two phases: *acquisition* and *tracking*. In the acquisition phase, all other relevant system parameters are still unknown and initial estimates of the symbol timing error and frequency offset are acquired. Then, the receiver will operate in the tracking mode until it detects out-of-sync state and has to restart the process again. During the tracking phase, the coarse estimates are further improved and adapted to channel variations in order to correct for small short-term deviations.

Symbol timing synchronization is usually the first task in the acquisition phase so that the FFT data window can be aligned correctly with the useful part of the symbols. During acquisition of the symbol timing, the carrier frequency offset is assumed to be unknown; therefore its effect has not been compensated leading to a loss of orthogonality. Demodulated outputs in the frequency domain are expected to be affected by strong intercarrier interference. Consequently, algorithms for coarse symbol timing synchronization usually exploit only time-domain samples for a fast and reliable acquisition.

The OFDM symbol boundaries can be determined by looking for the known data structures within the received time-domain signal. These structures can be either the null symbol [26, 52, 75, 41] and cyclic prefix [5] which are the intrinsic structures defined in the OFDM system, or additional training symbols [50, 65, 89] which are inserted

Data structure	Method	References
Repeated Training Symbols	maximum autocorrelation	Kim[50], Mizoguchi[65] Schmidl[89]
Cyclic Prefix	maximum likelihood	Beek [5]
Null Symbols	minimum signal power	Eyadeh[26], Kiviranta[52], Nogami[75],Huang[41]

Table 1.1: Classification of symbol timing synchronization algorithms in terms of the time-domain data structure that has been used in the algorithms

explicitly in the transmitted data stream. The symbol timing estimation algorithms can be classified in terms of these data structures as shown in Table 1.1.

1.4.1 Repeated Training Symbols

Schmidl and Cox [89] have defined a timing metric with reference to two special training symbols appended at the beginning of an OFDM frame. The two-symbol training sequence has the following format

$$\begin{cases} c_{1,k} = \sqrt{2}(x_{1,k} + j \cdot y_{1,k}) & k = 0, 2, \cdots, N-2 \\ c_{1,k} = 0 & k = 1, 3, \cdots, N-1 \\ c_{2,k} = x_{2,k} + j \cdot y_{2,k} & k = 0, 1, 2, \cdots, N-1 \end{cases} \tag{1.13}$$

where $\{x_{1,k}, y_{1,k}\}$ and $\{x_{2,k}, y_{2,k}\}$ are complex data to be transmitted at the k-th sub-carrier of the first and second training symbols respectively. Their values are generated from a pseudo-noise (PN) sequence v_k so that

$$v_k = \sqrt{2}\left(\frac{c_{2,k}}{c_{1,k}}\right) \tag{1.14}$$

The odd frequencies of the first symbol carry no data and are modulated with zeros. Therefore, in time-domain the two halves of the first training symbol are identical. Transmitted data will not be recognized as the start of the frame since the actual data symbol must contain odd frequencies. The PN sequence is scaled up by $\sqrt{2}$ to maintain constant symbol energy.

Upon reception, the first half of the first training symbol will be different from the second half for a phase shifted caused by the carrier frequency offset. Multiplying the conjugate of one sample from the first half $\{r_{d+m}\}$ by the corresponding sample from the second half $\{r_{d+m+N/2}\}$, and summing all the products give the result $P(d)$

$$P(d) = \sum_{m=0}^{N/2-1} r^*_{d+m} r_{d+m+N/2} \tag{1.15}$$

where d is the time index of the starting position of the sliding data window. This can also be implemented more efficiently with the iterative formula

$$P(d+1) = P(d) + (r^*_{d+N/2} r_{d+N}) - (r^*_d r_{d+N/2}) \tag{1.16}$$

The multiplication cancels the channel effect and each product will have a phase shift proportional to the frequency offset. At the beginning of the frame, the products of each of these pairs of samples will have approximately the same phase, so that the magnitude of the sum $P(d)$ will assume a large value. A timing metric is defined as the square of the sum $P(d)$ normalized by the received energy in the second half-symbol

$$M(d) = \frac{|P(d)|^2}{(R(d))^2} \tag{1.17}$$

where

$$R(d) = \sum_{m=0}^{N/2-1} |r_{d+m+N/2}|^2 \tag{1.18}$$

Finally, the symbol timing $\tilde{d}$ is found by sliding the summation window to determine the location that maximizes the metric $M(d)$.

$$\tilde{d} = \arg\max_d \{M(d)\} \tag{1.19}$$

For the additive white Gaussian channel, there is a plateau of length equal to the guard interval where the metric reaches the maximum. The plateau region leads to some uncertainty as to the start of the frame. However, there is usually some tolerance on the accuracy of symbol timing estimation after cyclic prefixes have been appended [107]. It has been suggested that a fixed bias can be added to the final estimate to advance the FFT window forward to ensure that it starts within the guard interval.

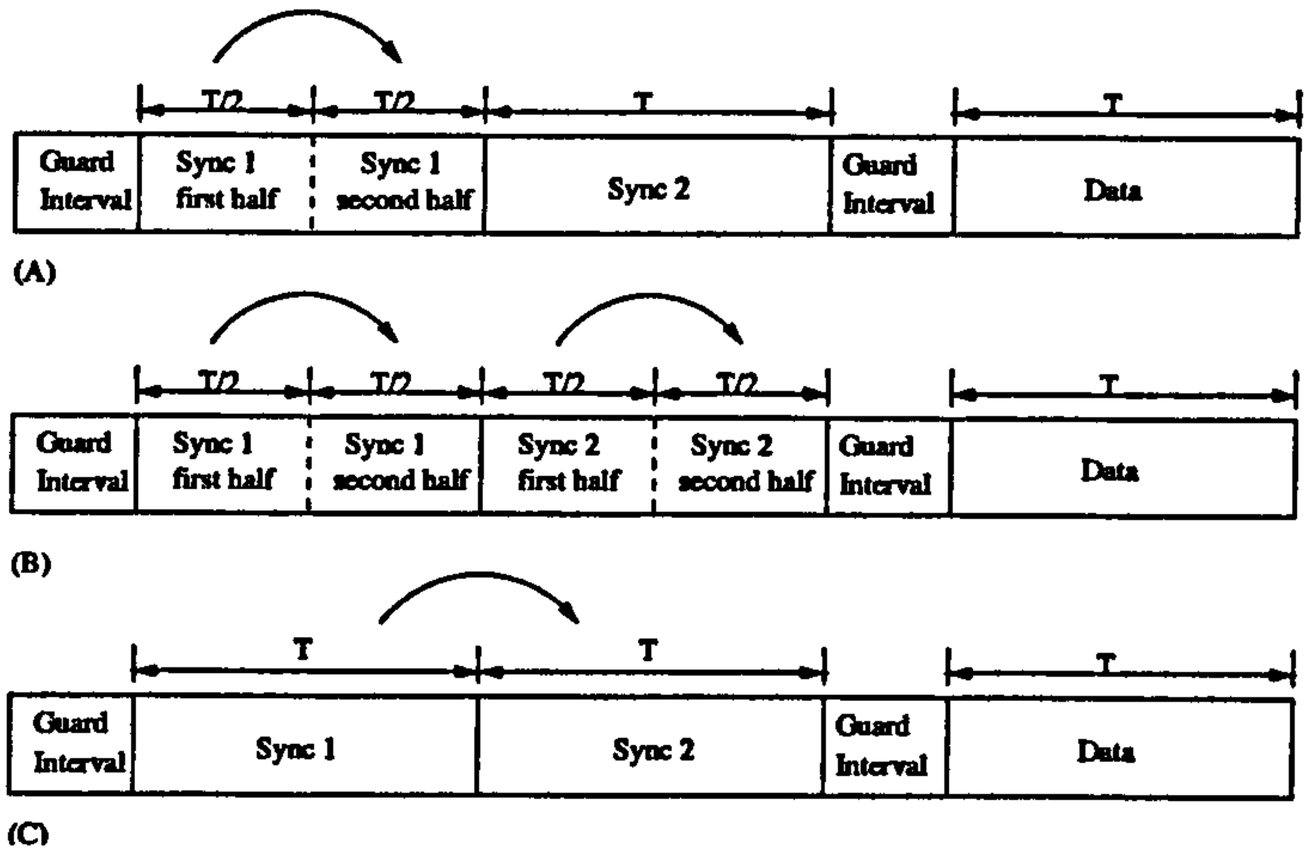

Figure 1.6: Training symbol structure in the (A) Schmidl's model [89] (B) Kim's model [50] and (C) Mizoguchi's model [65]. (Regions linked by '↷' are identical.)

In the Schmidl's method [89], the symbol timing metric does not depend on the second symbol, which is only used for channel measurement and coarse frequency estimation. Based on this method, alternative schemes are proposed by modifying the training symbol structure and making reference to the second symbol in the timing metric in order to improve the performance of the estimator. The modified training symbol structures are given in Figure 1.6. In [50], the first and the second training symbols are different but they have the same format; the first half of each symbol is identical to the corresponding second half. Alternatively, in [65] the second symbol is the replication of the first symbol and the limit of summation for calculation of $M(d)$ is increased from $(N/2-1)$ to $(N-1)$. The basic idea behind these alternative solutions is to increase the total number of samples used in averaging to increase the accuracy of the estimators.

1.4.2 Cyclic Prefix

Beek [5] states that the OFDM data symbols contain sufficient information to find the symbol timing and the fine frequency offset. This reduces the needs for training symbols and hence can increase the effective transmission data rate. In [5], an algorithm is proposed that exploits the time-domain correlation property between samples in the

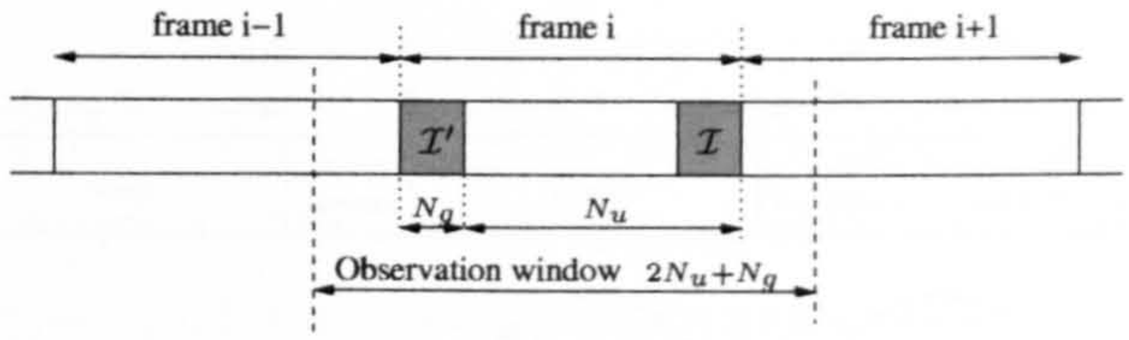

Figure 1.7: The observation window covering at least one complete OFDM symbol

cyclic prefix $\mathcal{I}'$ and its original copy at the end of the same symbol $\mathcal{I}$, as shown in Figure 1.7.

Suppose that samples $\{r_d\}$ can be modelled as independent random variables with zero mean and variance σ_s^2; the samples will be pairwise correlated as follows

$$E\{r_d r_{d+m}^*\} = \begin{cases} \sigma_s^2 + \sigma_n^2 & m = 0 \\ \sigma_s^2 e^{j2\pi\zeta} & m = N_u \\ 0 & \text{otherwise} \end{cases} \tag{1.20}$$

where ζ and σ_n^2 are the relative frequency offset and the variance of the zero-mean additive Gaussian noise respectively.

Let N_g and N_u be the length of the guard interval and the useful part respectively. The length of the observation window will be at least $(2N_u + Ng)$ to ensure that a complete OFDM symbol is covered. Based on the maximum likelihood criterion, Beek [5] has determined an estimate of the symbol starting location that is equal to

$$\widetilde{d} = \arg\max_d \left\{ \left| \sum_{m=d}^{d+N_g-1} r_m r_{m+N_u}^* \right| - \frac{\rho}{2} \sum_{m=d}^{d+N_g-1} \left(|r_m|^2 + |r_{m+N_u}|^2 \right) \right\} \tag{1.21}$$

where ρ is the signal-to-noise ratio (SNR) at the receiver input.

$$\rho = \frac{\sigma_s^2}{\sigma_s^2 + \sigma_n^2} = \frac{\text{SNR}}{\text{SNR} + 1} \tag{1.22}$$

A major drawback of this algorithm is that the SNR is usually unknown and has to be estimated at the receiver. This increases the complexity of the system.

1.4.3 Null Symbols

In general, a number of symbols are grouped and transmitted together in frames. The frame structure is fixed and is known to the receiver. The receiver can determine the

symbol timing from the frame structure once the starting positions of frames are known. Therefore, coarse frame synchronization also implies coarse symbol synchronization.

In the European digital audio broadcasting system, the first interval in each frame is defined as the synchronization channel [21] which consists of a *null symbol* and a *phase reference symbol*. Null symbols contain no energy and all carriers are switched off. Basically, it corresponds to a gap between two frames with length equal to one OFDM symbol period. Phase reference symbol constitutes the reference for the differential modulation for the next OFDM symbol.

Null symbols will cause dips in the signal power level. Therefore, coarse frame synchronization can be achieved by monitoring the received signal power in the time domain [52, 75, 41] with a simple amplitude detection circuit and comparing the outputs with predetermined thresholds. In [52], two thresholds are used adding hysteresis to the detector to suppress the effects of noise. Correct detection of a null symbol can also be cross-examined by checking if the next symbol is a phase reference symbol.

However, this method cannot be used in burst mode because there is no difference between null symbol and idle period between bursts.

1.5 Carrier Frequency Synchronization

The relative frequency offset is defined as the difference in frequency between oscillators in the transmitter and receivers normalized by intercarrier frequency spacing. It can be divided into an integer part and a fractional part, namely the *coarse frequency offset* [1] and *fine frequency offset* respectively. In general, the fine frequency offset is continuously estimated during the tracking phase, while either the whole frequency offset or only the coarse frequency offset is determined in the acquisition phase.

Frequency synchronization algorithms can be divided in two main categories. The first group are based on devoting specific training symbols [41, 50, 59, 65, 67, 89] or pilot carriers [68]. These data-aided schemes are suitable for the applications requiring fast and reliable synchronization [51]. However, the use of training data lowers the

[1] In this thesis, we have proposed algorithms to determine the coarse frequency offset.

Methods	sources	References
maximum likelihood	cyclic prefix	Daffara[23], McCormick[64], Van de Beek [5]
	one training symbol	Kim[51], Morelli[67]
	two training symbol	Moose[68], Schmidl[89], Yanzeng[106]
nonlinear least squares fitting	10 short + 2 long symbols	Li[56]
Expectation-maximization	M-PSK modulated data	Huq[40], Panayirci[84]
subspace-based	virtual carriers	Bolcskei[11], Ge[30], Liu[57], Tureli[100]
minimum power detection	virtual carriers	Barbarossa[4], Kim[49]

Table 1.2: An example of the categorization of the frequency offset estimators by the demodulation methods

achievable data rate. Therefore, alternate blind methods that do not make use of pilot symbols and training sequences are desirable. These second schemes are usually based on exploiting the cyclic prefix [5, 23, 64] or null subcarriers [30, 57, 61, 99].

From another point of view, the estimation can also be carried out in either time domain or frequency domain. Schmidl and Cox [89] propose an autocorrelation technique in the time domain between the two identical halves of the first training symbol. Only one training symbol is used in [51, 67] and the symbol is divided into identical parts. In [56], a preamble with 10 identical short OFDM symbols and two identical long symbols as defined in IEEE802.11a standard is used .

In the frequency domain, Moose [68] gives a maximum likelihood frequency estimator based on the autocorrelation of the two identical halves in the first training symbol. Subspace-based algorithms in [11, 30, 57, 99] exploit the low-rank properties of the virtual carriers. In [4, 49], the average energy falling across the virtual subcarriers at the guard band are measured and the oscillator frequency is updated until we reach a minimum of the measured energy.

Table 1.2 gives an example of categorization of the frequency offset estimators by the demodulation methods. Alternatively, the algorithms given in the literature can be roughly categorized into four classes with reference to the data sources as follows.

(1) Repeated symbols in time-domain

(2) Repeated symbols in frequency-domain

(3) Cyclic Prefix

(4) Virtual Subcarriers

1.5.1 Repeated Symbols (Time-domain)

The frame header in the Schmidl's model consists of two training symbols and two halves of the first training symbol are identical. Due to the frequency offset, the final down-converted baseband signal $r(t)$ will be different from $s(t)$ by a phase rotation factor such that

$$r(t) = s(t)e^{j2\pi\Delta_f t} \quad , 0 \leq t < T/2 \tag{1.23}$$

where $s(t)$ is the received signal, and Δ_f is the frequencies difference between the oscillators in the transmitter and the receiver. If the OFDM symbol rate is much higher than the channel fading rate, we will have $s(t+T/2) \approx s(t),\ 0 \leq t < T/2$. Therefore,

$$\begin{aligned} r(t)^* r(t+T/2) &= s(t)^* e^{-j2\pi\Delta_f t} \cdot s(t+T/2) e^{j2\pi\Delta_f (t+T/2)} \\ &\approx |s(t)|^2 e^{j2\pi\Delta_f T/2} \\ &= |s(t)|^2 e^{j\pi T\Delta_f} \end{aligned} \tag{1.24}$$

As shown, the main difference between the two halves of the first training symbol will be a phase difference ϕ given by

$$\phi = \pi T \Delta_f \tag{1.25}$$

After the symbol timing $\widetilde{d}$ has been found, the phase ϕ can be estimated by

$$\widetilde{\phi} = \tan^{-1}\left(\sum_{m=0}^{N/2-1} r^*_{\widetilde{d}+m} r_{\widetilde{d}+m+N/2}\right) \tag{1.26}$$

Then, the fine frequency offset estimate is determined by

$$\widetilde{\Delta}_f = \frac{\widetilde{\phi}}{\pi T} \tag{1.27}$$

On the other hand, the second training symbol in Schmidl's frame structure [89] is used to find the remaining coarse frequency offset which is equal to $2\hat{g}/T$. The parameter $\hat{g}$

is the number of even positions shifted and can be calculated by finding $\hat{g}$ to maximize the metric

$$B(g) = \frac{\left| \sum_{k \in \kappa} \tilde{c}_{1,k+2g}^{*} \; v_k^{*} \; \tilde{c}_{2,k+2g} \right|^2}{2 \left[\sum_{k \in \kappa} |\tilde{c}_{2,k}|^2 \right]^2} \tag{1.28}$$

where $\tilde{c}_{1,k}$ and $\tilde{c}_{2,k}$ are the FFT outputs of the two training symbols after the frequency offset $\tilde{\phi}/\pi T$ is corrected and $k \in \kappa = \{0, 2, \cdots, N-1\}$.

1.5.2 Repeated Symbols (Frequency Domain)

In [68], Moose proposed an algorithm to find the fine frequency offset by making use of repeated data symbols and comparing carriers phases between the two symbols. The algorithm works on the FFT outputs of the received signal, even though it is too noisy for satisfactory data recovery.

Assuming additive white Gaussian noise and slow fading channel, the maximum likelihood estimate [68] of the frequency offset ζ is given by

$$\zeta = \frac{1}{2\pi} \tan^{-1} \left\{ \frac{\sum_{k=0}^{N-1} \mathrm{Im}[c_{2,k} c_{1,k}^{*}]}{\sum_{k=0}^{N-1} \mathrm{Re}[c_{2,k} c_{1,k}^{*}]} \right\} \tag{1.29}$$

where $c_{1,k}$ and $c_{2,k}$ are the FFT outputs of the first and second symbol at the k-th carrier respectively. Im[·] and Re[·] are the imaginary and real parts of the complex value, respectively. Although derived for an AWGN channel, the estimator is insensitive to channel and can be used for a multipath environment. It has been shown that the error in estimation depends only on total symbol energy [68].

However, if the frequency offset is close to half of the carrier spacing, that is $\zeta \approx \pm 0.5$, there will be abrupt jumps in the estimator's output as shown in Figure 1.8. This is due to noise and intrinsic phase-wrapping property of the Moose's estimator, which is basically the output of an arc-tangent function. There are ambiguities in choosing the correct answer and *a priori* knowledge of the range of the frequency offset

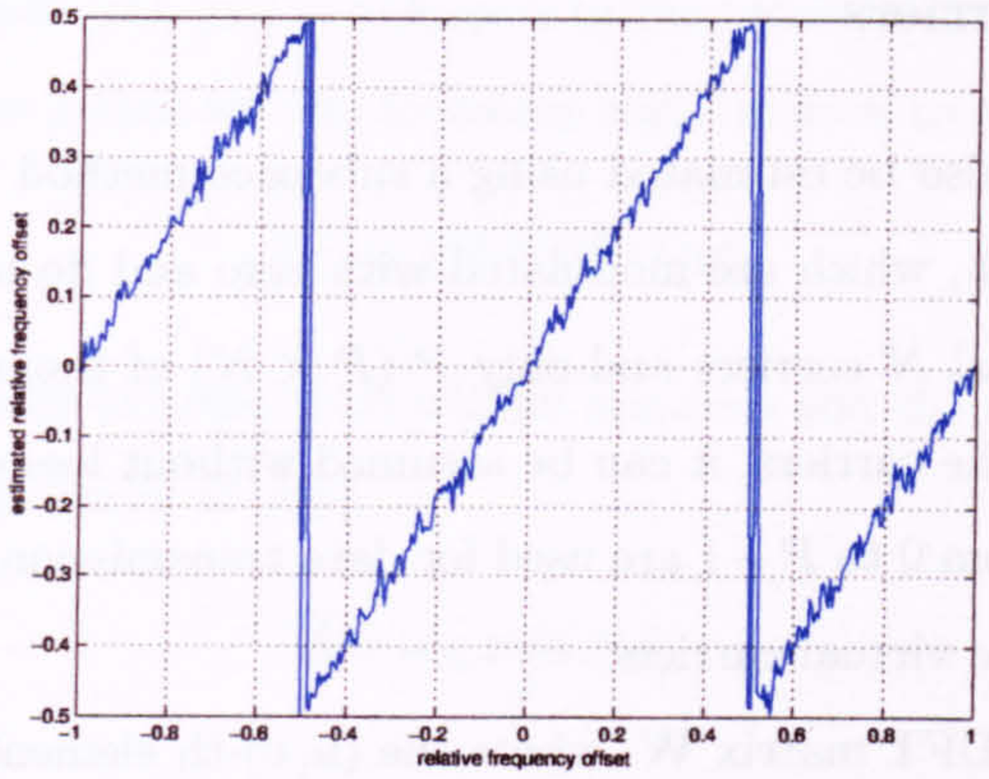

Figure 1.8: Outputs of the Moose's estimator (AWGN channel with S/N=1 dB and QPSK modulation on all carriers)

is required. Therefore, the tracking range of the estimator is limited to half of the carrier spacing. The tracking range can be increased by using shortened DFTs with larger carrier spacings so that the phase shift does not exceed $\pm\pi$.

1.5.3 Cyclic Prefix

Although the cyclic prefix is designed to combat intersymbol interference from multi-path echoes, it can also be used to estimate the fine frequency offset. The cyclic prefix and its original copy can be regarded as a pair of repeated symbols separated by a distance equal to the useful part of an OFDM data symbol and have fewer samples.

In [5], a joint algorithm for both symbol timing and fine frequency offset estimation has been proposed. From Equation 1.21, after the symbol timing $\widetilde{d}_{ML}$ has been found, the estimated fine frequency offset $\widetilde{\zeta}$ is given by

$$\widetilde{\zeta} = -\frac{1}{2\pi} \tan^{-1} \left(\sum_{m=\widetilde{d}_{ML}}^{\widetilde{d}_{ML}+N_g-1} r_m r^*_{m+N_u} \right) \tag{1.30}$$

It has been shown by simulations in [5] that above a certain level, increasing the cyclic prefix no longer improves the symbol timing estimation, and the improvement on frequency offset estimation is minimal. Therefore, the maximum useful cyclic prefix length is upper-bounded for a given SNR on an AWGN channel. There is no need to increase the length of the cyclic prefix beyond this value.

1.5.4 Virtual Carriers

Frequency offset can also be estimated using a subspace method with reference to the virtual carriers [57, 99], which are modulated with zero and do not carry useful data. Suppose there are total N carriers and only P ($P < N$) of them are modulated with data. By relabelling the carriers, it can be assumed without loss of generality that the carriers with index from 0 to $P-1$ are used for data transmission, while the remaining $N-P$ carriers are the virtual carriers.

The $N \times N$ unitary IDFT matrix $\mathbf{W}$, where the (u,v)-th element of $\mathbf{W}$ is

$$\mathbf{W}(u,v) = \exp\left(\frac{j2\pi uv}{N}\right) \qquad ,u,v = 0,\cdots,N-1 \tag{1.31}$$

can be partitioned into two parts

$$\mathbf{W} = [\mathbf{W_p}|\mathbf{W}_\perp] \tag{1.32}$$

The matrix $\mathbf{W_p}$ is a $N \times P$ submatrix of $\mathbf{W}$ with columns corresponding to the modulated carriers whereas $\mathbf{W}_\perp$ is the remaining N-P columns for the virtual carriers. Since $\mathbf{W}$ is unitary, the matrix $\mathbf{W}_p$ and $\mathbf{W}_\perp$ are orthogonal to each other. That is

$$\mathbf{W}_\perp^{\mathbf{H}}\mathbf{W_p} = 0 \tag{1.33}$$

Denote $\mathbf{H}_p$ as a $P \times P$ diagonal matrix whose entries are taken from the frequency transfer function of the channel that correspond to the P subcarriers. These subcarriers are modulated with data $\mathbf{c} = [c(0) \ \ldots \ c(P-1)]^T$.

Then, the received data $\mathbf{r} = [r(0) \ \ldots \ r(N-1)]^T$ is

$$\mathbf{r} = \mathbf{E}(\delta)\mathbf{W_p}\mathbf{H_p}\mathbf{c} \tag{1.34}$$

where $\mathrm{E} = diag(1, e^{j\delta}, \cdots, e^{j\delta(N-1)})$ and δ is the relative frequency offset. The received OFDM signal will be orthogonal to the space $\mathbf{E}(\delta)\mathbf{W}_\perp$ because

$$\begin{aligned}
(\mathbf{E}(\delta)W_\perp)^H\mathbf{r} &= \mathbf{W}_\perp^H\mathbf{E}^H(\delta)\mathbf{r} \\
&= \mathbf{W}_\perp^H\mathbf{E}^H(\delta)\mathbf{E}(\delta)\mathbf{W_p}\mathbf{H_p}\mathbf{c} \\
&= \mathbf{W}_\perp^H\mathbf{W_p}\mathbf{H_p}\mathbf{c} \qquad (\because \mathbf{E}^H(\delta)\mathbf{E}(\delta) = \mathbf{I}) \\
&= 0
\end{aligned} \tag{1.35}$$

In general δ differs from zero and is unknown to the receiver. It can be determined by searching for the value δ that set the following cost function to zero

$$J(\delta) = \|\mathbf{W}_{\perp}^{H}\mathbf{E}^{H}(\delta)\mathbf{r}\| \tag{1.36}$$

However, in the presence of noise, $J(\delta)$ will be non-zero and the carrier offset $\widetilde{\delta}$ will be estimated from the minimum of $J(\delta)$

$$\widetilde{\delta} = \arg\min_{\delta} J(\delta) \tag{1.37}$$

Computer simulations have been carried out to determine the trajectory of the cost function. It is assumed that $\delta = 0.1$, $N = 16$ or 32, the number of virtual carriers $V = 1, 2$ or 4 and each carrier is QPSK modulated by random data with unity variance. The trajectories of J are plotted in Figure 1.9. Then, the data are assumed to be corrupted by additive white Gaussian noise with S/N=1 dB and the results are plotted in Figure 1.10.

As shown in Figure 1.9, the outputs of the cost functions are zero when the variable δ is equal to the frequency offset. In the presence of noise as shown in Figure 1.10, the trajectories of the cost functions still achieve the minimum points at $\delta = 0.1$, but the corresponding values are different from zero. In addition, there are many sidelobes and the total number of sidelobes increases with the number of virtual carriers. These sidelobes will affect the accuracy of the estimator under noisy condition.

In addition, as shown in Figure 1.11, the tracking range of the estimator should be limited to [-0.5,+0.5] of the carrier spacing because there are multiple minimum points and *a priori* knowledge on the range of the true offset is required in order to resolve the ambiguity.

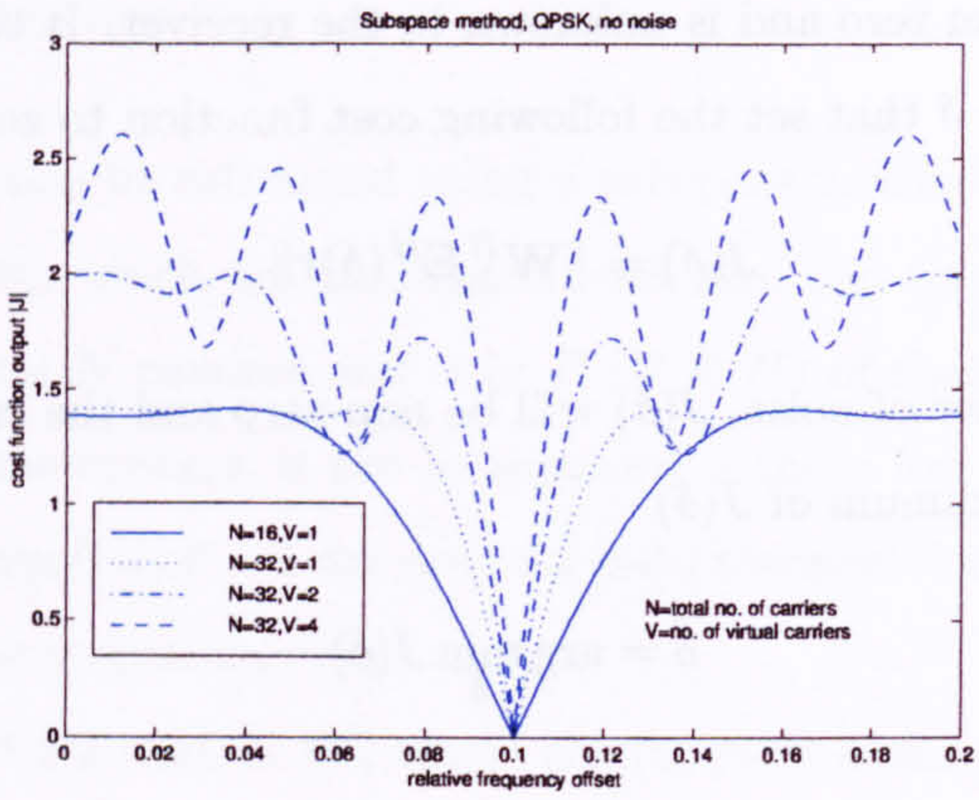

Figure 1.9: Direct computation of the cost function trajectories with various composition of data and virtual carriers (frequency offset $\delta = 0.1$)

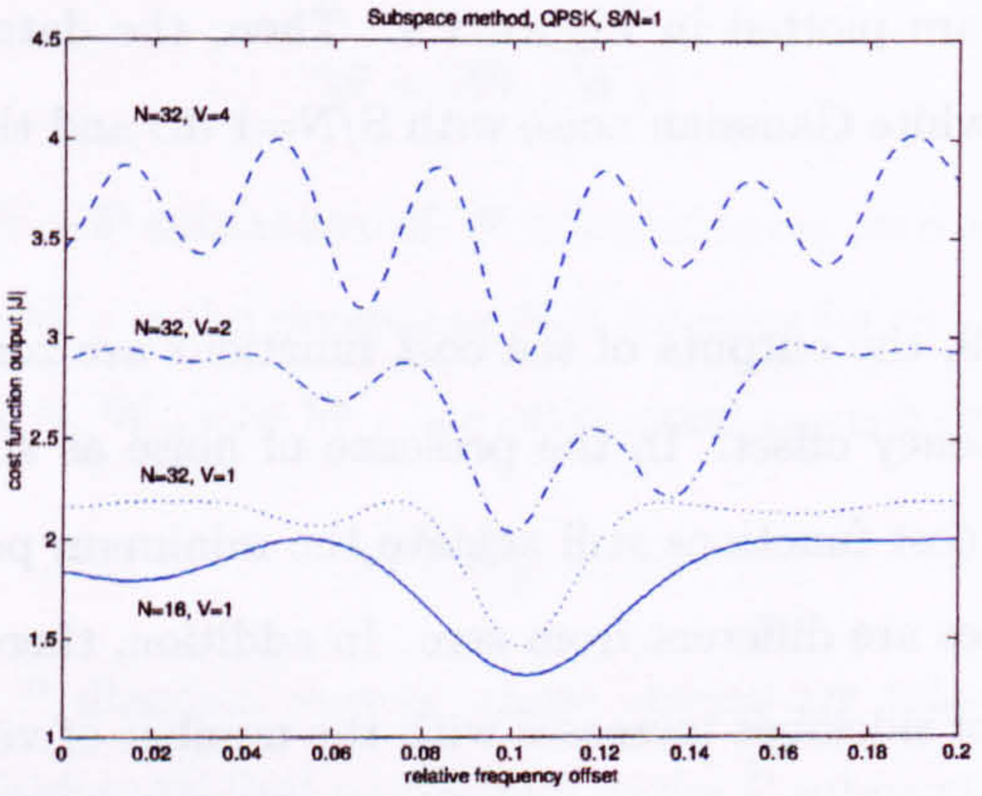

Figure 1.10: Cost function trajectories under noisy environment with additive white Gaussian noise, S/N=1 dB (frequency offset $\delta = 0.1$)

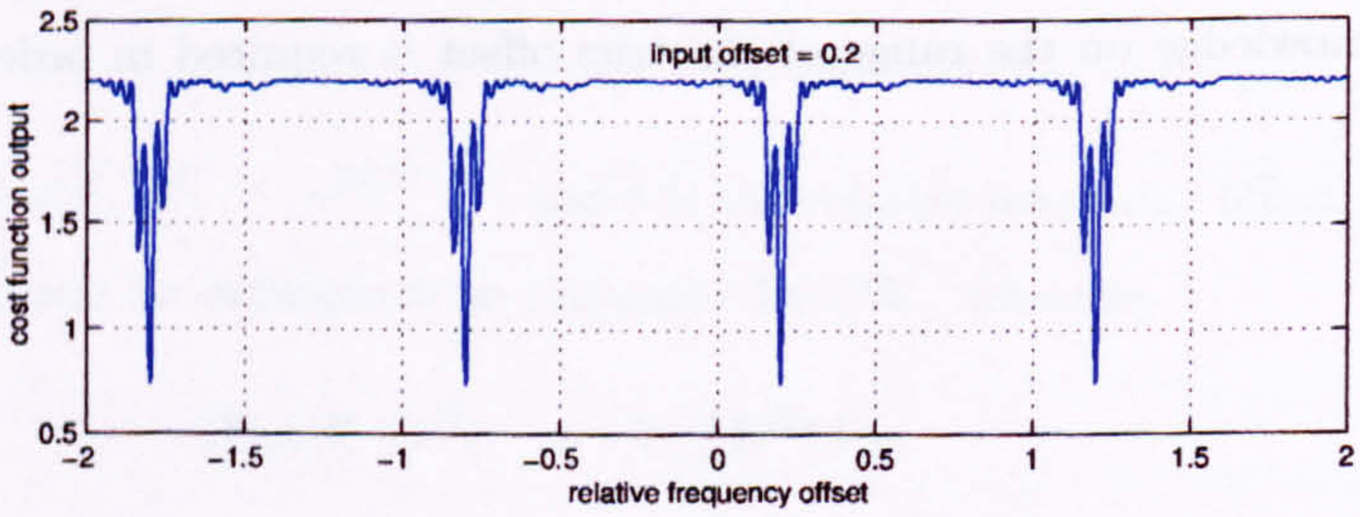

Figure 1.11: The cost function trajectory showing multiple minimum points ($\delta = 0.2$, QPSK data, N=32, V=2, S/N=10 dB)

Chapter 2

Effects Of Synchronization Defects

2.1 Introduction

OFDM offers advantages in transmission over multipath channels. However, the OFDM system is sensitive to synchronization defects. A receiver has to correctly align the data capture window with the useful part of OFDM symbols in order to remove the guard intervals. However, there may be errors in correctly locating the starting position of the OFDM symbols leading to symbol timing error. In addition, the RF oscillators and digital sampling clocks between the transmitter and receivers may run at different frequencies. In this chapter, we will discuss the effects of these synchronization defects on system performance.

At first, the effect of symbol timing error will be discussed. Then, assuming that there is no symbol timing error such that the useful part of the OFDM symbol is identified correctly, the effects due to the phase offset, frequency offset and sampling clock are determined analytically and are verified by computer simulations. Finally, a brief summary is given.

2.2 Effects of Symbol Timing Offset

In an OFDM communication system, data are transmitted in a continuous stream of symbols. Each symbol is divided into two parts: a guard interval and a useful part. The useful part consists of the payload data to be processed by the decoder. The guard interval is the cyclic extension of the useful part and has to be removed before passing the received data to the decoder.

First of all, a receiver has to find the starting position of the useful part. It has to align the data window with the useful part of an OFDM symbol and remove the guard interval. With this criterion, the optimum position will be the boundary between the guard interval and the useful part. The FFT data window will cover the useful part only when the data capturing window is placed in this position.

On the other hand, the FFT data window will cover the boundary of two adjacent symbols if the symbol timing offset is large. In this case, the input to the FFT demodulator will be the concatenation of segments coming from two different symbols which now interfere with each other. We conclude that there is strong inter-symbol interference when the data window covers the boundary of symbols. Since the system is effectively out of symbol timing synchronization, we are not interested in studying the effects of symbol timing offset under this situation. Therefore, from now on we assume that the symbol timing offset is small enough so that the FFT data window is always placed within the boundary of one symbol.

Suppose the useful part of an OFDM symbol is composed of N_u samples and there are N_g samples in the guard interval. Then the data, $c(k)$, modulated on the k-th subcarrier is given by

$$c(k) = \sum_{n=0}^{N_u-1} r(n) e^{-j\frac{2\pi kn}{N_u}} \tag{2.1}$$

where $r(n), n = -N_g \ldots N_u - 1$, is the received time-domain samples of the OFDM symbol.

The data window can be located at three possible positions as illustrated in Figure 2.1. It is τ_s samples shifted from the optimum position. Due to the multipath propagation, the guard interval will be affected by the preceding symbol. This noisy region is shaded

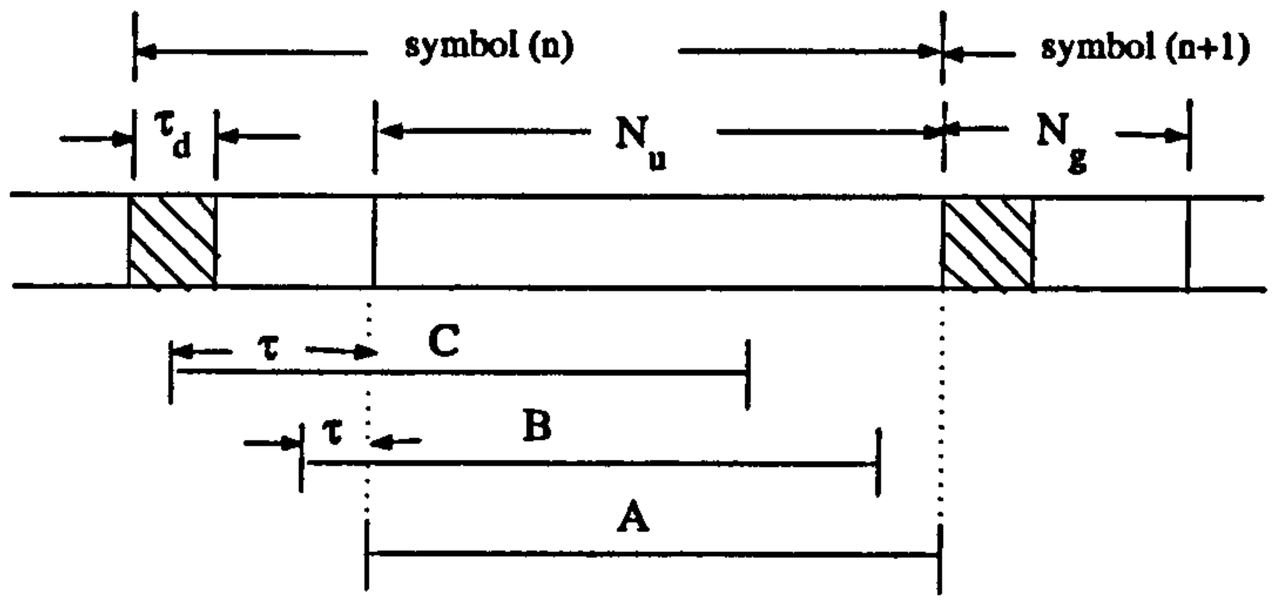

Figure 2.1: The data window can start at three possible positions: (A) $\tau_s = 0$, perfect alignment (B) $\tau_s \leq N_g - \tau_d$, no ISI (C) $\tau_s > N_g - \tau_d$, with ISI

in Figure 2.1. The length of this noisy region is equal to those of the channel impulse response function, and is indicated as τ_d in the Figure. We are going to discuss each case one-by-one.

Position A:

The position A is the optimum position in which the data window is exactly aligned with the useful part of the symbol. The symbol timing offset τ_s is equal to zero and the entire guard interval is discard. There will be no error on the outputs after taking FFT on the selected data.

Position B:

The symbol timing offset τ_s is greater than zero but less than $N_g - \tau_d + 1$. Total τ_s samples from the guard interval and $N_u - \tau_s$ samples from the useful part will be selected, which are still free from inter-symbol interference.

Since samples in the guard interval are copied from the tails of the useful part, the set of samples taken from the data window at position B is effectively a cyclicly shifted version of the original useful part. Although the useful part has finite duration, it behaves as if it were a periodic signal with respect to the data window by cyclicly extending into the guard interval. The symbol timing offset is equivalent to a time delay in digital sampling. It is a well-known fact that delay in the time domain can be represented by a linear phase shift in the frequency domain [77]. Therefore, the demodulated data of

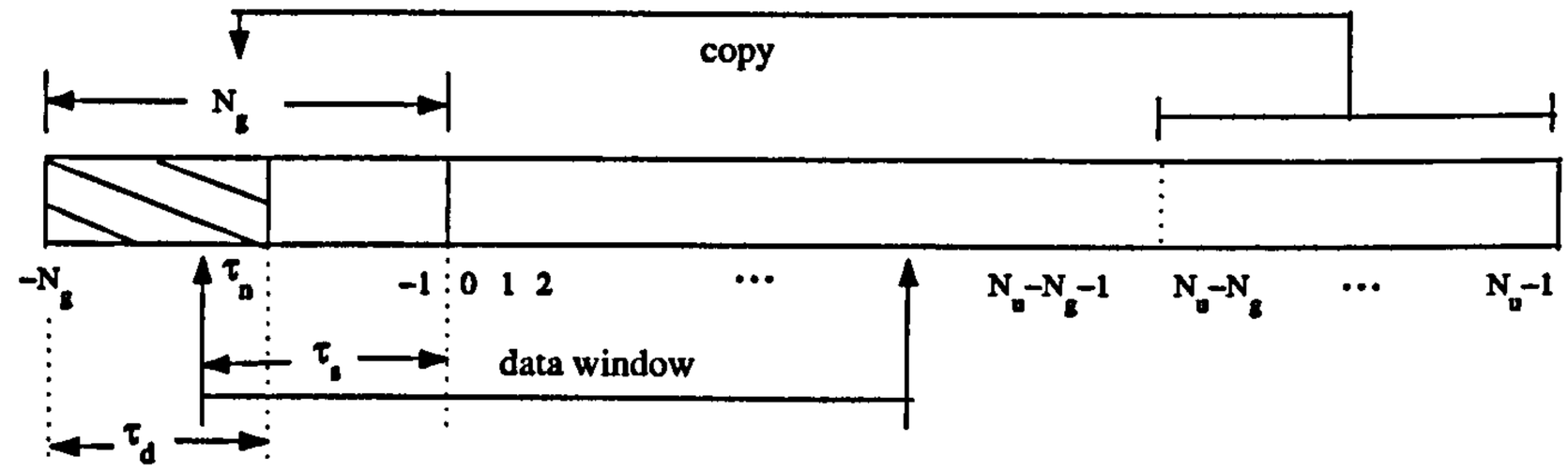

Figure 2.2: Illustration of the samples labelling scheme when $\tau_s > N_g - \tau_d$

the k-th subcarrier, $\tilde{c}(k)$, is equal to

$$\begin{aligned} \tilde{c}(k) &= \sum_{n=0}^{N_u-1} r(n-\tau_s) e^{\frac{-j2\pi kn}{N_u}} \\ &= c(k) e^{-j\frac{2\pi k\tau_s}{N_u}} \end{aligned} \tag{2.2}$$

As seen in Equation 2.2, the only effect due to the symbol timing offset is a change in phase, which increases linearly with the carrier index k. There is no inter-symbol interference as long as the starting position of the data window is within the ISI-free region of the guard interval.

Position C:

In position C, the symbol timing offset τ_s is greater than $N_g - \tau_d$. The data window is still within the symbol boundary. However, some samples will come from the noisy region of the guard interval that is corrupted by inter-symbol interference with the preceding symbol.

For the purpose of illustration, we label the samples of the OFDM symbol with indices varying from $-N_g$ to N_u-1 as shown in Figure 2.2. The samples can be represented by the set $\{r(-N_g), \cdots, r(-1), r(0), \cdots, r(N_u-1)\}$. In order to simply the presentation, we denote $\tau_{gd} \equiv N_g - \tau_d + 1$. Then, the set of samples taken from the data window at position C can be partitioned into two subsets:

- ISI-free: $\{r(-\tau_{gd}+1), r(-\tau_{gd}+2), \cdots, r(N_u-1-\tau_s)\}$
- with ISI: $\{r(-\tau_s), r(-\tau_s+1), \cdots, r(-\tau_{gd})\}$

By taking a summation on these two data sets separately, we have shown that [Appendix A.1] the demodulated data $\tilde{c}(k)$ is

$$\begin{aligned}\tilde{c}(k) &= \sum_{n=0}^{N_u-1} r(n-\tau_s)e^{\frac{-j2\pi kn}{N_u}} \\ &= c(k)e^{-j\frac{2\pi k\tau_s}{N_u}} + \mathcal{N}_{\text{ISI}} \end{aligned} \tag{2.3}$$

where

$$\mathcal{N}_{\text{ISI}} \equiv e^{-j\frac{2\pi k\tau_s}{N_u}} \sum_{n=-\tau_s}^{-(N_g-\tau_d+1)} \Big[r(n) - r(N_u+n)\Big] e^{-j\frac{2\pi kn}{N_u}} \tag{2.4}$$

By construction, the second samples set $\{r(-\tau_s), r(-\tau_s+1), \cdots, r(-\tau_{gd})\}$ is the copy of the samples $\{r(N_u-\tau_s), r(N_u-\tau_s+1), \cdots, r(N_u-\tau_{gd})\}$ and they should be identical. However, due to the intersymbol interference, the received signal $r(n)$ is no longer equal to $r(N_u+n)$. It follows that the term $\mathcal{N}_{\text{ISI}}$ in Equation 2.3 is non-zero. In other words, the demodulated data from one subcarrier is affected by adjacent subcarriers and they are not "orthogonal" to each other anymore leading to intercarrier interference. In conclusion, this interference term will affect the "orthogonality" between the OFDM carriers.

The length of the guard interval must be longer than that of the channel impulse response . The difference in length between the guard interval and the channel impulse response function limits the symbol timing offset that the system can tolerate. If the offset is within this limit, the noise term $\mathcal{N}_{\text{ISI}}$ will vanish and there is no intercarrier interference.

2.3 Relationship between Synchronization Errors

Suppose an OFDM symbol consists of N frequency carriers and all of them are used to transmit data. Let $c(k)$ be the complex data modulated on the frequency carrier k and ΔF be the intercarrier frequency spacing, which is equal to the reciprocal of the symbol duration. That is

$$\Delta F = \frac{1}{NT_s} \tag{2.5}$$

where T_s is the sampling period of the N-point IFFT modulation functional block. Then the transmitted complex envelope $s(t)$ of the OFDM symbol is given by

$$s(t) = \frac{1}{N}\sum_{k=0}^{N-1} c(k)e^{j2\pi f_k t} \qquad 0 \le t < NT_s \tag{2.6}$$

where

$$f_k = k\Delta F = \frac{k}{NT_s} \tag{2.7}$$

Let $h(t)$ be the impulse response of the channel and $H(k)$ be the corresponding frequency transfer function of the channel at the k-th subcarrier. It is assumed that the length of the cyclic prefix is longer than that of the channel impulse response $h(t)$, and the symbol timing has been correctly estimated so that the cyclic prefix is removed at the receiver completely.

Hence intersymbol interference can be ignored and the process of insertion and deletion of the guard interval is transparent to the data encoding and decoding units. Therefore, without affecting the results of the performance analysis, the guard interval will be excluded from the OFDM symbol model in order to simply the notation.

Denote Δf and θ as the frequency difference and phase offset between oscillators in the receiver and the transmitter, respectively. That is

$$\Delta f = \text{oscillator frequency at transmitter - oscillator frequency at receiver} \tag{2.8}$$

$$\theta = \text{oscillator phase at transmitter - oscillator phase at receiver} \tag{2.9}$$

After passing through a frequency selective fading channel, the received signal will be the convolution of the OFDM signal with the channel impulse response $h(t)$. The received baseband signal $r(t)$ is

$$\begin{aligned} r(t) &= e^{j(2\pi\Delta f t+\theta)}\Big\{s(t) * h(t)\Big\} \\ &= e^{j(2\pi\Delta f t+\theta)}\left\{\frac{1}{N}\sum_{k=0}^{N-1} c(k)H(k)e^{j2\pi f_k t}\right\} \end{aligned} \tag{2.10}$$

Define δ as the relative frequency offset of the baseband signal with respect to the intercarrier frequency spacing ΔF, that is

$$\delta \equiv \frac{\Delta f}{\Delta F} = NT_s\Delta f \tag{2.11}$$

From Equation 2.7 and Equation 2.11, the received signal $r(t)$ in Equation 2.10 can be represented as

$$r(t) = \frac{e^{j\theta}}{N} \sum_{k=0}^{N-1} c(k)H(k) \exp\left\{ j\frac{2\pi(k+\delta)t}{NT_s} \right\} \tag{2.12}$$

This signal will be digitized at the receiver by an A/D converter with sampling clock $(1-\epsilon)T_s$, where ϵ is the relative sampling clock error. The error ϵ is positive if the sampling clock in the receiver is running faster than that in the transmitter. From Equation 2.12

$$r(n) = \frac{e^{j\theta}}{N} \sum_{k=0}^{N-1} c(k)H(k) \exp\left\{ j\frac{2\pi(k+\delta)[n(1-\epsilon)]}{N} \right\} \tag{2.13}$$

Finally, the demodulated data $\tilde{c}(l)$ is obtained by taking FFT on $r(n)$

$$\begin{aligned} \tilde{c}(l) &= \sum_{n=0}^{N-1} r(n) \exp\left\{ -j\frac{2\pi ln}{N} \right\} \\ &= \frac{e^{j\theta}}{N} \sum_{n=0}^{N-1} \sum_{k=0}^{N-1} c(k)H(k) \exp\left\{ j\frac{2\pi(k+\delta)[n(1-\epsilon)]}{N} \right\} \exp\left\{ -j\frac{2\pi ln}{N} \right\} \end{aligned} \tag{2.14}$$

After simplifying and rearranging the terms [Appendix A.2], the demodulated data $\tilde{c}(l)$ can be written as

$$\tilde{c}(l) = c(l)H(l)e^{j\theta} \exp\left\{ j\frac{\pi[\delta-\epsilon(l+\delta)](N-1)}{N} \right\} \frac{\sin\pi[\delta-\epsilon(l+\delta)]}{N\sin\left[\frac{\pi[\delta-\epsilon(l+\delta)]}{N}\right]} + \mathrm{ICI}(l) \tag{2.15}$$

where

$$\mathrm{ICI}(l) = \sum_{\substack{k=0 \\ k\neq l}}^{N-1} c(k)H(k)e^{j\theta} \exp\left\{ j\frac{\pi[(k+\delta)(1-\epsilon)-l](N-1)}{N} \right\} \frac{\sin\pi[(k+\delta)(1-\epsilon)-l]}{N\sin\left[\frac{\pi[(k+\delta)(1-\epsilon)-l]}{N}\right]} \tag{2.16}$$

As shown in Equation 2.15, the demodulated data can be divided into two parts. The first part is the requested data $c(l)$ weighted by the channel transfer function at the same frequency, an exponential function and sine functions. The arguments of these weighting functions consist of the phase offset θ, frequency offset δ and the sampling clock error ϵ. These factors will modify both the phase and magnitude of the demodulated data.

The second part ICI(l) is the weighted summation of neighboring carriers. This term constitutes the intercarrier interference. If the numerical value of this term is large, the orthogonality between carriers in the OFDM system will be destroyed.

2.4 Effects of Phase Error

Suppose there are no frequency errors in the RF oscillators, but there is a phase error θ. In addition, the sampling clocks in the transmitter and the receiver are assumed to be running at the same frequency. Then δ and ϵ in Equation 2.16 can be set to zero. Hence the demodulated data of the l-th subcarrier will become

$$\widetilde{c}(l|\delta=0,\epsilon=0) = c(l)H(l)e^{j\theta} + \mathrm{ICI}(l|\delta=0,\epsilon=0) \tag{2.17}$$

$$\mathrm{ICI}(l|\delta=0,\epsilon=0) = \sum_{\substack{k=0\\k\neq l}}^{N-1} c(k)H(k)e^{j\theta}\exp\left\{j\frac{\pi(k-l)(N-1)}{N}\right\}\frac{\sin[\pi(k-l)]}{N\sin\left[\frac{\pi(k-l)}{N}\right]} \tag{2.18}$$

Since $k\in\mathbb{Z}$, $l\in\mathbb{Z}$, $k\neq l$ and $|k-l|<N$, we have

$$\frac{\sin[\pi(k-l)]}{\sin\left[\frac{\pi(k-l)}{N}\right]} = 0 \tag{2.19}$$

Therefore

$$\mathrm{ICI}(l|\delta=0,\epsilon=0) = 0 \tag{2.20}$$

It follows that [Appendix A.3]

$$\tilde{c}(l|\delta=0,\epsilon=0) = c(l)H(l)e^{j\theta} \tag{2.21}$$

Since the noise term ICI becomes zero, there is no intercarrier interference and carriers are mutually orthogonal. In other words, the phase error θ will not distort the amplitude of the demodulated data, but only introduce a phase rotation on all subcarriers. The amount of phase rotation is identical in all carriers and the direction of rotation will be in a clockwise direction if the oscillator in the receiver is leading that in the transmitter.

In practice, the term $e^{j\theta}$ can be combined with $H(l)$ and the joint effect can be resolved together during the process of channel estimation. Denote the modified channel transfer function $\tilde{H}(l)$ as

$$\tilde{H}(l) = H(l)e^{j\theta} \tag{2.22}$$

Then, the demodulated data can be determined by

$$\tilde{c}(l|\delta{=}0, \epsilon{=}0) = c(l)\tilde{H}(l) \tag{2.23}$$

2.5 Effects of Frequency Offset

The relative frequency offset δ is the ratio of the frequency difference Δf to the transmitted subcarrier spacing ΔF. In general, Δf will not be a whole integer multiples of ΔF. Instead, δ will be a real number and can be represented as the summation of an integer part m and a fractional part ζ as shown schematically in Figure 2.3. That is,

$$\Delta f = (m + \zeta)\Delta F \qquad m \in \mathbb{Z}, \quad |\zeta| \leq 0.5 \tag{2.24}$$

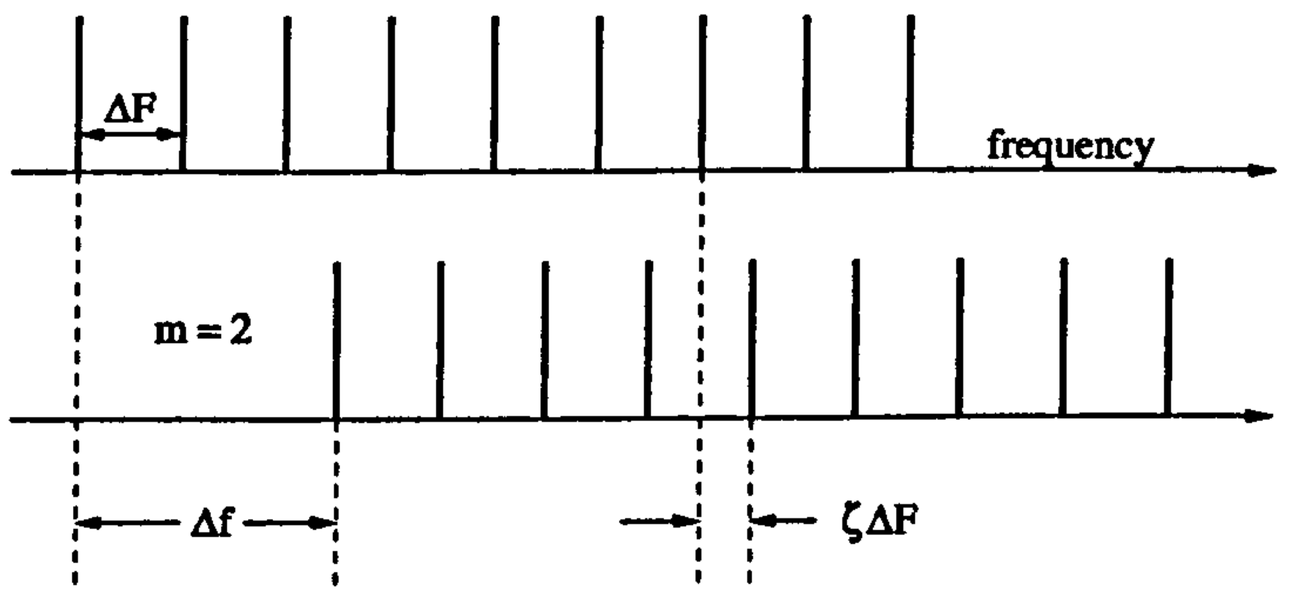

Figure 2.3: Components of the total frequency offset in an OFDM system

In other words, carrier frequency offset can be divided into coarse frequency offset and fine frequency offset. Coarse frequency offset, m, is the integer part of δ. It measures the frequency difference whose value is an integer multiple of subcarrier frequency spacing. Fine frequency offset, ζ, is the corresponding remainder and is the fractional part of δ whose value less than half of the subcarrier frequency spacing.

In order to study the effect of frequency offset on the demodulated OFDM data, we assume that there is no discrepancy between the sampling clocks, hence $\epsilon = 0$. Then, Equation 2.15 and Equation 2.16 can be reduced to

$$\tilde{c}(l|\epsilon{=}0) \;=\; c(l)\tilde{H}(l)\exp\left\{j\frac{\pi\delta(N-1)}{N}\right\}\frac{\sin\pi\delta}{N\sin\frac{\pi\delta}{N}} + \mathrm{ICI}(l|\epsilon{=}0) \tag{2.25}$$

$$ICI(l|\epsilon{=}0) = \sum_{\substack{k=0 \\ k\neq l}}^{N-1} c(k)\tilde{H}(k)\exp\left\{j\frac{\pi(k+\delta-l)(N-1)}{N}\right\}\frac{\sin\pi(k+\delta-l)}{N\sin\left[\frac{\pi(k+\delta-l)}{N}\right]} \tag{2.26}$$

2.5.1 Coarse Frequency Offset

Let us consider only the coarse frequency offset by assuming δ to be an integer equal to m. Since $\sin(m\pi) = 0, \forall\, m \in \mathbb{Z}$, the first term of $\tilde{c}(l)$ in Equation 2.25 will be equal to zero. Similarly, $\forall\, k \in \{0,\cdots,N{-}1\}, m \in \mathbb{Z}$ and $m \neq 0$, we have shown that [Appendix Equation A.16]

$$\frac{\sin\pi(k+m-l)}{N\sin\left[\frac{\pi(k+m-l)}{N}\right]} = \begin{cases} 1 & k = l-m \\ 0 & \text{otherwise} \end{cases} \tag{2.27}$$

In Equation 2.26, only the term corresponding to $k = l{-}m$ will remain and all other terms in the summation will be equal to zero. Therefore,

$$\tilde{c}(l|\epsilon{=}0, \delta{=}m \in \mathbb{Z}) = c(l-m)\tilde{H}(l-m) \tag{2.28}$$

The demodulated data at the l-th carrier is exactly equal to the $(l{-}m)$-th carrier in the original spectrum weighted by the corresponding channel transfer function. Since $c(l)$ is chosen arbitrarily and can be any one of the data carriers, it follows that not only $c(l)$ but the entire frequency spectrum is shifted by m intercarrier spacings.

In conclusion, the coarse frequency offset does not modify the spectrum shape of the original OFDM modulated data, but shifts the spectrum in frequency. Its absolute value determines the amount of shift expressed in the units of intercarrier frequency spacing while its polarity gives the direction. If the oscillator in the transmitter is running at higher frequencies than that in the receiver, the frequency offset m is positive and the frequency spectrum of the demodulated OFDM data will be shifted up. Otherwise, the frequency offset m will be a negative integer and the corresponding spectrum will be shifted down.

Alternatively, the shift of frequency spectrum can be explained by the time-frequency convolution relationship. From Equation 2.10, the received data in the time domain

results from the multiplication of a coarse frequency offset signal and the actual OFDM signal. In the time-domain, the coarse frequency offset signal is represented by the complex exponential function as shown in Equation 2.10. In the frequency-domain, this will be represented by an impulse located at the m-th frequency bin of the FFT output. Since multiplication in the time domain is equivalent to convolution in the frequency domain, the demodulated OFDM data will be the result of the convolution between this impulse function and the frequency spectrum of the original data. Therefore, the resulting frequency spectrum will be shifted accordingly.

2.5.2 Fine Frequency Offset

Assuming that the coarse frequency offset is known to be zero or it has been estimated and corrected so that the relative frequency offset is less than half of the intercarrier frequency spacing. That is, the integer part of the relative frequency offset is zero. From Equation 2.15 and Equation 2.16, the demodulated data will become

$$\tilde{c}(l|\epsilon=0,\delta=\zeta) = c(l)\tilde{H}(l)\exp\left\{j\frac{\pi\zeta(N-1)}{N}\right\}\frac{\sin\pi\zeta}{N\sin\frac{\pi\zeta}{N}} + I(l) \tag{2.29}$$

where $I(l) \equiv \mathrm{ICI}(l|\epsilon=0,\delta=\zeta)$ denotes the intercarrier interference from the neighboring carriers and is equal to

$$\mathrm{I}(l|\epsilon=0,\delta=\zeta) = \sum_{\substack{k=0\\k\neq l}}^{N-1} c(k)\tilde{H}(k)\exp\left\{j\frac{\pi(k+\zeta-l)(N-1)}{N}\right\}\frac{\sin\pi(k+\zeta-l)}{N\sin\left[\frac{\pi(k+\zeta-l)}{N}\right]} \tag{2.30}$$

Since $N \gg 1$ and $N \gg \pi\zeta$, $1/N \approx 0$ and $\sin(\pi\zeta/N) \approx \pi\zeta/N$. Therefore, $\tilde{c}(l)$ in Equation 2.29 can be approximated by

$$\tilde{c}(l|\epsilon=0,\delta=\zeta) \approx c(l)\tilde{H}(l)e^{j\pi\zeta}\left(\frac{\sin\pi\zeta}{\pi\zeta}\right) + I(l) \tag{2.31}$$

Unlike the coarse frequency offset, the fine frequency offset modifies both the phase and amplitude of the demodulated data. The amplitude is reduced by multiplying the original data by a function $\sin(\pi\zeta)/\pi\zeta$, while the phase is rotated by an angle proportional to the fine frequency offset ζ. The amount of phase rotation and amplitude degradation are independent of the frequency index of the carriers and all carriers are

equally affected. From Equation 2.30, if $\zeta \neq 0$, $\sin \pi(k+\zeta-l) \neq 0$, then $I(l) \neq 0$. Therefore, the carriers are no longer orthogonal to each other and they are suffering from intercarrier interference.

Since both the modulation data $c(k)$ and the channel transfer function $H(k)$ are assumed to be random variables and $I(l)$ is the weighted sum of these terms, $I(l)$ will be a random variables itself. According to the Central Limit Theorem, $I(l)$ can be approximated by a complex Gaussian random variable. Therefore, the effects of the intercarrier interference can be modelled as additional Gaussian noise superimposed on the original data. The signal-to-noise power ratio on each subcarrier can be found as shown in the following.

Assume that the average channel gain $E\{|H(l)|^2\}$ is constant over the observation period and equal to $|H|^2$. The original modulation data $c(l)$ are assumed to be uncorrelated with zero means. Hence, $E[c(l)] = 0$ and

$$E[c(l)c^*(k)] = \begin{cases} |c|^2 & l = k \\ 0 & \text{otherwise} \end{cases} \tag{2.32}$$

In addition, since $k, l \in \mathbb{Z}$,

$$\sin \pi(k+\zeta-l) = (-1)^{k-l} \sin \pi\zeta \tag{2.33}$$

Then, from Equation 2.30 the average power of the random process $I(l)$ will be equal to

$$E[|I(l)|^2] = |c|^2|H|^2(\sin \pi\zeta)^2 \sum_{\substack{k=0 \\ k\neq l}}^{N-1} \frac{1}{\left[N \sin\left(\frac{\pi(k-l+\zeta)}{N}\right)\right]^2} \tag{2.34}$$

Let $J(l)$ denote the sum in the above equation with $(k-l)$ substituted by p

$$\begin{aligned} J(l) &\equiv \sum_{\substack{k=0 \\ k\neq l}}^{N-1} \frac{1}{\left[N \sin\left(\frac{\pi(k-l+\zeta)}{N}\right)\right]^2} \\ &= \frac{1}{N^2} \sum_{\substack{p=-l \\ p\neq 0}}^{N-l-1} \frac{1}{\sin^2\left(\frac{\pi(p+\zeta)}{N}\right)} \\ &= \frac{2}{N^2} \sum_{\substack{p=-l \\ p\neq 0}}^{N-l-1} \left[1 - \cos\left(\frac{2\pi(p+\zeta)}{N}\right)\right]^{-1} \end{aligned} \tag{2.35}$$

Similarly

$$J(l-1) = \frac{2}{N^2} \sum_{\substack{p=-l+1 \\ p \neq 0}}^{N-l} \left[1 - \cos\left(\frac{2\pi(p+\zeta)}{N} \right) \right]^{-1} \tag{2.36}$$

Then, the difference between $J(l)$ and $J(l-1)$ can be written as

$$J(l) - J(l-1) = \frac{2}{N^2} \left\{ \left[1 - \cos\left(\frac{2\pi(-l+\zeta)}{N} \right) \right]^{-1} - \left[1 - \cos\left(\frac{2\pi(N-l+\zeta)}{N} \right) \right]^{-1} \right\} \tag{2.37}$$

But

$$\begin{aligned} \cos\left(\frac{2\pi(N-l+\zeta)}{N} \right) &= \cos\left(2\pi + \frac{2\pi(-l+\zeta)}{N} \right) \\ &= \cos\left(\frac{2\pi(-l+\zeta)}{N} \right) \end{aligned} \tag{2.38}$$

Therefore, $J(l) - J(l-1) = 0$. The value J does not depend on the carrier index l and hence $J(l) = J(l-1) = \cdots = J(1) = J(0)$. Substituting the value of J back to Equation 2.34, we can obtaining the average power $E[|I|^2]$ of intercarrier interference for all carriers. That is

$$\begin{aligned} E[|I|^2] &= |c|^2 |H|^2 (\sin \pi\zeta)^2 J(0) \\ &= |c|^2 |H|^2 (\sin \pi\zeta)^2 \sum_{k=1}^{N-1} \frac{1}{\left[N \sin\left(\frac{\pi(k+\zeta)}{N} \right) \right]^2} \end{aligned} \tag{2.39}$$

Similarly, from Equation 2.31, the average power of the corresponding useful signal $E[|C|^2]$ is

$$E[|C|^2] = |c|^2 |H|^2 \left(\frac{\sin \pi\zeta}{\pi\zeta} \right)^2 \tag{2.40}$$

where C represents the first useful component of the demodulated data $c(l)$.

As seen, the average power $E[|I|^2]$ is independent to the frequency index l. In other words, the fine frequency offset causes the same amount of intercarrier interference to all frequency carriers. Since ζ is assumed to be a non-zero fractional number with absolute value upper-bounded by 0.5 and $1 \leq k < N$, the ratio $(k+\zeta)/N$ would neither be zero nor an integer. In other words, all terms in J are finite and hence $E[|I|^2]$ is upper-bounded for a given N.

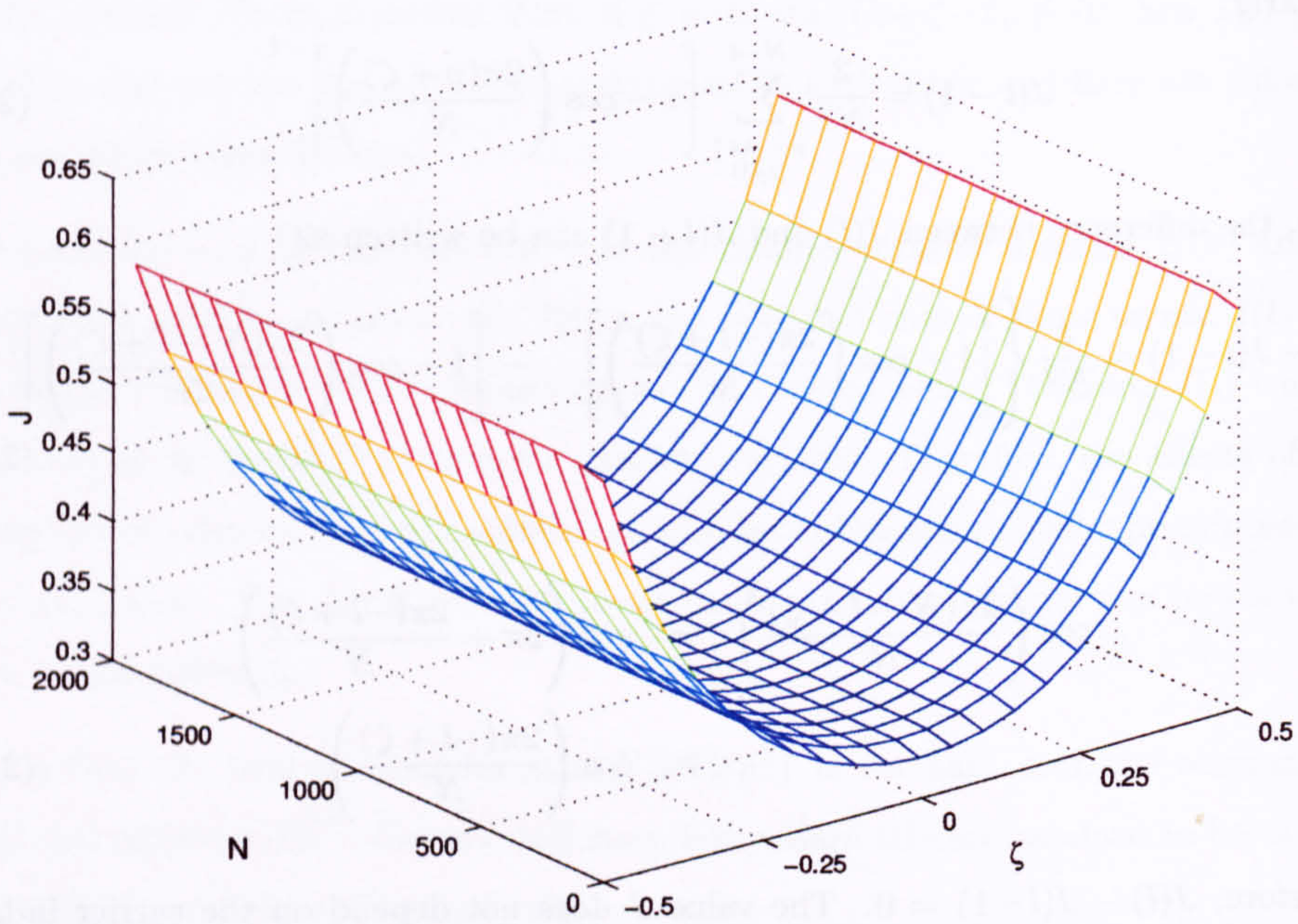

Figure 2.4: Variation of the sum J with parameters N and ζ

Finally, when data are corrupted by intercarrier interference only, the required signal-to-noise power ratio $\mathrm{SNR}_{\mathrm{ICI}}$ is equal to

$$\begin{aligned} \mathrm{SNR}_{\mathrm{ICI}} &= \frac{E[|C|^2]}{E[|I|^2]} \\ &= \left(\frac{1}{\pi\zeta}\right)^2 J^{-1} \end{aligned} \tag{2.41}$$

where

$$J = \sum_{k=1}^{N-1} \frac{1}{\left[N \sin\left(\frac{\pi(k+\zeta)}{N}\right)\right]^2} \tag{2.42}$$

The variation of the sum J with different number of carriers N is plotted in Figure 2.4, where $-0.5 \leq \zeta \leq 0.5$. It can be seen that J increases with the absolute value of ζ and it reaches the maximum value at both ends. The values of J for $|\zeta|$ equal to 0.5 are given in Table. 2.1. As shown, the maximum values of J do not change much when N is larger than 128. For practical application, it can be assumed that J is numerically upper bounded by 0.5947 for $|\zeta| \leq 0.5$ [1].

[1] This value agrees with that determined by Moose in [68]

N	J	N	J	N	J
2	0.5000000	128	0.5946949	8192	0.5947153
4	0.5732233	256	0.5947102	16384	0.5947153
8	0.5894665	512	0.5947140	32768	0.5947153
16	0.5934107	1024	0.5947149	65536	0.5947153
32	0.5943896	2048	0.5947152	131072	0.5947153
64	0.5946339	4096	0.5947152	262144	0.5947153

Table 2.1: Direct computation of J with different values of N ($|\zeta| = 0.5$)

Therefore,

$$\begin{aligned} \mathrm{SNR}_{\mathrm{ICI}} &\geq \left(\frac{1}{\pi\zeta}\right)^2 (0.5947)^{-1} \\ &\geqq \left(\frac{1}{0.5\pi}\right)^2 (0.5947)^{-1} \\ &\approx 0.6815 \qquad (-1.67 \text{ dB}) \end{aligned} \tag{2.43}$$

The $\mathrm{SNR}_{\mathrm{ICI}}$ should be as large as possible to ensure correct data recovery and synchronization. From Equation 2.41, the $\mathrm{SNR}_{\mathrm{ICI}}$ is inversely proportional to J and ζ^2. Since J and ζ are upper bounded, $\mathrm{SNR}_{\mathrm{ICI}}$ will have a lower limit.

As seen from Equation 2.43, the lower limit is approximately equal to 0.6815. In other words, the signal-to-noise power ratio can be reduced to -1.67 dB when the fine frequency offset is as large as half the carrier frequency spacing.

A computer simulation has been carried out to verify the variation of signal-to-noise power ratio with ζ. In particular, the number of carriers per symbol is set to 128 and each carrier is 16-QAM modulated by complex random data with unit variance. Total 10^6 symbols are generated at each ζ for $0.02 \leq \zeta \leq 0.5$. The results are plotted in Figure. 2.5.

As expected, the signal-to-noise ratio decreases with increasing fine-frequency offset. The theoretical values given by Equation 2.41 are also plotted to show a good agreement with the results of the simulation.

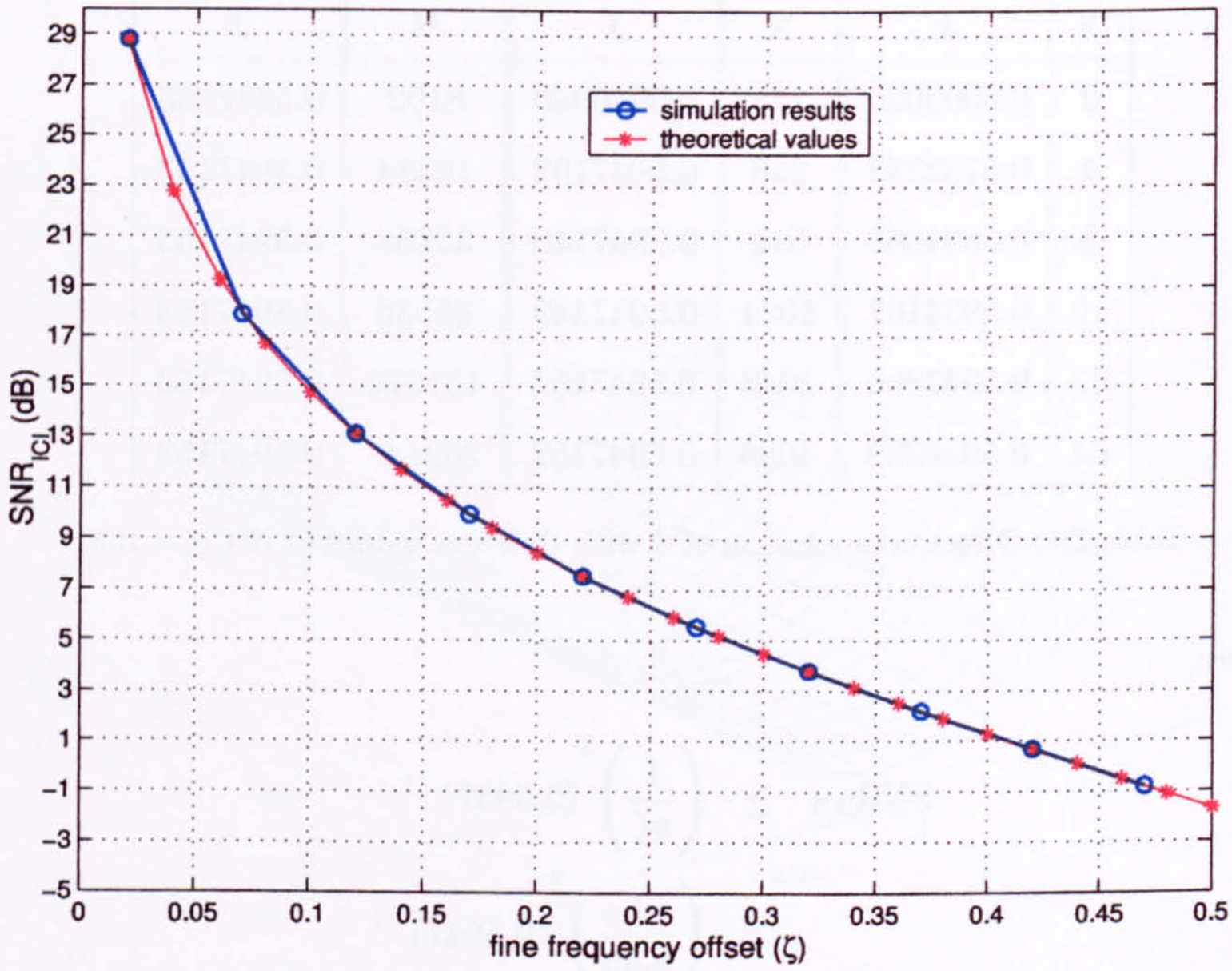

Figure 2.5: Variation of SNR_{ICI} with ζ

2.6 Effects of Sampling Clock Error

From Equation 2.15, the amount of additional phase rotation $\psi(l)$ on the useful component of the l-th carrier is

$$\psi(l) = \frac{\pi[\zeta - \epsilon(l+\zeta)](N-1)}{N} \tag{2.44}$$

where ζ and ϵ are the fractional part of the frequency offset and the sampling clock error respectively. The difference at two different carriers l_1 and l_2 is equal to

$$\psi(l_1) - \psi(l_2) = \frac{-\epsilon\pi(N-1)}{N}(l_1 - l_2) \tag{2.45}$$

From Equation 2.45, the difference of the phase rotation is a function of the difference in frequency $(l_1 - l_2)$ and ϵ, but is independent of ζ. In general, ϵ is very small and $|\zeta| < 0.5$. For example, ϵ would be approximately equal to 0.0001 if the accuracy of the oscillators is equal to 100 ppm, which is a common specification for low-cost oscillators. Since $|\zeta|$ is less than one, the product $\epsilon\zeta$ in Equation 2.44 is small enough to be ignored.

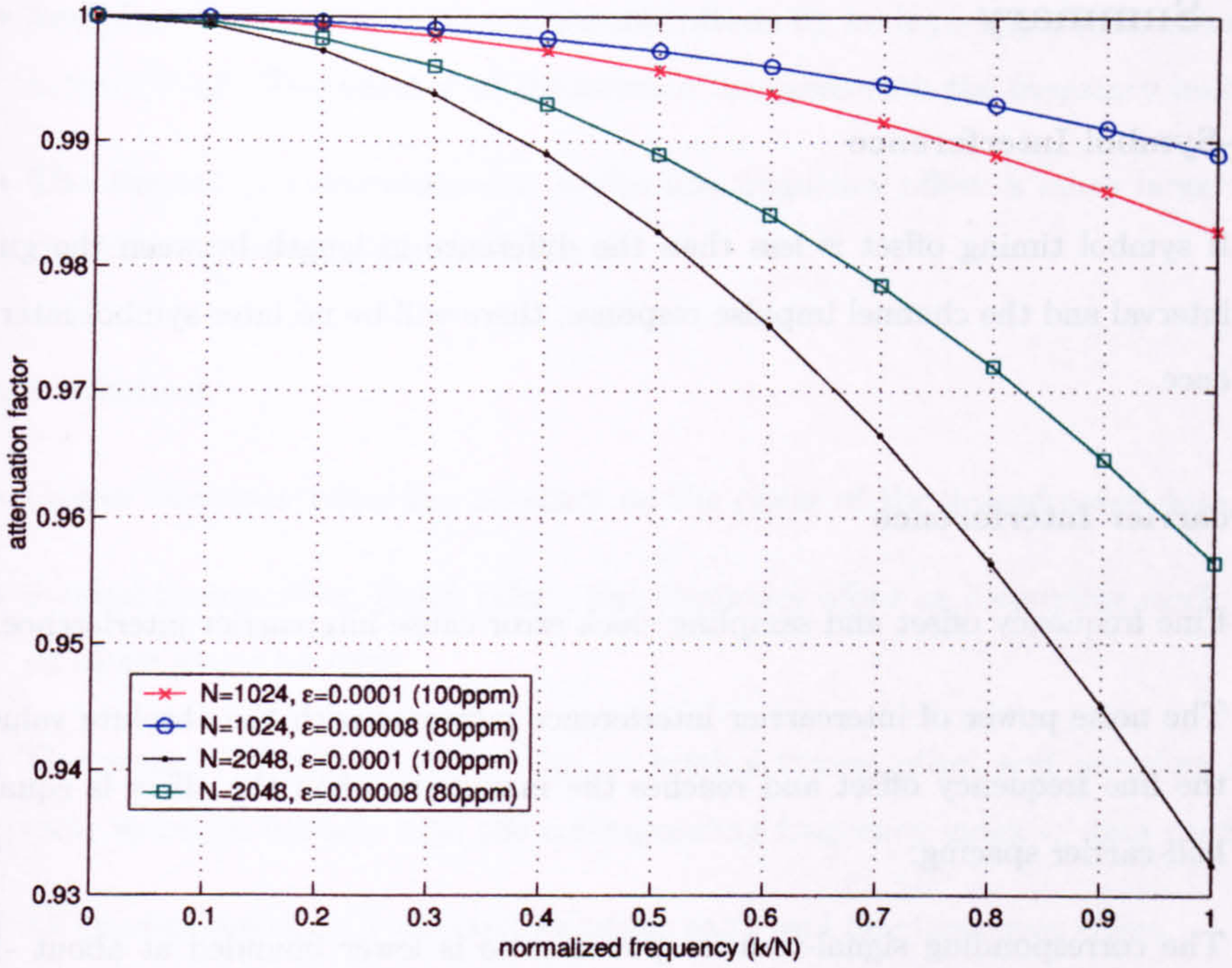

Figure 2.6: Direct computation of the attenuation factor $\frac{\sin \pi\epsilon k}{N \sin(\pi\epsilon k/N)}$ at different ζ and normalized frequency (k/N); $k = 0, \cdots, N-1$ is the carrier index and N is the total number of carriers per OFDM symbol.

That is, if $N \gg 1$, we have

$$\psi(l) \approx \pi(\zeta - \epsilon l) \tag{2.46}$$

The constant phase shift $\pi\zeta$ is due to the fine frequency offset. On the other hand, the phase shift $\pi\epsilon l$ is due to the sampling clock error and increases linearly with frequency. From Equation 2.15 and Equation 2.16, the sampling clock error also causes inter-carrier interference which attenuates the magnitude of the useful component by the factor $(\sin \pi\epsilon l/[N \sin(\pi\epsilon l/N)])$. The amount of attenuation increases with frequency and decreases with ϵ as shown in Figure. 2.6.

2.7 Summary

Inter-Symbol Interference

- If symbol timing offset is less than the difference in length between the guard interval and the channel impulse response, there will be no inter-symbol interference.

Intercarrier Interference

- Fine frequency offset and sampling clock error cause intercarrier interference.
- The noise power of intercarrier interference increases with the absolute value of the fine frequency offset and reaches the maximum when the offset is equal to half-carrier spacing.
- The corresponding signal-to-noise power ratio is lower bounded at about -1.67 dB.

Frequency Spectrum Shift

- The coarse frequency offset shifts the entire frequency spectrum of the demodulated data either up or down.
- If the oscillator in the transmitter is running faster than that in the receiver, the frequency spectrum will be shifted up. If the oscillator in the transmitter is running slower than that in the receiver, and frequency spectrum will be shifted down.

Magnitude Degradation

- Symbol timing offset, phase offset and coarse frequency have no effect on the magnitude of the received data.
- Fine frequency offset ζ attenuates the magnitude by multiplying it with a function $\sin(\pi\zeta)/\pi\zeta$. All carriers are equally affected.

- Sampling clock error attenuates the magnitude by multiplying it with a function $\sin(\pi\epsilon k)/\pi\epsilon k$. The amount of attenuation increases with the frequency index k.

- The amount of attenuation due to the fine frequency offset is much larger than that due to the sampling clock error.

Phase rotation

- Coarse frequency offset has no effect on the phase of the demodulated data.

- Symbol timing offset, phase offset, fine frequency offset and sampling clock error all cause phase rotation.

- The amount of phase rotation due to symbol timing offset and sampling clock error increases linearly with the corresponding frequency index of data carriers.

- All carriers are equally affected by phase error and fine frequency offset.

- The joint effects are shown schematically in Figure 2.7.

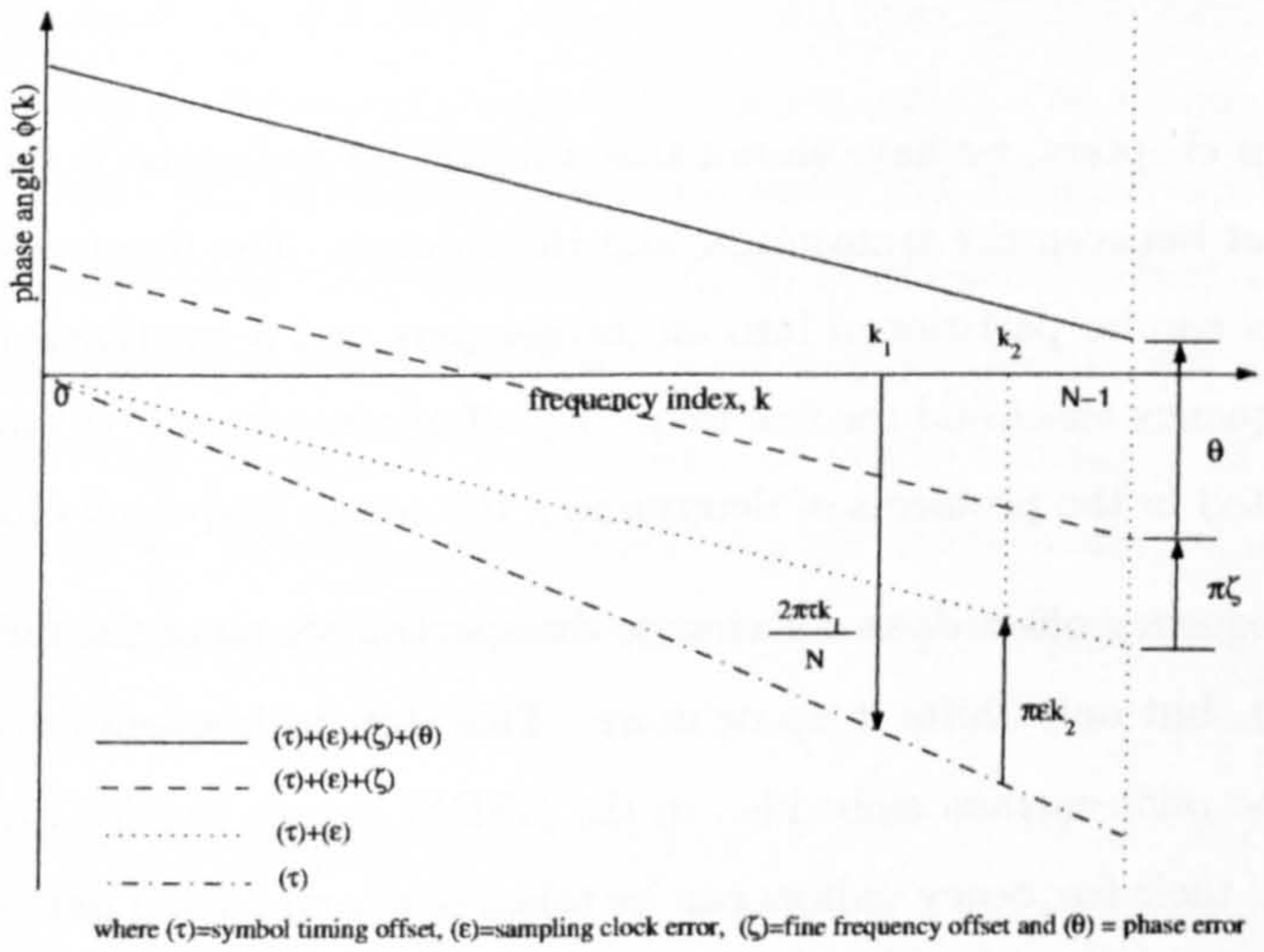

Figure 2.7: Joint effects of the synchronization defects to the phase of the demodulated data (assume all in anti-clockwise direction)

Chapter 3

Coarse Frequency Offset Estimation With Reference To Pilots Power

3.1 Introduction

In the previous chapters, we have shown that the OFDM technique is sensitive to the frequency offset between the transmitter and the receiver. The frequency offset in an OFDM system can be partitioned into an integer part and a fractional part, namely the coarse frequency offset and the fine frequency offset respectively. In particular, here we are interested in the problems of determining the coarse frequency offset.

The coarse frequency offset does not change the spectral shape of the OFDM demodulation output, but only shifts it up or down. This shift in frequency can be tracked by locating the pilot carriers embedded in the OFDM signal. If pilot carriers are not evenly spaced, their frequency indices can be taken out from a fixed pattern, the *pilots pattern*. The shift in the frequency spectrum can be tracked by sliding a data window along the frequency spectrum to determine the position that is matched to the pilots pattern. Based on this observation, a new *pilots-power-detection* algorithm for the coarse frequency synchronization is proposed in this chapter.

It is assumed that the effects of fading have not been corrected. Magnitude and phase errors are expected to occur at all frequencies. Therefore, phase modulation of the pilots is disregarded and only their power is exploited for non-coherent detection. Based on the maximum likelihood principle and the non-coherent signal processing of the received signals, we have derived a test statistic to estimate the coarse frequency offset. The test statistic is shown to be the summation of the instantaneous powers of subsets of frequency carriers. A subset is formed by selecting subcarriers whose indices are defined by a shifted version of the pilots pattern. When the searching window is located at the correct position, only pilot carriers are selected and the test statistic achieves the maximum value.

Alternatively, the searching process can be viewed as hypothesis testing. We have to make the decision that if the carriers selected to compute the test statistic are all pilots, but not a combination of pilots and data carriers. A specific distance measure between the target and the null hypothesis is defined. With the help of this statistical distance, we have studied the properties of the proposed algorithm and a simple design rule on the minimum number of pilot carriers is derived.

This chapter is organized as follows: after describing the OFDM system model briefly, the proposed pilots-power-detection algorithm is presented. The characteristics of the proposed algorithm are investigated after the statistical distance has been defined. Then, the performance of the proposed algorithm in frequency-selective fading channels, compared with the guard-band-power detection algorithm [48, 83] and maximum-correlation algorithm [48, 20], are investigated using the techniques of Monte Carlo computer simulations. Finally, the analytical studies of the computation complexity and the data throughput of the proposed algorithm are presented.

3.2 Frequency Offset Estimator

3.2.1 System Model

It is assumed that both the symbol timing error and the fine frequency offset have been estimated and their effects have been corrected. Therefore, intercarrier interference

can be ignored and all carriers are assumed to be mutually independent. In addition, the cyclic prefix is assumed to be longer than the channel impulse response so that inter-symbol interference can be ignored as well. However, the frequency transfer function of the channel is assumed to be unknown. Hence, the effects of the channel on carriers cannot be corrected. Magnitude and phase errors are expected to occur at all frequencies. Phase modulation of pilots is therefore disregarded and only their power is exploited for non-coherent detection.

Let x_k and y_k be the in-phase and quadrature components of a carrier at frequency f_k with frequency index k. The instantaneous power u_k is the summation of the square of these two components. That is

$$u_k = x_k^2 + y_k^2 \tag{3.1}$$

The collection of instantaneous power values at all carriers form a set $\{U\}$

$$U = \{u_0, u_1, \ldots, u_{N-1}\} \tag{3.2}$$

where N is the total number of carriers.

We assume that there are only two types of carriers in the OFDM system: pilot carriers and data carriers. Among the N carriers, only N-L carriers are modulated with data. The remaining L carriers are pilot carriers which are not used for data transmission. The pilots are inserted with frequency indices taken from a fixed set $\{K\}$, which is known to the receiver. Without loss of generality, we can assign the first subcarrier to be the first pilot. In other words, the pilots pattern $\{K\}$ can be represented as

$$K = \{0, k_1, \ldots, k_{L-1}\} \tag{3.3}$$

where k_i is the frequency index of the i-th pilots.

In Chapter 2, we have shown that the coarse frequency offset shifts the frequency spectrum of an OFDM signal. If the oscillator's frequency in the transmitter is higher than that in the receiver, the frequency spectrum will be shifted up. Suppose the coarse frequency offset is τ intercarrier spacing. Then the shifted pilots pattern will become $\{K+\tau\} = \{\tau, k_1+\tau, \ \ldots, \ k_{L-1}+\tau\}$. Here, we have assumed that the amount of frequency difference is bounded in such a way that the whole set of pilots always

remain inside the available range of frequency with indices given by $\{0, \cdots, N-1\}$. Otherwise, the out-of-band signal will be severely attenuated by the bandpass filters in the receiver leading to unrecoverable errors. Since we are not interested in this case, we assume that the first index of the shift pilots pattern τ is non-negative and the last pilot frequency index $k_{L-1} + \tau$ is always less than N. It follows that

$$0 \leq \tau \leq (N - 1 - k_{L-1}) \tag{3.4}$$

Let us denote the set $U_K(\tau) \subset U$ be the collection of instantaneous power of pilots with frequency indices taken out from the shifted pilots pattern $\{K + \tau\}$. That is,

$$U_K(\tau) = \left\{ u_i : u_i \in U, i = \tau + k, k \in K \right\} \tag{3.5}$$

where $\tau = 0, 1, \cdots, (N - 1 - k_{L-1})$.

3.2.2 Finding the Maximum Likelihood Estimator

Our objective is to find the frequency index τ from a given set $\{U\}$ of the instantaneous power of all carriers. Let m be the current position of a searching window. An *ad hoc* procedure is to use the known pilots pattern $\{K\}$ as the matching template sliding along $\{U\}$ to find a value m such that the subset $U_K(m)$ is the most likely equal to $U_K(\tau)$. This procedure is equivalent to finding an m that maximizes the *a posterior* probability $P(\tau = m \mid U)$.

By Bayes's rules,

$$P(\tau = m|U) = \frac{P(U|\tau = m)\ P(\tau = m)}{P(U)} \tag{3.6}$$

Since τ is equally likely to be any one of the possible positions in the range $\{0, N - k_{L-1} - 1\}$, we have

$$P(\tau = m) = \frac{1}{N - k_{L-1}} \qquad , \tau = 0 \ldots N - 1 - k_{L-1} \tag{3.7}$$

In other words, $P(\tau = m)$ is independent of m, the current position of the searching window. Since $P(U)$ is a constant for a given OFDM symbol, it is independent of m too. It follows that maximizing Equation (3.6) is equivalent to maximizing the likelihood function $P(U|\tau = m)$. That is,

$$\max_m \ P(\tau = m|U) \equiv \max_m \ P(U|\tau = m) \tag{3.8}$$

Let σ_p^2 and σ_d^2 be the average received power of the pilots and data carriers respectively. We have assumed that the channel attenuation does not change over the symbol observation period and is uniform across the whole frequency spectrum so that all data carriers have the same average received power σ_d^2. Similarly, all pilot carriers have the same average received power σ_p^2. However, σ_p^2 and σ_d^2 can be different.

In a Rayleigh fading model, each instantaneous power $u_i \in U$ has an exponential distribution. The corresponding probability density function is given by

$$P(u_i) = \frac{1}{\sigma_i^2} \exp\ (-\frac{u_i}{\sigma_i^2}) \tag{3.9}$$

where

$$\sigma_i^2 = \begin{cases} \sigma_p^2 = E\ [\ u_i | u_i \in U_K(\tau)\ ] \\ \sigma_d^2 = E\ [\ u_i | u_i \notin U_K(\tau)\ ] \end{cases} \tag{3.10}$$

Since the fine frequency offset has been corrected, it can be assumed that there is no intercarrier interference and carriers are mutually independent. It follows that the random variables u_i are independent and the joint probability $P(U|\tau = m)$ is equal to the product of the individual probabilities $P(u_i)$, where $u_i \in \{U|\tau = m\}$ and

$$\{U|\tau = m\} = \{\underbrace{u_0, u_1, \ldots, u_{m-1}}_{data\ carriers}, u_m, \underbrace{u_{m+1}, \ldots, u_{m+k_1-1}}_{data\ carriers}, u_{m+k_1}, \ldots, u_{N-1}\} \tag{3.11}$$

Therefore,

$$\begin{aligned} & \max_m\ P(U|\tau = m) \\ = & \max_m \left\{ \prod_{u_i \in U_K(m)} P(u_i) \right\} \left\{ \prod_{u_j \notin U_K(m)} P(u_j) \right\} \\ = & \max_m \left\{ \left(\frac{1}{\sigma_p^2}\right)^L \exp\left(-\frac{1}{\sigma_p^2} \sum_{u_i \in U_K(m)} u_i\right) \right\} \left\{ \left(\frac{1}{\sigma_d^2}\right)^{N-L} \exp\left(-\frac{1}{\sigma_d^2} \sum_{u_j \notin U_K(m)} u_j\right) \right\} \\ = & \max_m \left\{ \exp\left[-\left(\frac{1}{\sigma_p^2} \sum_{u_i \in U_K(m)} u_i + \frac{1}{\sigma_d^2} \sum_{u_j \notin U_K(m)} u_j \right) \right] \right\} \end{aligned} \tag{3.12}$$

The term $\exp\left(1/\sigma_d^2 \sum\ u_j\right)$ where $u_j \in U$, is the exponential of the weighted sum of instantaneous power of all received carriers. It is a constant for a given OFDM symbol

and is independent of m. Multiplying this term to Equation 3.12 will not affect the final result of searching for the maximum. Therefore,

$$\begin{aligned}
&\max_m \; P(U|\tau = m) \\
\equiv \;& \max_m \; P(U|\tau = m) \exp\left[\frac{1}{\sigma_d^2} \sum_{u_j \in U} u_j\right] \\
= \;& \max_m \left\{ \exp\left[-\left(\frac{1}{\sigma_p^2} \sum_{u_i \in U_K(m)} u_i + \frac{1}{\sigma_d^2} \sum_{u_j \notin U_K(m)} u_j \right) \right] \exp\left[\frac{1}{\sigma_d^2} \sum_{u_j \in U} u_j\right] \right\} \\
= \;& \max_m \left\{ \exp\left[\frac{1}{\sigma_d^2} \left(\sum_{u_j \in U} u_j - \sum_{u_j \notin U_K(m)} u_j \right) - \frac{1}{\sigma_p^2} \sum_{u_i \in U_K(m)} u_i \right] \right\} \\
= \;& \max_m \left\{ \exp\left[\frac{1}{\sigma_d^2} \sum_{u_j \in U_K(m)} u_j - \frac{1}{\sigma_p^2} \sum_{u_i \in U_K(m)} u_i \right] \right\} \\
= \;& \max_m \left\{ \exp\left[\left(\frac{1}{\sigma_d^2} - \frac{1}{\sigma_p^2} \right) \sum_{u_i \in U_K(m)} u_i \right] \right\}
\end{aligned} \tag{3.13}$$

If pilot carriers are transmitted at boosted power, then $\sigma_p^2 > \sigma_d^2$ and hence

$$\frac{1}{\sigma_d^2} - \frac{1}{\sigma_p^2} > 0 \tag{3.14}$$

It follows that the exponent in Equation 3.13 is always positive. An exponential function of a positive argument is a monotonically increasing function. Therefore, maximizing Equation 3.13 is equivalent to maximizing the sum inside the exponent which is the only part depending on the parameter m. In other words, the starting carrier index τ of the shifted pilots pattern can be estimated by determining the integer m that maximize the following test statistic

$$\overline{U}_K(m) = \sum_{u_i \in U_K(m)} u_i \tag{3.15}$$

Therefore, the frequency offset Δf can be estimated by the following procedures:

1. Compute the instantaneous power u_k of all received carriers f_k and form a set U.

$$U = \{u_0, u_1, \ldots, u_{N-1}\}$$

2. Generate subsets $U_K(m)$ by taking elements from U with indices equal to the sum of the integer $m \in \{0 \ldots N-1-k_{L-1}\}$ and elements in $K = \{0, k_1, \ldots, k_{L-1}\}$

$$U_K(m) = \left\{ u_i : u_i \in U, i = m + k, k \in K \right\}$$

3. Compute the test statistic $\overline{U}_K(m)$ by adding all elements in each subset $U_K(m)$ and store the results.

$$\overline{U}_K(m) = \sum_{u_i \in U_K(m)} u_i$$

4. Compare all $\overline{U}_K$ and locate the maximum. The corresponding index $\tilde{m}$ gives the starting position of the shifted pilots pattern.

$$\tilde{m} = \max_m \overline{U}_K(m)$$

5. Let m_o be the initial starting position of the pilots pattern. Then, the amount of frequency offset Δf is equal to

$$\Delta f = (\tilde{m} - m_o) \cdot \Delta F \tag{3.16}$$

where ΔF is the intercarrier frequency spacing.

For simplicity, we have assumed $m_0 = 0$ arbitrary and the frequency indices of the shifted pilots are increased in the positive direction. In general, the frequency spectrum can be shifted either up or down by the coarse frequency offset. Therefore instead of aligning with either end of the frequency spectrum, the pilot carriers should be assigned in the middle region of the allowable frequency spectrum to maximize the acquisition range of frequency shifts in either direction.

3.3 Probability Distribution of $\overline{U}_K$

In a Rayleigh fading model, the in-phase and quadrature components, x_k and y_k, result from the combination of several multipaths with random angles of arrival and propagation delays. The two components can be modelled as independent zero-mean random variables with Gaussian distribution having the following properties:

$$E[x_k] = E[y_k] = 0 \tag{3.17}$$

$$var[x_k] = var[y_k] = \frac{1}{2}\sigma_k^2 \tag{3.18}$$

where

$$\sigma_k = \begin{cases} \sigma_p & \text{for pilot carrier at frequency } f_k \\ \sigma_d & \text{for data carrier at frequency } f_k \end{cases} \tag{3.19}$$

Recall from Equation 3.1 that the instantaneous power u_k is the sum of the square of x_k and y_k, and it has an exponential distribution. Alternatively, it can be regarded as having a χ^2 distribution with two degrees of freedom [79]. It can be shown that the mean and variance of u_k are equal to (see Appendix (B.1)

$$E[u_k] = \sigma_k^2 \tag{3.20}$$

$$var[u_k] = \sigma_k^4 \tag{3.21}$$

Consequently, the total power $\overline{U}_K$ has a χ^2 distribution with 2L degrees of freedom, where L is equal to the number of components u_k being added. In multicarrier OFDM systems, L is usually larger than 15 and can be as large as thousands in the DVB-T system. Therefore, the sum $\overline{U}_K$ can be approximated by a Gaussian distribution. Since u_k are assumed to be mutually uncorrelated, the mean and variance of $\overline{U}_K$ are equal to the sum of the means and variances of individual elements u_k, respectively. That is,

$$E[\overline{U}_K] = \sum_{u_i \in U_K} E[u_i] \tag{3.22}$$

$$var[\overline{U}_K] = \sum_{u_i \in U_K} var[u_i] \tag{3.23}$$

The mean and variance of the distribution $\overline{U}_K$ depend on the numbers of data carriers and pilot carriers included in the data set $\{U_K\}$. Suppose that $\overline{U}_K$ are composed of n_p pilot carriers and L-n_p data carriers, we have the following two cases:

<u>Case 1</u> $\mathbf{H_1 : n_p = L}$

The test statistic $\overline{U}_K$ is the summation of instantaneous power of all pilot carriers. The searching window is located at the exact position where the shifted pilots are.

- Mean

$$E[\overline{U}_K|H_1] = \sum_{i=0}^{L-1} E[u_i|\text{pilot carrier at } f_i] = L\sigma_p^2 \tag{3.24}$$

- Variance

$$var[\overline{U}_K|H_1] = \sum_{i=0}^{L-1} var[u_i|\text{pilot carrier at } f_i] = L\sigma_p^4 \tag{3.25}$$

Case 2 $\mathbf{H_0 : 0 \leq n_p < L}$

In general, U_k is a combination of stray pilot carriers [1] and data carriers. The number of stray pilot carriers n_p is greater than zero and the remaining L-n_p carriers are data carriers. The number n_p is determined by the sidelobe level of the noncoherent autocorrelation function of the pilots pattern. If none of the pilots coincide with the searching window, n_p will be zero and only data carriers are selected. This corresponds to the conditions that the sidelobe level of the autocorrelation function of the pilots pattern are zero at the corresponding shifted positions.

- Mean

$$E[\overline{U}_K|H_0] = \sum^{n_p} E[u_i|\text{pilot carrier at } f_i] + \sum^{L-n_p} E[u_i|\text{data carrier at } f_i] = n_p\sigma_p^2 + (L-n_p)\sigma_d^2 \tag{3.26}$$

- Variance

$$var[\overline{U}_K|H_0] = \sum^{n_p} var[u_i|\text{pilot carrier at } f_i] + \sum^{L-n_p} var[u_i|\text{data carrier at } f_i] = n_p\sigma_p^4 + (L-n_p)\sigma_d^4 \tag{3.27}$$

[1] The pilots 'falling' into the shifted pilots patterns will be referred as the *stray pilots*.

3.4 Performance Measure

3.4.1 Definition of Distance Criterion

The estimation procedure can be viewed as multiple binary hypotheses testing in which we want to select H_1 and reject H_0 by exploiting the test statistic $\overline{U}_K$. Recall that τ is the first frequency index of the shifted pilots pattern. If the corresponding first frequency index of H_1 and H_0 are m_1 and m_0 respectively, the two hypothesis can be restated as

$$\begin{cases} H_1 : \tau = m_1 \\ H_0 : \tau = m_0 \end{cases} \tag{3.28}$$

and

$$\overline{U}_K|H_1 \underset{\text{accept } H_0}{\overset{\text{accept } H_1}{\gtrless}} \overline{U}_K|H_0 \tag{3.29}$$

An example of the distributions of $\overline{U}_K$ under H_0 and H_1 is shown in Figure. 3.1 which is a histogram plot of 10^6 samples. The specification of the parameters n_p, L, σ_d^2 and σ_p^2, and the corresponding means and standard deviations of the distributions are given in Table. 3.1.

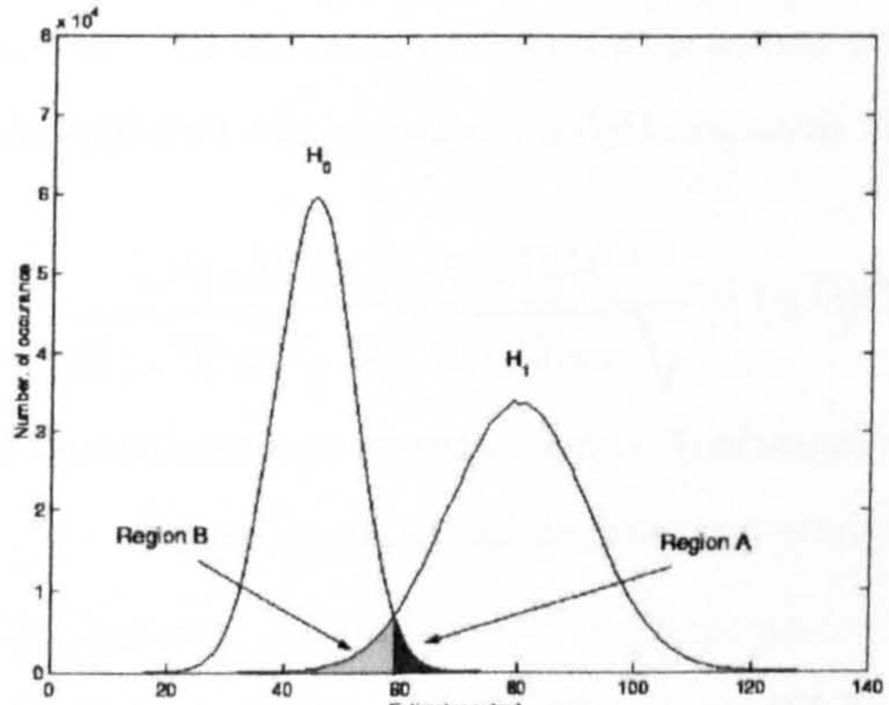

Figure 3.1: Histogram of $\{\overline{U}_K|H_0\}$ and $\{\overline{U}_K|H_1\}$ (Specification is given in Table. 3.1)

The overlapping regions of the two distributions are shaded in Figure 3.1. There are errors in correct detection of H_1 whenever $\{\overline{U}_K|H_1\} < \{\overline{U}_K|H_0\}$. This corresponds to the situation that the test statistics $\{\overline{U}_K|H_1\}$ falls into region B while $\{\overline{U}_K|H_0\}$

	Specification				Simulation Results	
	n_p	$L-n_p$	σ_d^2	σ_p^2	mean	$\sqrt{\text{variance}}$
H_1	45	0	-	1.78	80	11.9
H_0	0	45	1.0	-	45	6.7

Table 3.1: An example of H_1 and H_0

falls into region A. If the area of overlapping is large, there is a higher probability of incorrect detection of H_1.

The area of overlapping can be reduced in two ways. Firstly, the centers of the two distributions can be shifted further away from each other by increasing the difference between the conditional means. Secondly, the spreading of the distributions can be reduced by decreasing the standard deviation of the distributions.

$$\begin{aligned} E[\overline{U}_K|H_1] - E[\overline{U}_K|H_0] &= L\sigma_p^2 - (n_p\sigma_p^2 + (L-n_p)\sigma_d^2) \\ &= (L-n_p)(\sigma_p^2 - \sigma_d^2) \\ &= > 0 \qquad (\because \ \sigma_p > \sigma_d) \end{aligned} \tag{3.30}$$

From Equation 3.30, the difference of the conditional means is always a positive number. Therefore, it can be use as a criterion to measure the 'distance' between the two distributions. A specific distance $\mathcal{D}(\overline{U}_K)$ between the two hypothesis H_1 and H_0 can be defined as

$$\mathcal{D}(\overline{U}_K) = \frac{E[\overline{U}_K|H_1] - E[\overline{U}_K|H_0]}{\sqrt{var[\overline{U}_K|H_1]} + \sqrt{var[\overline{U}_K|H_0]}} \tag{3.31}$$

It corresponds to the geometric distance between the conditional means when the conditional standard deviations are used as the units of length.

3.4.2 Properties of Distance $\mathcal{D}$

Substituting the means and variances from Equation 3.24 to Equation 3.27 into Equation 3.31, the distance $\mathcal{D}(\overline{U}_K)$ is equal to

$$\mathcal{D}(\overline{U}_K) = \frac{L\sigma_p^2 - (n_p\sigma_p^2 + (L-n_p)\sigma_d^2)}{\sqrt{(L\sigma_p^4)} + \sqrt{n_p\sigma_p^4 + (L-\sigma_p)\sigma_d^4}}$$

$$\begin{aligned}\mathcal{D}(\overline{U}_K) &= \frac{(L-n_p)(\sigma_p^2-\sigma_d^2)}{\sigma_p^2\sqrt{L}+\sqrt{n_p\sigma_p^4+(L-\sigma_p)\sigma_d^4}} \\ &= \frac{\sqrt{L}(1-(n_p/L))(\sigma_p^2/\sigma_d^2-1)}{\sigma_p^2/\sigma_d^2+\sqrt{(n_p/L)(\sigma_p^4/\sigma_d^4)+(1-n_p/L)}}\end{aligned}$$

In order to simply the notation, we define the ratios σ_p^2/σ_d^2 and n_p/L as the *boosted power ratio* and the *sidelobe level ratio* respectively as follows.

- **Boosted power ratio:** $(b > 1)$

$$\begin{aligned}b &= \frac{\text{average power of a pilot carrier}}{\text{average power of a data carrier}} \\ &= \frac{\sigma_p^2}{\sigma_d^2}\end{aligned} \tag{3.32}$$

- **Sidelobe level ratio:** $(0 \le s \le 1)$

$$\begin{aligned}s &= \frac{\text{number of pilots being added in } \overline{U}_K}{\text{total number of carriers being added in } \overline{U}_K} \\ &= \frac{n_p}{L}\end{aligned} \tag{3.33}$$

Then, the distance $\mathcal{D}(\overline{U}_K)$ can be expressed in terms of s and b. That is,

$$\begin{aligned}\mathcal{D}(\overline{U}_K) &= \frac{\sqrt{L}(1-s)(b-1)}{b+\sqrt{sb^2+(1-s)}} \\ &= \sqrt{L}\left(\frac{(1-s)(b-1)}{b+\sqrt{s(b^2-1)+1}}\right)\end{aligned} \tag{3.34}$$

In order to determine the variation of the distance $\mathcal{D}$ with the sidelobe level s and the boosted power ratio b, we realize Equation 3.34 numerically based on the parameters in the DVB-T 2k mode system. In the DVB-T system, there are 45 pilots and the average power ratio of a pilot carrier to a data carrier is 1.78 (2.5 dB). In the computer simulations, while holding the average power of the data carriers unchanged, the average power of the pilots is arbitrary set to ± 1 dB,+3 dB and +6 dB about the nominal value. In other words, we have assumed that L = 45, and b = 1.41, 1.78, 2.24, 3.56 or 7.12. The variations of $\mathcal{D}$ against s are determined and the results are plotted in Figure 3.2. The normalized distance $\mathcal{D}(\overline{U}_K)/\sqrt{L}$ are also determined and plotted in Figure 3.3.

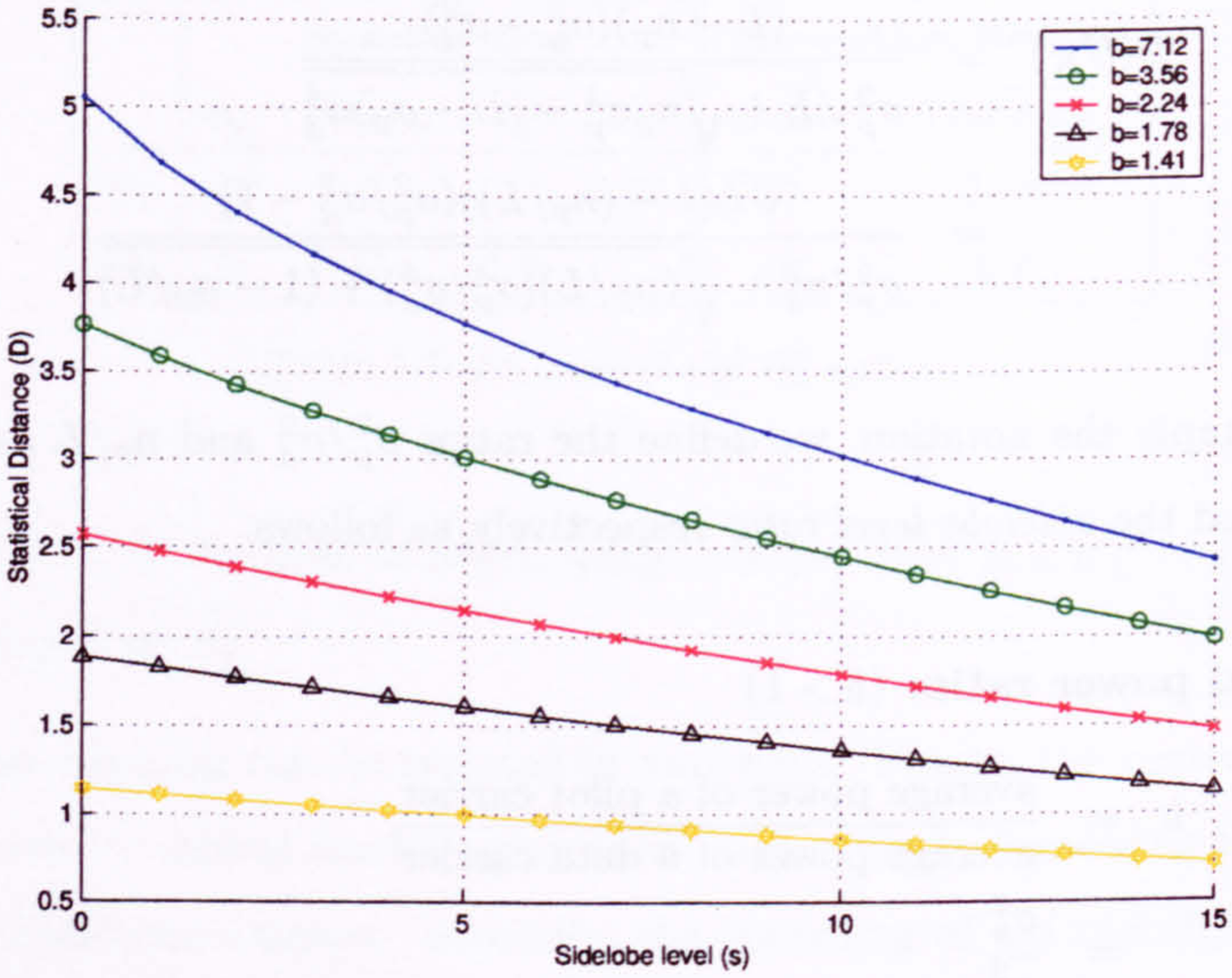

Figure 3.2: Variation of distance with sidelobe level and pilots power (L=45)

As shown in Figure 3.2, the distance $\mathcal{D}$ is reduced with increasing sidelobe level for a given boosted power ratio. This is because for a given total number of pilots, increasing the sidelobe level is equivalent to increasing the number of stray pilots in H_0. The stray pilots can be regarded as strong tonal interferences, which increase the mean and standard deviation of $(\overline{U}_K|H_0)$. Therefore, the distance is reduced.

On the other hand, the distance $\mathcal{D}$ is increased with increasing power of pilots for a given sidelobe level. This can be explained by inspecting Equation 3.34. Suppose both L and s are fixed, then $\mathcal{D}$ will depend on the factor $\frac{b-1}{b+\sqrt{s(b^2+1)+1}}$ only. The factor can be expanded into two terms as the following:

$$\frac{b-1}{b+\sqrt{s(b^2+1)+1}} \equiv 1 - \frac{1+\sqrt{s(b^2+1)+1}}{b+\sqrt{s(b^2+1)+1}} \tag{3.35}$$

Since $b > 1$, the magnitude of the second term is always less than one and decreases with increasing b. Therefore, the magnitude of the whole factor increases with increasing b. It follows that the distance $\mathcal{D}$ increases monotonically with increasing b too. That is,

$$\begin{aligned} \mathcal{D}(\overline{U}_K) &\leq \lim_{b\to\infty} D(\overline{U}_K) \\ &= \lim_{b\to\infty} \sqrt{L}\left[\frac{(1-s)(b-1)}{b+\sqrt{s(b^2-1)+1}}\right] \end{aligned}$$

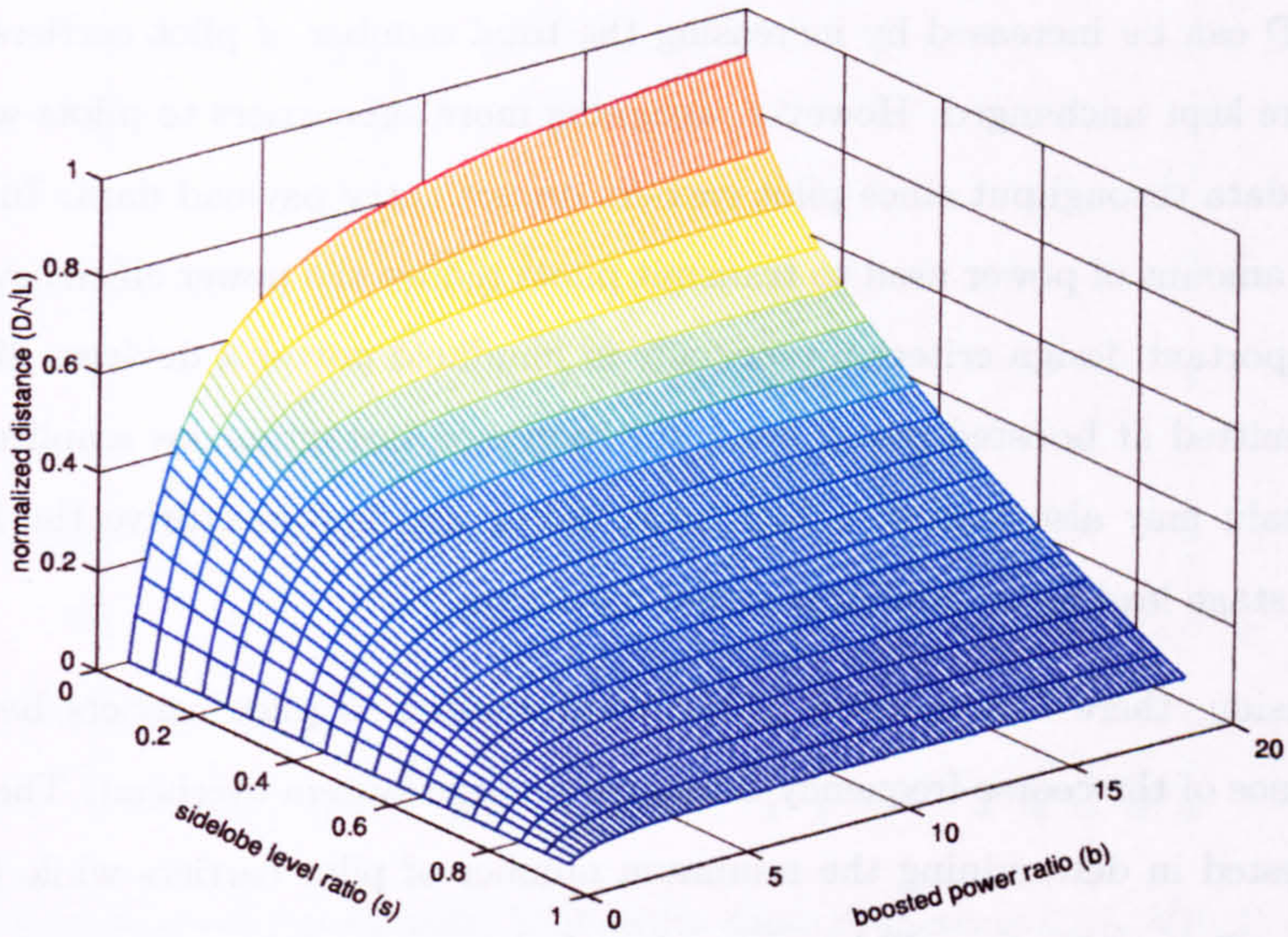

Figure 3.3: Plot of normalized $\mathcal{D}$ against b and s

$$\begin{aligned}
\mathcal{D}(\overline{U}_K) &= \sqrt{L} \lim_{b\to\infty} \frac{(1-s)(1-\frac{1}{b})}{1+\sqrt{s(1-\frac{1}{b^2})+\frac{1}{b^2}}} \\
&= \sqrt{L}\left(\frac{1-s}{1+\sqrt{s}}\right) \\
&\leq \sqrt{L} \qquad (\because 0 \leq s \leq 1) \qquad (3.36)
\end{aligned}$$

Therefore, the distance $\mathcal{D}$ is upper bounded by $\sqrt{L}$. This can be verified by plotting the variation of $\mathcal{D}/\sqrt{L}$ against s and b. The results are shown in Figure 3.3. The curves become flatter and the rate of increment decreases after the boosted power ratios have reached certain levels, which in turn depend on the corresponding sidelobe level ratio. In other words, the distance $\mathcal{D}$ is upper bounded by the structure of the pilots pattern and it cannot be increased indefinitely simply by boosting the power of pilot carriers.

3.5 Total Number of Pilot Carriers

One of the objectives of a good system design is to minimize the amount of overlapping of the tails of the two distributions $\{\overline{U}_K|H_0\}$ and $\{\overline{U}_K|H_1\}$, while the overall amount

of the system overhead is kept to the minimum. From Equation 3.34, the statistical distance $\mathcal{D}$ can be increased by increasing the total number of pilot carriers L, while b and s are kept unchanged. However, assigning more subcarriers to pilots will reduce the total data throughput since pilot carriers do not carry payload data. In addition, the extra amount of power used to transmit pilots reduce the power efficiency, which is a very important design criterion especially in handheld portable devices. Since pilots are transmitted at boosted power level, the increased instantaneous amplitude in the time domain may also lead to a high peak factor and may overdrive the RF power amplifier stage leading to nonlinear signal distortion.

In conclusion, there is a tradeoff in the total number of pilot carriers between the performance of the coarse frequency estimator and the system overhead. Therefore, we are interested in determining the minimum number of pilot carriers while the coarse frequency offset estimator still has a good performance.

Firstly, we are going to determine the corresponding number of pilot carriers when the distributions of the two hypothesis H_0 and H_1 just overlap with each other. From Equations 3.26, 3.27, 3.24 and 3.25, the mean (center) and the variance (spread) of the distributions can be changed by adjusting L, n_p, σ_d and σ_p. Suppose L_{min} is the required minimum number of pilot carriers under the worst case condition in which the number of stray pilot carriers n_p in H_0 achieves the maximum. Then, we can adjust the relative power of the data carriers and the pilot carriers so that the right tail of the distribution of H_0 just overlap with the left tail of the distribution of H_1.

Let λ_0 and λ_1 be the intermediate distances from the point of intersection of the two distributions to the centers of the respective distributions H_0 and H_1 in the unit of their standard deviations, σ_0 or σ_1, respectively. Then, from Equation 3.31, the statistical distance $\mathcal{D}$ is given by

$$\mathcal{D} = \frac{\lambda_1\sigma_1 + \lambda_0\sigma_0}{\sigma_1 + \sigma_0} \tag{3.37}$$

where σ_1 and σ_0 are the standard deviations of $(\overline{U}_K|H_1)$ and $(\overline{U}_K|H_0)$ respectively.

In Section 3.3, we have shown that the distributions $\{\overline{U}_K|H_0\}$ and $\{\overline{U}_K|H_1\}$ can be approximated by Gaussian distributions. It is well-known that for a Gaussian distribution, the amount of area under the probability density function beyond the point

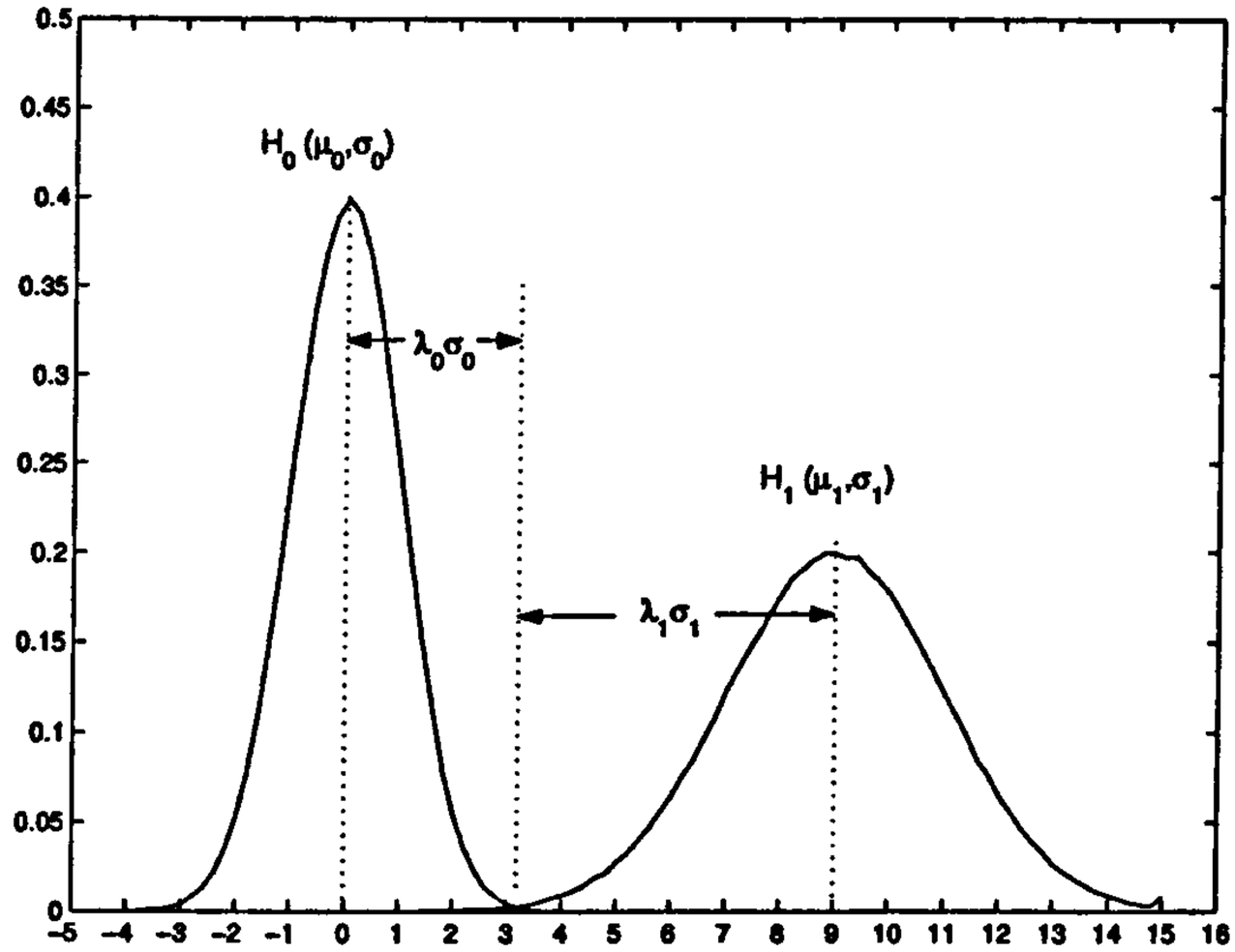

Figure 3.4: An example of two Gaussian probability density functions $H_0 \sim \mathcal{N}(0,1)$ and $H_1 \sim \mathcal{N}(9,2)$

at 3.1 times of its standard deviation away from the center is only about 0.1% of the total area [95]. An example of two Gaussian probability density functions $\mathcal{N}(0,1)$ and $\mathcal{N}(9,2)$ are plotted schematically in Figure 3.4 for illustration, where $\mathcal{N}(\mu,\sigma)$ represents a Gaussian density function with mean μ and standard deviation σ. Therefore, we can assume that the area of overlapping between the distributions H_1 and H_0 is negligible if both $\lambda_1 \geq 3.1$ and $\lambda_0 \geq 3.1$. From Equation 3.37, the corresponding distance $\mathcal{D}$ is

$$\mathcal{D} \geq \frac{3.1\sigma_1 + 3.1\sigma_0}{\sigma_1 + \sigma_0} = 3.1 \tag{3.38}$$

From Equation 3.36, if the number of pilot carriers is fixed at L_{min}, $\mathcal{D}$ will be upper bounded by $\sqrt{L_{min}}$. That is,

$$\mathcal{D} \leq \sqrt{L_{min}} \tag{3.39}$$

Combining Equation 3.38 and Equation 3.39, we have

$$L_{min} \geq 3.1^2 \approx 10 \tag{3.40}$$

The equality in Equation 3.39 holds only when $s = 0$ and $b \to \infty$. Therefore, more pilot carriers are required in practical applications. However, as a rule of thumb the total number of pilot carriers should be more than ten for any reliable system design.

3.6 Statistical Distance $\mathcal{D}_n$ under Noisy Environment

In the previous sections, the effects of noise have not been considered during the studies of the statistical distance $\mathcal{D}$. In this section, an extension of $\mathcal{D}$ under noisy environment, $\mathcal{D}_n$, will be defined. It is assumed that the in-phase and quadrature components, x_{nk} and y_{nk}, at frequency f_k are corrupted by independent zero-mean additive Gaussian noise, n_k, with variance $\sigma_n^2/2$. That is,

$$x_{nk} = x_k + n_k \tag{3.41}$$

$$y_{nk} = y_k + n_k \tag{3.42}$$

Similarly, the instantaneous power u_{nk} is given by

$$u_{nk} = x_{nk}^2 + y_{nk}^2 \tag{3.43}$$

Let $\mathcal{N}(\mu, \sigma^2)$ represents a Gaussian distribution with mean μ and variance σ^2. The probability distributions of x_k and y_k are Gaussian and are equal to either $\mathcal{N}(0, \frac{1}{2}\sigma_p^2)$ or $\mathcal{N}(0, \frac{1}{2}\sigma_d^2)$ depending on whether the carrier at f_k is a pilot or a data carrier, respectively. Since x_{nk} and y_{nk} are the sum of two independent Gaussian random variables, their distributions are Gaussian [79]. Therefore, u_{nk} has a χ^2 distribution with two degrees of freedom. The mean and variance of u_{nk} are equal to [Appendix B.2]

$$E[u_{nk}] = \sigma_k^2 + \sigma_n^2 \tag{3.44}$$

$$var[u_{nk}] = (\sigma_k^2 + \sigma_n^2)^2 \tag{3.45}$$

where σ_n^2 is the variance of the additive white Gaussian noise n_k, and

$$\sigma_k = \begin{cases} \sigma_p & \text{for pilot carrier at frequency } f_k \\ \sigma_d & \text{for data carrier at frequency } f_k \end{cases} \tag{3.46}$$

Recall from Section 3.3 that the instantaneous power u_k also has a χ^2 distribution with two degrees of freedom. It follows that the statistical models for both the noisy and noiseless environment are basically identical and only the numerical values of the means and variances of the instantaneous power are changed from those defined in Equation 3.20 and Equation 3.21 to Equation 3.44 and Equation 3.45, respectively.

Therefore, the test statistic $\overline{U}_{nK}(\tau)$ used to determine the coarse frequency offset under noisy environment still has the same format. That is,

$$\overline{U}_{nK}(\tau) = \sum_{i \in \{K+\tau\}} u_{ni} \tag{3.47}$$

where $\{K\}$ is the set of frequency indices of the pilots pattern.

Similarly, if $\overline{U}_{nK}$ are composed of n_p pilot carriers and $L-n_p$ data carriers, we have the following two cases:

<u>Case 1</u> $\mathbf{H_{n1} : n_p = L}$

- Mean

$$E[\overline{U}_{nK}|H_{n1}] = L(\sigma_p^2 + \sigma_n^2) \tag{3.48}$$

- Variance

$$var[\overline{U}_{nK}|H_{n1}] = L(\sigma_p^2 + \sigma_n^2)^2 \tag{3.49}$$

<u>Case 2</u> $\mathbf{H_{n0} : 0 \leq n_p < L}$

- Mean

$$E[\overline{U}_{nK}|H_{n0}] = n_p(\sigma_p^2 + \sigma_n^2) + (L - n_p)(\sigma_d^2 + \sigma_n^2) \tag{3.50}$$

- Variance

$$var[\overline{U}_{nK}|H_{n0}] = n_p(\sigma_p^2 + \sigma_n^2)^2 + (L - n_p)(\sigma_d^2 + \sigma_n^2)^2 \tag{3.51}$$

The difference between the two conditional means is given in Equation 3.52. The noise term, σ_n, has vanished and hence the additive noise does not change the relative positions of the mean of the two distributions.

$$\begin{aligned} E[\overline{U}_{nK}|H_{n1}] - E[\overline{U}_{nK}|H_{n0}] &= L(\sigma_p^2 + \sigma_n^2) - n_p(\sigma_p^2 + \sigma_n^2) - (L - n_p)(\sigma_d^2 + \sigma_n^2) \\ &= (L - n_p)\Big(\sigma_p^2 + \sigma_n^2 - (\sigma_d^2 + \sigma_n^2)\Big) \\ &= (L - n_p)(\sigma_p^2 - \sigma_d^2) \end{aligned} \tag{3.52}$$

Rearranging the term $var[\overline{U}_{nK}|H_{n0}]$ in Equation 3.51 yields

$$\begin{aligned} var[\overline{U}_{nk}|H_{n0}] &= n_p\Big(\sigma_p^2+\sigma_n^2\Big)^2+(L-n_p)\Big(\sigma_d^2+\sigma_n^2\Big)^2 \\ &= n_p\Big[\Big(\sigma_p^2+\sigma_n^2\Big)^2-\Big(\sigma_d^2+\sigma_n^2\Big)^2\Big]+L\Big(\sigma_d^2+\sigma_n^2\Big)^2 \\ &= n_p\Big[(\sigma_p^2-\sigma_d^2)(\sigma_p^2+\sigma_d^2+2\sigma_n^2)\Big]+L\Big(\sigma_d^2+\sigma_n^2\Big)^2 \end{aligned} \tag{3.53}$$

Finally, substituting Equation 3.49, Equation 3.51 and Equation 3.52 into Equation 3.31, the required statistical distance $\mathcal{D}_n$ under noisy environment is given by

$$\begin{aligned} \mathcal{D}_n &= \frac{E[\overline{U}_{nK}|H_{n1}]-E[\overline{U}_{nK}|H_{n0}]}{\sqrt{var[\overline{U}_{nK}|H_{n1}]}+\sqrt{var[\overline{U}_{nK}|H_{n0}]}} \\ &= \frac{(L-n_p)(\sigma_p^2-\sigma_d^2)}{\sqrt{L}(\sigma_p^2+\sigma_n^2)+\left\{n_p\Big[(\sigma_p^2-\sigma_d^2)(\sigma_p^2+\sigma_d^2+2\sigma_n^2)\Big]+L\Big(\sigma_d^2+\sigma_n^2\Big)^2\right\}^{\frac{1}{2}}} \\ &= \frac{L\sigma_d^2(1-s)(b-1)}{\sqrt{L}\sigma_d^2\left\{\Big(b+\frac{1}{S_dNR}\Big)+\left(s(b-1)\Big(b+1+\frac{2}{S_dNR}\Big)+\Big(1+\frac{1}{S_dNR}\Big)^2\right)^{\frac{1}{2}}\right\}} \\ &= \frac{\sqrt{L}(1-s)(b-1)}{b+\frac{1}{S_dNR}+\left(s(b-1)\Big(b+1+\frac{2}{S_dNR}\Big)+\Big(1+\frac{1}{S_dNR}\Big)^2\right)^{\frac{1}{2}}} \end{aligned} \tag{3.54}$$

where

$$S_dNR=\frac{\sigma_d^2}{\sigma_n^2} \tag{3.55}$$

If $\sigma_d^2 \gg \sigma_n^2$, then $\frac{1}{S_dNR} \approx 0$ and hence

$$\begin{aligned} \mathcal{D}_n(\overline{U}_{nK}|\sigma_d^2 \gg \sigma_n^2) &\approx \frac{\sqrt{L}(1-s)(b-1)}{b+\sqrt{s(b-1)(b+1)+1}} \\ &= \frac{\sqrt{L}(1-s)(b-1)}{b+\sqrt{s(b^2-1)+1}} \\ &= \mathcal{D}(\overline{U}_K) \qquad \text{(cf. Equation 3.34)} \end{aligned}$$

As seen, the distance $\mathcal{D}_n$ reduces to $\mathcal{D}$ under high signal-to-noise condition. In general, the additive noise reduces the statistical distance of the test statistic $\overline{U}_{nK}$ and hence increase the error rate of the proposed coarse frequency offset estimator.

3.7 Tolerance on Fine Frequency Offset

The proposed coarse frequency estimator is developed under the assumption that the fine frequency offset has been corrected and the effects due to intercarrier interference can be ignored. However, in practical applications, there may be still a residue error whose value depends on the accuracy and tracking speed of the fine frequency offset estimator. In this section, we will determine the limit of the fine frequency offset that the proposed coarse frequency estimator can tolerate.

If the total power of noise is larger than the power difference between the pilots and the data carriers, the accumulated power of the noisy data carriers will be larger than that of the pilots. It follows that the pilots cannot be differentiated from data carriers by exploiting only the received signal power, and hence the proposed coarse frequency synchronization algorithm will not work properly.

Let us define the *noise margin* (η) as the difference in the received power of the pilots and the data carriers. From Equation 2.40, the power of the received signals is attenuated by a factor $(\sin \pi\zeta/\pi\zeta)^2$, where ζ is the amount of the fine frequency offset. Therefore, the noise margin can be determined by

$$\eta = (\sigma_p^2 - \sigma_d^2)\left(\frac{\sin \pi\zeta}{\pi\zeta}\right)^2 \tag{3.56}$$

The noise margin defines the maximum amount of noise power that the system can tolerate for correct coarse frequency synchronization. Therefore, the noise margin η must be greater than the sum of the average noise power due to intercarrier interference $E[|I_d|^2]$ and the additive Gaussian noise σ_n^2. That is,

$$\eta > E[|I_d|^2] + \sigma_n^2 \tag{3.57}$$

With reference to Equation 2.39 and assuming a unity average channel gain at all frequencies, the average noise power $E[|I_d|^2]$ due to the intercarrier interference on data carriers is given by

$$E[|I_d|^2] = \sigma_d^2(\sin \pi\zeta)^2 \sum_{k=1}^{N-1} \frac{1}{\left[N \sin\left(\frac{\pi(k+\zeta)}{N}\right)\right]^2} \tag{3.58}$$

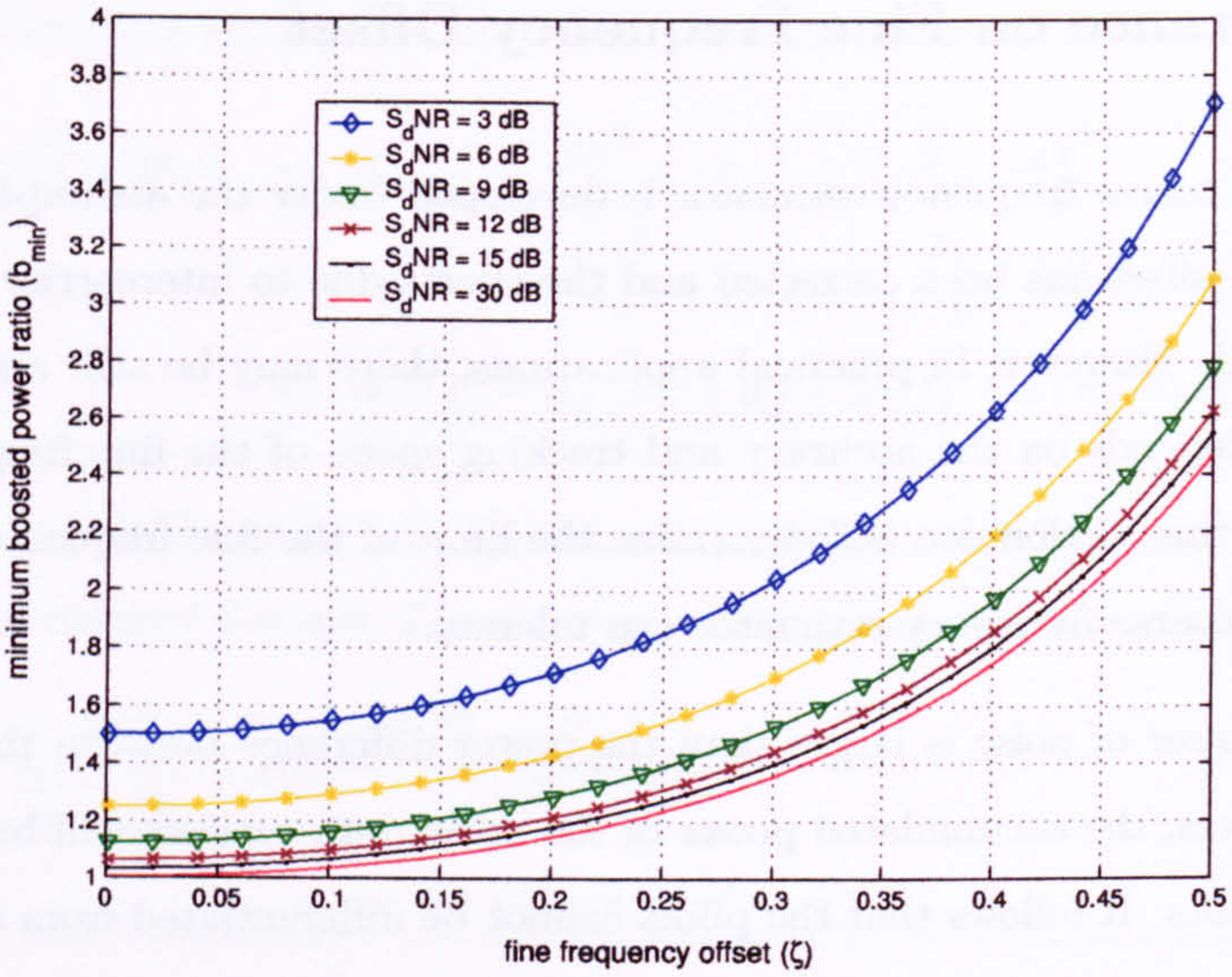

Figure 3.5: Minimum boosted power ratio for various SNR of data subcarriers, $0 \leq \zeta \leq 0.5$

From Equation 3.56, Equation 3.57 and Equation 3.58,

$$\begin{aligned}
\eta &> E[|I_d|^2] + \sigma_n^2 \\
(\sigma_p^2 - \sigma_d^2)\left(\frac{\sin \pi\zeta}{\pi\zeta}\right)^2 &> \sigma_d^2 (\sin \pi\zeta)^2 \sum_{k=1}^{N-1} \left[\frac{1}{N \sin\left(\frac{\pi(k+\zeta)}{N}\right)}\right]^2 + \sigma_n^2 \\
(b-1)\left(\frac{\sin \pi\zeta}{\pi\zeta}\right)^2 &> (\sin \pi\zeta)^2 \sum_{k=1}^{N-1} \left[\frac{1}{N \sin\left(\frac{\pi(k+\zeta)}{N}\right)}\right]^2 + \frac{1}{S_d NR} \\
b &> (\pi\zeta)^2 \sum_{k=1}^{N-1} \left[\frac{1}{N \sin\left(\frac{\pi(k+\zeta)}{N}\right)}\right]^2 + \left(\frac{\pi\zeta}{\sin \pi\zeta}\right)^2 \frac{1}{S_d NR} + 1
\end{aligned} \tag{3.59}$$

where $b = \sigma_p^2/\sigma_d^2$ and $S_d NR = \sigma_d^2/\sigma_n^2$.

Let us denote the right-hand side of Equation 3.59 as b_{min} for clarity. The numerical values of b_{min} for various $S_d NR$ and $0 \leq \zeta \leq 0.5$ are determined and the results are plotted in Figure. 3.5. From these design curves, we can determine the minimum boosted power ration b_{min} for a given range of ζ and $S_d NR$. For example, suppose the residue fine frequency offset is known to vary between 0 and 0.25. Then, the boosted power ratio should be at least 1.3 if the signal-to-noise power ratio is about 12 dB. Inspection of Figure 3.5 reveals that whenever the boosted power ratio is larger than

about 1.6, the amount of the fine frequency offset is allowed to be as large as 0.1 (20% of the maximum range), which should be larger than the residue error of any practical fine frequency offset estimators. It justifies the assumption of neglecting the fine frequency offset during the development of the coarse frequency synchronization algorithm. On the other hand, the boosted power ratio in DVB-T is 1.78. This confirms that 1.6 is a practical amount of power boosting in real applications.

Notice that the parameters determined from the design curves in Figure 3.5 are necessary, but not sufficient conditions for reliable coarse frequency synchronization using the proposed pilots-power-detection algorithm. The overall performance also depends on other parameters, such as the total number of pilots, stray pilots distribution and the power of outliers.

3.8 Simulation and Results

3.8.1 OFDM Parameters

In this section, we will demonstrate the performance of the coarse frequency synchronization algorithm by computer simulations. The OFDM parameters used in the simulations are based on the 2k-mode European DVB-T (Digital Video Broadcasting - Terrestrial) standard [25] in which the FFT size is equal to 2048. There are total 2048 subcarriers in each OFDM symbol, including 1660 data carriers, 45 pilot carriers and the remaining subcarriers are virtual carriers. The virtual carriers carriers are all set to zero and are evenly assigned on both sides of the signal spectrum.

The data carriers are modulated with complex data values, $c(k)$, randomly generated using the 16-QAM modulation mapping scheme (see Figure.3.6) as defined in the DVB-T standard [25]. The data values $c(k)$ are obtained by scaling the constellation points z with a normalization factor $\sqrt{10}$ (i.e. $c(k) = z/\sqrt{10}$) so that $E[c(k) \cdot c(k)^*] = 1$.

On the other hand, the pilot carriers are bi-phase modulated as follows.

$$\begin{cases} \mathrm{Re}\{c_k\} = \sqrt{b} \times w_k \\ \mathrm{Im}\{c_k\} = 0 \end{cases} \tag{3.60}$$

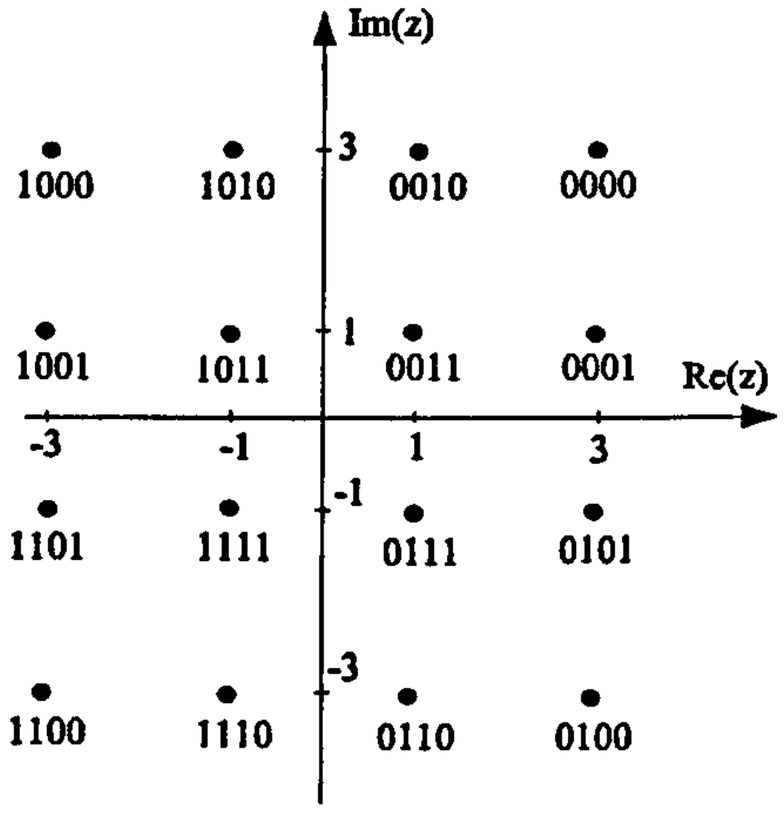

Figure 3.6: The 16-QAM mappings and the corresponding bit patterns representing a complex modulation symbol z [25]

The amplitude is equal to the square-root of the boosted power ratio b and w_k is a pseudo-random binary sequence generated by the generator polynomial $X^{11} + X^2 + 1$. The numerical values of w_k are listed in Table. 3.2. The boosted power ratio is equal to 16/9 as defined in the DVB-T standard. The time sampling duration (T) is 109.375 ns. The overall symbol duration is 252 μs ($2112T$), which includes a useful symbol duration of 224 μs ($2048T$) and a guard interval of 28 μs ($256T$). The intercarrier frequency spacing is 4464 Hz. The OFDM system parameters used in the simulations are summarized in Table 3.3.

3.8.2 Propagation Channels

In the simulations, the algorithms are investigated in an additive white Gaussian noise channel and dispersive channels. A simple tapped delay line model [87] is used for the dispersive channels simulation. This model is chosen because of its simplicity. The channels are assumed to be Rayleigh faded, and the tap coefficients are modelled as independent zero-mean complex valued Gaussian random processes. The tap coefficients are generated by Jakes's model [45], which is a simulation model for generating independent zero-mean complex valued Gaussian random variables.

k	0	48	54	87	141	156	192	201	255	279
w_k	-1	-1	-1	1	-1	1	-1	-1	1	1
k	282	333	432	450	483	525	531	618	636	714
w_k	1	-1	-1	1	1	1	1	1	1	-1
k	759	765	780	804	873	888	918	939	942	969
w_k	1	1	-1	1	1	1	1	-1	1	1
k	984	1050	1101	1107	1110	1137	1140	1146	1206	1269
w_k	1	-1	-1	1	-1	1	-1	1	1	-1
k	1323	1377	1491	1683	1704					
w_k	-1	1	1	-1	-1					

Table 3.2: Modulation values $\{w_k\}$ of the pilots carriers with frequency indices $\{k\}$

Number of FFT point	2048
Number of useful subcarrier	1705
Number of data subcarrier	1660
Number of pilot subcarrier	45
Number of virtual subcarrier	343
Duration of useful part (T_u)	224 μs
Guard Interval (T_g)	28 μs
Symbol duration ($T_g + T_u$)	252 μs
Carrier spacing ($1/T_u$)	4464 Hz
Bandwidth of OFDM	7.61 MHz
Modulation Method	16-QAM

Table 3.3: Specification of OFDM parameters used in the simulations

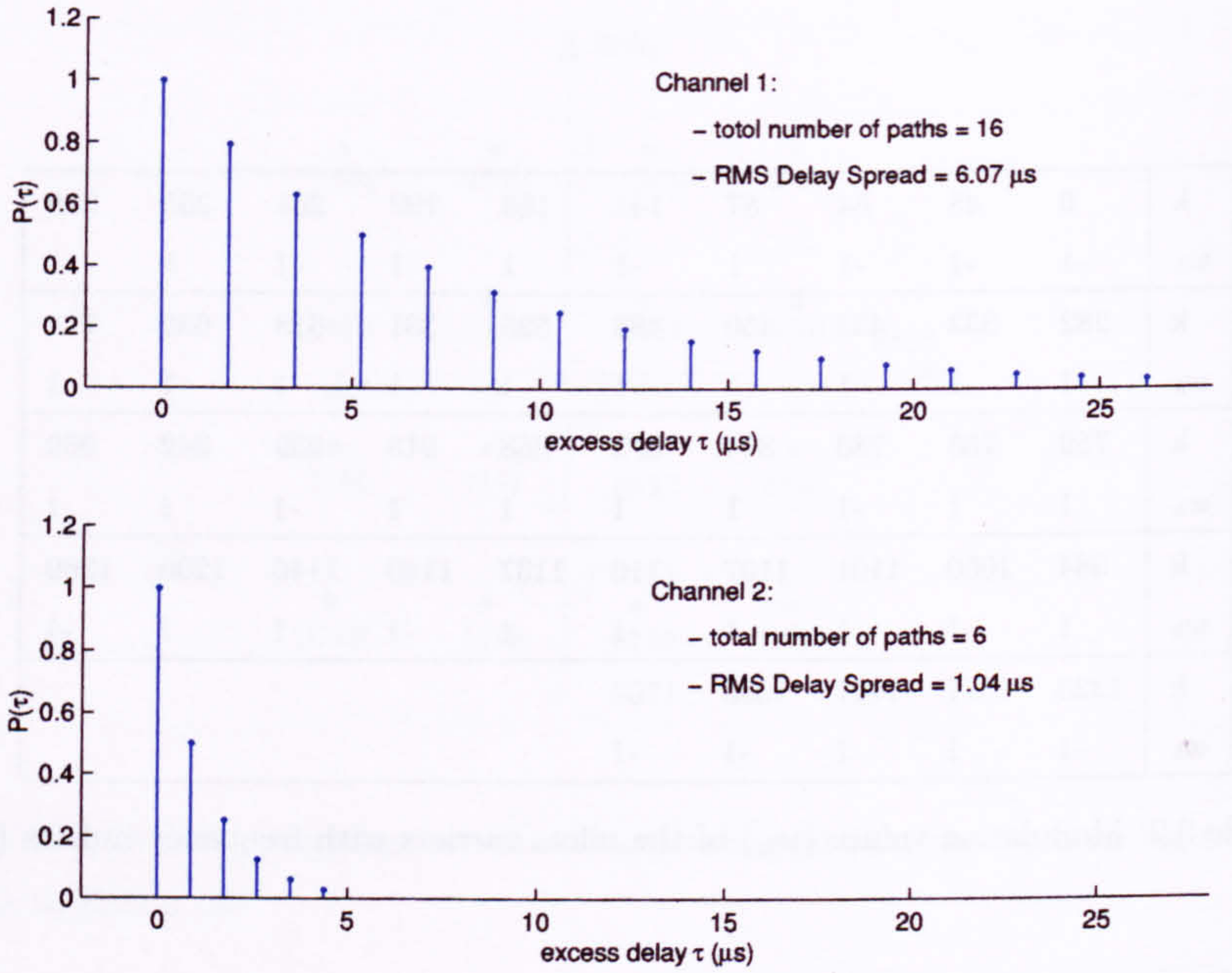

Figure 3.7: Power delay profiles of the multipath channels used in the simulations

Two multipath channels, Channel 1 and Channel 2, are used to evaluate the performance of the algorithms in different fading conditions. Figure 3.7 is the power delay profiles of the two channels and are obtained by plotting the normalized power of the signal arriving from different paths against the corresponding excess delay. The excess delay, τ_n, is the time delay of the n-th path measured relative to the first detectable signal arriving at the receiver at $\tau_1 = 0$. The power level of signal coming via different paths are normalized by those coming from the first path.

Channel 1 has 16 paths with identical delays, 1.75 μs, between adjacent paths. Similarly, Channel 2 has 6 paths with identical delays, 0.875 μs , between adjacent paths. The power delay profiles of Channel 1 and Channel 2 decay exponentially with rate equal to -1 dB/tap and -3 dB/tap, respectively.

We design the channel models in such a way that they have the same time dispersive properties of multipath channels reported in literatures [22, 75, 14]. The time dispersive properties of a multipath channel are most commonly quantified by the mean excess delay and the root-mean squared (rms) delay spread. The mean excess delay, which is

	Channel 1	Channel 2
no. of paths	16	6
inter-paths delay	1.75 μs	0.875 μs
maximum excess delay	26 μs	4.375 μs
mean excess delay	6.04 μs	0.79 μs
rms delay spread	6.07 μs	1.04 μs
power decay rate	-1 dB/path	-3 dB/path

Table 3.4: Parameters of the Channel 1 and Channel 2 used in the simulations

the first moment of the power delay profile $P(\tau_n)$, is defined to be [87]

$$\overline{\tau} = \frac{\sum_n P(\tau_n)\tau_n}{\sum_n P(\tau_n)} \tag{3.61}$$

On the other hand, the rms delay spread σ_τ is defined to be [87]

$$\sigma_\tau = \sqrt{\overline{\tau^2} - (\overline{\tau})^2} \tag{3.62}$$

where

$$\overline{\tau^2} = \frac{\sum_n P(\tau_n)\tau_n^2}{\sum_n P(\tau_n)} \tag{3.63}$$

According to the literature [22, 14, 75], typical values of the delay spread are 7 μs for an urban area and 0.7 μs for a rural area. Using the definitions given in Equation 3.62, the rms delay spread of Channel 1 and Channel 2 are determined and are equal to 6.07 μs and 1.04 μs respectively. Therefore, we will use Channel 1 and Channel 2 to simulate the performance of the estimator in an urban area and a rural area respectively.

On the other hand, the coherent time (T_c) characterizes the time rate of change of a channel. The coherent time is inversely proportional to the maximum Doppler frequency f_d, and it can be approximated by the equation [87]

$$T_c = \frac{0.423}{f_d} \tag{3.64}$$

In the simulations, the maximum mobile speed is assumed to be 70 km/hour, which is the vehicle speed limit on highways in Hong Kong. It follows that the maximum Doppler frequency is 30.5 Hz at a radio center carrier frequency of 470 MHz. From Equation 3.64, the coherent time is 13.8 ms, which is much larger than the OFDM

symbol duration, 252 μs. Therefore, we can assume that the channel coefficients are time-invariant and can be kept constant throughout the time period of one OFDM symbol. However, a new set of channel coefficient will be generated for every OFDM symbols. In addition, there will be no inter-symbol interference since the maximum path delays, 26.25 μs, is less than the guard interval duration, 28 μs. Table 3.4 summarizes the parameters of Channel 1 and Channel 2 used in the simulations.

3.8.3 Algorithms

In this chapter, the performance of the proposed pilots power detection algorithm (PPD) are studied using computer simulations. For the purpose of comparison, we have included two other algorithms found in the literatures [48, 83, 20] in the simulations to estimate the coarse frequency offset. The three algorithms are summarized as follows:

Algorithm 1: Pilots Power Detection (PPD)

$$\widehat{m} = \max_{m} \left\{ \sum_{i=0}^{n_p-1} u_{k_i+m+K_{min}} \right\} \tag{3.65}$$

Algorithm 2: Guard-band Power Detection (GPD) [48, 83]

$$\widehat{m} = \min_{m} \left\{ \sum_{k=K_{min}-N_v/2}^{K_{min}-1} u_{k+m} + \sum_{k=K_{max}+1}^{K_{max}+N_v/2} u_{k+m} \right\} \tag{3.66}$$

Algorithm 3: Maximum Correlation (MC) [20, 48]

$$\widehat{m} = \max_{m} \left\{ \left| \sum_{i=0}^{n_p-1} c_{k_i+m+K_{min}} \; w_{k_i}^{*} \right|^2 \right\} \tag{3.67}$$

The symbol $\widehat{m}$ is the estimated starting frequency index of the shifted signal frequency spectrum, u_k is the instantaneous power of the k-th subcarrier, n_p is total number of pilot carriers, N_v is the total length of the guard band at both sides of the signal frequency spectrum, k_i is the frequency index value of the i-th pilot carrier, c_{k_i} and w_{k_i} are the demodulated data value and the modulation value of the k_i-th pilot subcarrier, $K_{min} = 172$ and $K_{max} = 1876$ are the smallest and the largest indices of the data subcarriers, respectively. The subcarriers of an OFDM symbol are labelled from 0 to 2047.

The guard-band is a "band" of subcarriers at both ends of the frequency spectrum where the transmitted power of the subcarriers are all set to zero and carry no useful information. The subcarriers in the guard-band are sometimes referenced as "virtual carriers" in the literature [21]. The second method, guard-band power detection (GPD) algorithm, uses the fact that when the signal component is not within the sliding window, the total component power within the sliding window includes only noise component. Therefore, the shifted version of the signal spectrum due to the frequency offset can be estimated by locating the position where the total component power of the sliding window reaches the minimum [48].

The maximum correlation (MC) algorithm is based on the maximum likelihood estimation theory by using the correlation between the transmitted known symbol pattern and the values of the received data [20, 48].

3.8.4 Error Rate

Figure 3.8 plots the simulations results of the error rate of the three algorithms in the additive white gaussian noise channel. As seen, the MC algorithm has the best performance and it works well even under a very noisy condition. The error rate will be less than 10^{-4} whenever the signal-to-noise power ratio (SNR) is above -5 dB. On the other hand, both the PPD and GPD algorithms have very poor performance whenever the SNR is below 0 dB. This can be explained by the fact that both algorithms count on the difference in signal power between the data carriers and the non-data carriers. The non-data carriers are either the virtual carriers in GPD or the pilot carriers in PPD algorithms. At such a low SNR, there will be no significant different in signal power between subcarriers and therefore both the PPD and GDP algorithms break down. As expected, the performance improves with increasing SNR. The error rate of the PPD algorithm drops below 10^{-4} whenever the SNR is above 7 dB. The performance of the proposed PPD algorithm is roughly 3 dB better than that of the GDP algorithm in AWGN channel under high SNR.

Figure 3.9 plots the simulations results of the error rate of the three algorithms in multipath fading channels. Channel 1 and Channel 2 model the multipath conditions

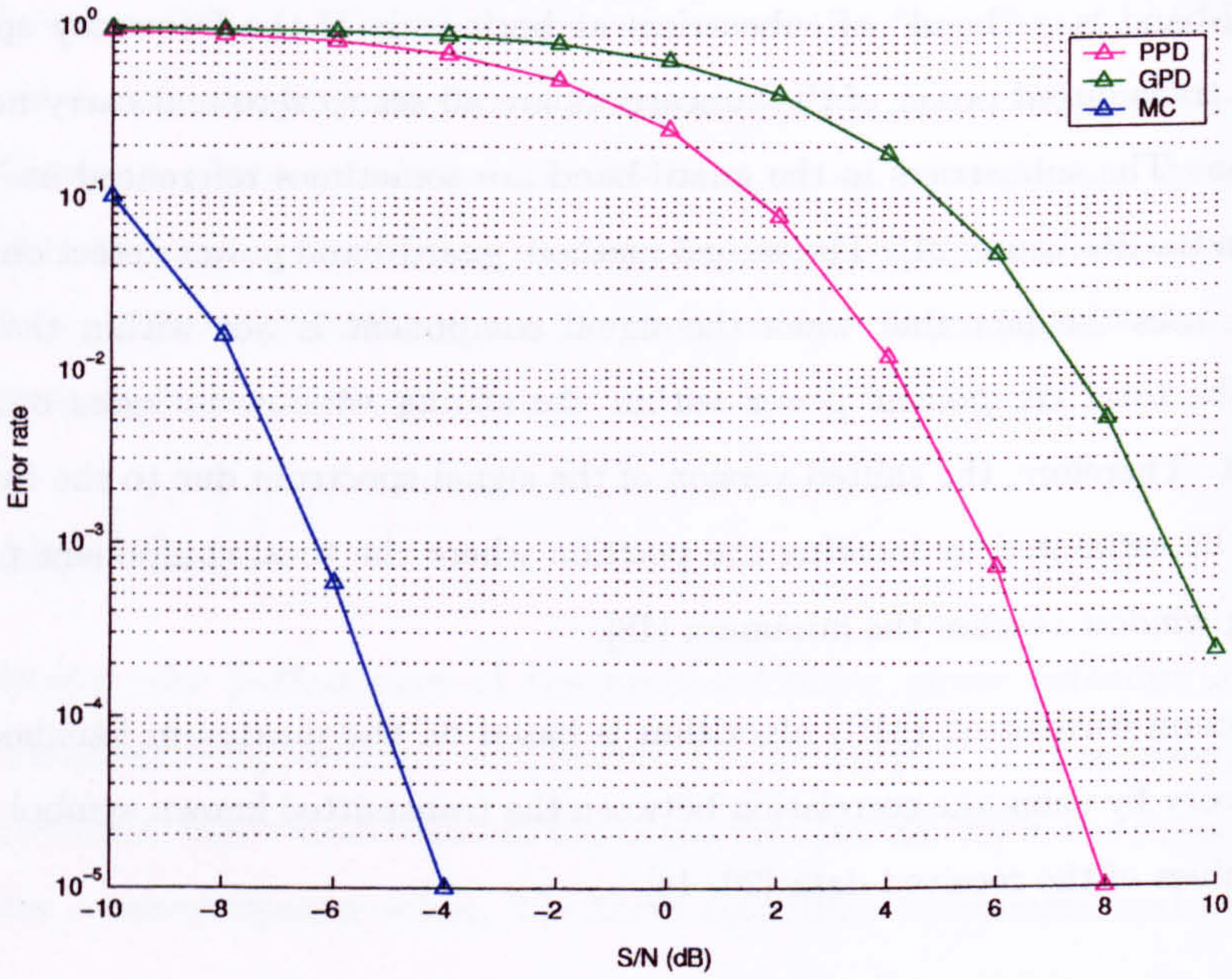

Figure 3.8: Error rate of the coarse frequency offset estimation algorithms in the additive white Gaussian noise channel

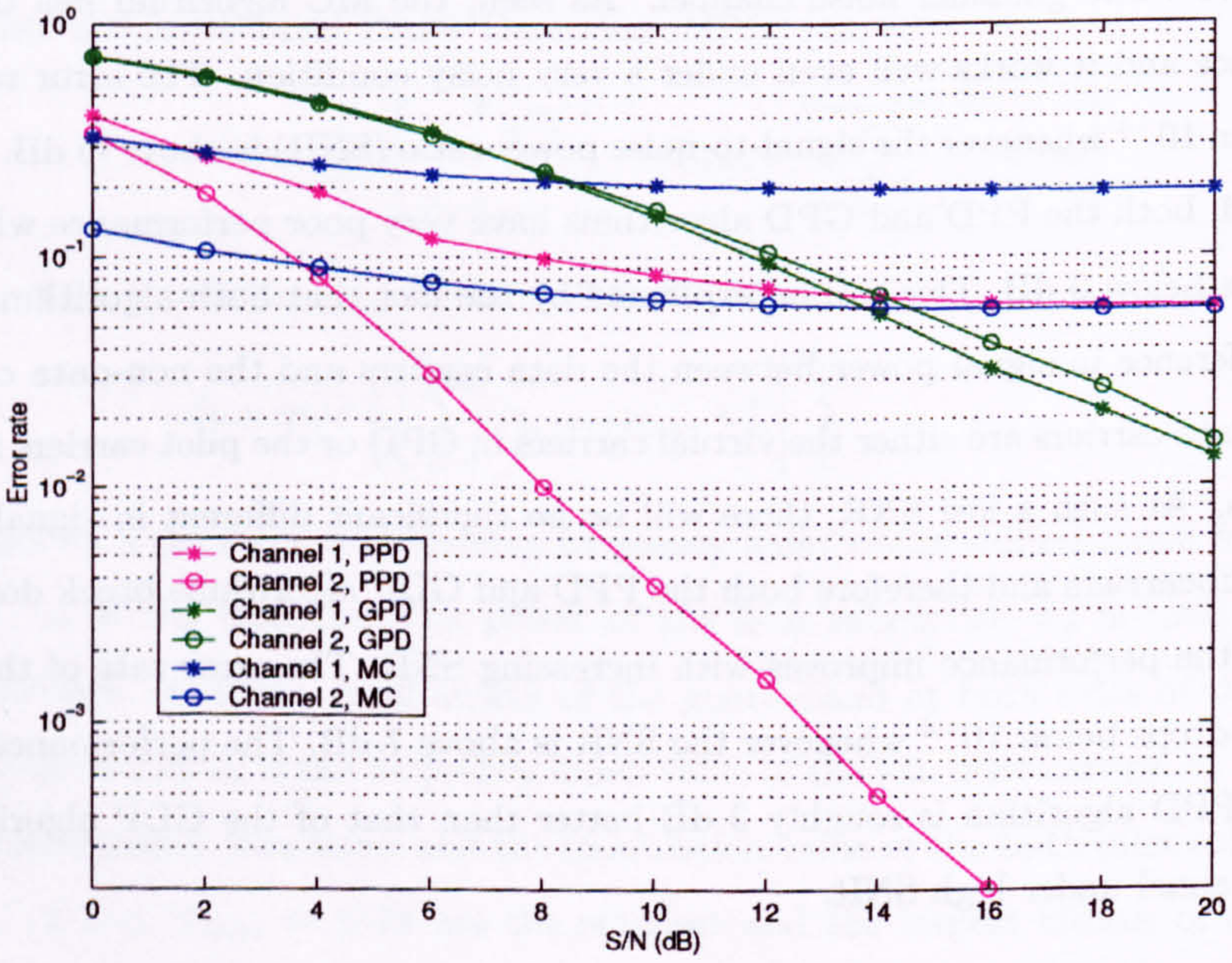

Figure 3.9: Error rate of the coarse frequency offset estimation algorithms in the multipath fading channels

in an urban area and a rural area, and the results are marked with "*" and "o", respectively. Both the PPD and MC algorithms have better performance in Channel 2, while GPD has similar performance in both channels. Unlike in AWGN channel where the MC algorithm always has better performance than the other two algorithms under the same signal-to-noise conditions, the MC algorithm now has larger amount of errors when the SNR is higher than some thresholds. In addition, the curves of the MC algorithm are rather flat with increasing SNR showing little improvement in the performance.

The performance of the proposed PPD algorithm is always better than that of the GPD algorithm in Channel 2. In Channel 1, the error rate of the PPD algorithm is also lower than that of the GPD algorithm until the SNR has reached a threshold at about 14 dB above which the GPD algorithm has a better performance.

The threshold or in equivalent the performance of the proposed PPD algorithm depends on the relative power ratio of the pilots to the data carriers. We have determined the variations of the error rate of the PPD algorithm with the boosted power ratio in the AWGN channel, Channel 1 and Channel 2, and the simulation results are given in Figure 3.10, 3.11 and 3.12 respectively. As seen in the figures, the error rate decreases with increasing SNR and the boosted power ratio.

The performance of the three algorithms, when the pilot carriers are transmitted at power ratio other than 16/9 as defined in the DVB-T standard, are also evaluated and the results of the simulations are plotted in Figure 3.13. The green curves (GPD algorithm) move down with the increasing SNR and they are under the blue curves (MC algorithm) when the SNR is equal to 16 dB. In other words, the performance of the GDP algorithm will be better than that of the MC algorithm whenever SNR is above 16 dB no matter what the boosted power ratio is. On the other hand, the proposed PPD algorithm can out-perform the others whenever the boosted power ratio is sufficiently large.

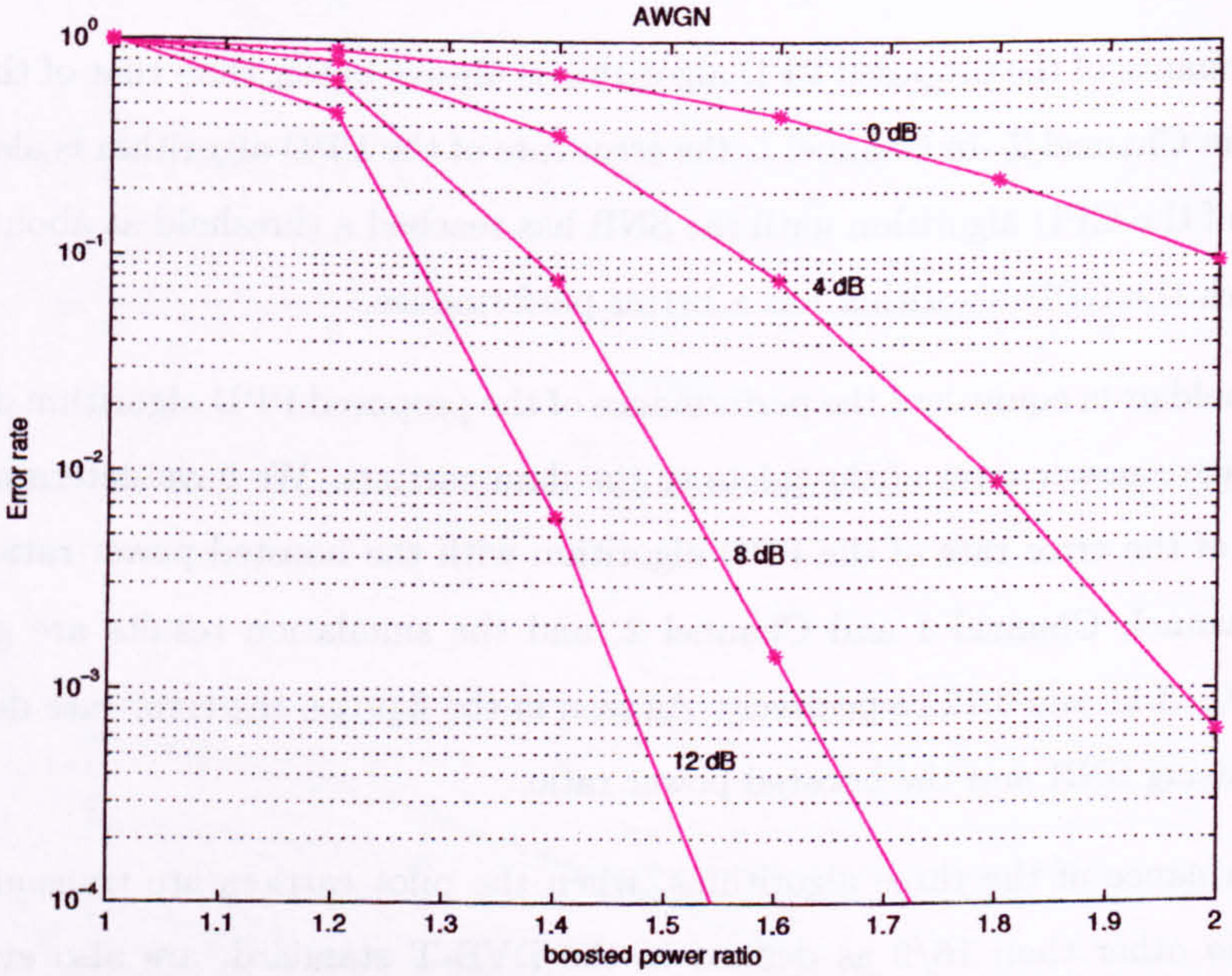

Figure 3.10: Performance of the PPD algorithm at different boosted power ratio in AWGN channel

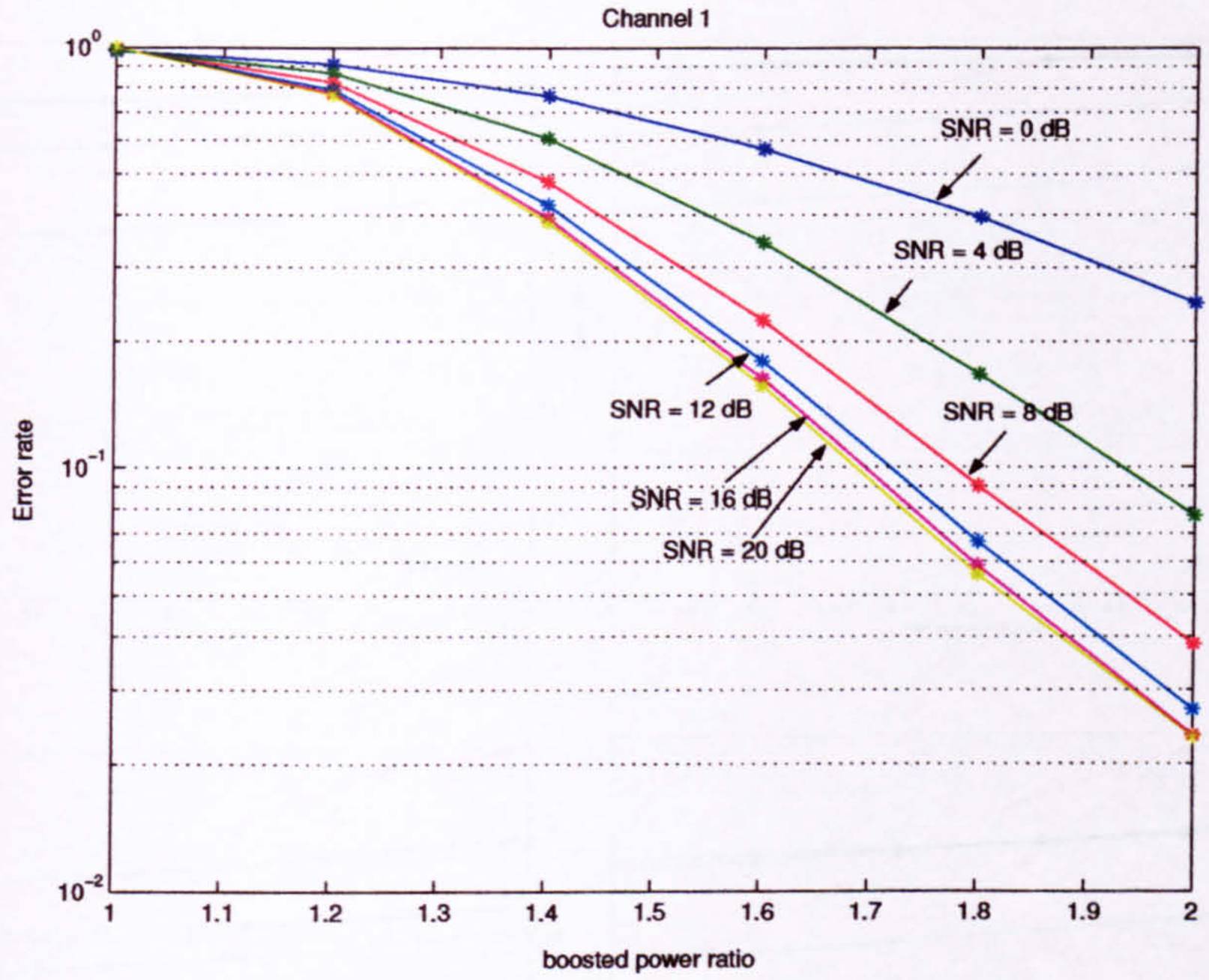

Figure 3.11: Performance of the PPD algorithm at different boosted power ratio in Channel 1 with AWGN

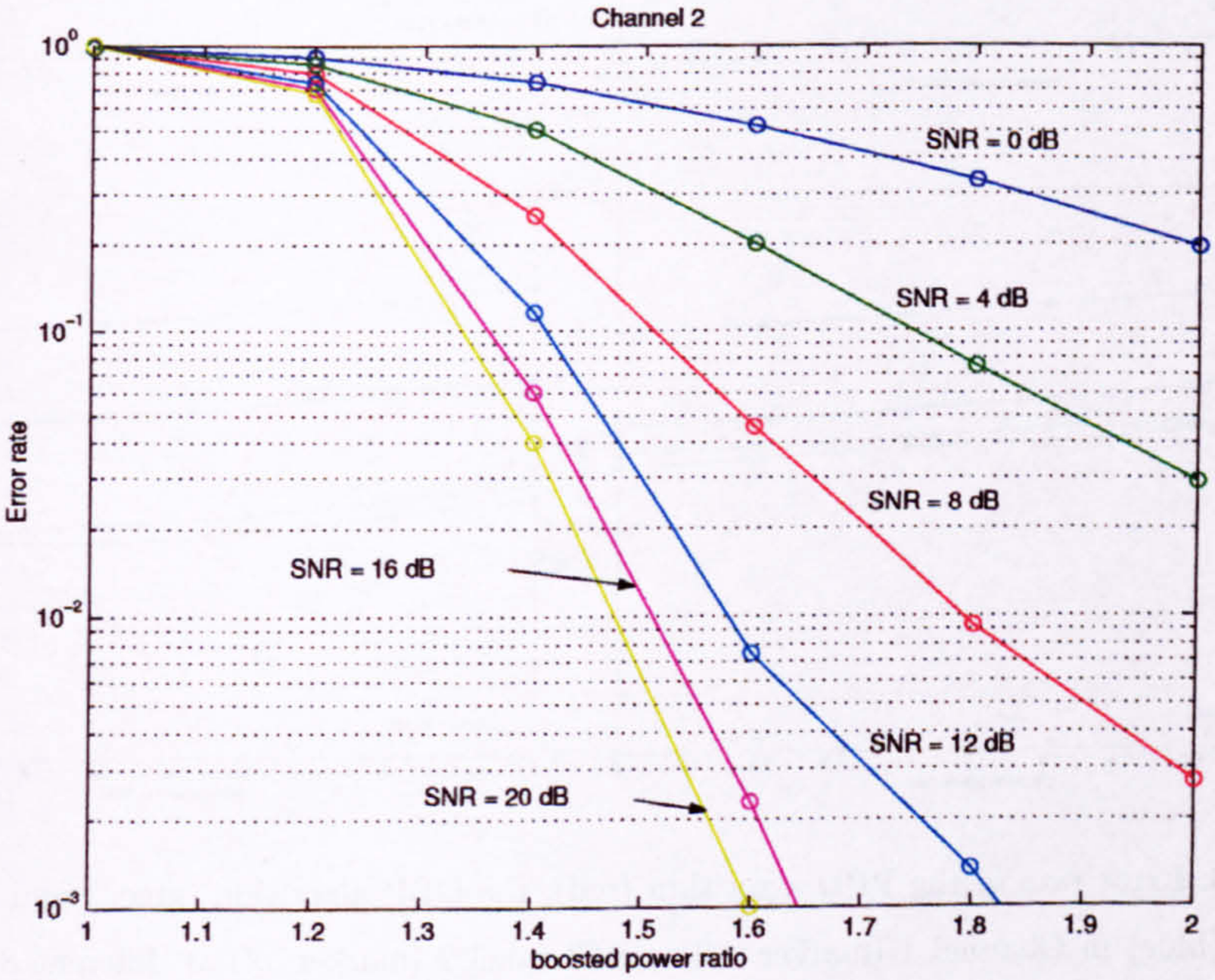

Figure 3.12: Performance of the PPD algorithm at different boosted power ratio in Channel 2 with AWGN

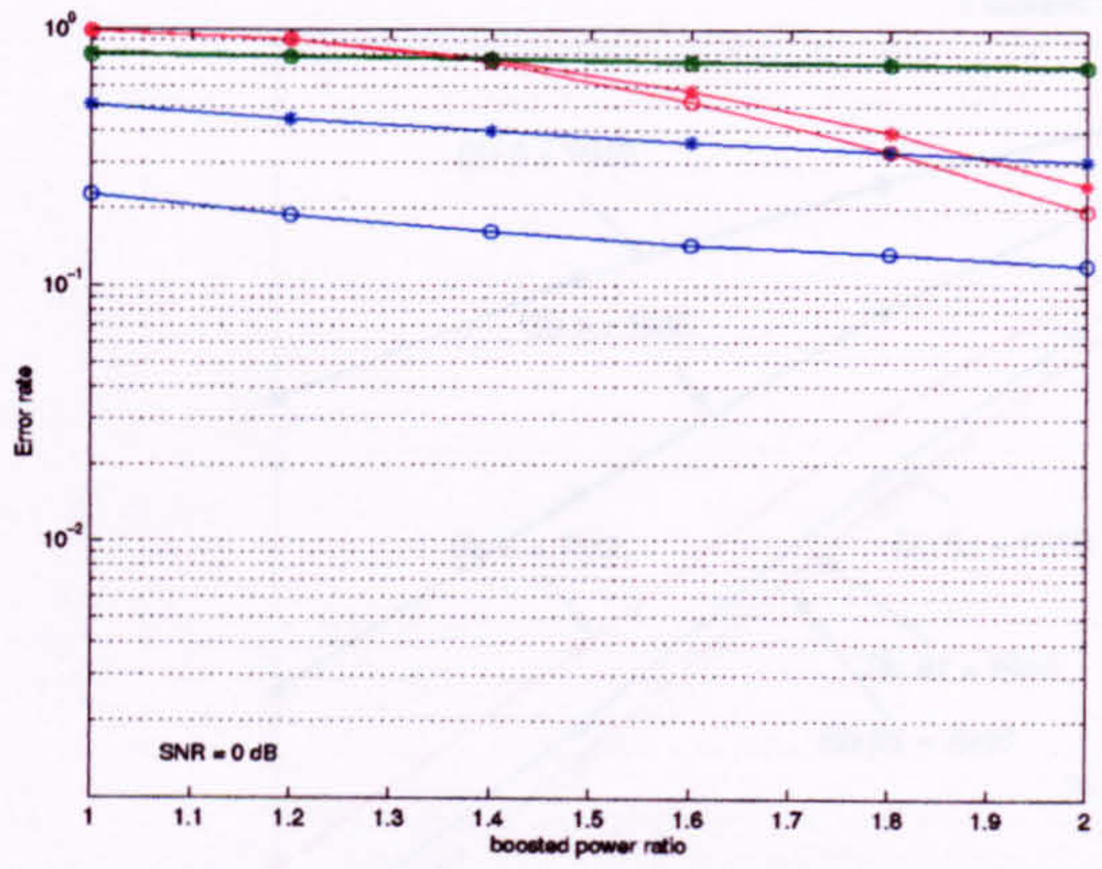

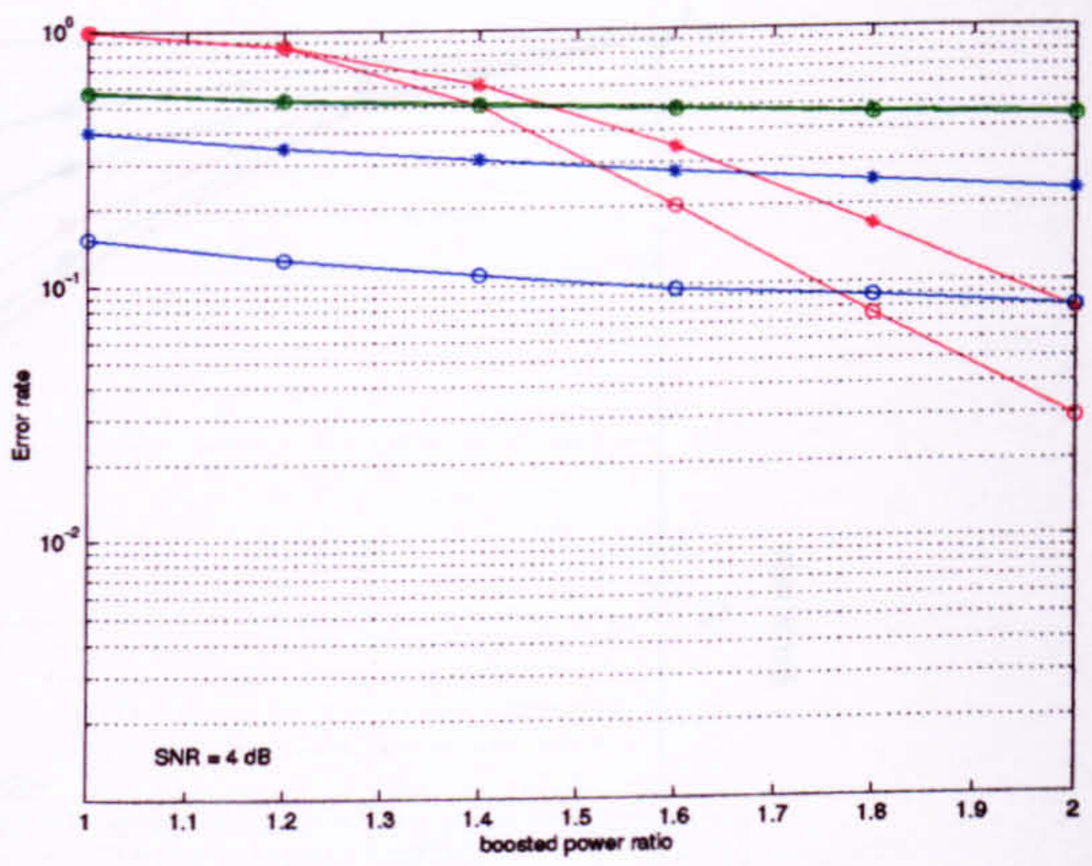

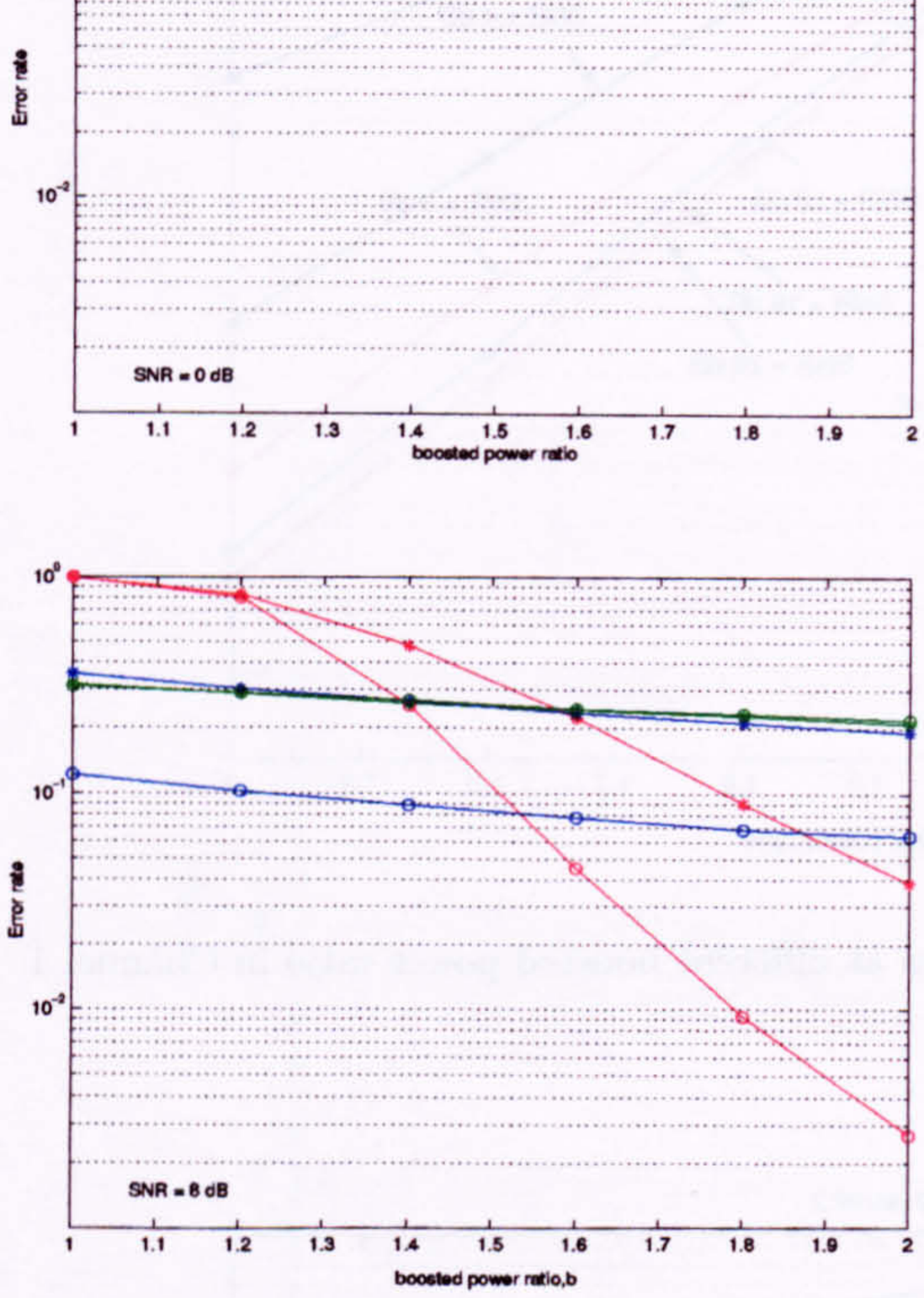

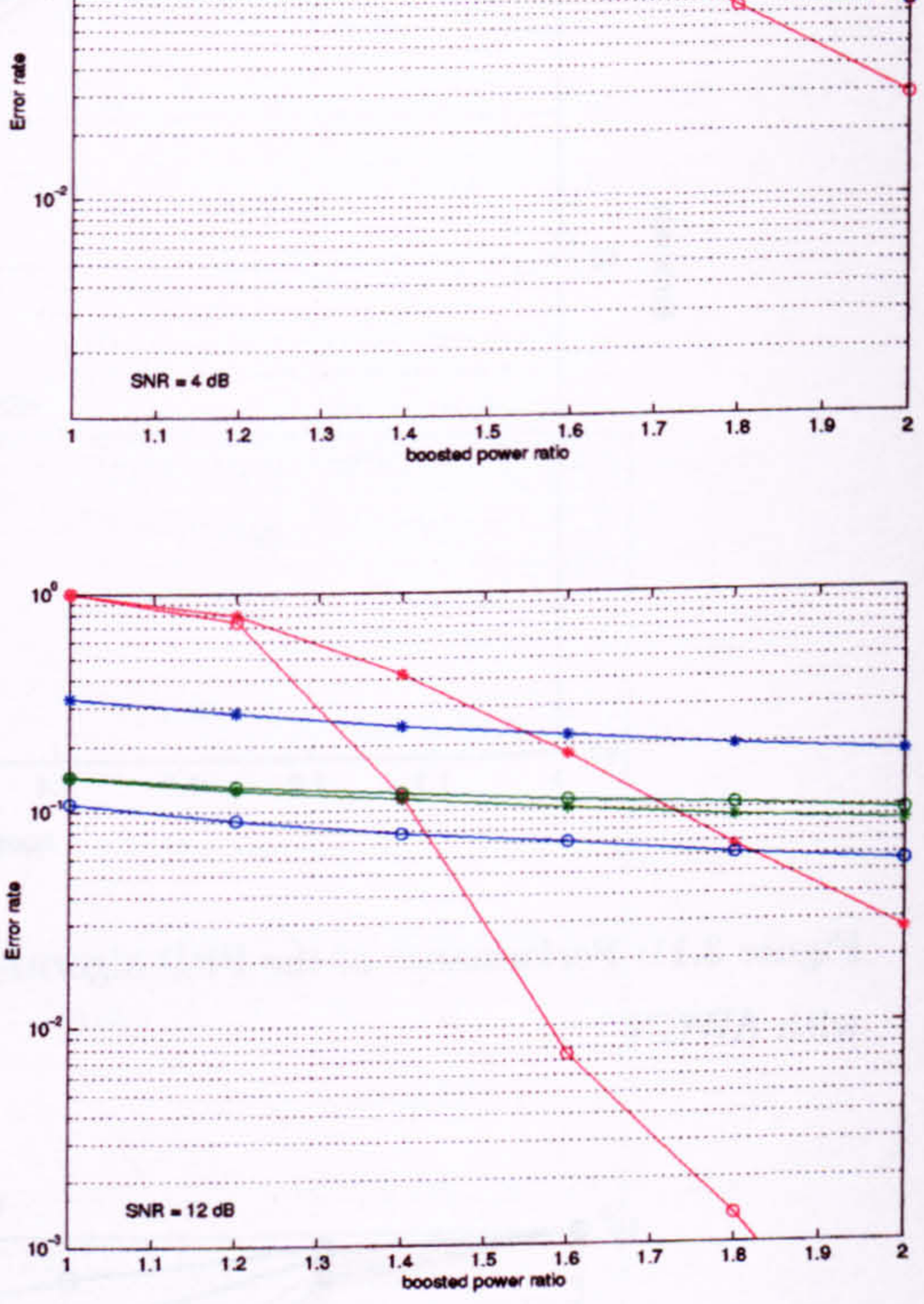

Figure 3.13: Error rate of the PPD algorithm (red), the GBP algorithm (green) and the MC algorithm (blue) in Channel 1 (marker '*') and Channel 2 (marker 'o') at different SNR and boosted power ratio

3.8.5 Complexity

We compare the complexity of the algorithms by determining the total amount of arithmetic operations required to implement the algorithms. The calculations are based on the direct implementation of the algorithms from the definitions. We only count the total number of real-number multiplication, real-number addition and magnitude comparison that take either the OFDM data or the intermediate results as the operands. For simplicity, steps involved in the supporting operations such as the generation of carriers indices and the updating of the loop counters are ignored. Otherwise, the analysis will become too complicate and too specific to a particular method of the implementation. However, the theoretical results of this simplified model will be verified with computer experiments in which the complete algorithms are implemented and the required amount of execution time are recorded.

This section includes four parts. In part (A), we determine the complexity of the proposed pilots power detection algorithm and derive an expression for it in terms of the cost of the basic arithmetic operations. Similarly, the complexity analysis of the guard band power detection algorithm and the maximum correlation algorithm are given in part (B) and part (C), respectively. Finally, part (D) includes a comparison of their complexity and the results of the computer simulations.

(A) Pilots Power Detection (PPD)

(A.1) Algorithm:

$$\widehat{m} = \max_{m}\{U_m\} \qquad U_m = \sum_{i=0}^{n_p-1} u_k \quad , \; k = k_i + m + K_{min} \tag{3.68}$$

(A.2) Analysis:

Suppose the amount of frequency shift is less than $L_s/2$ intercarrier spacing in either left or right directions. Therefore, the search starts at the subcarrier with index $(K_{min} - L_s/2)$ and stops at the subcarrier with index $(K_{max} + L_s/2)$. The shifted frequency spectrum will be found at either one of the $(L_s + 1)$ possible positions. Figure 3.14 illustrates the two extreme positions of the sliding window. The searching window

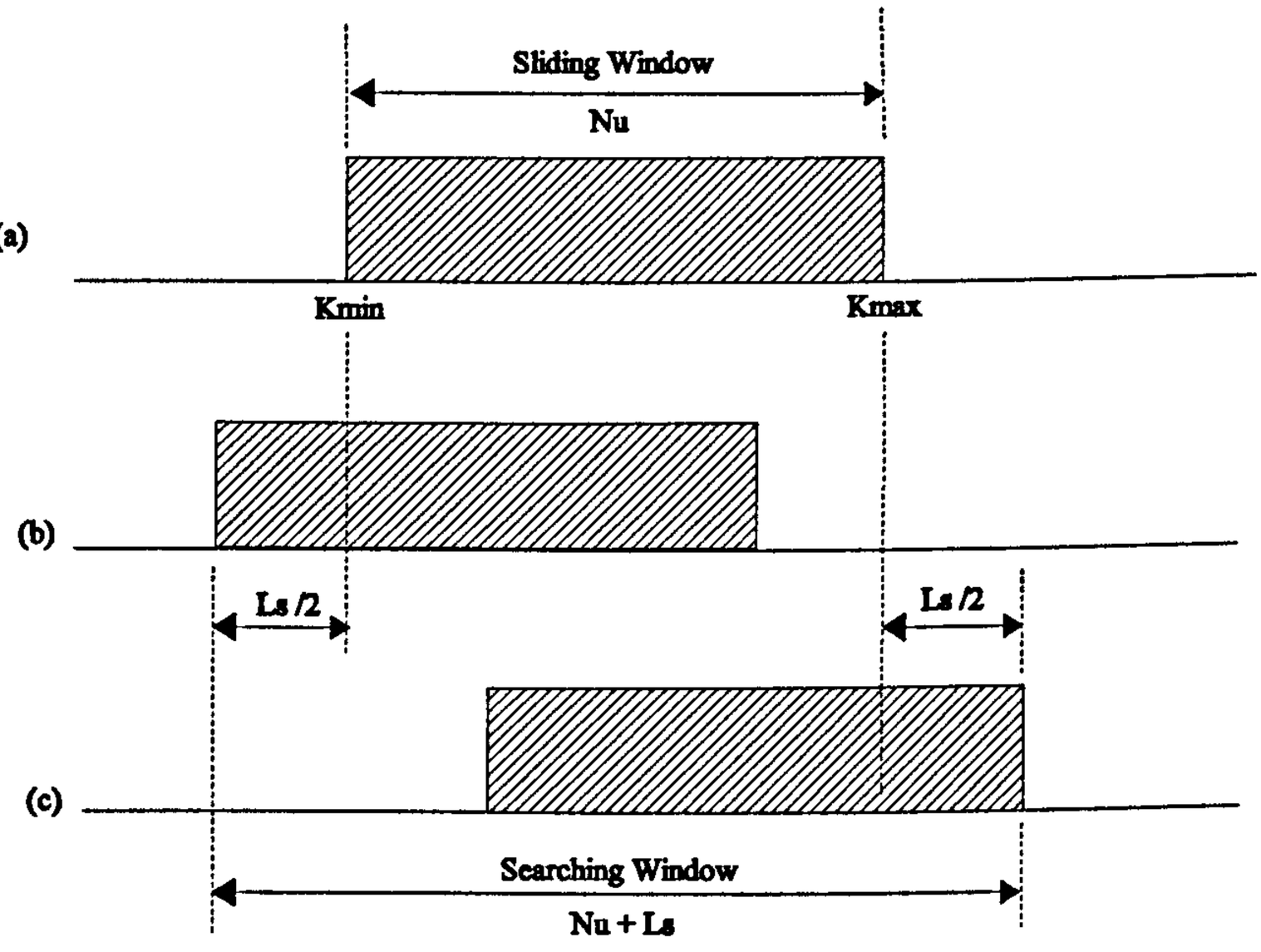

Figure 3.14: Illustrative drawing of the sliding window at the (a) nominal position, (b) left-most position and the (c) right-most position in the proposed pilots power detection algorithm

covers total $(N_u + L_s)$ subcarriers, where $N_u = K_{max} - K_{min} + 1$ is the total number of useful carriers in each OFDM symbol.

Suppose the sliding window is now m_0 subcarrier away from the nominal position. First of all, we have to determine the instantaneous power u_k of the subcarriers inside the sliding window with frequency indices specified by the pilots pattern. Each u_k is defined as

$$u_k = x_k^2 + y_k^2 \tag{3.69}$$

and is the sum of square of the real and imaginary components of the received data $(x_k + j\ y_k)$. It takes two real-number multiplications and one real-number addition to compute one u_k. Each U_m is the sum of n_p different u_k. It takes $2n_p$ multiplications and n_p additions to compute all u_k, and $(n_p - 1)$ additions to sum them up. Therefore, it takes total $2n_p$ multiplications and $(2n_p - 1)$ additions to compute one U_m. Since there are total $(L_s + 1)$ possible U_m, where $m = -L_s/2, \cdots, L_s/2$, total $2n_p(L_s + 1)$ multiplications and $(2n_p - 1)(L_s + 1)$ additions are required. Finally, we have to carry

Algorithm: $\widehat{m} = \max_m\{U_m\}$ $U_m = \sum_{i=0}^{n_p-1} u_k$, $k = k_i + m + K_{min}$				
Operations	**Number of Multiplication**	**Number of Addition**	**Number of Comparison**	**Notes**
(1) Compute one u_k, $m = m_o$	2	1	0	$u_k = x_k^2 + y_k^2$
(2) Compute all u_k, $m = m_o$	$2n_p$	n_p	0	there are n_p items
(3) Compute U_{m_o} (u_k are known)	0	$n_p - 1$	0	$U_{m_o} = \sum$ (n_p items)
(4) Compute U_{m_o} (u_k are unknown)	$2n_p$	$2n_p - 1$	0	(2)+(3)
(5) Compute all U_m	$2n_p(L_s + 1)$	$(2n_p - 1)(L_s + 1)$	0	there are $L_s + 1$ items
(6) Select the largest U_m	0	0	L_s	$m = -L_s/2, \cdots, L_s/2$
Total	$2n_p(L_s + 1)$	$(2n_p - 1)(L_s + 1)$	L_s	

Table 3.5: Computation complexity analysis of the proposed pilot power detection algorithm in terms of the total number of multiplication, addition and comparison

out L_s magnitude comparison to select the largest U_m. The complexity analysis is summarized in Table. 3.5.

Let us define the implementation cost of the algorithm as

$$\begin{aligned} \text{Cost} &= \text{Number of addition} \times \text{Cost of addition } (C_a) \\ &\quad + \text{Number of multiplication} \times \text{Cost of multiplication } (C_m) \\ &\quad + \text{Number of comparison} \times \text{Cost of comparison } (C_c) \end{aligned} \tag{3.70}$$

Then, the cost of the pilots power detection algorithm (C_{ppd}) is given by the following equation

$$C_{ppd} = (2n_p - 1)(L_s + 1)C_a + 2n_p(L_s + 1)C_m + L_sC_c \tag{3.71}$$

(B) Guard-band Power Detection (GPD)

(B.1) Algorithm:

$$\widehat{m} = \min_m \{U_m\} \qquad U_m = \sum_{k=K_{min}-N_v/2+m}^{K_{min}-1+m} u_k + \sum_{k=K_{max}+1+m}^{K_{max}+N_v/2+m} u_k \tag{3.72}$$

(B.2) Analysis:

The guard-band is the set of subcarriers with frequency indices in $\{0, 1, \cdots, K_{min} - 1\}$ and $\{K_{max} + 1, \cdots, N - 2, N - 1\}$, where N is the total number of subcarriers of an OFDM symbol, K_{min} and K_{max} are the minimum and the maximum frequency index of the useful subcarriers respectively. At the transmitter, the guard-band is assigned with virtual carriers whose output power values are set to zero. When the signal frequency

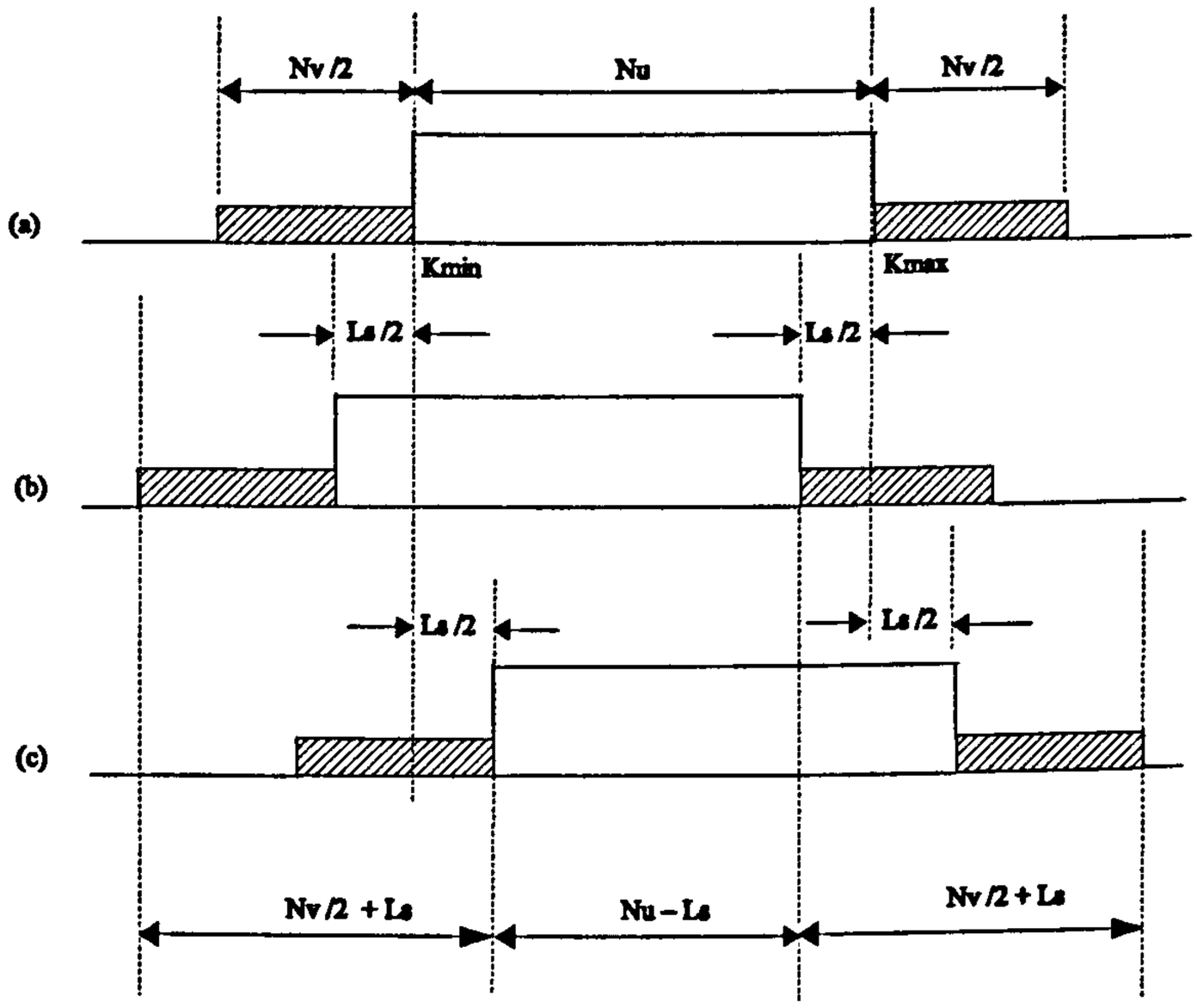

Figure 3.15: Illustrative drawing of the sliding window at the (a) nominal position, (b) left-most position and the (c) right-most position in the GPD algorithm; the shaded area is the search window

spectrum is shifted due to the coarse frequency offset, some of the useful subcarriers will fall into the guard-band.

In the guard-band power detection algorithm, two equal length sliding windows separated by N_u subcarriers are used to determine the new position of the shifted frequency spectrum. The two sliding windows are moved in the same way simultaneously with identical offset $m \in \{-L_s/2, \cdots, L_s/2\}$ from their nominal positions. Total N_v subcarriers ($N_v/2$ subcarriers from each sliding window) are selected and the sum of the power of these subcarriers are determined. When the sliding windows are moved to the correct positions at which only the virtual subcarriers in the guard bands are selected, the sum of the instantaneous power of the selected subcarriers will reach the minimum.

For simplicity, we have fixed the length of the two sliding windows to be identical and is an even number. However, this simplification will not affect the result of the complexity

Algorithm: $\hat{m} = \min_m\{U_m\}$ $U_m = \sum_{k=K_{min}-N_v/2+m}^{K_{min}-1+m} u_k + \sum_{k=K_{max}+1+m}^{K_{max}+N_v/2+m} u_k$				
Operations	**Number of Multiplication**	**Number of Addition**	**Number of Comparison**	**Notes**
(1) Compute one $u_k, m = m_o$	2	1	0	$u_k = x_k^2 + y_k^2$
(2) Compute all $u_k, m = m_o$	$2N_v$	N_v	0	no. of $u_k = N_v$
(3) Compute U_{m_o} (u_k are known)	0	$N_v - 1$	0	$(\frac{N_v}{2} - 1) + (\frac{N_v}{2} - 1) + 1$
(4) Compute U_{m_o} (u_k are unknown)	$2N_v$	$2N_v - 1$	0	(2)+(3)
(5) Compute all U_m	$2N_v(L_s + 1)$	$(2N_v - 1)(L_s + 1)$	0	$m = -L_s/2, \cdots, L_s/2$
(6) Select the smallest U_m	0	0	L_s	total no. of $U_m = L_s + 1$
Total	$2N_v(L_s + 1)$	$(2N_v - 1)(L_s + 1)$	L_s	

Table 3.6: Computation complexity analysis of the guard-band power detection algorithm in terms of the total number of multiplication, addition and comparison

analysis as long as the total length remain the same and hence the same total number of subcarriers are selected. Figure. 3.15 illustrates the two extreme positions of the sliding windows. In Figure. 3.15(b), the sliding windows have been moved to the left-most positions with offset $m = -L_s/2$, while in Figure. 3.15(c) the sliding windows have been moved to the right-most positions with offset $m = L_s/2$. Only subcarriers in the shaded region are used to determine the test statistics U_m.

Firstly, we have to determine the total number of computations involved when the sliding windows are fixed at one position, $m = m_0$ say. If all u_k are known, it takes only $N_v - 1$ additions to sum them up. Since the total length of the sliding windows is N_v, and each u_k requires two multiplications and one addition to be determined, it takes total $2N_v$ multiplications and N_v additions to compute all u_k of the selected subcarriers. Therefore, in order to determine one U_m, we have to carry out total $2N_v$ multiplications and $(2N_v - 1)$ additions. Secondly, the offset m_o can vary between $-L_s/2$ and $L_s/2$. There are total $(L_s + 1)$ different U_m and hence total $2N_v(L_s + 1)$ multiplications and $(2N_v - 1)(L_s + 1)$ additions are required to determine all U_m. Finally, we have to select the minimum out of the (L_s+1) different U_m; total L_s comparisons are required. Table. 3.6 summarizes the steps of the analysis.

Using the same definition of the computation cost in Equation. 3.70, the cost of the GPD algorithm (C_{gpd}) can be determined by the following equation:

$$C_{gpd} = (2N_v - 1)(L_s + 1)C_a + 2N_v(L_s + 1)C_m + L_sC_c \tag{3.73}$$

Algorithm: $\hat{m} = \max_m \{U_m\}$ $U_m = \left[\sum_{i=0}^{n_p-1} \text{Real}(c_k)w_{k_i}\right]^2 + \left[\sum_{i=0}^{n_p-1} \text{Imag}(c_k)w_{k_i}\right]^2$, $k = k_i + m + K_{min}$				
Operations	**Number of Multiplication**	**Number of Addition**	**Number of Comparison**	**Notes**
(1) $\sum \text{Real}(c_k)w_{k_i}, m = m_o$	n_p	$n_p - 1$	0	w_{k_i} is a real-number
(2) $\sum \text{Imaginary}(c_k)w_{k_i}, m = m_o$	n_p	$n_p - 1$	0	
(3) Compute U_{m_o}	$2n_p + 2$	$2(n_p - 1) + 1 = 2n_p - 1$	0	$U_m = (\cdot)^2 + (\cdot)^2$
(4) Compute all U_m	$2(n_p + 1)(L_s + 1)$	$(2n_p - 1)(L_s + 1)$	0	no. of $U_m = L_s + 1$
(5) Select the largest U_m	0	0	L_s	$m = -L_s/2, \cdots, Ls/2$
Total	$2(n_p + 1)(L_s + 1)$	$(2n_p - 1)(L_s + 1)$	L_s	

Table 3.7: Computation complexity analysis of the maximum correlation algorithm in terms of the total number of multiplication, addition and comparison

(C) Maximum Correlation (MC)

(C.1) Algorithm:

$$\hat{m} = \max_m \{U_m\} \qquad U_m = \left| \sum_{i=0}^{n_p-1} c_{k_i+m+K_{min}} \; w^*_{k_i} \right|^2 \tag{3.74}$$

(C.2) Analysis:

Only a binary {1,-1} sequence $\{w\}$ is assumed in the simulations. Therefore the product $\{c \cdot w\}$ only involves real number multiplications between the sequence with both the real and imaginary components of c. We can rearrange U_m into two parts as follows

$$U_m = \left[\sum_{i=0}^{n_p-1} \text{Real}(c_{k_i+m+K_{min}})w_{k_i}\right]^2 + \left[\sum_{i=0}^{n_p-1} \text{Imaginary}(c_{k_i+m+K_{min}})w_{k_i}\right]^2 \tag{3.75}$$

To determine each part, we need to carry out n_p multiplications and $n_p - 1$ additions to compute the correlation of the received data with the modulation sequence, and one multiplication to determine the magnitude square. Therefore, it requires total $2(n_p+1)$ multiplications and $(2n_p - 1)$ additions to determine one U_m. Suppose the offset m of the searching window is allowed to vary between $-L_s/2$ and $L_s/2$. There will be total (L_s+1) different U_m. It follows that we have to carry out total $2(L_s+1)(n_p+1)$ multiplications and $(L_s+1)(2n_p-1)$ additions to compute all U_m. Finally, we have to compare L_s different pairs of U_m in order to find the maximum.

Using the same definition of the computation cost in Equation. 3.70, the cost of the MC algorithm (C_{mc}) can be determined by the following equation.

$$C_{mc} = (2n_p - 1)(L_s + 1)C_a + 2(L_s + 1)(n_p + 1)C_m + L_sC_c \tag{3.76}$$

(D) Comparison

In order to compare the the costs of the three algorithms easily, we grouped the Equations (3.71), (3.73) and (3.76) together in Equation (3.77).

$$\begin{cases} C_{ppd} = & (2n_p - 1)(L_s + 1)C_a + 2n_p(L_s + 1)C_m + L_sC_c \\ C_{gpd} = & (2N_v - 1)(L_s + 1)C_a + 2N_v(L_s + 1)C_m + L_sC_c \\ C_{mc} = & (2n_p - 1)(L_s + 1)C_a + 2(n_p + 1)(L_s + 1)C_m + L_sC_c \end{cases} \tag{3.77}$$

From Equation (3.77), $C_{ppd} < C_{mc}$ by a factor of $2(L_s + 1)C_m$. In other words, the complexity of the proposed PPD algorithm is lower than that of the MC algorithm. The equations to compute C_{ppd} and C_{gpd} are very similar, and in fact they will become identical if n_p is replaced by N_v, or vise versa. Therefore, if the PPD and GPD algorithms are compared on the same ground that the same amount of system resources are being used, that is $N_v = n_p$, the same amount of efforts are required to implement the algorithms.

The costs of the arithmetic operations, C_a, C_m and C_c, depend on the actual implementation methods. There are two different ways to characterize the costs. They can be measured in terms of the size of the chip area if they are implemented in hardware using an application specific integrated circuit (ASIC). In this case, the size of the chip area used to build a multiplier is much larger than those required to build a comparator and an adder. Therefore, $C_m \gg C_a$ and $C_m \gg C_m$. Alternatively, if the algorithms are implemented in software using a state-of-the-art floating-point digital signal processor, it will take similar amount of time to compute addition, comparison and multiplication. In this case, we have $C_m \approx C_a \approx C_c$.

The theoretical complexity given in Equation 3.77 are evaluated numerically assuming that there are 1705 useful subcarriers (N_u), $N_v = n_p = 44$ and either (1) $C_m = 10C_a$ and $C_m = 10C_c$ or (2) $C_m = C_a = C_c$. Notice that the scaling factor 10 is assumed arbitrary to approximate the conditions of $C_m \gg C_a$ and $C_m \gg C_c$. The results are expressed in the units of C_a and are plotted in Figure 3.16. Since $C_{ppd} = C_{gpd}$ whenever $N_v = n_p$, only one curve is shown in Figure 3.16 to represent both C_{ppd} and C_{gpd}.

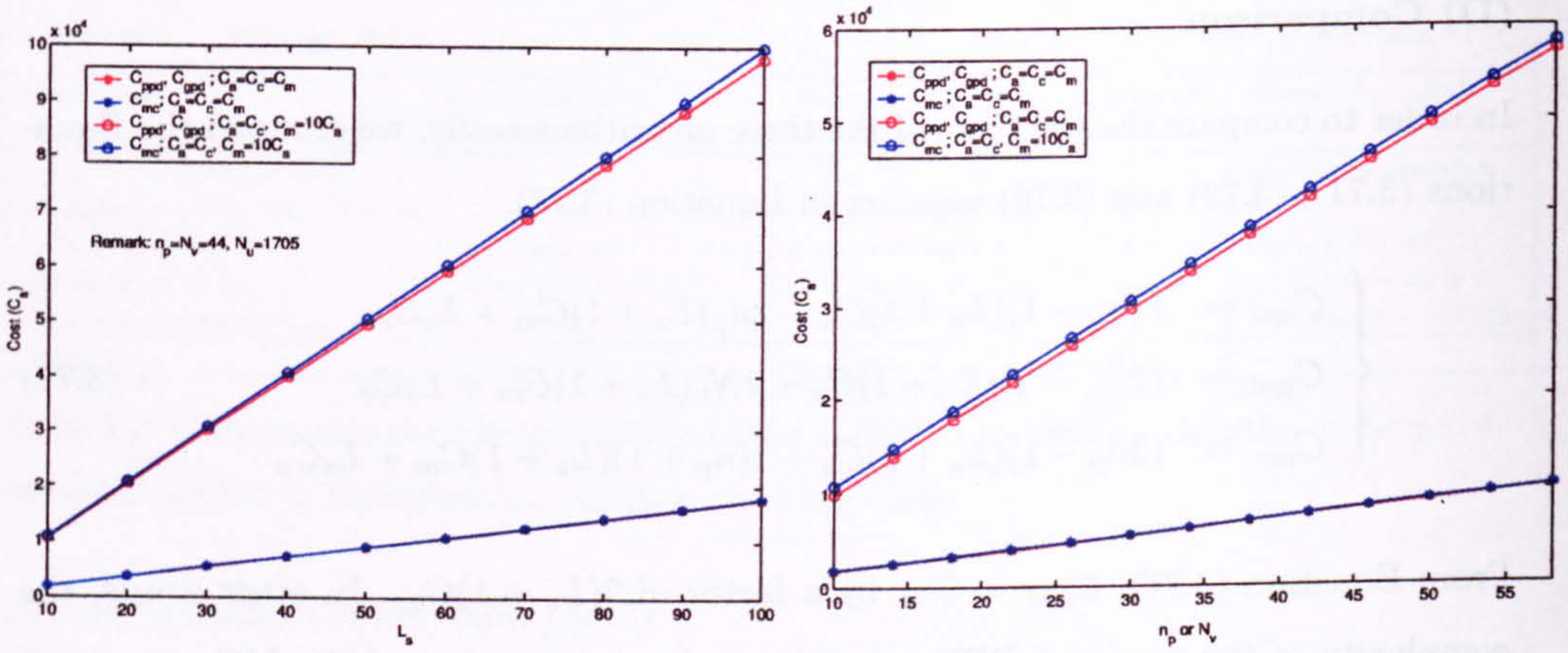

Figure 3.16: The theoretical variation of the complexity of the algorithms with parameters L_s, n_p and N_v; the complexity is expressed in the unit of the cost of addition C_a

As shown, the complexity increase linearly with the length of the search window (L_s) and the number of pilots (n_p). It is more complex to implement the algorithms in hardware than in software. In addition, the cost to implement the multiplication has a major contribution to the total cost required for the complete implementation of the algorithms.

The algorithms are implemented in "C" and are run on a 1.8GHz Pentium 4 computer. The total amount of time to run 50000 trials is recorded and the average time required to compute each algorithm is determined. The results are plotted in Figure 3.17.

Comparing the algorithms under the same conditions, the MC algorithm requires the longest amount of time as predicted by the theoretical analysis. However, the PPD algorithm also takes longer time than the GPD algorithm does. From Equation 3.77, they should have taken the same amount of time whenever $N_v = n_p$. This discrepancy may due to the over-simplicity of the theoretical model. Since the pilots in the PPD algorithm are scattered around but not continuous as in the GPD algorithm, the PPD algorithm requires additional steps to determine these pilots indices. However, this additional overhead has been ignored during the theoretical analysis which accounts for the discrepancy.

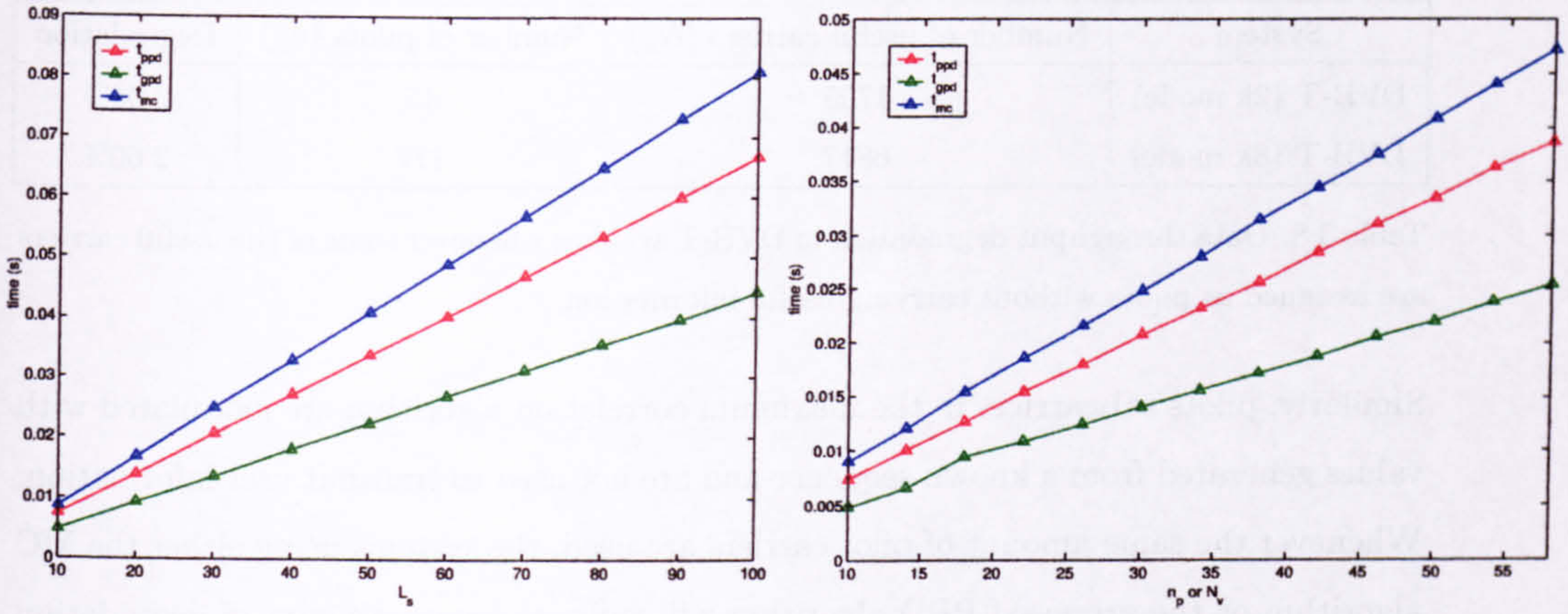

Figure 3.17: Experimental measurement of the amount of time required by different algorithms to determine the coarse frequency offset

3.8.6 Data Throughput

We have shown that the performance of the proposed pilots power detection algorithm increases with the total number of pilot carriers. However, pilot carriers carry no user information and hence the data throughput will be reduced with the increasing number of pilots. In other words, there is a trade-off between the total number of pilots and the data throughput.

The degradation in throughput is due to the fact that for a fixed amount of useful carriers, allocating more subcarriers to pilots reduces the amount of data carriers, and hence there are fewer carriers available to carry user information. Therefore, we can measure the degradation in data throughput by the ratio of the number of pilot carriers to the total number of useful subcarriers. That is,

$$\begin{aligned} \text{Degradation} &= \frac{\text{number of pilot carriers}}{\text{number of useful carriers}} \times 100\ \% \\ &= \frac{n_p}{N_u} \times 100\ \% \ . \end{aligned} \tag{3.78}$$

Using this definition, the amount of throughput degradation in DVB-T system, whenever some of the useful carriers are assigned as pilots, are determined and the results are listed in Table. 3.8. As shown, the system throughput in the DVB-T system will be reduced by roughly 2.64% in the 2k mode and 2.60% in the 8k mode.

System	Number of useful carriers (N_u)	Number of pilots (n_p)	Degradation
DVB-T (2k mode)	1705	45	2.64%
DVB-T (8k mode)	6817	177	2.60%

Table 3.8: Data throughput degradation in DVB-T systems whenever some of the useful carriers are assigned as pilots without carrying useful information

Similarly, pilots subcarriers in the maximum correlation algorithm are modulated with values generated from a known sequence and are not used to transmit user information. Whenever the same amount of pilot carriers are used, the systems using either the MC algorithm or the proposed PPD algorithm will suffer the same amount of degradation in the data throughput.

On the other hand, the GPD algorithm only makes use of the virtual carriers. Virtual carriers are located in the guard-bands which are assigned at both ends of the frequency spectrum of the OFDM system. The output of the OFDM signal has to be band-limited to reduce any out-of-band radiation that will cause interference to adjacent channels. However, a brick-wall shape filter that changes abruptly to zero at the cut-off frequency cannot be realized physically. The main objective of setting up the guard-bands is to relief the design constraint of the band-pass filter in the transmitter so that the filter's output in the frequency domain can roll-off slowly to the specified power level at the end of the allocated frequency spectrum. Therefore, the existence of the guard-band has nothing to do with the coarse frequency synchronization. The guard-band power detection algorithm only make use of the system redundancy and does not consume any additional system resources. From this point of view, the application of the guard-band power detection algorithm has no effect to the data throughput.

In conclusion, the channel efficiency corresponding to the pilots power detection algorithm is lower than that of the guard-band power detection algorithm. However, this result is only applicable when the algorithms are compared during the design stage. If the PPD algorithm is applied to a well-defined standard, such as the DVB-T system in which some subcarriers have been allocated to pilot carriers for other purposes already, no *additional* system resources are required. In other words, the application of the PPD algorithm causes no degradation in the data throughput.

Chapter 4

Low-Complexity Coarse Frequency Synchronization using the Pilot Phase

4.1 Introduction

A special frame header is usually transmitted at the beginning of a number of OFDM symbols for high level synchronization. However, the pilot subcarriers in the conventional frame header, as defined in the Schmidl and Cox's model [89], are usually evenly distributed. Therefore, the coarse frequency offset estimator proposed in Chapter 3 will not be applicable in this application because the pilot subcarriers in the pilots power detection algorithm have to be arranged in a special pattern.

In this chapter, we propose a new two-symbol frame header and a low-complexity data-aided algorithm to estimate the coarse frequency offset with reference to the phase of the pilot subcarriers in the frame header. A known binary sequence is differentially encoded in the phases of the pilot subcarriers between the two symbols of the frame header. In the conventional two-symbol frame header, the two useful parts are transmitted consecutively without a gap between them as shown in Figure 4.1(A). Since the two symbols carry different data, the end of the first symbol is not the cyclic extension

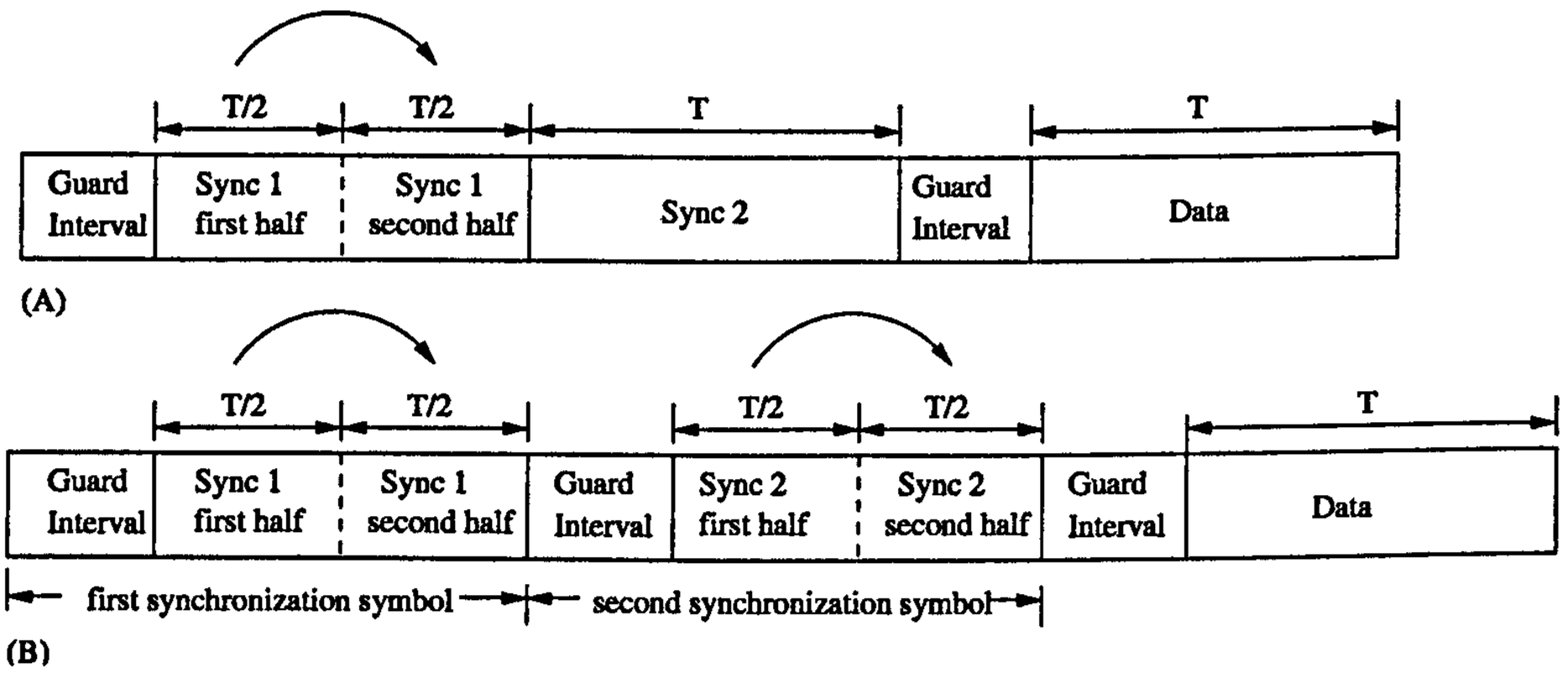

Figure 4.1: Frame header structure in (a) Schmidl and Cox's model and (b) the proposed model (Regions linked by '$\curvearrowright$' are identical)

of the second symbol. Therefore, the data acquired from the second symbol can be corrupted by intersymbol interference. The proposed frame header is an extension of the Schmidl and Cox's model by inserting an additional cyclic prefix between the two symbols as shown in Figure 4.1(B). The amount of intersymbol interference under multipath environment will be reduced with the expenses of a minor reduction in the overall data throughput and a minor increment in the amount of time required to reach synchronization.

This chapter is organized as follows. At first, we define the new frame header structure and the proposed coarse frequency offset estimation algorithm. Then, the system model used to simulate the performance of the estimator and the results of the simulations are described. The drawbacks of the new frame header in the system throughput and the response time are discussed. Finally, a low-complexity hardware architecture for the realization of the algorithm is given.

4.2 Structure of Frame Header

The proposed structure of the frame header is shown schematically in Figure 4.1(B). Similar to the conventional frame header, the new frame header has two OFDM symbols. The subcarriers at the odd frequencies are modulated with zeros. Therefore, the

two halves of each of the symbols are identical in the time domain [89] and the payload data symbol will not be mistaken as the frame header because they must contain non-zero odd frequencies.

Suppose r_m is the m-th time sample of the received signal and N is the FFT size. Then, the timing metric $M(d)$, given by Schmidl and Cox [89], can be written as

$$M(d) = \frac{|P(d)|^2}{(R(d))^2} \tag{4.1}$$

where

$$P(d) = \sum_{m=0}^{N/2-1} r^*_{d+m} r_{d+m+N/2} \tag{4.2}$$

$$R(d) = \sum_{m=0}^{N/2-1} |r_{d+m+N/2}|^2 \tag{4.3}$$

The starting position of the frame can be determined by locating the peak of the timing metric. The major difference between the proposed and the conventional frame header structure is the insertion of an addition guard interval between the first and the second symbol. In the Schmidl and Cox's model, there is only one guard interval appended in front of the first symbol while the useful parts of the two symbols are transmitted consecutively without gap. Since the two symbols of the frame header carry different data, the end of the first symbol cannot be used as the cyclic extension of the second symbol. Therefore, the second symbol will be affected by the intersymbol interference.

Figure 4.2 illustrates this situation graphically. In the multipath environment, the received signal is the linear combination of signals coming from various paths with different propagation delays. For simplicity, it is assumed that there are only two different signal paths. The demodulation data window for the first symbol is placed at the beginning of the useful part of the signal coming from either (a) the first signal path or (b) the second signal path. However, there are two different ways to place the data window for the second symbol depending on the frame structure. Firstly, there will be no time gap between the two data windows if the conventional frame header is used. Secondly, the two demodulation data windows will be separated by an interval equal to the time duration of the guard interval if the new frame header is used.

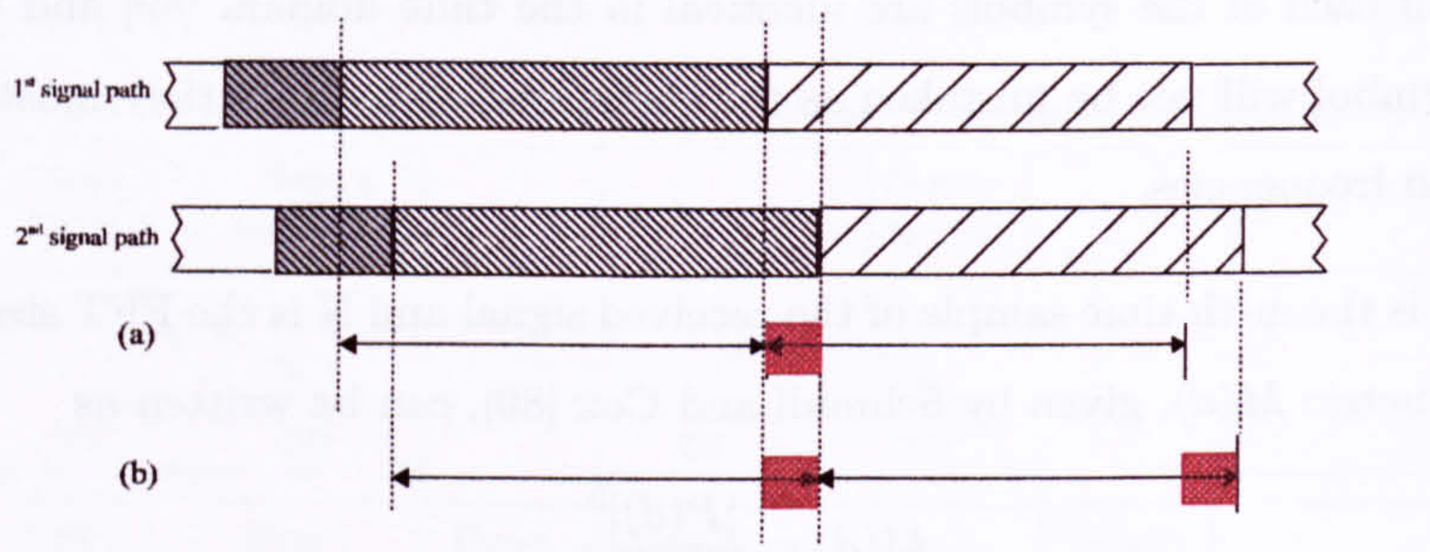

(A) without intersymbol guard interval

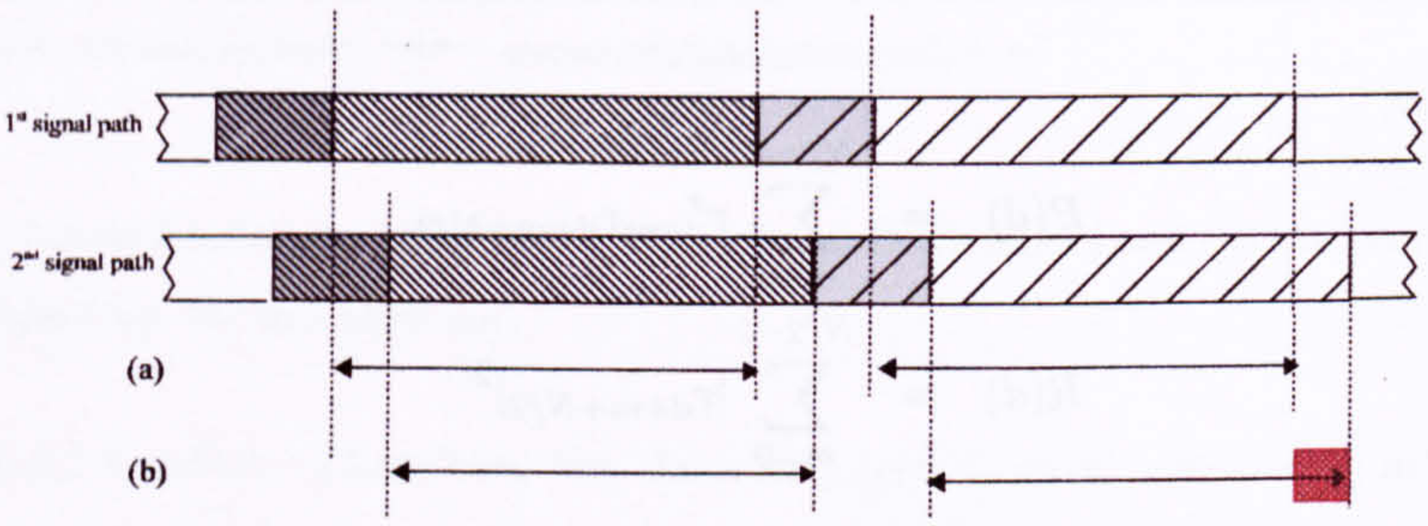

(B) with intersymbol guard interval

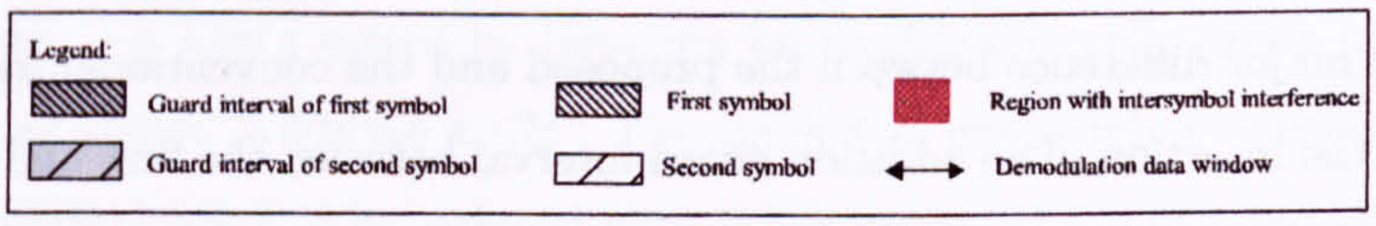

Figure 4.2: Illustration of the overlapping of the frame header signals coming from two different paths

The data windows that cover the overlapping regions of the two symbols will be corrupted by intersymbol interference. These regions are shaded in red in Figure 4.2. As shown, provided that the estimated symbol starting position is within the guard interval of the first symbol, inserting a guard interval in front of the second symbol allows the captured signal in the second data window free from intersymbol interference.

On the other hand, all OFDM symbols now have identical symbol structure. This simplifies the implementation of the system in hardware because the system needs to handle only one type of symbol structure. However, there are drawbacks in reducing the data throughput and the system response time. These will be explained in details at the end of this chapter.

4.3 Coarse Frequency Offset Estimation Algorithm

First of all, let us define the notations to be used here. Let $\{c_1(k_{2n}), c_2(k_{2n})\}$ be the data transmitted at the k_{2n}-th subcarrier, τ be the symbol timing offset, N be the total number of subcarriers, H be the channel transfer function and θ be the phase offset. All odd subcarriers are modulated with zero and hence $c_1(k_{2n+1}) = c_2(k_{2n+1}) = 0$, where $n = 0, 1, \ldots, (N/2-1)$.

If H and θ change slowly with respect to the symbol duration, they can be regarded as constant and cause the same effects to the two symbols in the frame header. It has been shown in Chapter 2 that both H and θ cause a fixed phase shift to the demodulated data while the symbol timing offset causes an additional phase rotation on the demodulated data with value depending on the frequency index. The amount of phase rotation due to the symbol timing offset is equal to $\frac{2\pi k_{2n}\tau}{N}$, which increases linearly with the frequency index k_{2n}. Therefore, the phases of the demodulated data $\{\tilde{c}_1(k_{2n}), \tilde{c}_2(k_{2n})\}$ can be written as

$$\angle\, \tilde{c}_1(k_{2n}) = \angle\, c_1(k_{2n}) + \angle\, H(k_{2n}) + \theta - \frac{2\pi k_{2n}\tau}{N} \tag{4.4}$$

$$\angle\, \tilde{c}_2(k_{2n}) = \angle\, c_2(k_{2n}) + \angle\, H(k_{2n}) + \theta - \frac{2\pi k_{2n}\tau}{N} \tag{4.5}$$

The corresponding phase difference $\phi(k_{2n})$ between the a pair of subcarriers in the two symbols is given by

$$\phi(k_{2n}) \equiv \angle\, \tilde{c}_1(k_{2n}) - \angle\, \tilde{c}_2(k_{2n}) \tag{4.6}$$

$$= \angle\, c_1(k_{2n}) - \angle\, c_2(k_{2n}) \tag{4.7}$$

As shown, the terms H, τ and θ are cancelled. In other words, the receiver can remove the effect of the propagating channel, the symbol timing offset and the phase offset by employing differential demodulation between the pair of subcarriers at the same frequency in the two symbols.

At the transmitter side, we can differentially encoded a binary sequence on these pairs of subcarriers. The even subcarriers are bi-phase modulated with respect to a {+1,1} binary sequence. If $c_1(k_{2n}) \in \{1, -1\}$ and $c_2(k_{2n}) \in \{1, -1\}$, we have $\angle c_1(k_{2n}) \in \{0, \pi\}$ and $\angle c_2(k_{2n}) \in \{0, \pi\}$, and hence $|\angle c_1(k_{2n}) - \angle c_2(k_{2n})| \in \{0, \pi\}$. Suppose $g(n)$ is a

{+1,-1} binary sequence with $N/2$ elements and it has good aperiodic autocorrelation property. With reference to the sequence $g(n)$, the even subcarriers are modulated accordingly so that the absolute value of the differential phase difference $|\phi(k_{2n})|$ is π when $g(n) = +1$, or 0 when $g(n) = -1$. That is,

$$\left|\phi(k_{2n})\right| = \left|\angle\, c_1(k_{2n}) - \angle\, c_2(k_{2n})\right| = \begin{cases} \pi & \text{g(n)} = +1 \\ 0 & \text{g(n)} = \text{-1} \end{cases} \tag{4.8}$$

Then, we can determine the coarse frequency offset $\tilde{m}$ by locating the position that maximize the cross-correlation between the known sequence $g(n)$ and the demodulated binary data as follows.

$$\tilde{m} = \max_{m} \sum_{n=0}^{N/2-1} p\Big\{\phi(k_{2(n+m)})\Big\}\, g(n) \tag{4.9}$$

where

$$p(\phi) = \begin{cases} +1 & |\phi| > \frac{\pi}{2} \\ -1 & |\phi| \leq \frac{\pi}{2} \end{cases} \tag{4.10}$$

Assuming that the noise is independent to the data and has a symmetrical distribution about its mean, we have set the detection threshold to $\pi/2$, the mid-point between the nominal values 0 and π. The mapping function $p(\phi)$ converts the phase difference from a fractional number with high numerical resolution into a two-level integer. The cross-correlation can be computed efficiently using simple binary number multiplication and addition. Therefore, the computation complexity of the estimator is low.

4.4 Simulations

4.4.1 System Model

In our simulations, the data symbol structure is identical to those defined in the Hiperlan/2 standard [43]. Each OFDM symbol has 64 subcarriers, which are indexed from 0

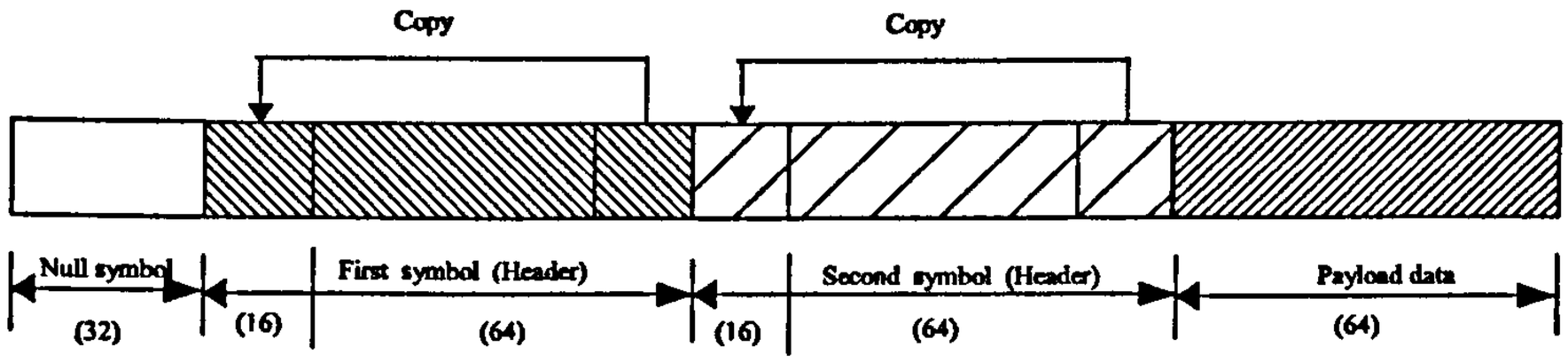

Figure 4.3: Structure of the OFDM frame used in the simulations (the numbers in the brackets are the time duration of the corresponding regions in the unit of samples)

The remaining 12 subcarriers resides in the guard-band and are modulated with zero. The cyclic prefix is composed of 16 samples and the digital sampling rate is 20 MHz.

The frame structure shown in Figure 4.3 is assumed. Each frame is composed of a null symbol, a two-symbol frame header and one data symbol. In multipath environment, the frame header of a signal coming from one path may overlap with the data symbol of the signal coming from the other paths. The objective of including the data symbol is to enable the simulations of intersymbol interference in the frame header when it happens. For simplicity, it is sufficient to include only one data symbol in order to reduce the total amount of time required to run the simulations.

A null symbol with 32 samples is appended at the beginning of a frame to simply the implementation of adding path delay in the simulations. Physically we have assumed that the packets are transmitted in burst mode with at least 32 samples time gap between successive bursts. This assumption will only affect the overall data throughput, but will not affect the characteristics of the coarse frequency offset estimator. The symbol timing estimator is the direct implementation of the Cox's algorithm [89].

4.4.2 Channels

We evaluate the performance of the estimator in both an additive white Gaussian noise (AWGN) channel and dispersive multipath fading channels. The impulse response of the dispersive channels is modelled to consist of two independent Rayleigh fading taps with equal average power. This channel model is selected because of its simplicity.

	h(n)	Path delay (μs)
Channel A	$h_0\delta(n) + h_1\delta(n-4)$	0.2
Channel B	$h_0\delta(n) + h_1\delta(n-8)$	0.4
Channel C	$h_0\delta(n) + h_1\delta(n-12)$	0.6
Remark:	(1) $E[\|h_0\|^2] = E[\|h_1\|^2] = 0.5$	
	(2) unit delay = 1 sampling period = 50 ns	

Table 4.1: Specification of the channel impulse response functions of the three two-path Rayleigh fading channels used in the simulations

The channel impulse response function is represented by $h(t) = h_0\delta(t) + h_1\delta(t-T)$, where $E[|h_0|^2] = E[|h_1|^2] = 0.5$, T is the differential paths delay in seconds and $\delta(t)$ is the Dirac delta function. Three channels have been defined with different values of T which are equal to either 0.2 μs (Channel A), 0.4 μs (Channel B) or 0.6 μs (Channel C), corresponding to 25% (4 samples), 50% (8 samples) or 75% (12 samples) of the duration of a guard interval (16 samples), respectively. The receiving station is assumed to be moving at a maximum speed of 70 km/hour, which is the vehicle speed limit on highways in Hong Kong. This results in a maximum Doppler frequency of 336 Hz at a radio frequency of 5.18 GHz. Table 4.1 summarizes the specifications of these three channels.

4.4.3 Symbols Generation

(A) Data symbol

Data subcarriers are QPSK modulated with values uniformly distributed among the constellation points $\{\frac{1}{\sqrt{2}}(1+j)\ ,\ \frac{1}{\sqrt{2}}(1-j)\ ,\ \frac{1}{\sqrt{2}}(-1+j)\ ,\ \frac{1}{\sqrt{2}}(-1-j)\}$. Comparing with the synchronization symbols in the frame header, there are double number of non-zeros subcarriers in the data symbol. This is because all subcarriers at the odd frequency in the frame header are modulated with zero. Therefore, the real and the conjugate components of subcarriers in the data symbol are normalized by $\sqrt{2}$ in order to maintain a constant average power over the entire frame.

(B) Frame Header

Different frame headers are generated by selecting various combinations of two pseudo-random sequences, namely g_1 and g_2. The first sequence g_1 is used to modulate the data carriers in the first synchronization symbol. Then the sequence g_2 is differentially encoded onto the subcarriers in the second symbol with reference to the subcarriers at the same frequency in the first symbol. Although there are only 26 subcarriers in the synchronization symbol, our choices of the sequences are not limited to those sequences with length exactly equal to 26. This is because the length of a periodic sequence with good autocorrelation is usually well-defined by its structure already and usually not exactly equal to 26. The original sequence can be truncated to length 26 if its original length is longer than necessary.

In the simulations, we have used two different maximal length sequence (m-sequences), $g_1^{(m_1)}$ and $g_1^{(m_2)}$, to obtain g_1 and five pseudo-random sequences to obtain g_2. The first m-sequence $g_1^{(m_1)}$ has period $2^5-1=31$ with primitive polynomial $g(x)=x^5+x^2+1$. The next m-sequence $g_1^{(m_2)}$ is generated using the primitive polynomial $g(x)=x^7+x^4+1$ that is the sequence used to randomize the reference signal in Hiperlan/2 system [43]. The period of $g_1^{(m_2)}$ is equal to $2^7-1=127$.

The five sequences used to generate the second symbol are the m-sequence $g_2^{(m)}$, Golay sequence $g_2^{(golay)}$, Gold sequence $g_2^{(gold)}$, and two computer-generated sequences $g_2^{(fan)}$ and $g_2^{(uniform)}$. The sequence $g_2^{(m)}$ is a truncated m-sequence with a generating polynomial $g(x)=x^5+x^4+x^3+x^2+1$. Similarly, the sequence $g_2^{(golay)}$ is a truncated 26-element Golay sequence and is equal to

$$g_2^{(golay)}(n)=\begin{cases}+1 & \text{if } \sin\pi(\sqrt{14}-\sqrt{13})^2(n+\frac{1}{2})^2>0\\ -1 & \text{if } \sin\pi(\sqrt{14}-\sqrt{13})^2(n+\frac{1}{2})^2\le 0\end{cases} \tag{4.11}$$

The generator of the Gold sequence $g_2^{(gold)}$ is $g(x)=x^{10}+x^9+x^8+x^6+x^5+x^3+1$. The last two sequences $g_2^{(fan)}$ and $g_2^{(uniform)}$ are not constructed analytically. The sequence $g_2^{(fan)}$ [28] is found based on exhaustive computer search with the criterion of small peak autocorrelation function (ACF) sidelobes and large merit factor. The merit factor specify the ratio of the energy of ACF mainlobe to the energy of the ACF sidelobes. Finally, we have generated the sequence $g_2^{(uniform)}$ arbitrary using a random-number

$c_1 = g_1$	$-g_1$	g_2	$c_2 = -g_1 \cdot g_2$	$\lvert \angle c_1 - \angle c_2 \rvert$
1	-1	1	-1	π
1	-1	-1	1	0
-1	1	1	1	π
-1	1	-1	-1	0

Table 4.2: Various combinations in the construction of a pair of subcarriers

generator of which the outputs are uniformly distributed in the interval (0.0 , 1.0). Then the elements are replaced by -1 if they are less than 0.5. Otherwise, the elements are replaced by +1.

From Equation 4.8, the two symbols in the frame header can be defined in terms of the selected sequences, $g_1(n)$ and $g_2(n)$, using the following equations:

$$c_1(n) = \begin{cases} g_1(\frac{n-6}{2}) & n = 6, 8, \cdots, 56 \\ 0 & \text{otherwise} \end{cases} \tag{4.12}$$

$$c_2(n) = \begin{cases} -g_1(\frac{n-6}{2}) \cdot g_2(\frac{n-6}{2}) & n = 6, 8, \cdots, 56 \\ 0 & \text{otherwise} \end{cases}$$

where $c_1(n)$ and $c_2(n)$ are the modulation values of the n-th subcarriers of the first symbol and the second symbol, respectively. Table 4.2 illustrates the construction of a pair of c_1 and c_2 with all possible combinations of g_1 and g_2. Recall that the output of the mapping function ϕ will be +1 if the input is less than $\pi/2$, or -1 otherwise. Therefore, $\phi(\lvert \angle c_1 - \angle c_2 \rvert) = g_2$ as shown in Table 4.2.

In summary, the two symbols can be generated by the following steps:

1. Label the subcarriers of each OFDM symbol from 0 to 63.

2. Select a pseudo-random sequence $g_1(n) \in \{-1, +1\}$, where $n = 0, 1, \ldots, 25$.

3. Assign the values of g_1 to the subcarriers of the first symbol c_1 starting from the 6-th subcarriers and then every other two subcarriers.
   That is, $c_1(2n + 6) = g_1(n)$,where $n = 0, 1, 2, \ldots, 25$.
   The remaining subcarriers with odd frequency indices are modulated with 0.

4. Select another pseudo-random sequence $g_2(n) \in \{-1, +1\}$.

Sequence	Elements
$g_1^{(m_1)}$	-1 -1 -1 -1 +1 -1 -1 +1 -1 +1 +1 -1 -1 +1 +1 +1 +1 +1 -1 -1 -1 +1 +1 -1 +1 +1
$g_1^{(m_2)}$	+1 +1 +1 +1 -1 -1 -1 +1 -1 -1 -1 -1 +1 +1 -1 +1 -1 -1 +1 +1 -1 +1 +1 -1 +1 +1
$g_2^{(m)}$	-1 -1 -1 +1 -1 +1 -1 +1 +1 -1 +1 -1 -1 -1 -1 +1 +1 -1 -1 +1 -1 -1 +1 +1 +1 +1
$g_2^{(golay)}$	+1 +1 +1 +1 +1 +1 +1 -1 -1 -1 +1 +1 +1 -1 -1 +1 -1 -1 +1 -1 -1 +1 -1 +1 -1 +1
$g_2^{(gold)}$	-1 -1 -1 +1 +1 +1 -1 -1 +1 +1 -1 -1 -1 +1 +1 +1 -1 -1 +1 -1 +1 -1 +1 -1 +1 -1
$g_2^{(fan)}$	+1 -1 -1 -1 +1 +1 +1 -1 -1 -1 -1 -1 -1 -1 +1 -1 +1 -1 +1 +1 -1 +1 +1 -1 -1 +1
$g_2^{(uniform)}$	+1 -1 -1 +1 +1 -1 -1 +1 +1 +1 -1 +1 +1 +1 -1 -1 +1 -1 -1 +1 -1 -1 +1 +1 -1 -1

Table 4.3: Elements of sequences that are used to generate the frame headers

Sequence	Type	Original Length	Generator
$g_1^{(m_1)}$	m-sequence	31	$g(x) = x^5 + x^2 + 1$
$g_1^{(m_2)}$	m-sequence	127	$g(x) = x^7 + x^4 + 1$
$g_2^{(m)}$	m-sequence	31	$g(x) = x^5 + x^4 + x^3 + x^2 + 1$
$g_2^{(golay)}$	Golay sequence	27	$g(x) = \begin{cases} +1 & \text{if } \sin\pi(\sqrt{14}-\sqrt{13})^2(x+\frac{1}{2})^2 > 0 \\ -1 & \text{if } \sin\pi(\sqrt{14}-\sqrt{13})^2(x+\frac{1}{2})^2 \leq 0 \end{cases}$
$g_2^{(gold)}$	Gold sequence	31	$g(x) = x^{10} + x^9 + x^8 + x^6 + x^5 + x^3 + 1$
$g_2^{(fan)}$	Exhaustive search	26	Nil
$g_2^{(uniform)}$	Uniform distributed	26	Nil

Table 4.4: Specification of the sequences used to generate the frame headers

5. Initialize the odd subcarriers of the second symbol c_2 to zero.

6. Total 26 subcarriers with frequency indices in the range $\{6, 8, \ldots, 56\}$ are modulated with respect to the sequence g_2 and the first symbol c_1 as follows:

   If $g_2(n) = +1$

   $$c_2(2n+6) = -c_1(2n+6), \text{ where } n = 0, 1, \ldots, 25$$

   else if $g_2(n) = -1$

   $$c_2(2n+6) = c_1(2n+6), \text{ where } n = 0, 1, \ldots, 25.$$

The specifications of the sequences under testing are summarized in Table 4.3 and Table 4.4. Figure 4.4 plots the autocorrelation function of the two sequences $g_1^{(m_1)}$ and $g_1^{(m_2)}$. The autocorrelation function of the other five sequences are plotted in Figure 4.5.

In the simulations, we have assumed that there is an uncompensated phase offset of $\pi/4$. Therefore, the subcarriers are modulated with {1+j,-1-j} instead of {+1,-1}, respectively.

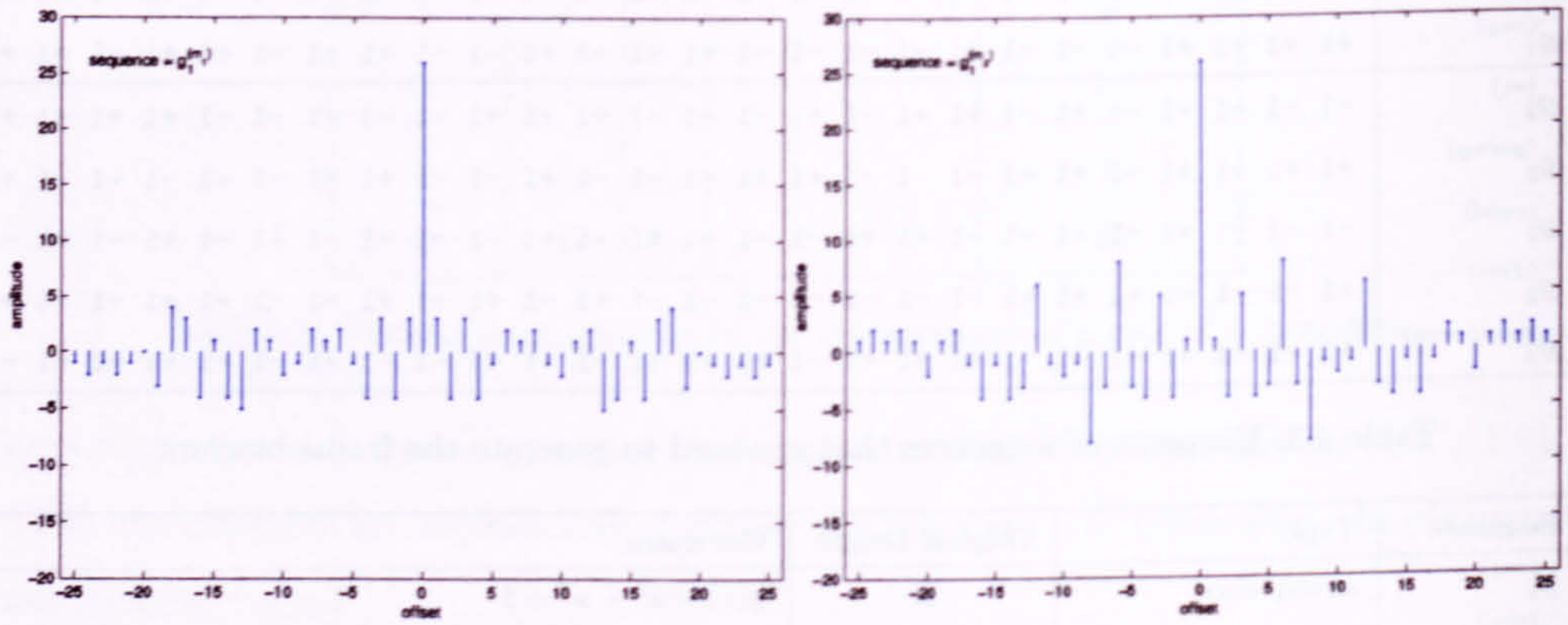

(a) ACF of the sequence $g_1^{(m_1)}$ (b) ACF of the sequence $g_1^{(m_2)}$

Figure 4.4: Autocorrelation function (ACF) of the sequences that generate the first symbol

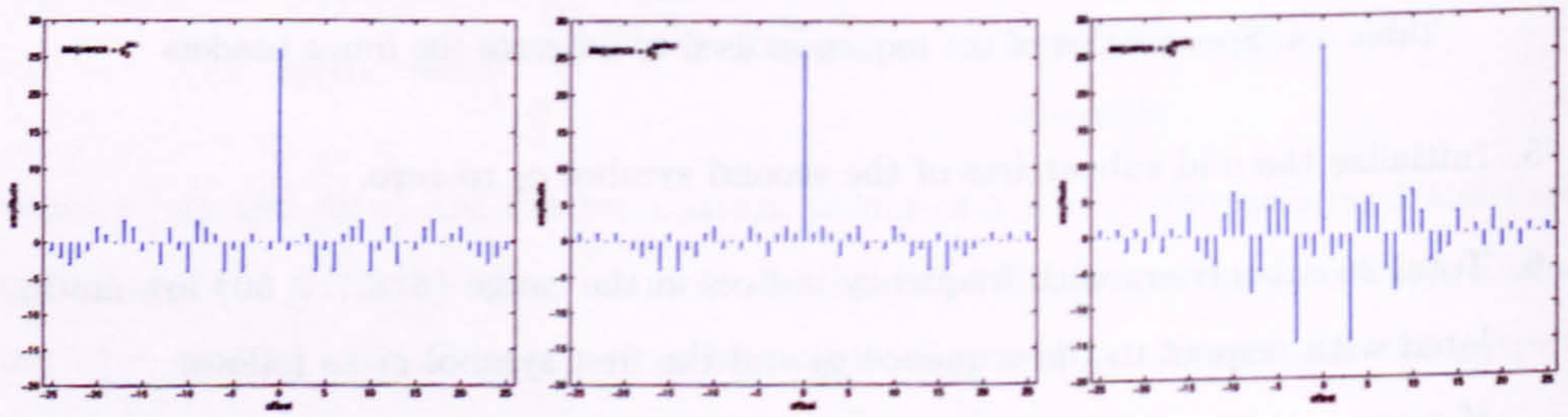

(a) ACF of $g_2^{(m)}$ (b) ACF of $g_2^{(golay)}$ (c) ACF of $g_2^{(gold)}$

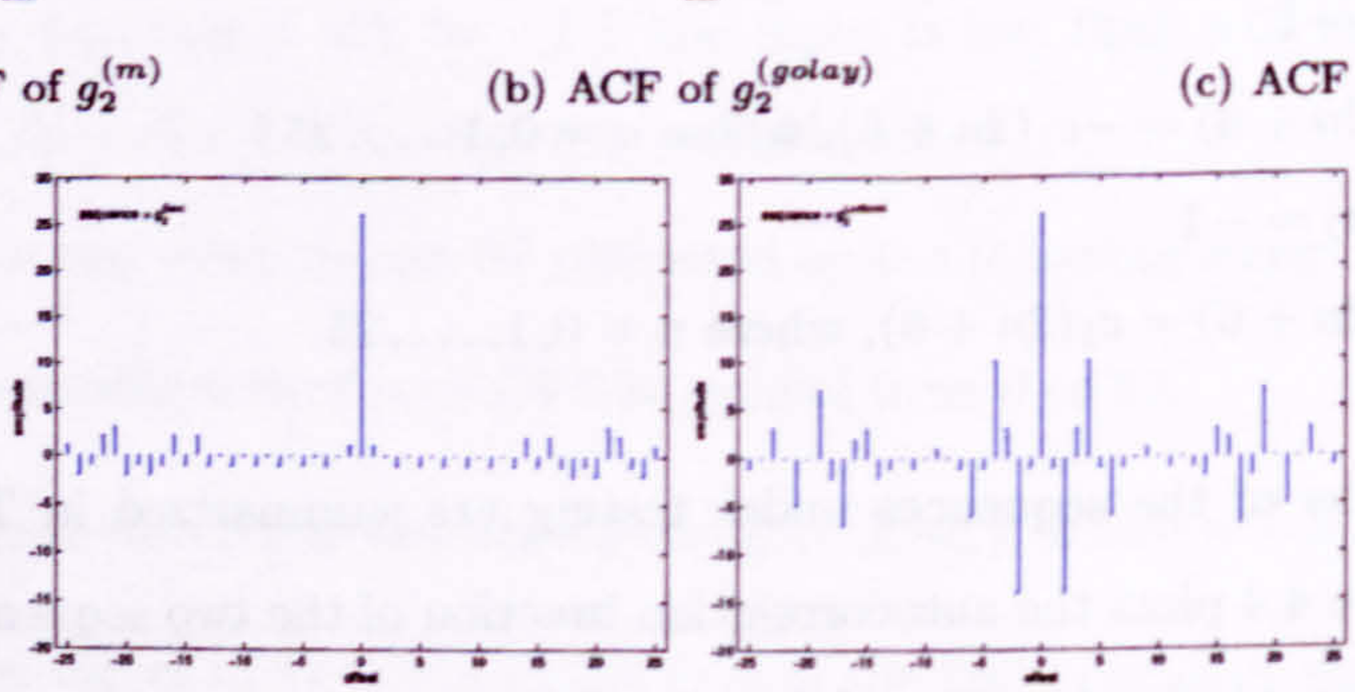

(d) ACF of $g_2^{(fan)}$ (e) ACF of $g_2^{(uniform)}$

Figure 4.5: Autocorrelation function (ACF) of the sequences that are differentially encoded between pairs of subcarriers in the frame header

4.5 Results of the Simulations

4.5.1 Estimation of the Symbol Timing

Figure 4.6 and Figure 4.7 plot the real and imaginary components of the complex waveforms of the first symbol that are generated based on the m-sequence $g_1^{(m_1)}$ and $g_2^{(m_2)}$, respectively. However, as shown clearly in the figures, the first half of the waveform is identical to the second half irrespective to the actual sequence used to generate the symbol. It is this repeating property that the system is using to determine the symbol timing.

Although the second symbol is not used for the determination of the symbol timing, the waveforms of the second symbol are also plotted in Figure 4.8 and Figure 4.9 for reference. As in the first symbol, all odd frequency subcarriers in the second symbol are modulated with zero and therefore the first half and the second half of the waveforms are also identical.

Figure 4.10 plots the timing metrics $M(d)$ against the timing index d. In each graph, there are two curves plotting in different color. The timing metrics are plotted in blue when the new frame header is used. Similarly, they are plotted in red when the conventional frame header is used. An AWGN channel with 30 dB signal-to-noise ratio (SNR) is assumed.

As shown in Figure 4.10, the blue curves have two plateaus in the regions of the guard intervals where the timing metrics reach the maximum. The symbol starting position can be taken from anywhere within the first plateau. However, only one plateau can be found in the red curves. The second plateau, as in the blue curves (new frame header), the plateau is replaced by a sharp peak at the boundary between the two training symbols. Since the only difference between the two frame headers is the addition of an intersymbol guard interval in the new one and now the timing metrics for the new frame header show an additional plateau, we can conclude that the plateau is due to the guard interval.

In addition, the envelope in all different cases are very similar indicating that the timing metric is robust to the detail structure of the synchronization symbols.

(a) Real component

(b) Imaginary component

Figure 4.6: Waveform of the (a) real and (b) imaginary component of the first symbol in the frame header when $g_1 = g_1^{(m_1)}$

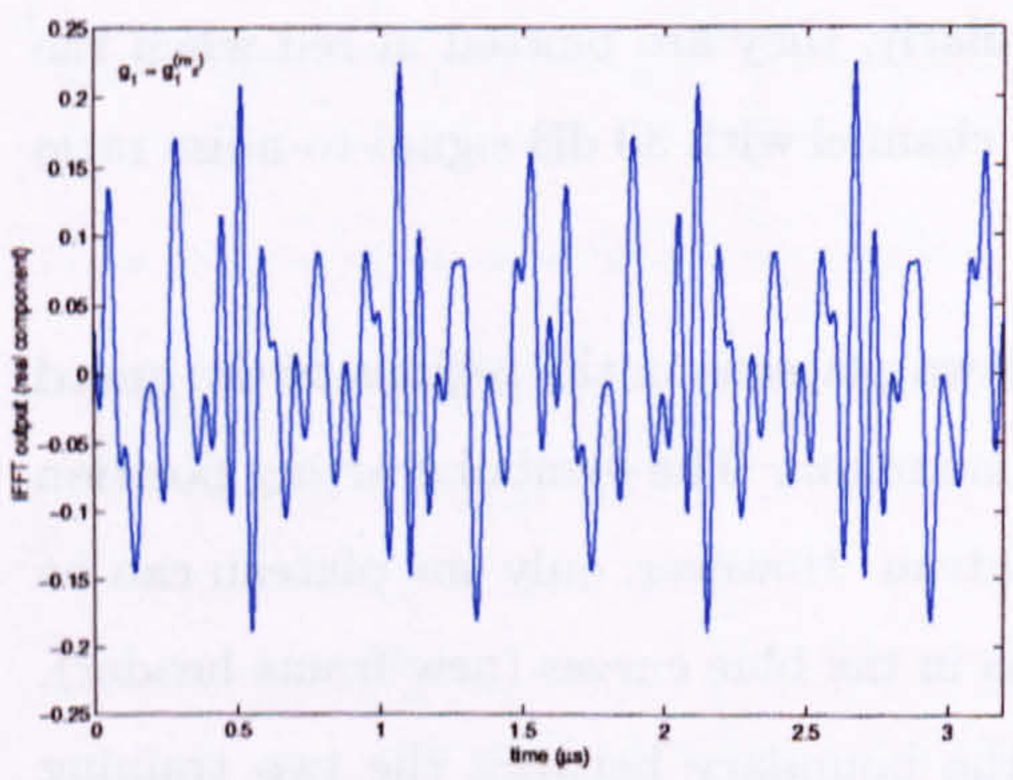

(a) Real component

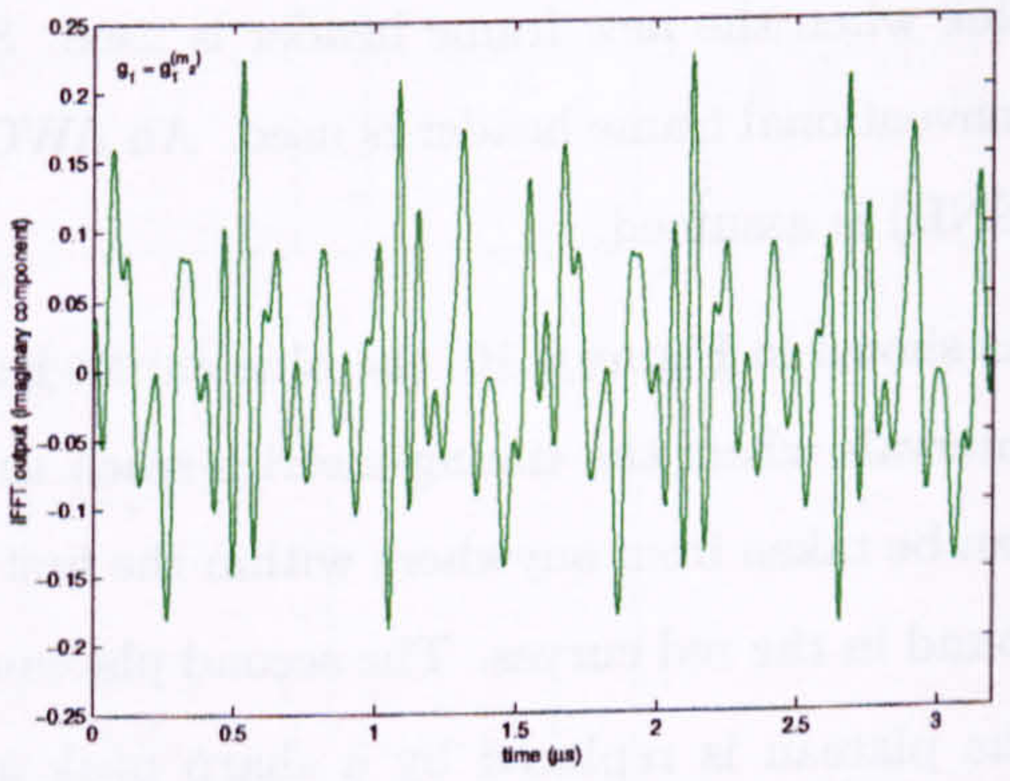

(b) Imaginary component

Figure 4.7: Waveform of the (a) real and (b) imaginary component of the first symbol in the frame header when $g_1 = g_1^{(m_2)}$

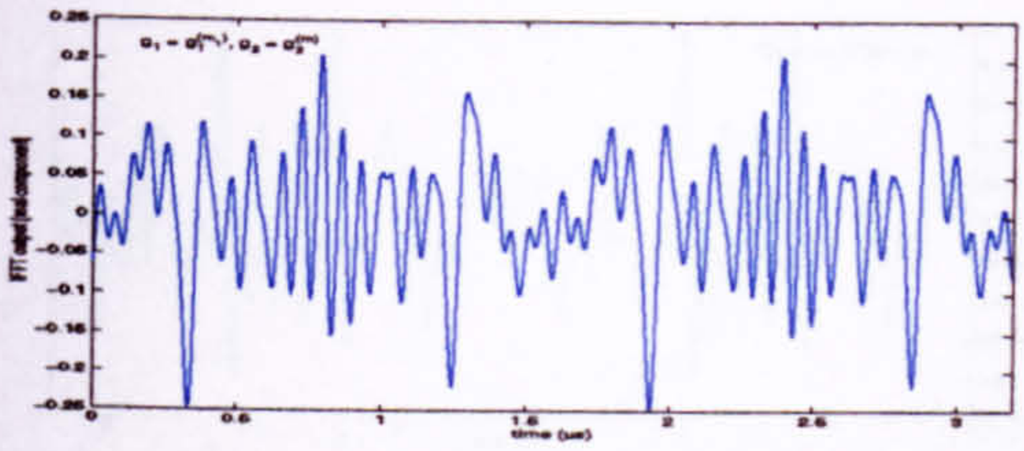

(a) Real component, $g_2 = g_2^{(m)}$

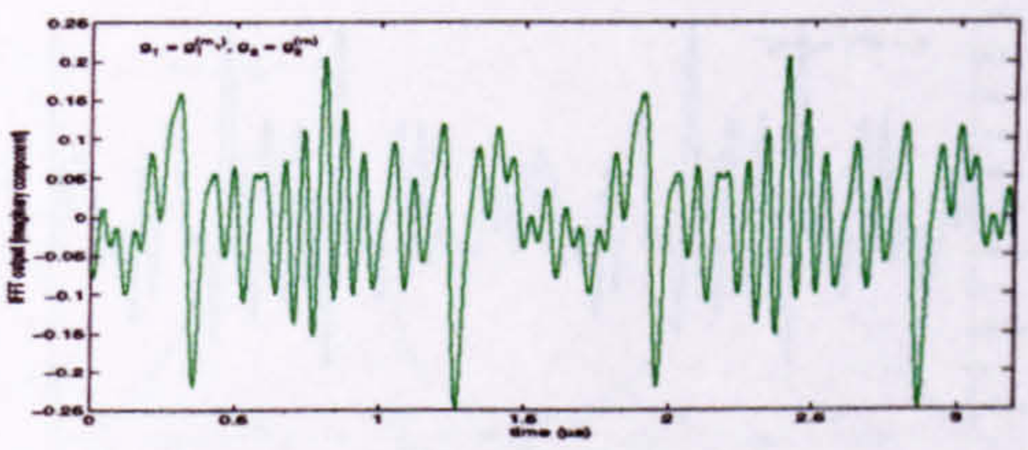

(b) Imaginary component, $g_2 = g_2^{(m)}$

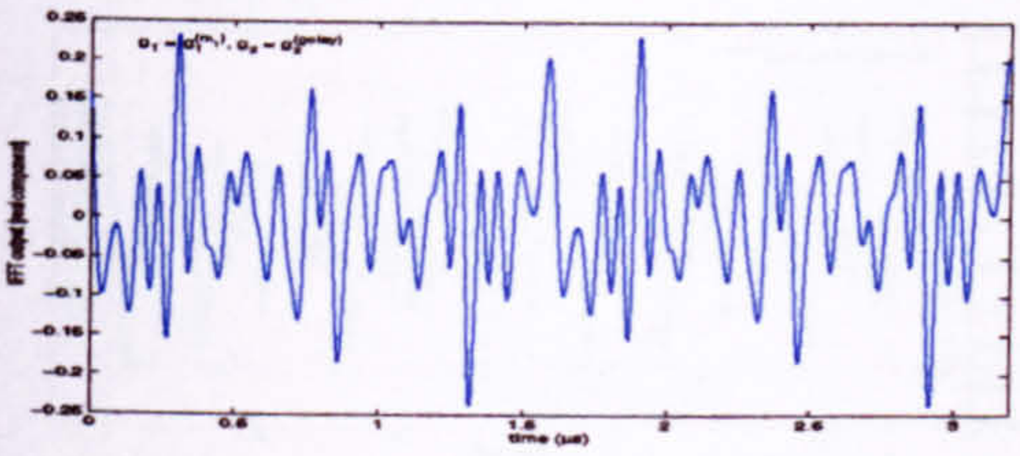

(c) Real component, $g_2 = g_2^{(golay)}$

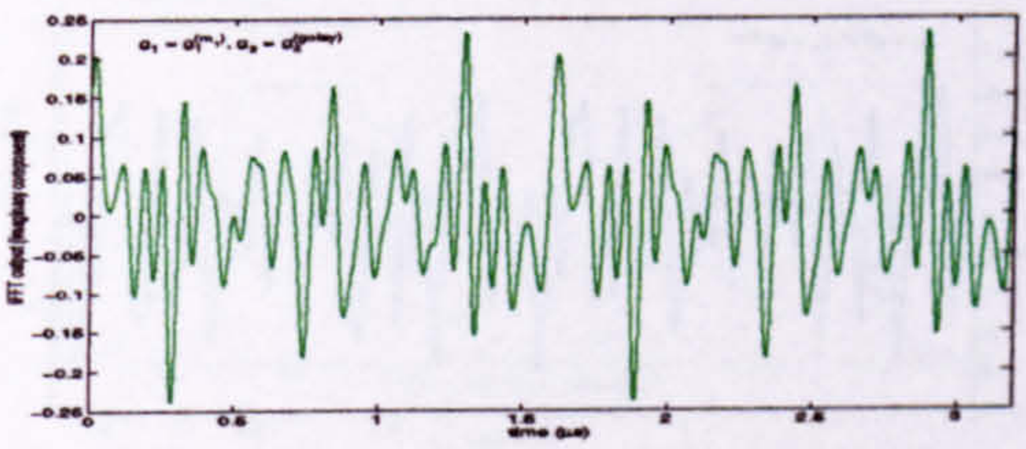

(d) Imaginary component, $g_2 = g_2^{(golay)}$

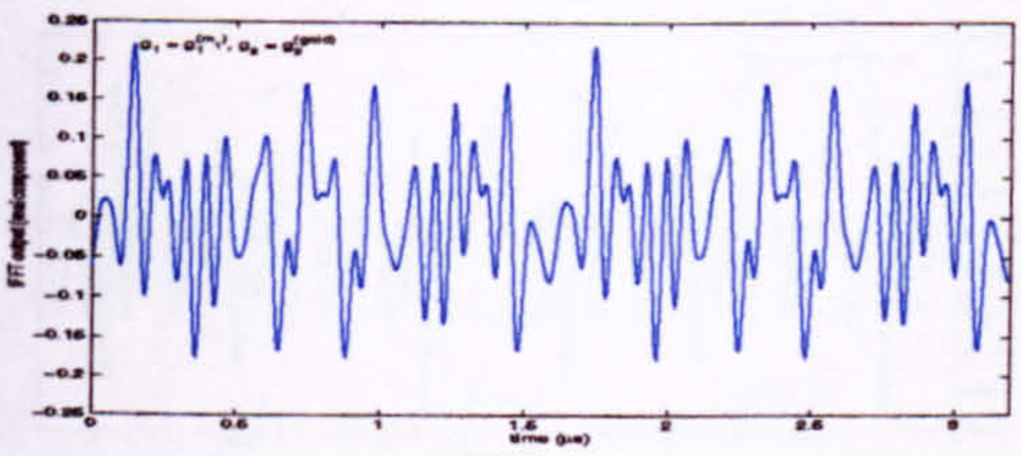

(e) Real component, $g_2 = g_2^{(gold)}$

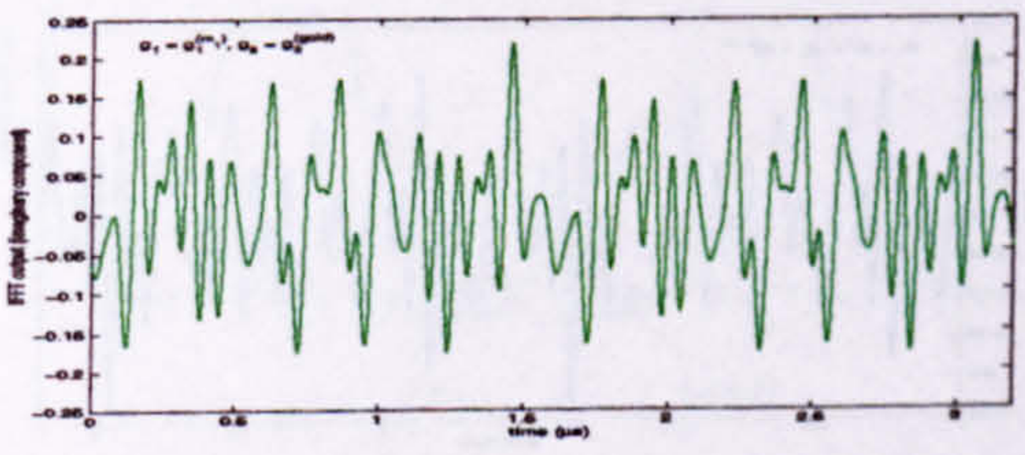

(f) Imaginary component, $g_2 = g_2^{(gold)}$

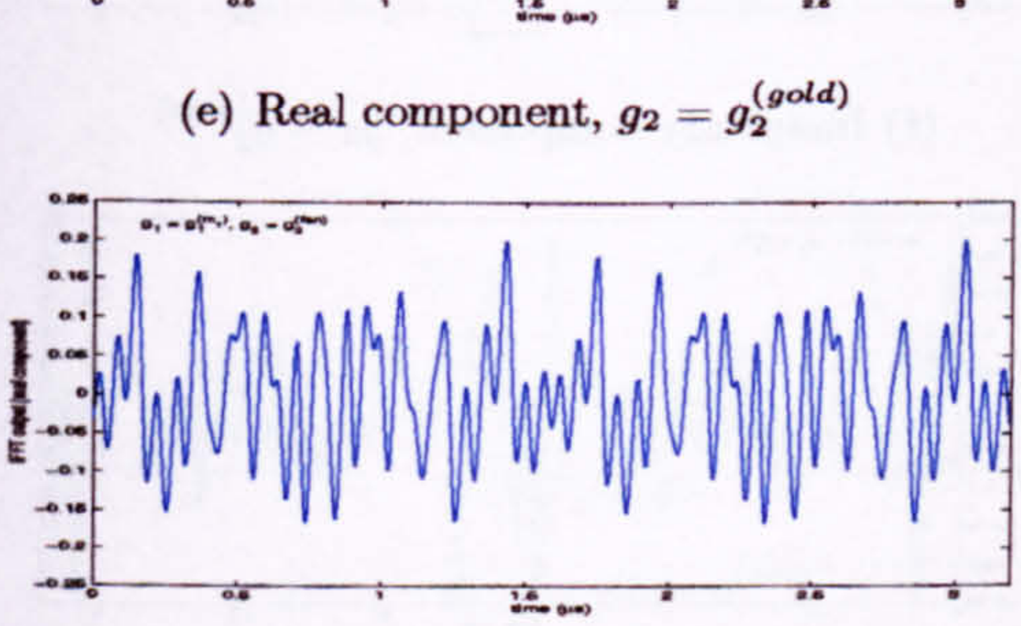

(g) Real component, $g_2 = g_2^{(fan)}$

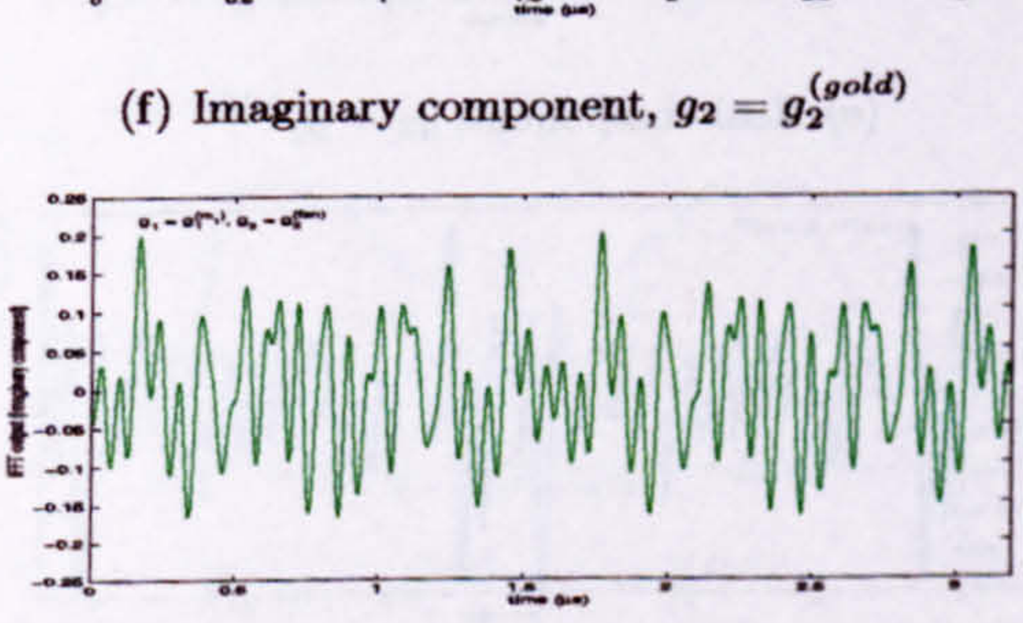

(h) Imaginary component, $g_2 = g_2^{(fan)}$

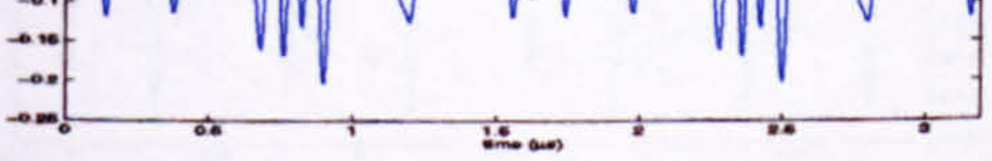

(i) Real component, $g_2 = g_2^{(uniform)}$

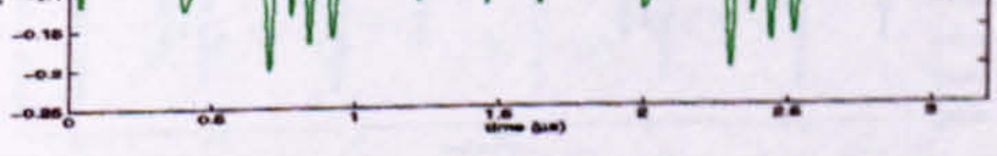

(j) Imaginary component, $g_2 = g_2^{(uniform)}$

Figure 4.8: Real and imaginary components of the waveform of the second symbol in the frame header when $g_1 = g_1^{(m_1)}$

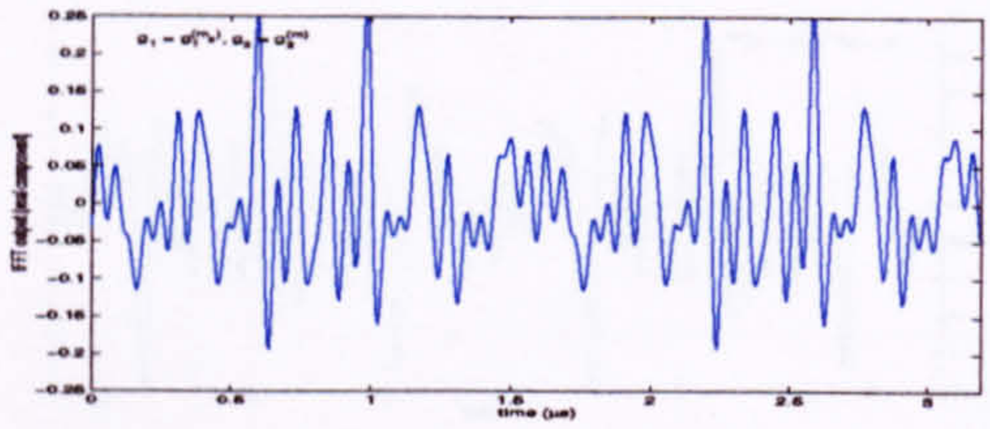

(a) Real component, $g_2 = g_2^{(m)}$

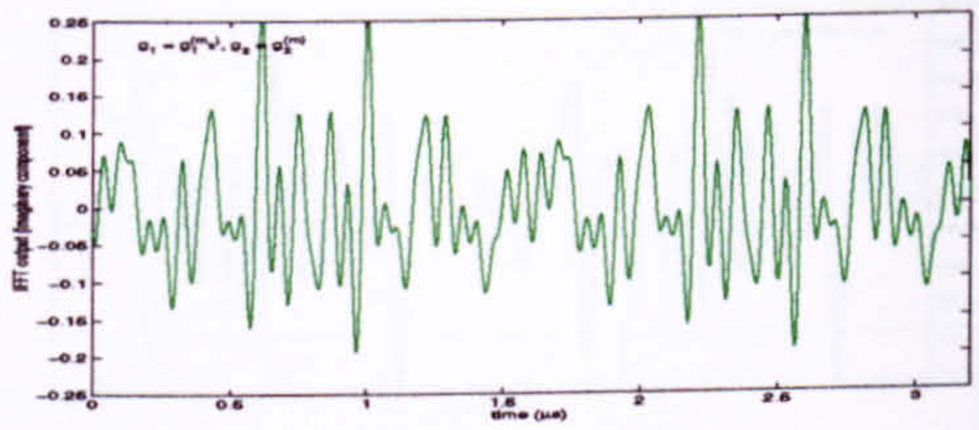

(b) Imaginary component, $g_2 = g_2^{(m)}$

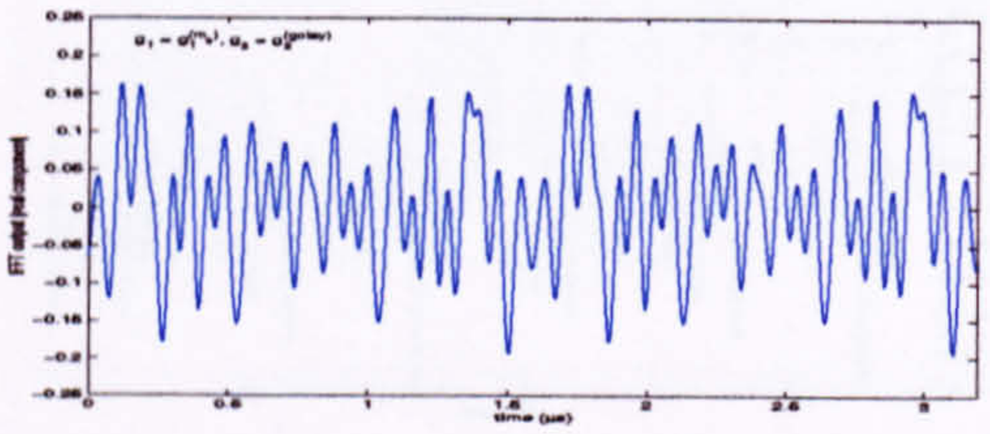

(c) Real component, $g_2 = g_2^{(golay)}$

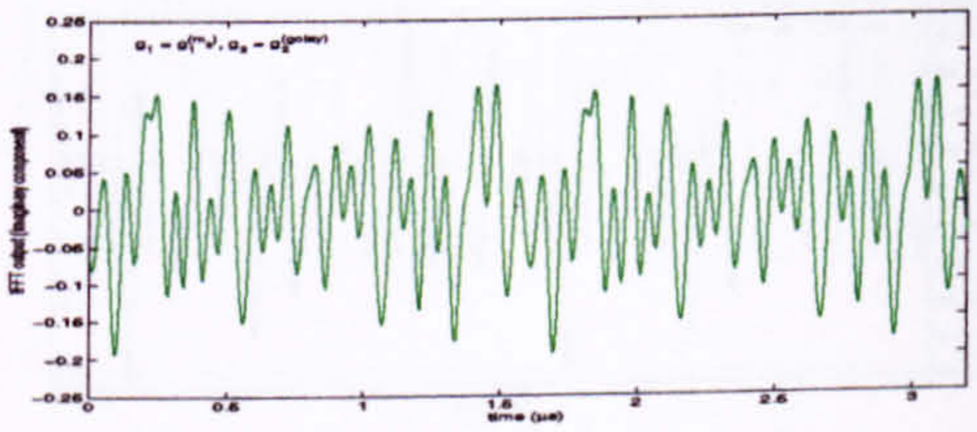

(d) Imaginary component, $g_2 = g_2^{(golay)}$

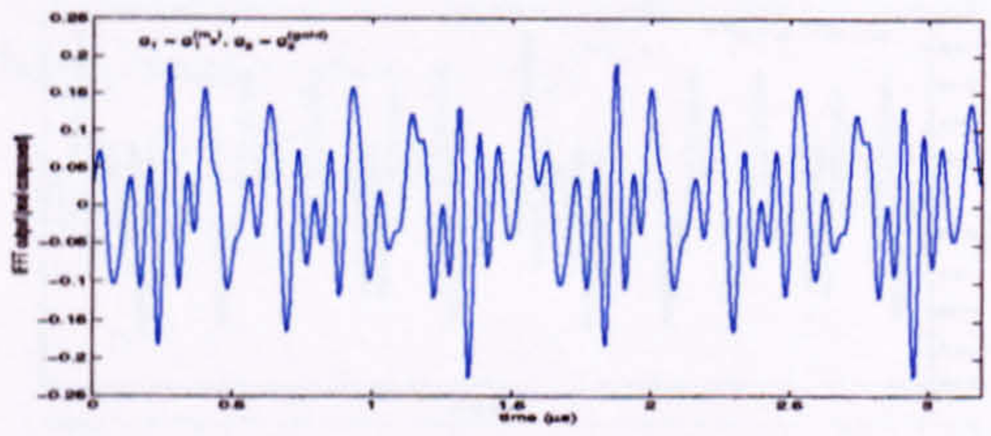

(e) Real component, $g_2 = g_2^{(gold)}$

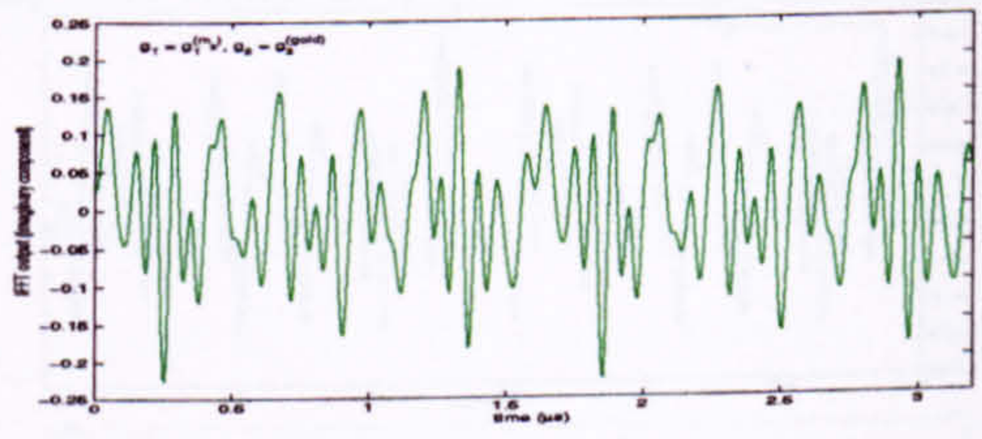

(f) Imaginary component, $g_2 = g_2^{(gold)}$

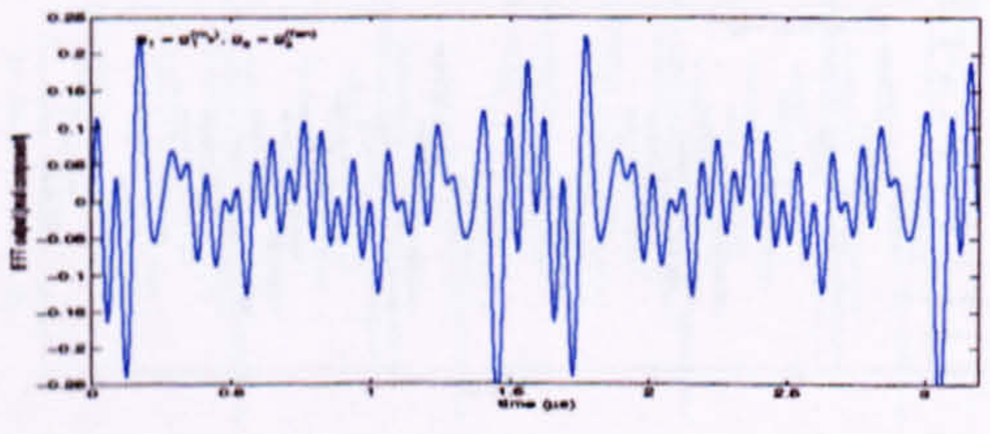

(g) Real component, $g_2 = g_2^{(fan)}$

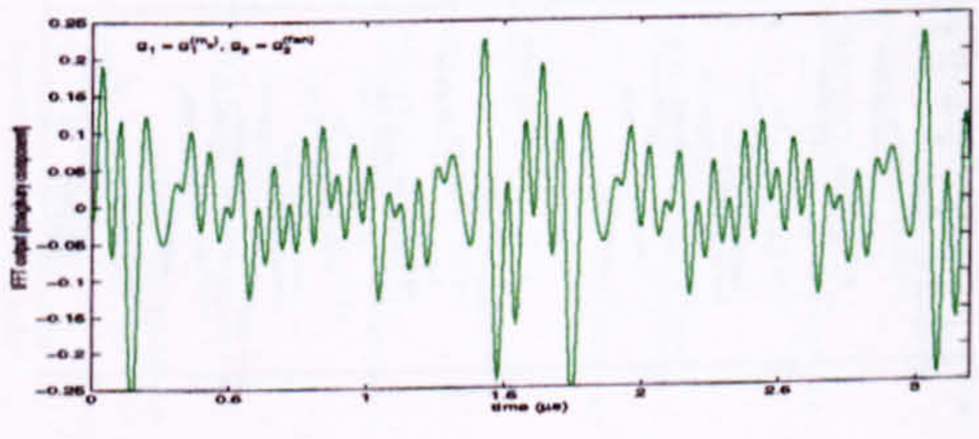

(h) Imaginary component, $g_2 = g_2^{(fan)}$

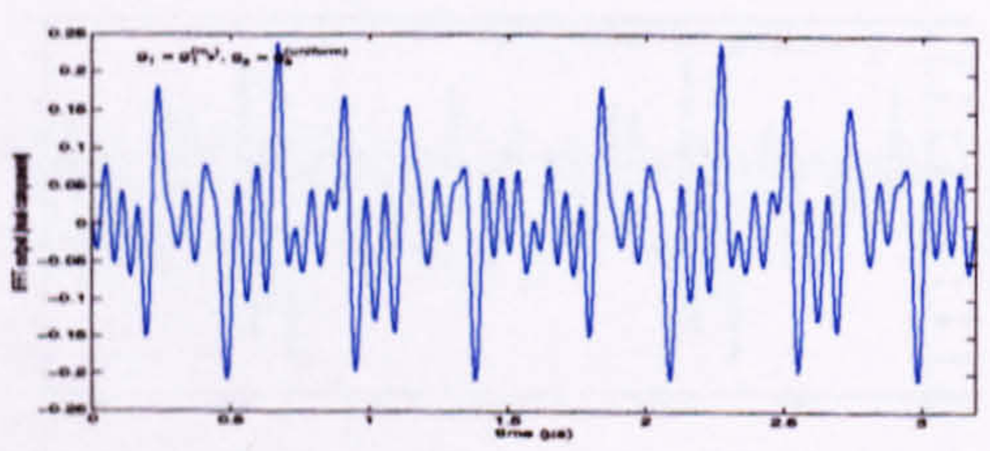

(i) Real component, $g_2 = g_2^{(uniform)}$

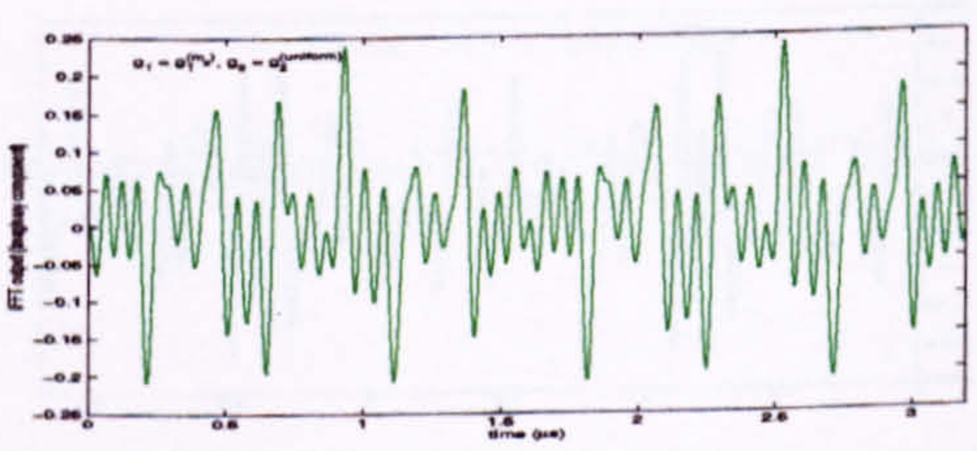

(j) Imaginary component, $g_2 = g_2^{(uniform)}$

Figure 4.9: Real and imaginary components of the waveform of the second symbol in the frame header when $g_1 = g_1^{(m_2)}$

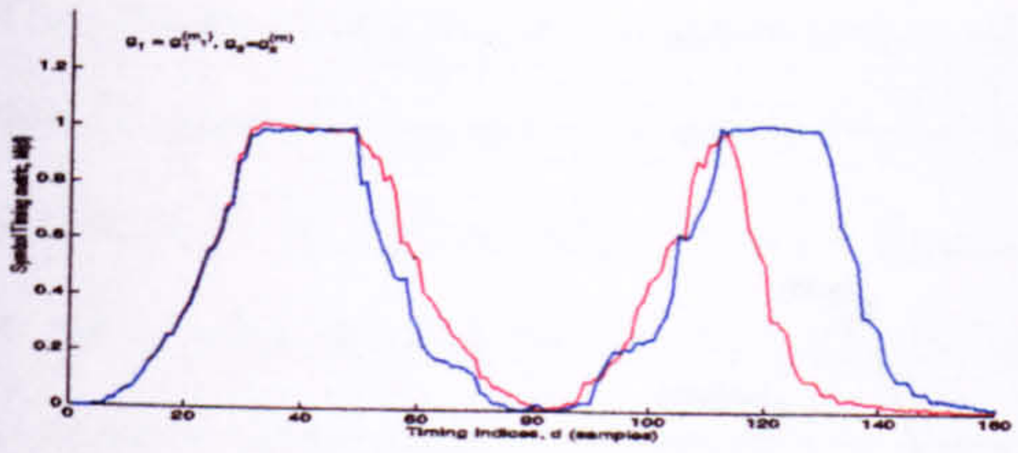

(a) $g_1 = g_1^{(m_1)}$, $g_2 = g_2^{(m)}$

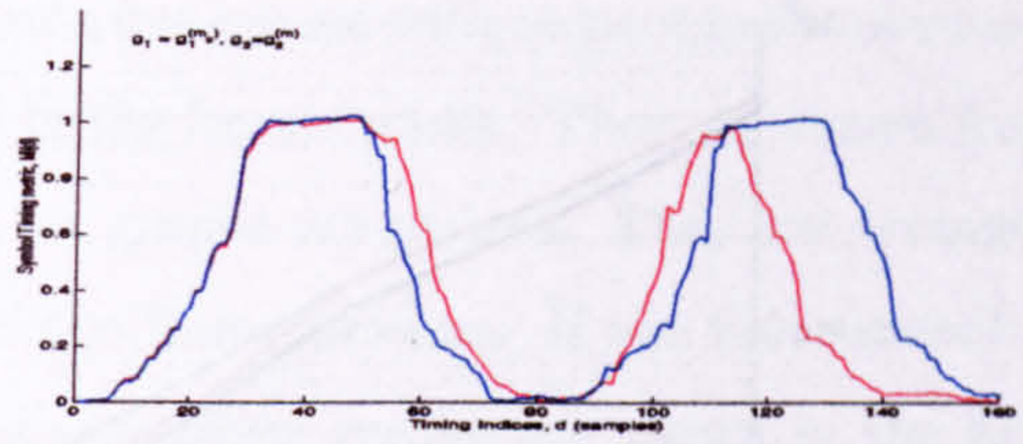

(b) $g_1 = g_1^{(m_2)}$, $g_2 = g_2^{(m)}$

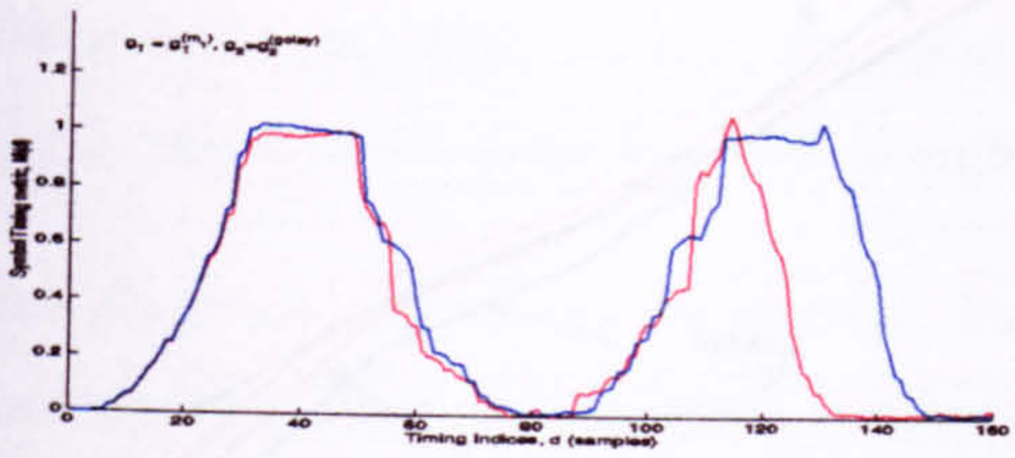

(c) $g_1 = g_1^{(m_1)}$, $g_2 = g_2^{(golay)}$

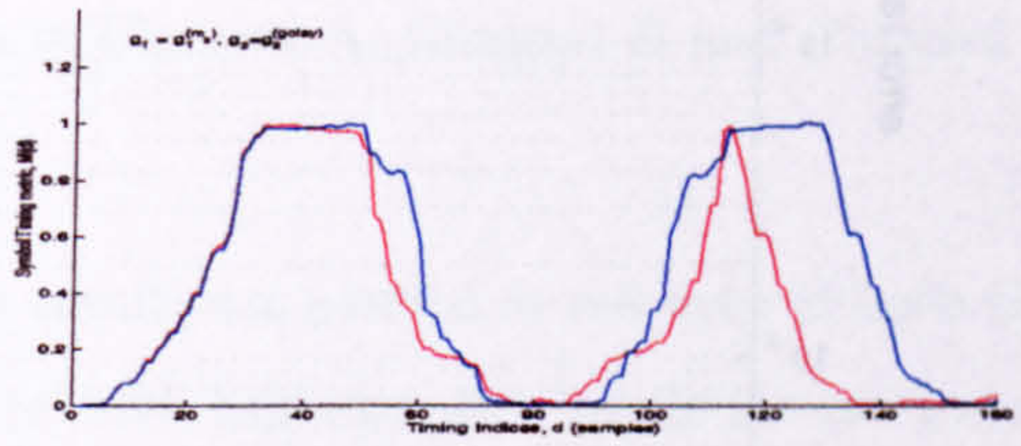

(d) $g_1 = g_1^{(m_2)}$, $g_2 = g_2^{(golay)}$

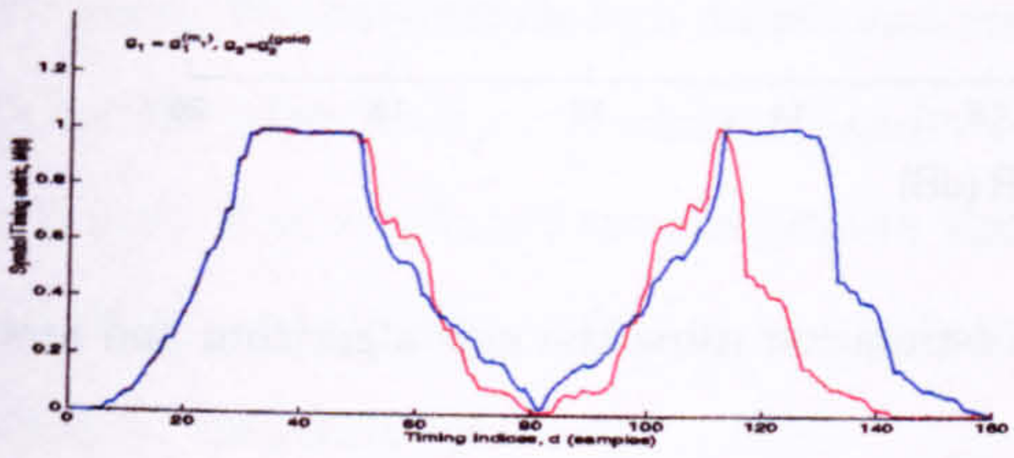

(e) $g_1 = g_1^{(m_1)}$, $g_2 = g_2^{(gold)}$

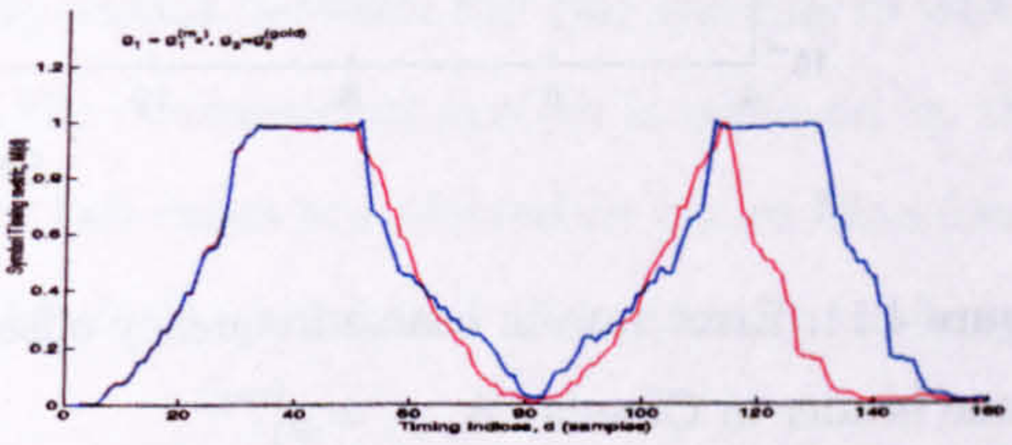

(f) $g_1 = g_1^{(m_2)}$, $g_2 = g_2^{(gold)}$

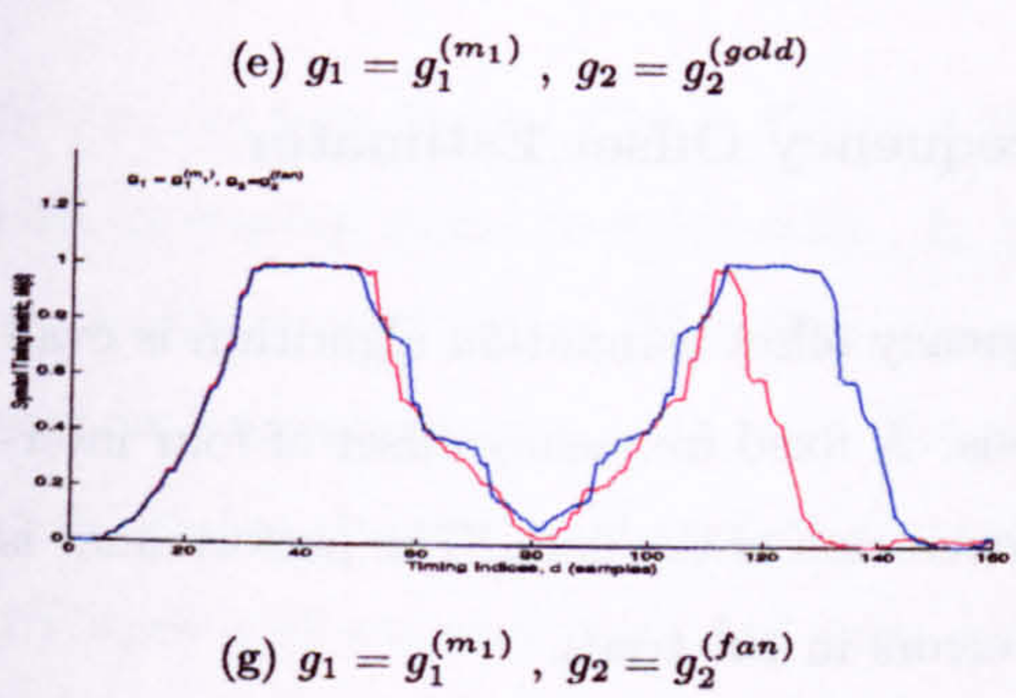

(g) $g_1 = g_1^{(m_1)}$, $g_2 = g_2^{(fan)}$

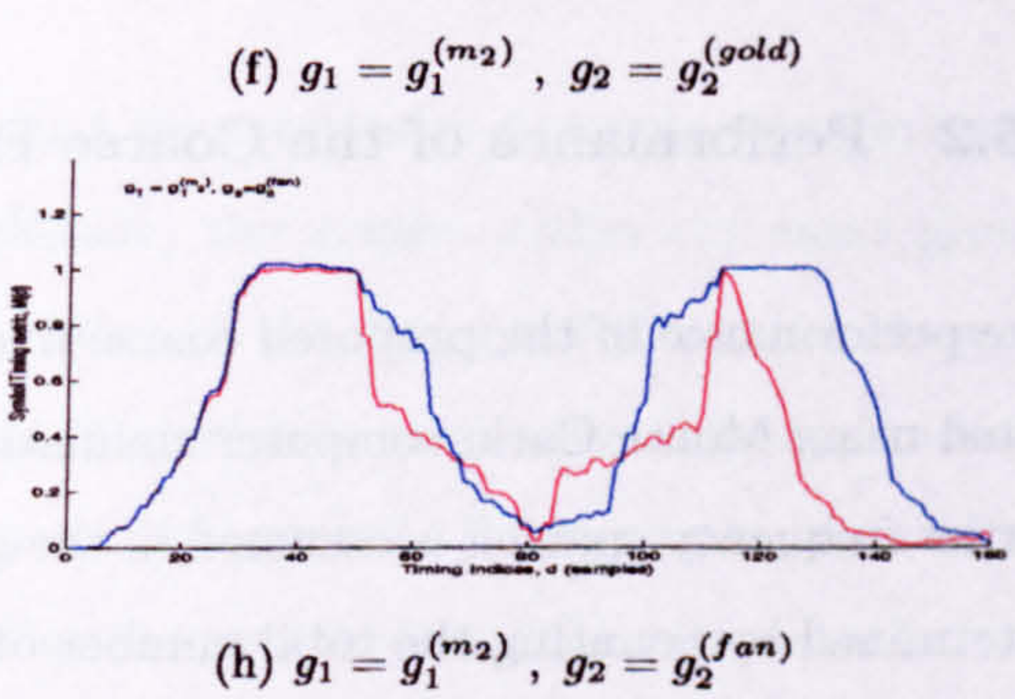

(h) $g_1 = g_1^{(m_2)}$, $g_2 = g_2^{(fan)}$

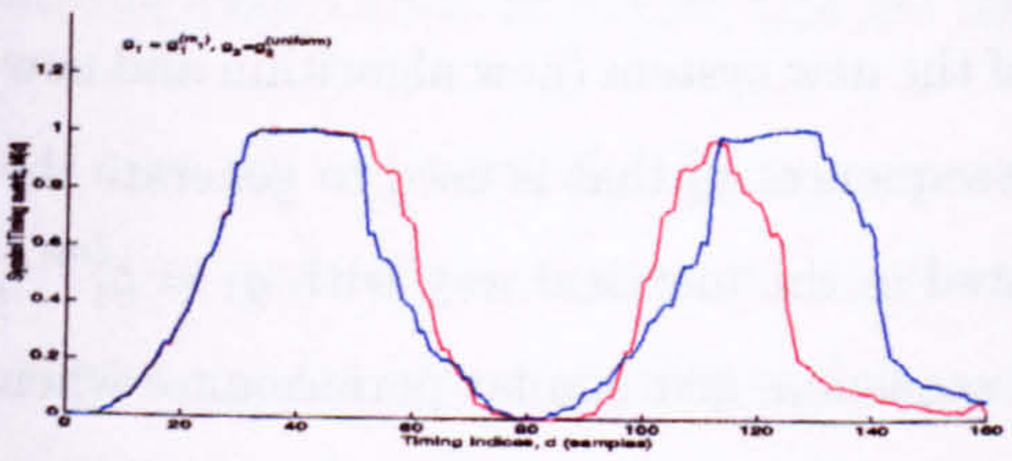

(i) $g_1 = g_1^{(m_1)}$, $g_2 = g_2^{(uniform)}$

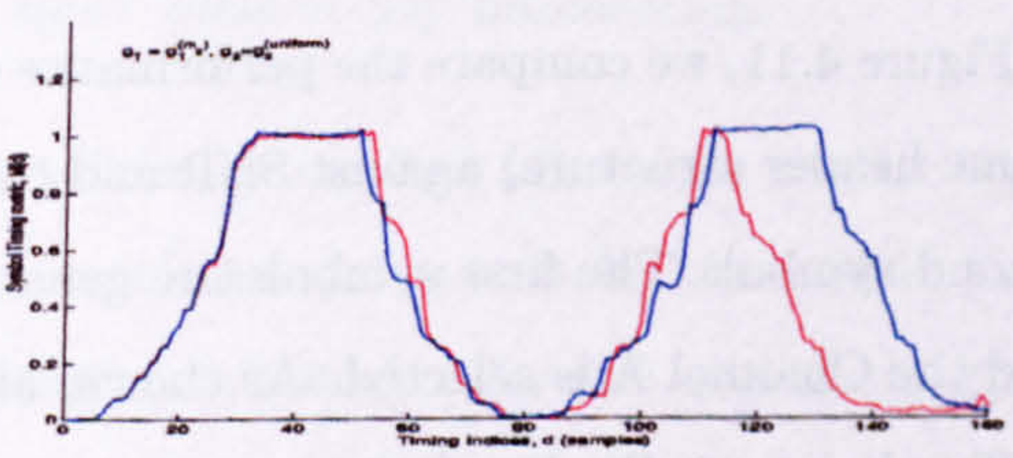

(j) $g_1 = g_1^{(m_2)}$, $g_2 = g_2^{(uniform)}$

Figure 4.10: Plots of the Schmidl and Cox's timing metrics $M(d)$ in AWGN channel, SNR = 30 dB; the results are plotted in blue (red) if the new (conventional) header structure is used.

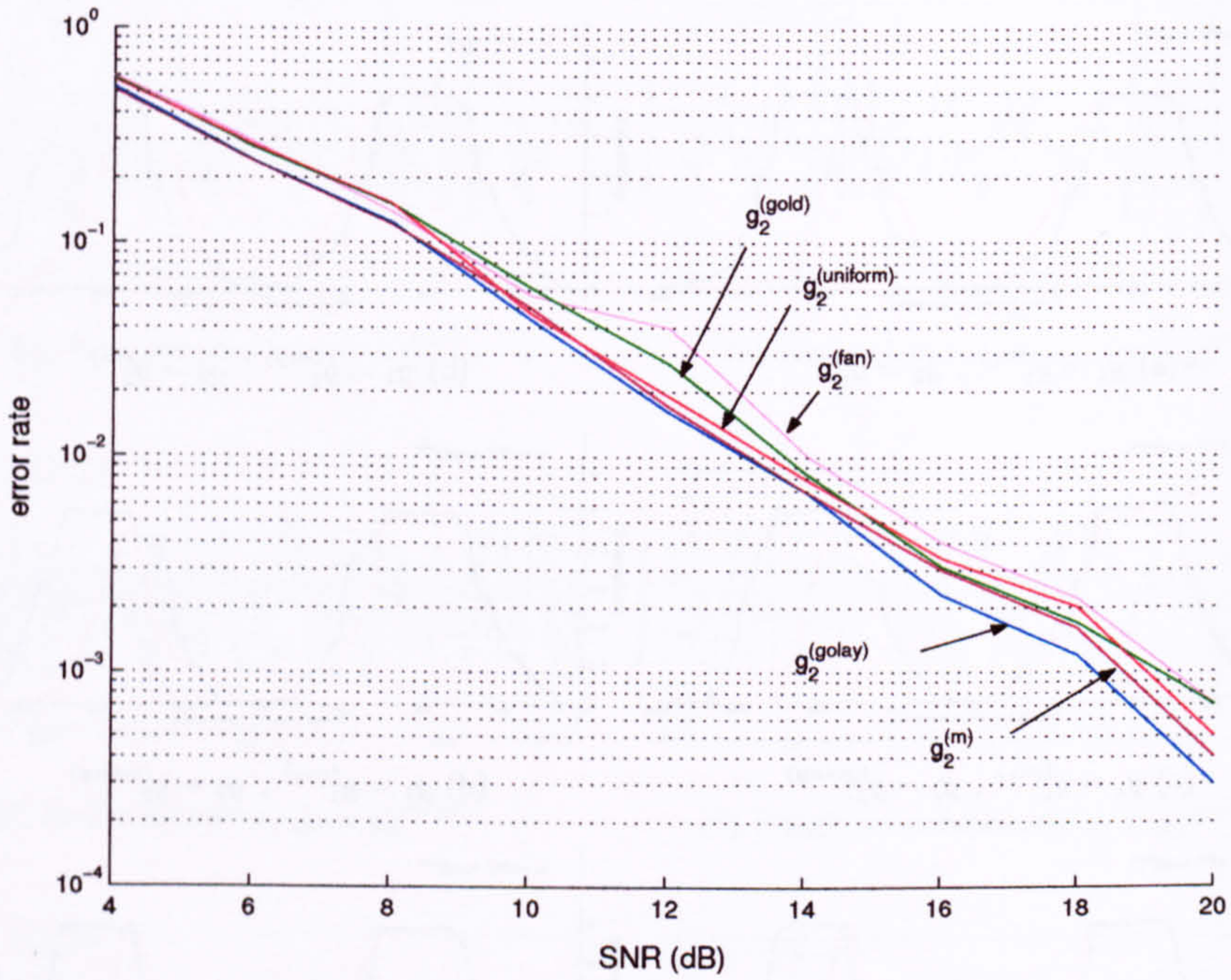

Figure 4.11: Error rate in coarse frequency offset estimation using the new algorithm and new frame header in Channel A, $g_1 = g_1^{(m_1)}$

4.5.2 Performance of the Coarse Frequency Offset Estimator

The performance of the proposed coarse frequency offset estimation algorithm is evaluated using Monte Carlo computer simulations. A fixed frequency offset of four inter-carrier frequency spacing is assumed in the generation of the data. The performance is determined by counting the total number of errors in 10^5 trials.

In Figure 4.11, we compare the performance of the new system (new algorithm and new frame header structure) against SNR and the sequences g_2 that is used to generate the second symbol. The first symbols are generated in the identical way with $g_1 = g_1^{(m_1)}$, and the Channel A is selected. As shown, all sequences give similar performance when SNR is below 10 dB. The Golay sequence outperforms the others at high SNR. However, the difference in the performance between all sequences is about 1 dB only. Therefore, the performance of the new system is robust to the selection of the pseudo-random sequence g_2.

The results of the simulations are arranged into five groups with respect to the sequence that is used to generate the second symbol in the frame header. They are shown from Figure 4.12 to Figure 4.16. In each figure, six graphs are plotted. They are arranged in rows with respect to the first symbol of the frame headers. If the first symbol is generated using the sequence $g_1^{(m_1)}$, the corresponding results are shown in the first row. Otherwise, it is generated using the sequence $g_1^{(m_2)}$ and the results are shown in the second row. Within a row, the results in Channel A, Channel B and Channel C are arranged in the order from left to right.

In each graph, four curves are plotted. The results are plotted in red color if both the new algorithm and the new frame header are used. Likewise, the results are plotted in green color if both the conventional algorithm and the conventional header structure are used. We have made two additional comparisons between the two systems in which either the algorithm or the frame header in the conventional system is replaced by the new one. The results of simulations in these two cases are plotted in either blue (new algorithm, conventional frame header) or black (conventional algorithm, new frame header), respectively.

We can see from Figure 4.12 to Figure 4.16 that the error rates decrease monotonically with increasing signal-to-noise ratio. In addition, the graphs within the same group are similar to each other. Therefore, the selection of the first symbol and the channel have little effects on the error rate. However, the relative error rates between various configuration depend on the selection of the second symbol. For example, the curves in Figure 4.15 are very close and even overlap at many points, while the blue curves and the black curves in Figure 4.14 are far apart without any intersection.

The blue curves (new algorithm, conventional frame header) always lie at the top. In other words, if we compare the performance of the systems at the same SNR, the system using the new algorithm and the conventional frame header will have the largest amount of errors. This suggests that the proposed new algorithm is more sensitive than the conventional algorithm to the intersymbol interference in the second symbol. The intersymbol interference is caused by the overlapping of the signals coming from different paths and the lack of the guard interval between the two training symbols in

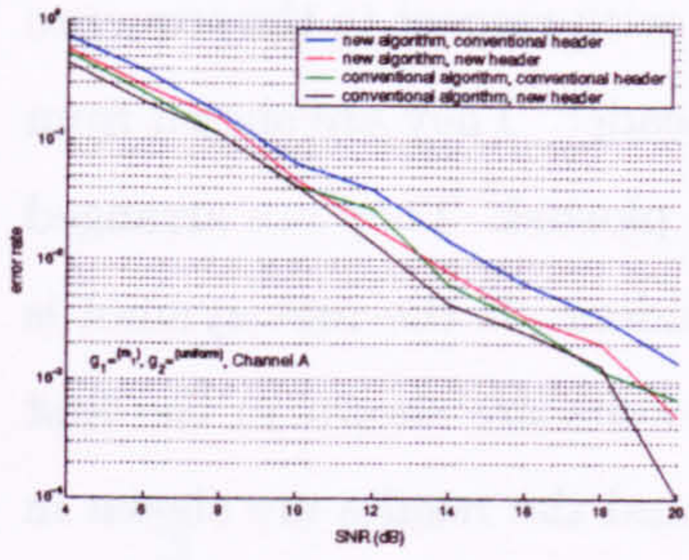

(a) $g_1 = g_1^{(m_1)}$, Channel A

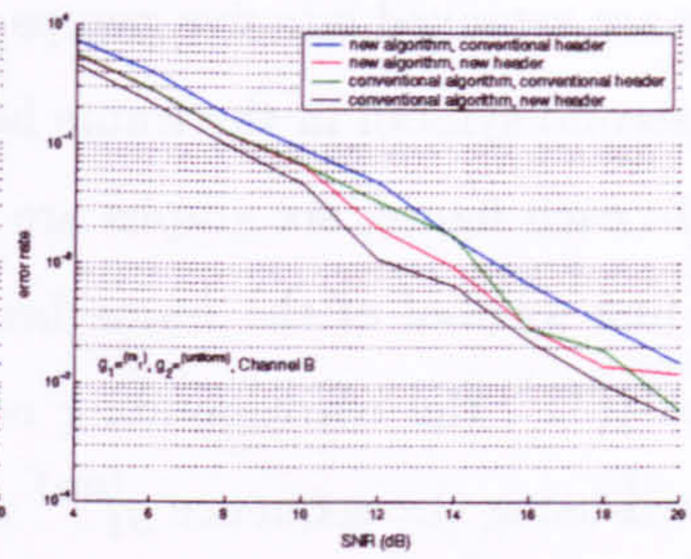

(b) $g_1 = g_1^{(m_1)}$, Channel B

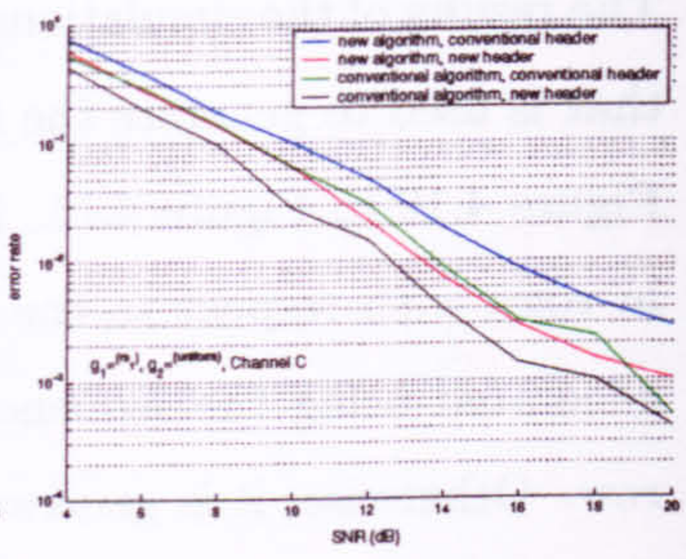

(c) $g_1 = g_1^{(m_1)}$, Channel C

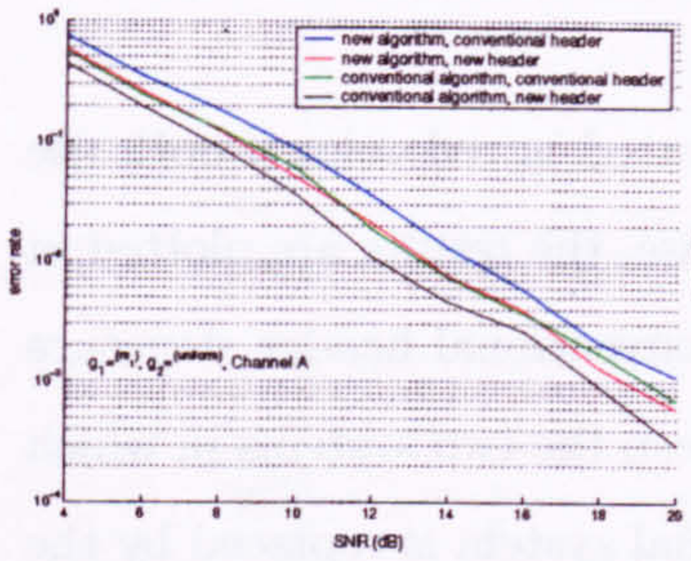

(d) $g_1 = g_1^{(m_2)}$, Channel A

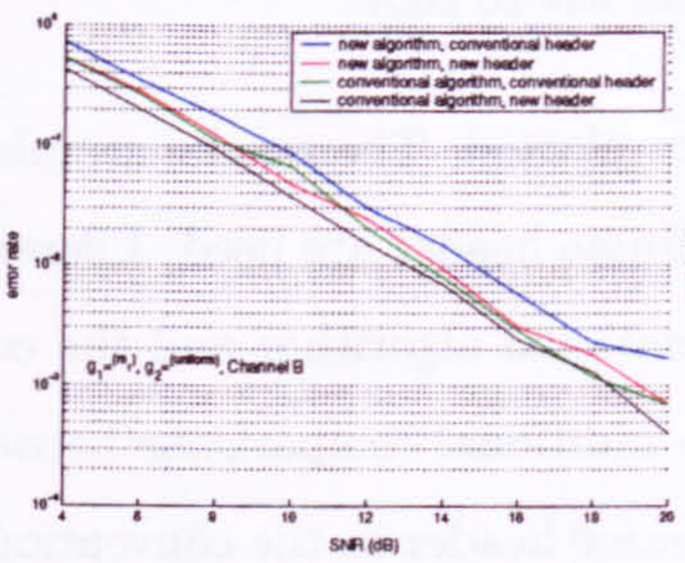

(e) $g_1 = g_1^{(m_2)}$, Channel B

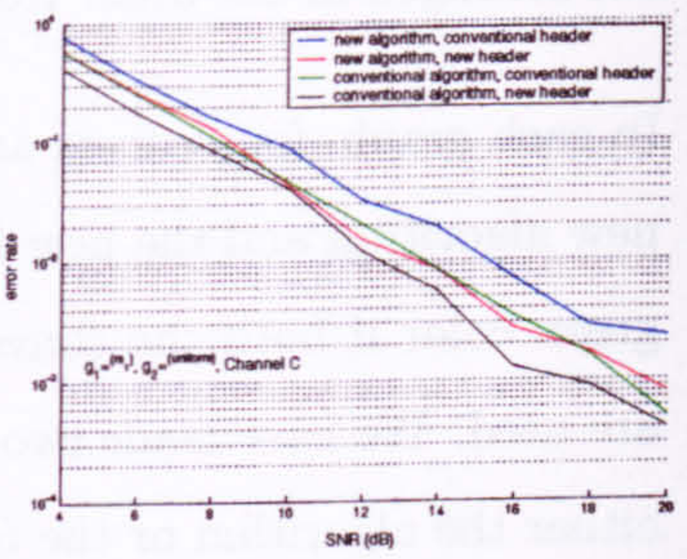

(f) $g_1 = g_1^{(m_2)}$, Channel C

Figure 4.12: Error rate of the coarse frequency offset estimators in multipath fading channels when subcarriers are differentially modulated with the computer generated sequence $g_2^{(uniform)}$

the frame header. Similarly, a system using the conventional algorithm and the new frame header structure will have the best performance because the corresponding black curves always lie at the bottom.

In general, the red curves (new algorithm, new frame header) and the green curves (conventional algorithm, conventional frame header) are very close to each other. In other words, the new system and the conventional system have similar performance. However, the new system has an additional advantage of lower complexity in comparison with the conventional system. This is because we do not have to carry out complex number multiplications and additions during the search of the coarse frequency offset as in the conventional system. Only simple binary number operations are required in the new system. This will simply the hardware implementation of the system.

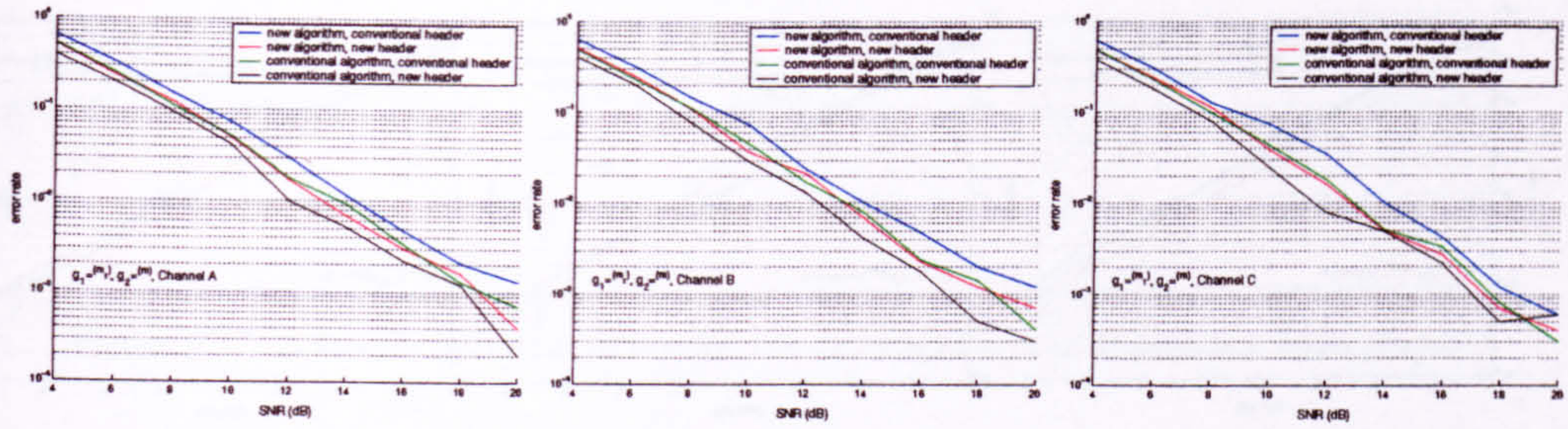

(a) $g_1 = g_1^{(m_1)}$, Channel A (b) $g_1 = g_1^{(m_1)}$, Channel B (c) $g_1 = g_1^{(m_1)}$, Channel C

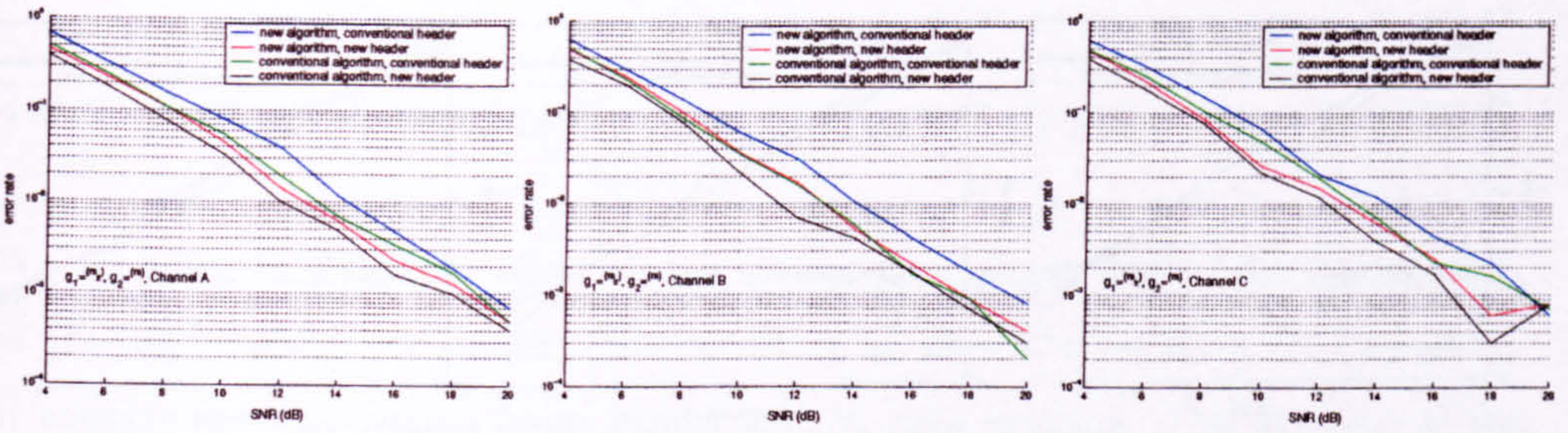

(d) $g_1 = g_1^{(m_2)}$, Channel A (e) $g_1 = g_1^{(m_2)}$, Channel B (f) $g_1 = g_1^{(m_2)}$, Channel C

Figure 4.13: Error rate of the coarse frequency offset estimators in multipath fading channels when subcarriers are differentially modulated with the m-sequence $g_2^{(m)}$

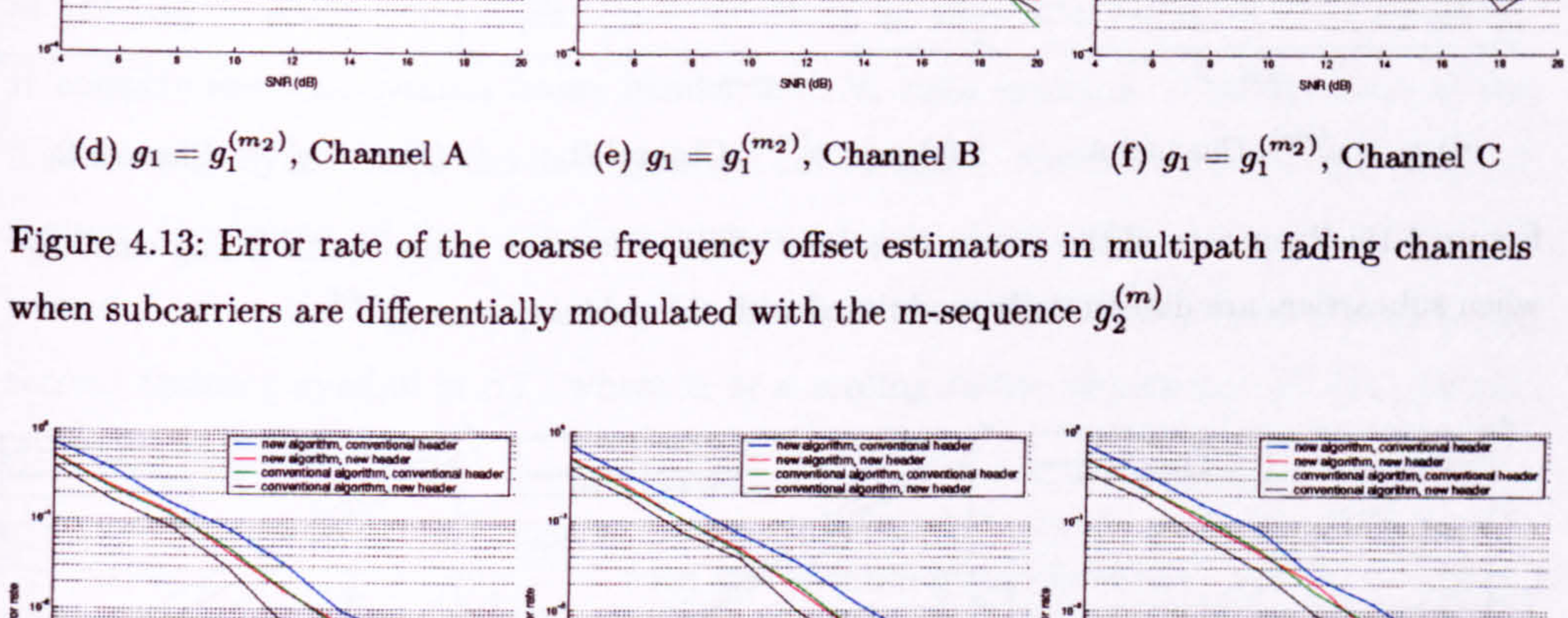

(a) $g_1 = g_1^{(m_1)}$, Channel A (b) $g_1 = g_1^{(m_1)}$, Channel B (c) $g_1 = g_1^{(m_1)}$, Channel C

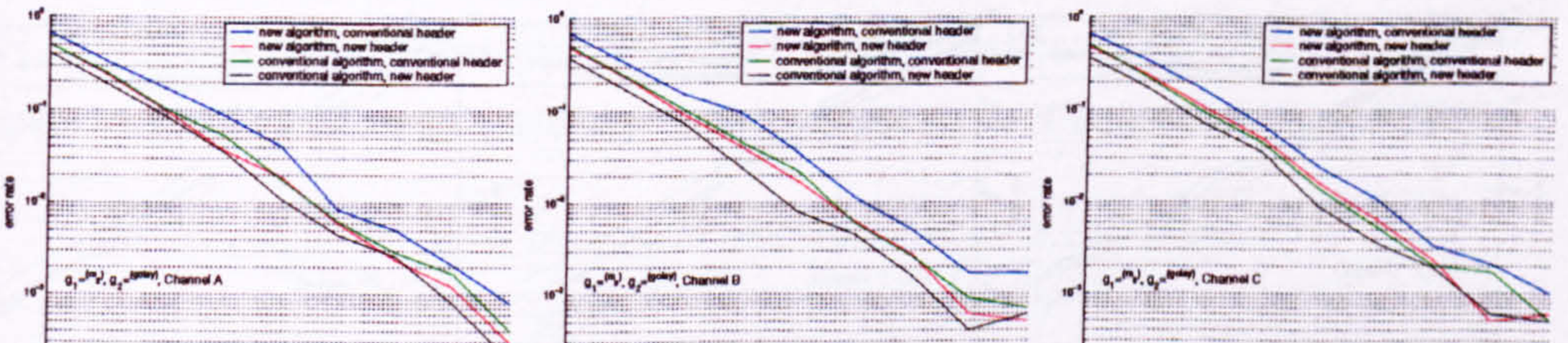

(d) $g_1 = g_1^{(m_2)}$, Channel A (e) $g_1 = g_1^{(m_2)}$, Channel B (f) $g_1 = g_1^{(m_2)}$, Channel C

Figure 4.14: Error rate of the coarse frequency offset estimators in multipath fading channels when subcarriers are differentially modulated with the Golay sequence $g_2^{(golay)}$

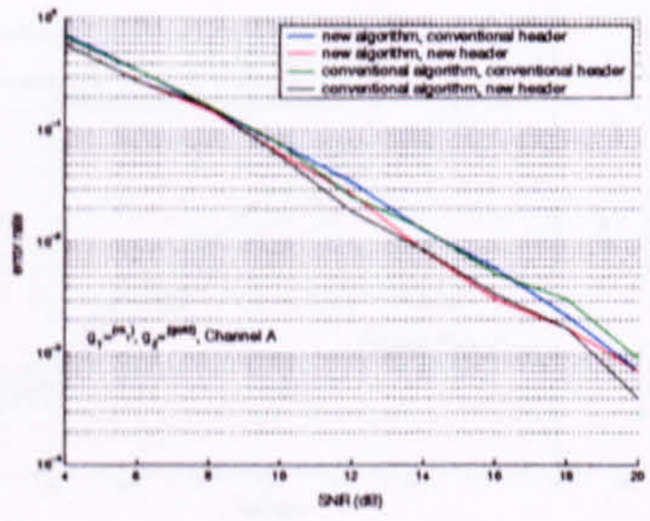

(a) $g_1 = g_1^{(m_1)}$, Channel A

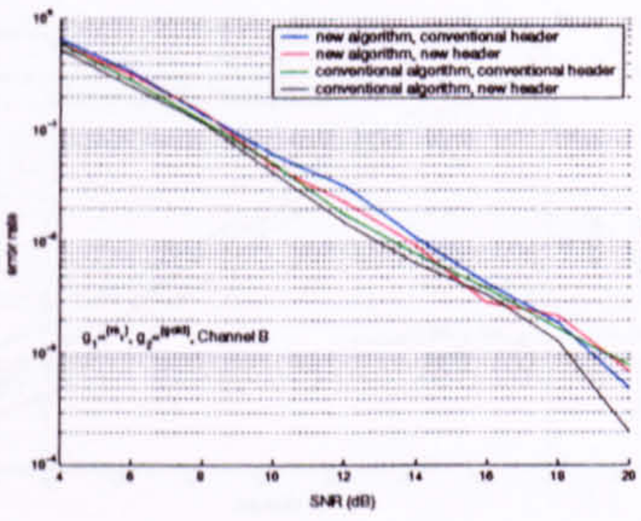

(b) $g_1 = g_1^{(m_1)}$, Channel B

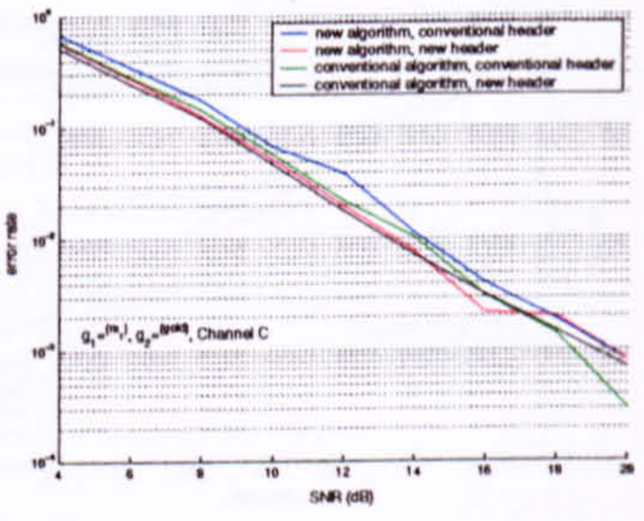

(c) $g_1 = g_1^{(m_1)}$, Channel C

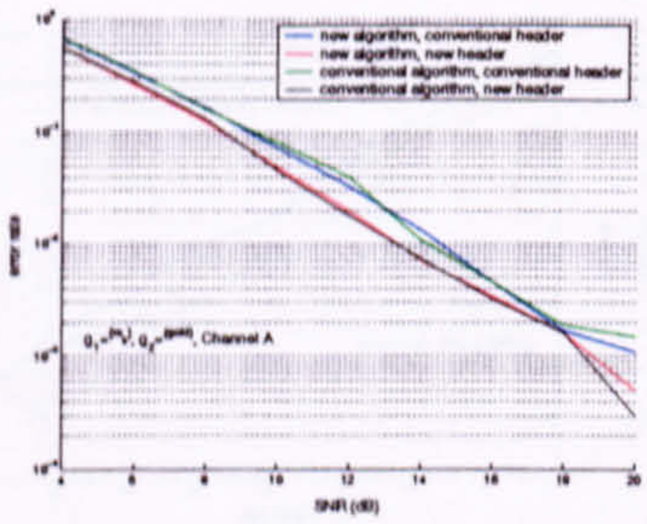

(d) $g_1 = g_1^{(m_2)}$, Channel A

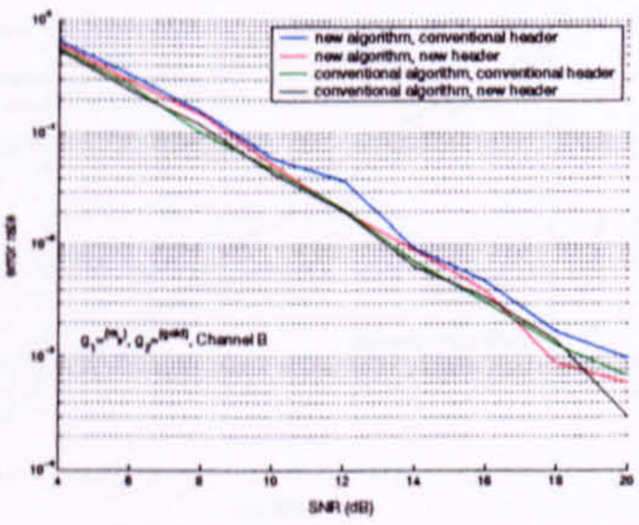

(e) $g_1 = g_1^{(m_2)}$, Channel B

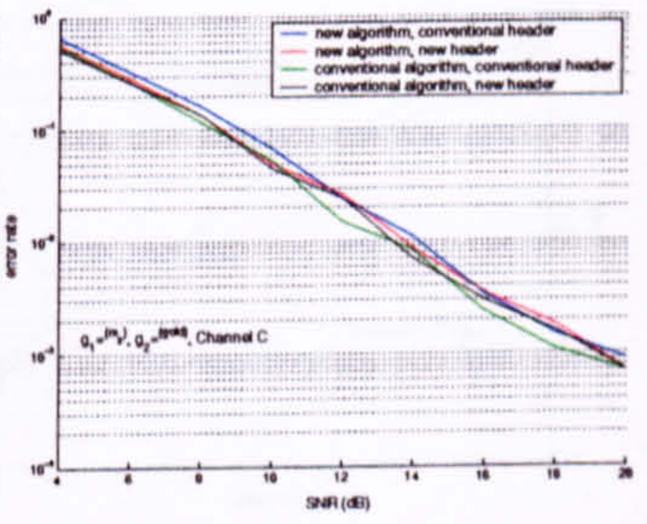

(f) $g_1 = g_1^{(m_2)}$, Channel C

Figure 4.15: Error rate of the coarse frequency offset estimators in multipath fading channels when subcarriers are differentially modulated with the gold sequence $g_2^{(gold)}$

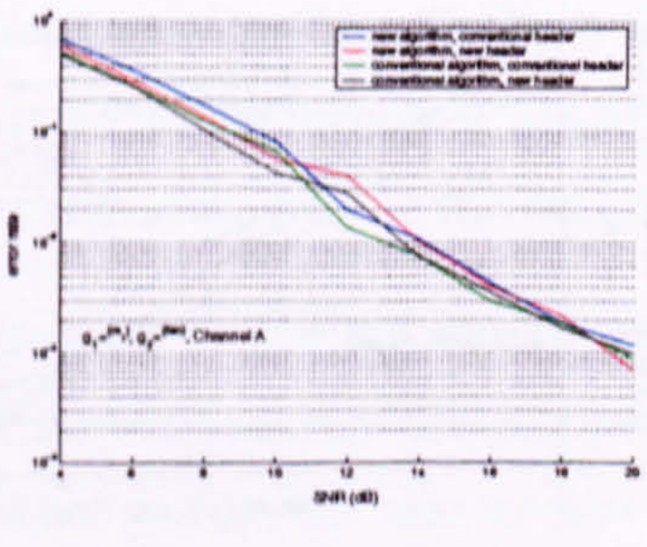

(a) $g_1 = g_1^{(m_1)}$, Channel A

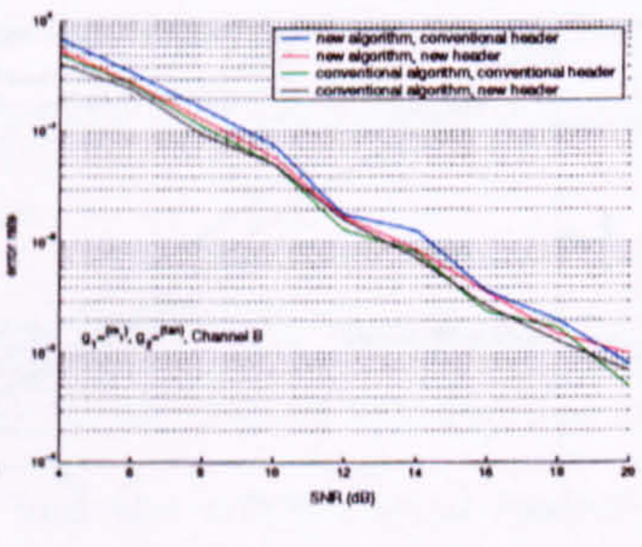

(b) $g_1 = g_1^{(m_1)}$, Channel B

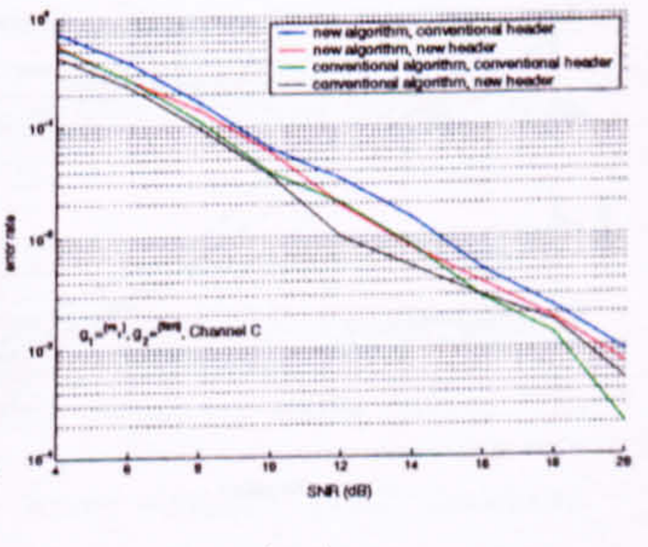

(c) $g_1 = g_1^{(m_1)}$, Channel C

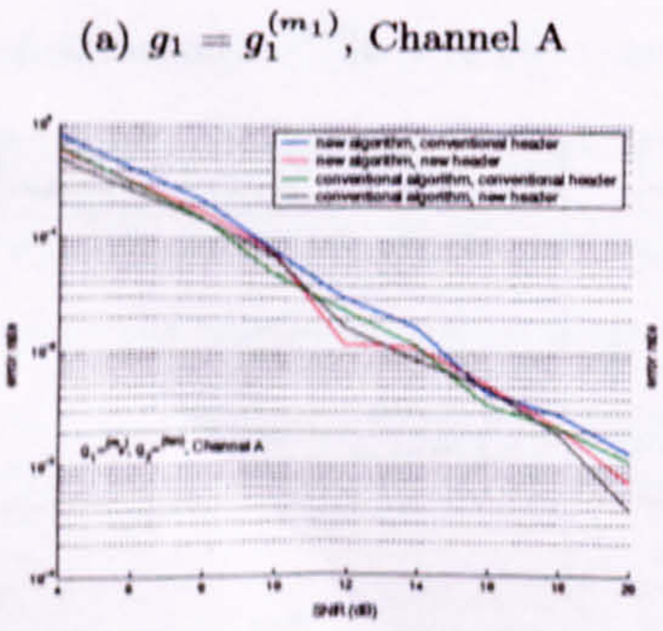

(d) $g_1 = g_1^{(m_2)}$, Channel A

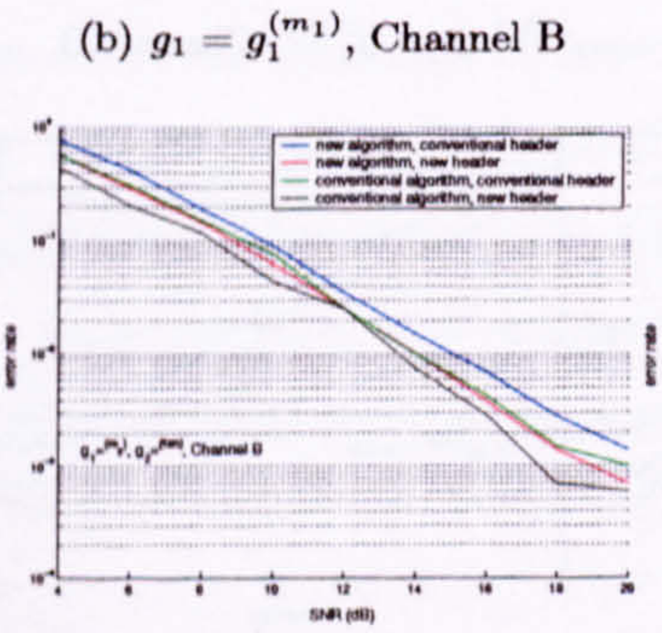

(e) $g_1 = g_1^{(m_2)}$, Channel B

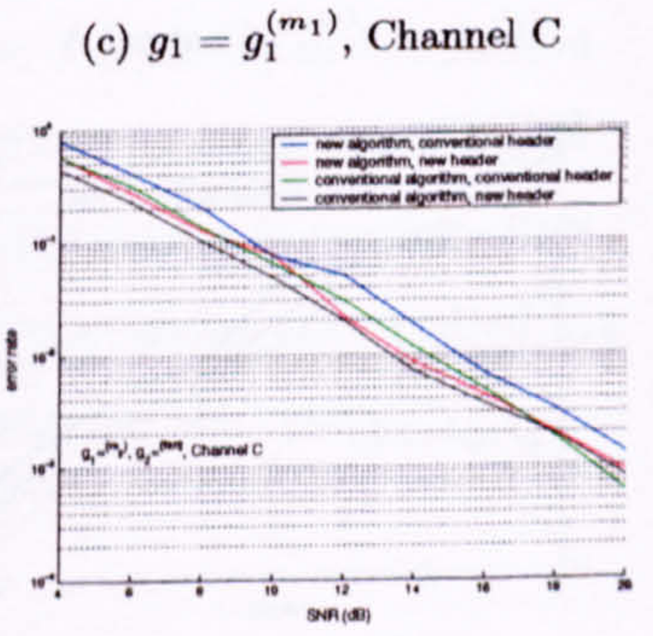

(f) $g_1 = g_1^{(m_2)}$, Channel C

Figure 4.16: Error rate of the coarse frequency offset estimators in multipath fading channels when subcarriers are differentially modulated with the Fan's sequence $g_2^{(fan)}$

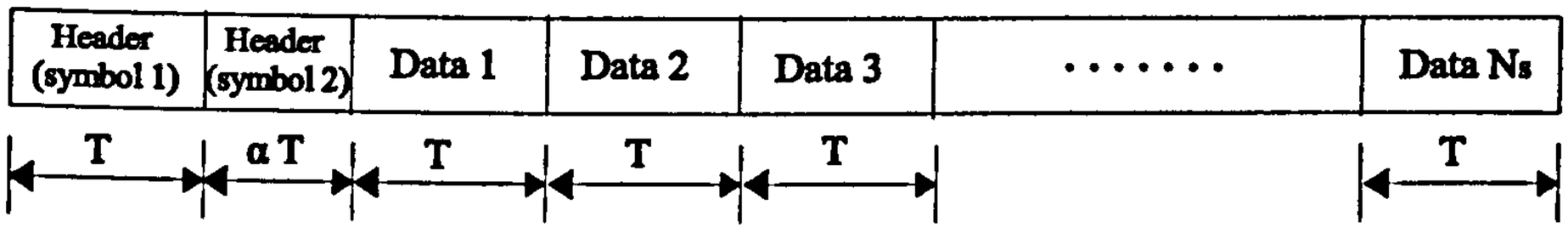

Figure 4.17: A simple frame structure for the determination of the system throughput

4.6 Drawback of the New Frame Header

4.6.1 System Throughput

We are going to study the effect on the system throughput due to the introduction of the frame header. A simple frame structure as shown in Figure 4.17 is assumed. It consists of a two-symbol frame header and N_s data symbols. The duration of the first training symbol and the data symbols are identical. However, in the conventional system, the length of the second training symbol is shorter than the normal symbol period T since the intersymbol guard interval is removed. The time duration of the second training symbol is αT, where α is a scaling factor depending on the symbol structure as follows.

$$\alpha = \begin{cases} 1 & \text{with intersymbol guard interval} \\ \frac{N_u}{N_u+N_g} & \text{without intersymbol guard interval,} \end{cases} \tag{4.13}$$

N_u and N_g are the number of samples in the useful part and the guard interval respectively. Let $\mathcal{R}_s$ be the raw data rate per OFDM symbol, which is defined as the total number of bits transmitted in the time duration of one OFDM symbol. Total $\mathcal{R}_s N_s T$ bits are transmitted per frame. The time duration of one frame is equal to $(N_s + 1 + \alpha)T$. Therefore, the effective data rate $\mathcal{R}$ of the frame-based system is

$$\mathcal{R} = \frac{\text{Total number of bits transmitted in one frame}}{\text{The time duration of one frame}} \tag{4.14}$$

$$= \frac{\mathcal{R}_s N_s T}{(N_s + 1 + \alpha)T}$$

$$= \frac{\mathcal{R}_s N_s}{N_s + 1 + \alpha} \tag{4.15}$$

	α			
N_s	0.67	0.89	0.80	1
16	9.43%	10.11%	10.55%	11.11%
32	4.95%	5.33%	5.57%	5.88%
64	2.53%	2.73%	2.87%	3.03%
128	1.28%	1.38%	1.45%	1.54%
512	0.33%	0.35%	0.37%	0.39%
1024	0.16%	0.18%	0.18%	0.19%

Table 4.5: Amount of reduction in effective data rate when a two-symbol frame header is transmitted together with N_s data symbols in one frame; frame header length = $(1+\alpha)$ times the length of one data symbol

The data rate is reduced from $\mathcal{R}_s$ to $\mathcal{R}$. Hence, the reduction in the overall system throughput can be determined by

$$\begin{aligned} \text{reduction in throughput} &= \left(\frac{\mathcal{R}_s - \mathcal{R}}{\mathcal{R}_s}\right) \times 100\% \\ &= \left(1 - \frac{N_s}{N_s + 1 + \alpha}\right) \times 100\% \end{aligned} \tag{4.16}$$

If the length of the guard interval is either 1/5, 1/4 or 1/2 of the length of the useful part, α will be equal to 0.89, 0.80 or 0.67 respectively. Table 4.5 gives some examples of the reduction in the system throughput for various combination of N_s and α.

As shown in Table 4.5, the reduction in the system throughput become less significant when the total number of data symbols in one frame is large. In particular, we are interested in the effect of the additional intersymbol guard interval in the frame header. This can be determined by subtracting the last column ($\alpha = 1$) with the other three column. For example, if there are 64 symbols in one frame and the length of the guard interval is 1/4 of the useful part ($\alpha = 0.4$), the new frame header will cause an additional 3.03%-2.73%=0.3% reduction in the system throughput. Therefore, there is only a minor reduction in the system throughput by adding the intersymbol guard interval in the new frame header.

4.6.2 Response Time

The frame header should be kept short for fast synchronization. However, adding a guard interval between the two symbols in the frame header will increase the system response time. The system now takes longer time to transmit all the useful information to the receiver and the symbol timing estimator will take longer time to wait for the reception of the entire training symbols. The additional time delay is equal to the length of the guard interval times the sampling period. For example, the sampling rate in Hiperlan/2 is 20MHz and hence the time duration between adjacent samples is equal to 0.05 μs. If the guard interval has 16 samples, there will be an additional delay of $0.05\mu s \times 16 = 0.8\mu$s before the system can reach synchronization.

4.7 Low-Complexity Hardware Implementation

In our proposed algorithm, the coarse frequency offset $\widetilde{m}$ is determined by

$$\widetilde{m} = \max_{m} \sum_{n=0}^{N/2-1} p\Big\{\phi(k_{2(n+m)})\Big\}\, g(n) \tag{4.17}$$

where

$$p(\phi) = \begin{cases} +1 & |\phi| > \frac{\pi}{2} \\ -1 & |\phi| \leq \frac{\pi}{2} \end{cases} \tag{4.18}$$

The function ϕ determines the phase difference of the 2(n+m)-th subcarriers in the two symbols of the frame header. The function **p** then translates this amount of phase difference into either +1 or -1. Table 4.6 lists the multiplication table of the product $(\mathbf{p} \cdot \mathbf{g})$ and the truth table of the standard exclusive-nor function. Comparing the entries in the two tables, we can find that the two operations can be made identical if we associate "-1" to "0".

Suppose we redefine the function **p** as a {0,1} mapping function whose outputs are either 0 or 1 depending on the input phase difference $|\angle c_1 - \angle c_2|$. Then, the product $(\mathbf{p} \cdot \mathbf{g})$ can be realized as a bitwise exclusive-nor operation, which can be implemented with very low complexity in hardware. Likewise, the mapping function **p** can be implemented easily using a look-up table stored in the read-only-memory (ROM).

p	g	$p \cdot g$
-1	-1	1
-1	1	-1
1	-1	1
1	1	1

input 1	input 2	xor	$\overline{\text{xor}}$
0	0	0	1
0	1	1	0
1	0	1	0
1	1	0	1

Table 4.6: Multiplication table of $(p \cdot g)$ [left] and the truth-table of exclusive-nor [right]

Figure 4.18 is a block diagram of an implementation of the proposed coarse frequency offset estimation algorithm in hardware. Here, we have assumed that the size of the IFFT is 64, which is a common value used in the standard for wireless network such as the IEEE 802.11a and the Hiperlan/2. In addition, the new two-symbol frame header is assumed.

The outputs of the FFT pass through a two-level pipeline buffer before they are sent to the data decoding unit for further processing. If we are at the beginning of a frame, the frame header will be captured in the two buffers, Symbol 1 and Symbol 2. Whenever a frame header is captured, the amplitude of the odd frequency subcarriers in both Symbol 1 and Symbol 2 will be zero, or in a very low value in practice. Therefore, it is simple to build a frame header detection unit by comparing the power sum of all odd subcarriers with a predefined threshold. The frame detection signal can be used to reset the internal state of the estimator and kick start the estimation process. For clarity, the frame header detection unit is drawn by a box in broken lines enclosing the two buffers without the full internal details.

Since the frame header and the payload data have identical symbol structure, we do not have to handle these two types of data separately. Otherwise, we have to build two separate data buses to pass the outputs of the FFT to the data decoding unit and the synchronization unit. With the expense of additional delay in propagating data through the pipeline, this reduce the hardware complexity and the cost. This is one of the merit of including an intersymbol guard interval in the frame header.

Since the sequence g is known already, it can be pre-loaded to the internal 26-bit registers. The correlation can be carried out quickly using an array of exclusive-nor

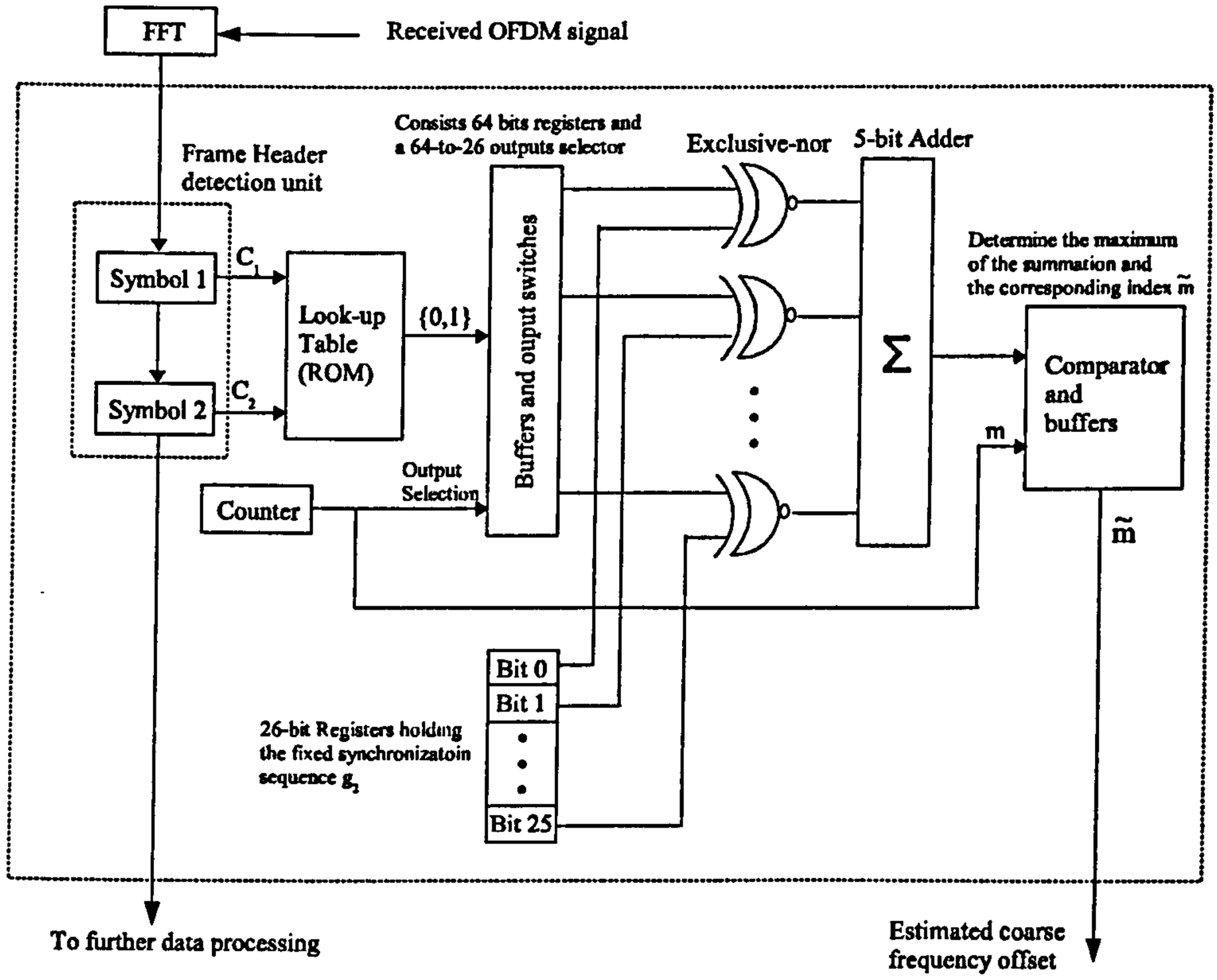

Figure 4.18: Block diagram of the implementation of the proposed coarse frequency offset estimator in hardware

gates and an adder. Since the maximum output of the adder is 26, only a simple 5-bit adder is required. The current output of the adder is then compared with the previous stored one. If the current sum is larger than the previous one, it will replace the one in the buffer and the current running index m is saved. At last, the index $\tilde{m}$ that corresponds to the largest output of the adder is the estimated coarse frequency offset.

Chapter 5

Synchronization Pilots Pattern

5.1 Introduction

In the previous chapter, we have discussed the technique to estimate the coarse frequency offset in an OFDM system by exploiting the noncoherent autocorrelation function of pilot carriers. We have pointed out that the sidelobes of the noncoherent autocorrelation function affects the performance of the proposed pilots-power-detection coarse frequency offset estimator. Therefore, the pilots pattern should be designed properly to reduce the sidelobes.

In this chapter, we will study the effects of the pilots pattern to the performance of the proposed coarse frequency estimator using computer simulations. The OFDM system model is based on the terrestrial digital television (DVB-T) standard. The European Telecommunication Standards Institute (ETSI) has adopted OFDM as the standard transmission scheme for terrestrial digital television broadcasting (DVB-T) in Europe. Two modes of operation have been defined in the DVB-T standard, namely *2k mode* and *8k mode*. Parameters such as the total number of carriers, frequency spacing between carriers and symbol duration are different in these two modes. The parameters used in the simulations are based on the 2k mode.

This chapter is arranged as follows. At first, we will describe the OFDM symbol structure in the DVB-T system and the characteristics of the original pilots pattern. After

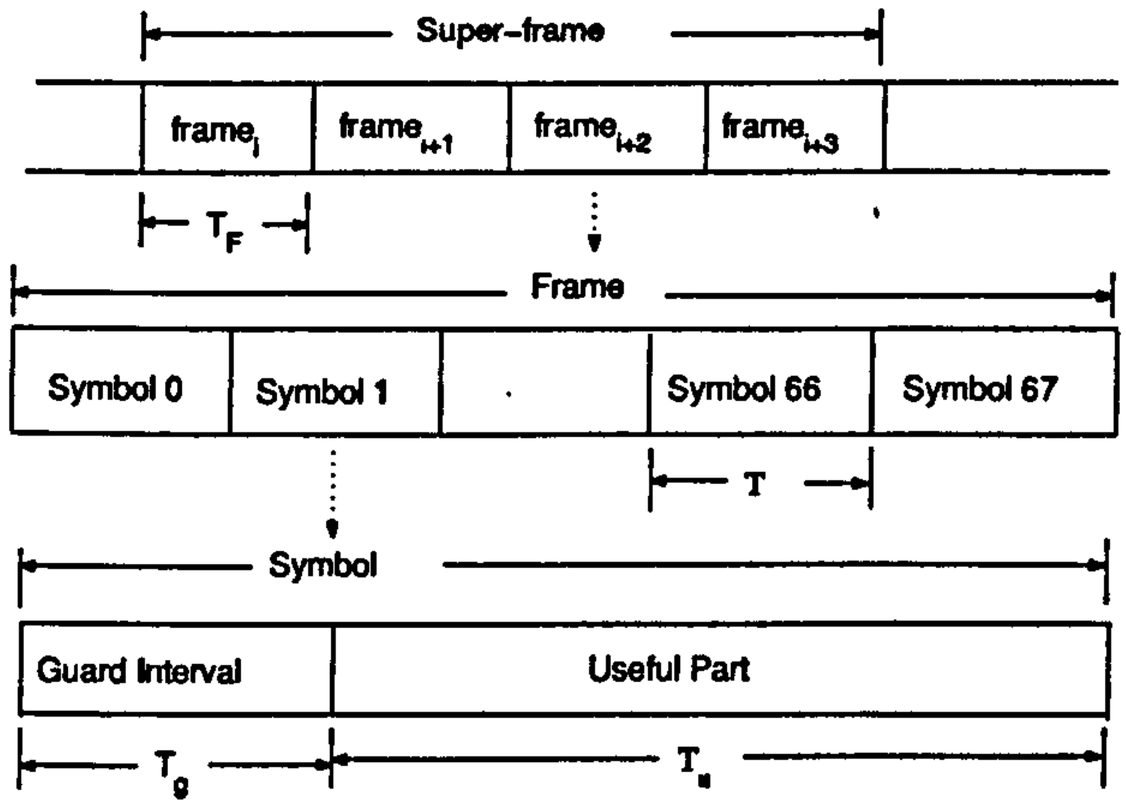

Figure 5.1: Frame structure in a DVB-T system

a brief review on the properties of binary sequences, some aperiodic binary sequences with good autocorrelation properties are given. Usually, the number and power of interferers as well as their time of appears are unknown during the design of the system. It will be shown that the robustness of the coarse frequency estimator can be improved by one-sided trimming in order to reject the outliers. Then, an algorithm to detect the failure of the coarse frequency offset estimator is proposed. Finally, we present the simulation results in the performance of the estimator using the original pilots pattern in DVB-T 2k system and a proposed pilots pattern.

5.2 DVB-T System

5.2.1 Frame Structure

The OFDM transmitted signal is organized in frames [25, 76]. As shown in Figure 5.1, each frame has a duration of T_F seconds, and consists of 68 OFDM symbols. Four consecutive frames form one super-frame. The DVB-T standard defines two modes of operation, namely *2k mode* and *8k mode*. Each mode has different sets of operating parameters as shown in Table 5.1 and Table 5.2. Each symbol is constituted by a set of 1705 carriers in 2k mode and 6817 carriers in 8k mode, and is transmitted with a duration T. A symbol is built up by two parts: a useful part with duration T_u and

Mode	8k mode				2k mode			
Guard Interval T_g/T_u	1/4	1/8	1/16	1/32	1/4	1/8	1/16	1/31
Duration of symbol part	$8192*T_s$ 896 μs				$2048*T_s$ 224μs			
Duration of guard interval T_g	$2048*T_s$ 224 μs	$1024*T_s$ 112μs	$512*T_s$ 56μs	$2567*T_s$ 28μs	$512*T_s$ 56μs	$256*T_s$ 28μs	$128*T_s$ 14μs	$64*T_s$ 7μs
Symbol duration $T = T_g + T_u$	$10240*T_s$ 1120μs	$9216*T_s$ 1008μs	$8740*T_s$ 952μs	$8448*T_s$ 924μs	$2560*T_s$ 280μs	$2304*T_s$ 252μs	$2176*T_s$ 238μs	$2112*T_s$ 231μs
Frame duration T_F	76.160ms	68.544ms	64.736ms	62.832ms	19.040ms	17.136ms	16.184ms	15.708ms
Elementary period T_s = 7/64 μs								

Table 5.1: Timing specification in the DVB-T system [25]

Parameter	8k mode	2k mode
Number of carriers K	6817	1705
Value of carrier number K_{min}	0	0
Value of carrier number K_{max}	6816	1704
Duration T_u	896 μ s	224 μ s
Carrier spacing $1/T_u$	1116 Hz	4464 Hz
Spacing between carriers K_{min} and K_{max}	7.61 MHz	7.61 MHz

Table 5.2: Numerical values of the OFDM parameters in DVB-T system [25]

a guard interval with a duration T_g. The guard interval is a cyclic extension of the useful part and is inserted before it. Four values of guard intervals are defined in the standard.

In addition to transmitting data, some frequency carriers are modulated with reference information whose transmitted value is known to the receiver. They are *scattered pilot carriers*, *continual pilot carriers* and *transmission parameter signalling (TPS) carriers*. The TPS carriers are used for the purpose of signalling parameters related to the channel coding and modulation. Only continual pilots and scattered pilots are transmitted at boosted power level, but not TPS carriers.

Since the average transmitted power of TPS carriers is equal to that of the data carriers, the statistical behavior of TPS carriers is identical to that of data carriers from the point of view of the pilots-power-detection algorithm proposed in Chapter 3. Therefore, TPS carriers are modelled as data carriers throughout the discussion in this chapter.

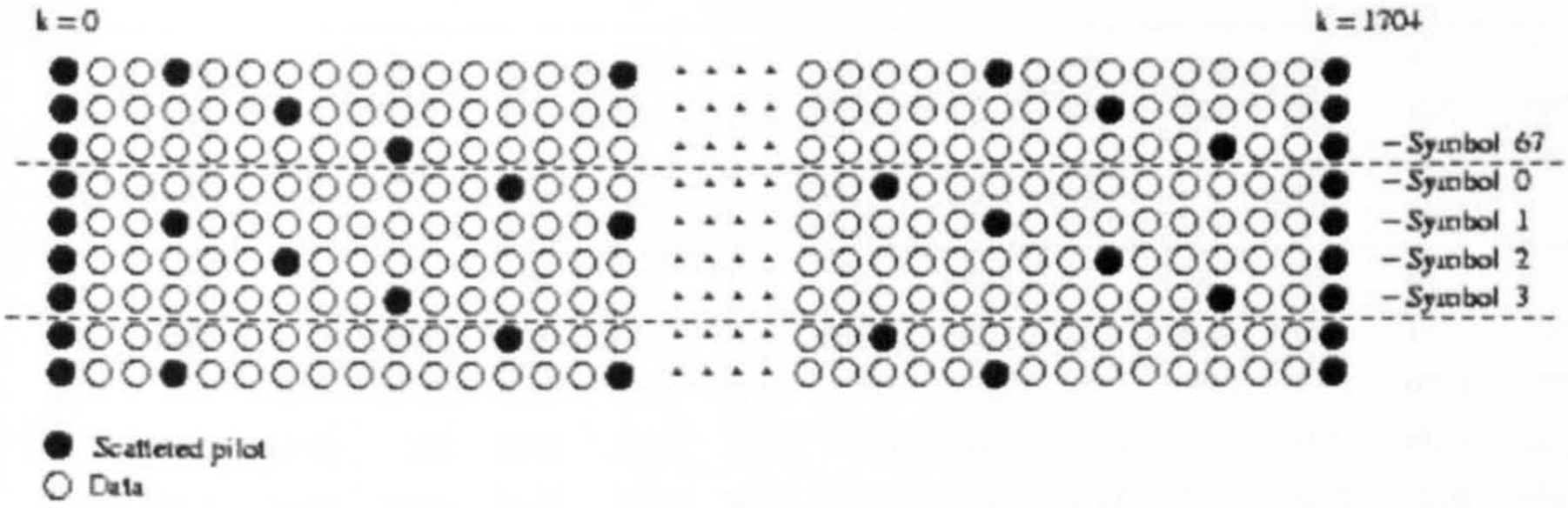

Figure 5.2: Location of scattered pilots in DVB-T 2k system [25]

5.2.2 Location of Scattered Pilots

The frequency indices $\{K_{sp}\}$ of scattered pilots for symbol $I \in \{0 \ldots 67\}$ is given by

$$\{K_{sp}\} = \{k : k = K_{min} + 3 * (I \ mod \ 4) + 12p, \quad p \geq 0, \ K_{min} \geq k \geq K_{max}\} \qquad (5.1)$$

where p is an integer that makes k all possible values greater than or equal to zero provided that the resulting value for k does not exceed the valid range $[K_{min}, K_{max}]$ as defined in Table. 5.2. There is one scattered pilot every twelve carriers. The insertion pattern is periodic within a symbol and the pattern repeats every four symbols. In other words, there are four different ways to assign the scattered pilots in an OFDM symbol as shown in Figure 5.2. In this chapter, these scattered pilots pattern will be referred as *symbol 0, symbol 1, symbol 2* and *symbol 3* that are corresponding to I=0, 1, 2 and 3 respectively.

5.2.3 Location of Continual Pilots

The "continual" means that the pilots occur on all symbols [25] and each continual pilot coincides with a scattered pilot every fourth symbol. Unlike scattered pilots, the locations of continual pilots on all symbols are identical. The frequency indices are given in Table. 5.3. The first 45 continual pilots in 8k mode is just the duplication of those in 2k mode.

2k mode														
0	48	54	87	141	156	192	201	255	279	282	333	432	450	483
525	531	618	636	714	759	765	780	804	873	888	918	939	942	969
984	1050	1101	1107	1110	1137	1140	1146	1206	1269	1323	1377	1491	1683	1704
8k mode														
0	48	54	87	141	156	192	201	255	279	282	333	432	450	483
525	531	618	636	714	759	765	780	804	873	888	918	939	942	969
984	1050	1101	1107	1110	1137	1140	1146	1206	1269	1323	1377	1491	1683	1704
1752	1758	1791	1845	1860	1896	1905	1959	1983	1986	2037	2136	2154	2187	2229
2235	2322	2340	2418	2463	2469	2484	2508	2577	2592	2622	2643	2646	2673	2688
2754	2805	2811	2814	2841	2844	2850	2910	2973	3027	3081	3195	3387	3408	3456
3462	3495	3549	3564	3600	3609	3663	3687	3690	3741	3840	3858	3891	3933	3939
4026	4044	4122	4167	4173	4188	4212	4281	4296	4326	4347	4350	4377	4392	4458
4509	4515	4518	4545	4548	4554	4614	4677	4731	4785	4899	5091	5112	5160	5166
5199	5253	5268	5304	5313	5367	5391	5394	5445	5544	5562	5595	5637	5643	5730
5748	5826	5871	5877	5892	5916	5985	6000	6030	6051	6054	6081	6096	6162	6213
6219	6222	6249	6252	6258	6318	6381	6435	6489	6603	6795	6816			

Table 5.3: Frequency indices of continual pilots in DVB-T system [25]

5.2.4 Power Level of Pilots

Scattered pilots and continual pilots are transmitted at boosted power with respect to that of the data carriers. The corresponding normalized modulation level is given by

$$\begin{cases} |x_k| = \frac{4}{3} \\ |y_k| = 0 \end{cases} \tag{5.2}$$

and the normalized power level of pilots and data carriers are 16/9 and 1, respectively.

5.3 Characteristics of the pilots pattern in DVB-T

Since the DVB-T system has built-in boosted power continual pilots in every symbols, it will be a good candidate to implement the proposed pilots-power-detection algorithm to estimate the coarse frequency offset. The continual pilots pattern will be used as the framework of the search window that slides along the shifted frequency spectrum. In this section, we will study the characteristic of the pilots pattern in two steps. At first, we will study the intrinsic property of the continual pilots pattern by evaluating its autocorrelation function. Secondly, we will evaluate the cross-correlation function

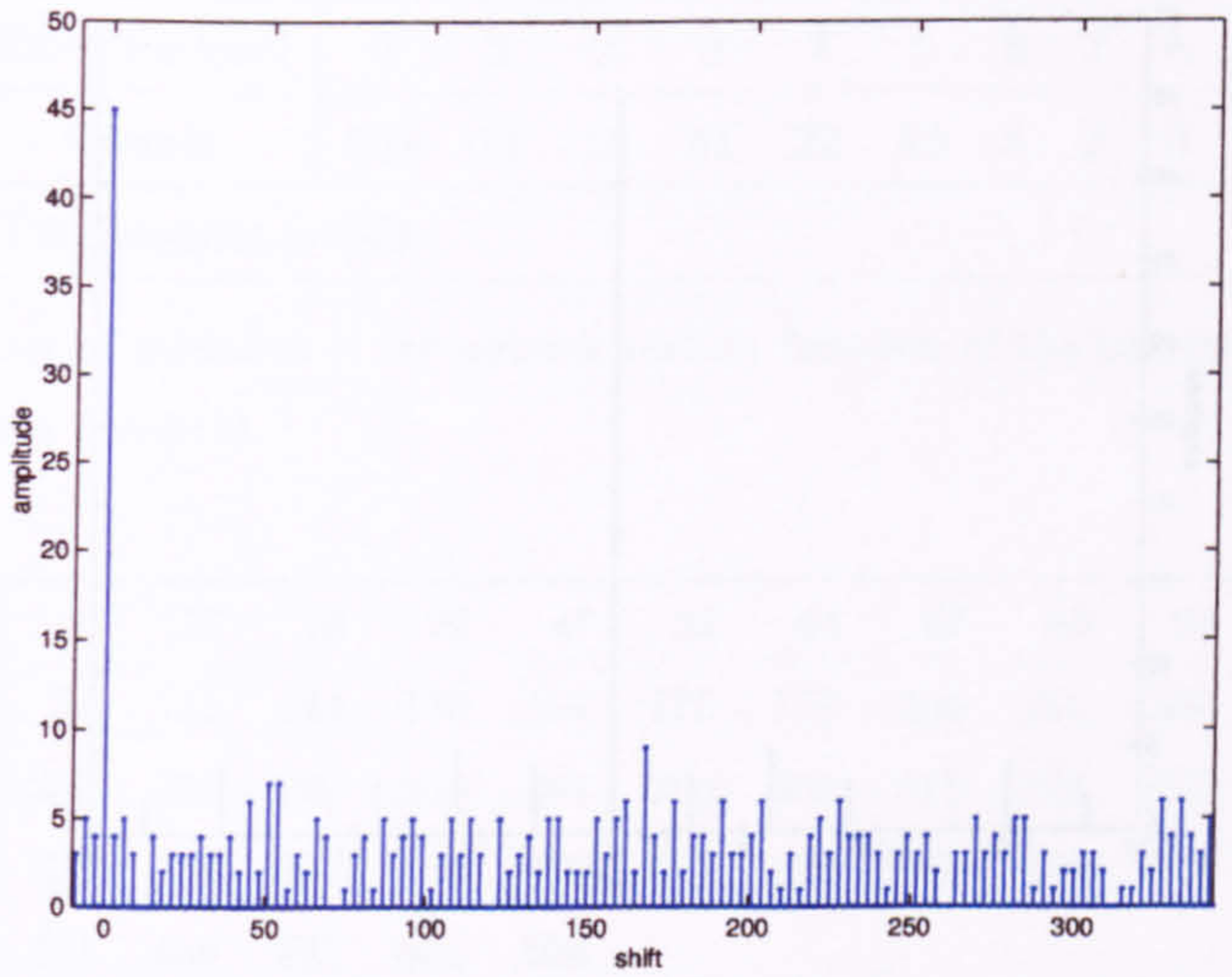

Figure 5.3: Autocorrelation function of the continual pilots pattern in DVB-T 2k mode

between the continual pilots pattern and the combined patterns of the scattered pilots and the continual pilots. The latter case applies to the real applications in which a symbol in the DVB-T system consists of both continual pilots and scattered pilots. Since both of them are transmitted at the same power, we are interested in studying the joint effect of these two types of pilot subcarriers.

5.3.1 Continual Pilots Only

Let K_{cp} be the set of frequency indices of continual pilots in 2k mode as shown in Table. 5.3. The continual pilots pattern is a {0,1} sequence $\mathcal{S}_c$ such that $\forall\ c(i) \in \mathcal{S}_c$,

$$c(i) = \begin{cases} 1 & \text{if } i \in K_{cp} \\ 0 & \text{otherwise} \end{cases} \tag{5.3}$$

Then, we can define the autocorrelation function of the continual pilots pattern in 2k mode as

$$E[c(i)c(i+m)] = \sum_{i=0}^{1704} c(i)c(i+m) \tag{5.4}$$

where $m \in \mathbb{Z}$ is equivalent to a shift in frequency.

The autocorrelation function of the continual pilots pattern is plotted in Figure 5.3. Since the autocorrelation function is symmetric about the zero-shift position, only the

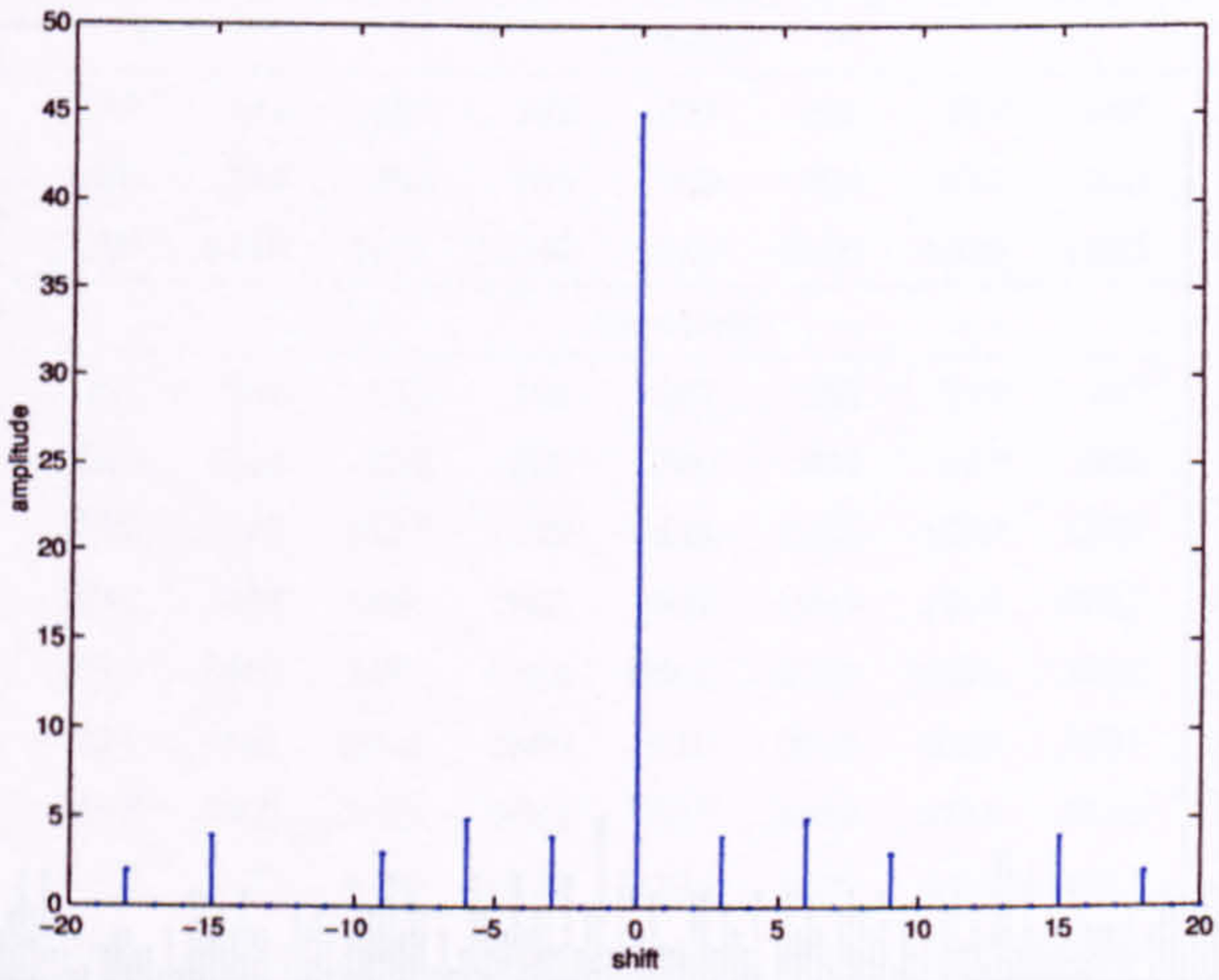

Figure 5.4: Autocorrelation function of the continual pilots pattern in DVB-T 2k mode with shift $= \pm$ 20

positive region is shown for clarity. It is also assumed that the maximum amount of coarse frequency offset is less than $2048 - 1705 = 343$ so that the complete set of pilots is always covered by the 2048-point FFT window. Otherwise, the excess frequency components will be filtered out by the channel selection bandpass filter leading to unrecoverable errors.

As shown in Figure 5.3, the autocorrelation function of the pilots pattern achieves its maximum at the zero shift position and is equal to 45, which is equal to the total number of the continual pilots. In an ideal situation, the pattern should be designed in such a way that the level of sidelobes are either zero or unity so that the stray pilots will not contribute additional interference to the estimator. However, as shown in Figure 5.3, the autocorrelation function has many sidelobes and their magnitudes are much larger than unity. For an example, the sidelobe level is equal to 9 (20% of the maximum level at the zero shift position) when the amount of shift is equal to 168. The distribution of the sidelobes level is summarized in Table 5.4.

On the other hand, we found that the autocorrelation function of the pilots pattern has an "almost" periodic structure. We plot the autocorrelation function again in Figure 5.4 with the amount of shift varies only from 0 to $\pm$20 for a higher display resolution. The autocorrelation function is non-zero whenever the amount of shift is

Sidelobe level	0	1	2	3	4	5	6	7	8	9
Counts	234	11	18	31	22	16	8	2	0	1
Total counts = 343										

Table 5.4: Number of sidelobes of the autocorrelation function of the continual pilots pattern (shifts ranges from 1 to 343)

0	16	18	29	47	52	64	67	85	93
94	111	144	150	161	175	177	206	212	238
253	255	260	268	291	296	306	313	314	323
328	350	367	369	370	379	380	382	402	423
441	459	497	561	568					

Table 5.5: Internal structure of continual pilot carriers in DVB-T 2k mode

an integer multiple of 3. In other words, the sidelobes are non-zero for every three shifts in position towards either direction starting from the center with exceptions in only few places. This periodic structure accounts for the high sidelobe level of the autocorrelation function of the pilots pattern.

This periodic structure can be explained by looking into the structure of the pilots pattern. Although the construction method of the continual pilots has not been explained in the DVB-T standard document [25], we found that the pattern has an internal structure as shown in Table 5.5. The frequency indices of the continual pilots can be generated by multiplying each element in Table 5.5 by 3. It follows that the continual pilots pattern has "1" only at the positions whose corresponding frequency indices are integer multiple of 3, and has "0" elsewhere. This explain the phenomenon that there are high level sidelobes at the points where the amount of shift is the integer multiple of 3, but zero-level sidelobe elsewhere. Similar periodic structure can also be found in the continual pilots pattern defined for the 8k mode.

In conclusion, the continual pilots patterns specified in the DVB-T standard is not optimum for noncoherent coarse frequency offset estimation because of their poor autocorrelation property.

5.4 Joint Effect of Continual Pilots and Scattered Pilots

Since scattered pilots and continual pilots are transmitted at the same power level, the scattered pilots behave as if the stray continual pilots during the search of the shifted continual pilots pattern. Therefore, the inclusion of scattered pilots in the data window can be modelled as an increase in the number of stray pilots. The joint effects of the continual pilots and scattered pilots can be examined by studying the cross-correlation function between the continual pilots pattern and the combination of both patterns.

Because of the modulus operation in the generation of the scattered pilots indices in Equation 5.1, the scattered pilots pattern repeats every four symbols. Therefore, the cross-correlation function has four different forms depending on the symbol index. Let $K_{sp}(j)$ be the sets of carrier indices of scattered pilots in either symbol $j \in \{0,1,2,3\}$ and $\check{c}_j(i)$ be an element of a {0,1} sequence such that

$$\check{c}_j(i) = \begin{cases} 1 & \text{if } i \in K_{cp} \cup K_{sp}(j) \\ 0 & \text{otherwise} \end{cases} \tag{5.5}$$

Then the required cross-correlation function for symbol j in 2k mode can be defined as follows:

$$E[c(i)\ \check{c}_j(i+m)] = \sum_{i=0}^{1704} c(i)\ \check{c}_j(i+m) \tag{5.6}$$

where $m \in \{-343, 343\}$ is equivalent to a shift in frequency.

The cross-correlation functions for all four symbols are plotted in Figure 5.5. The zoom-in versions with shift varying in the range $\{-20, \cdots, 20\}$ are given in Figure 5.6. We have determined the distribution of the sidelobe level from these plots and the results are summarized in Table. 5.6.

As seen, the cross-correlation functions for all symbols have the similar profile. The maximum value of the cross-correlation function is still 45 at the zero-shift position. However, the cross-correlation function is now asymmetric about the zero-shift position. In addition, the sidelobe levels are increased. In particular, the maximum of the sidelobe level is increased from 9 to 19.

Sidelobe level	0	8	9	10	11	12	13	14	15	16	17	18	19
Symbol 0	458	1	10	15	31	48	48	44	14	12	3	1	1
Symbol 1	458	2	5	16	28	49	45	45	25	10	2	1	0
Symbol 2	458	0	9	13	41	45	47	42	23	5	3	0	0
Symbol 3	458	0	5	17	34	51	50	46	16	7	1	1	0
Total counts = 343x2+1 = 687													

Table 5.6: Distribution of the sidelobe level of the cross-correlation functions; shifts limited in the range ±343

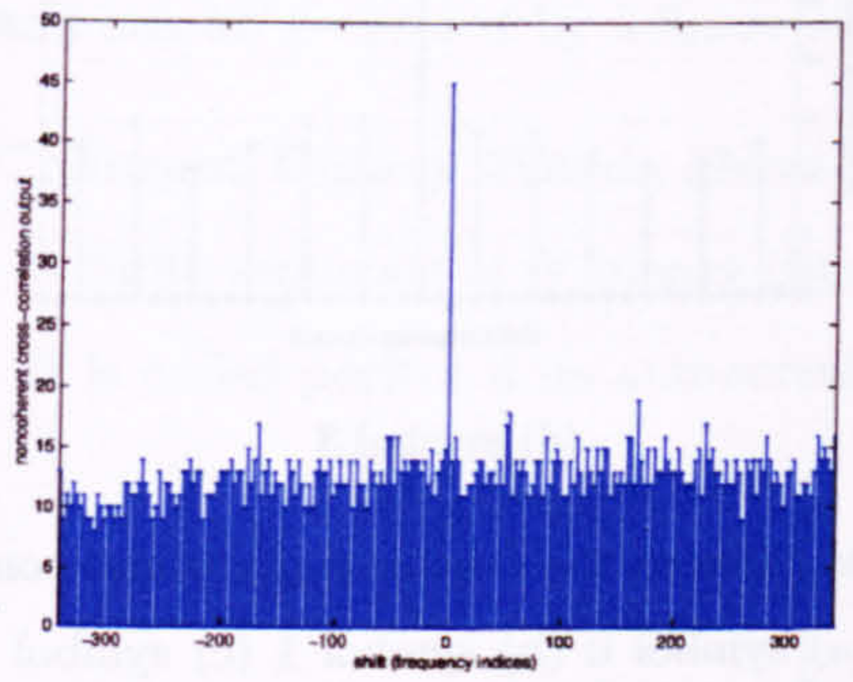

(a) symbol 0

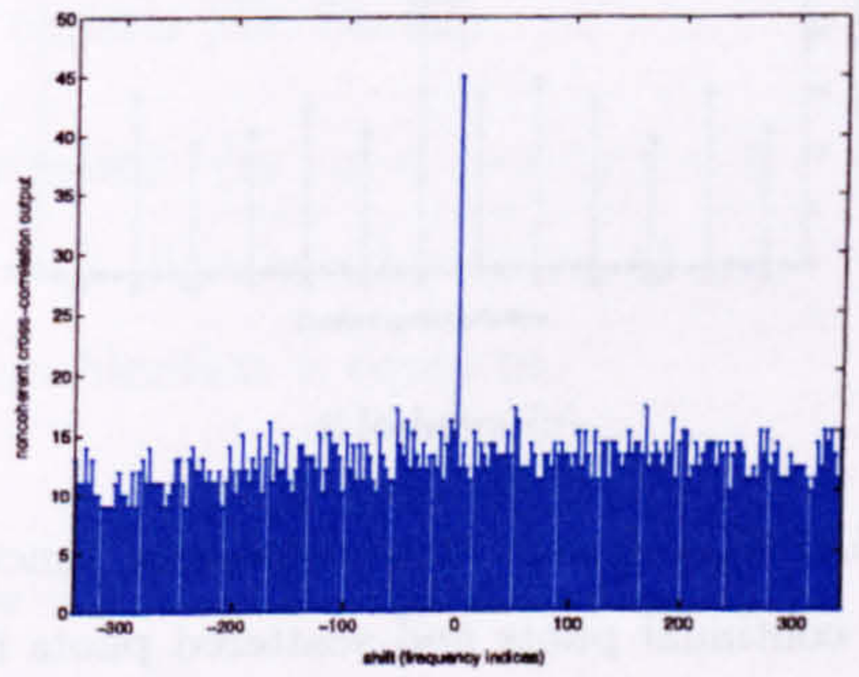

(b) symbol 1

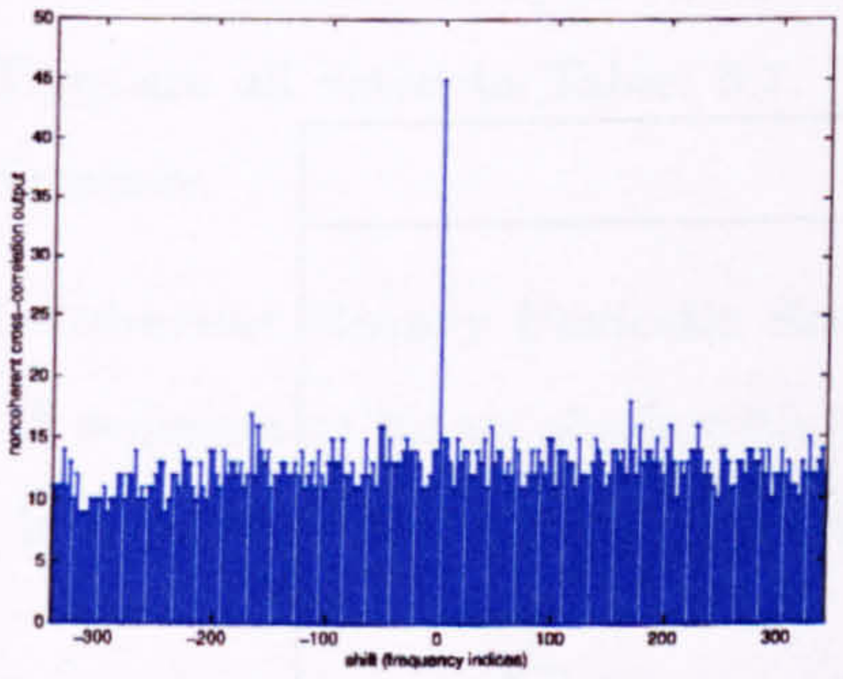

(c) symbol 2

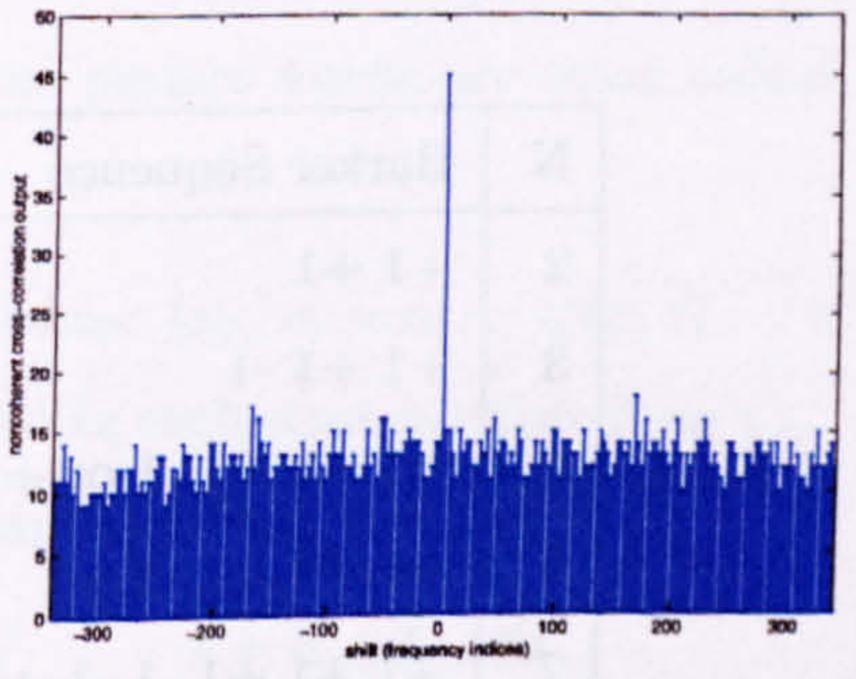

(d) symbol 3

Figure 5.5: Noncoherent cross-correlation function for (a)symbol 0 (b)symbol 1 (c)symbol 2 and (d) symbol 3

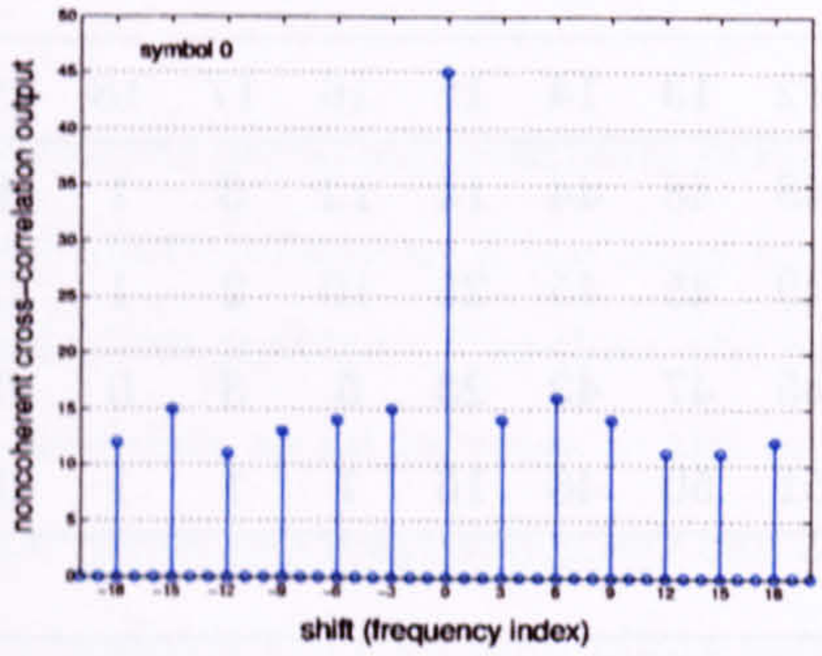

(a) symbol 0

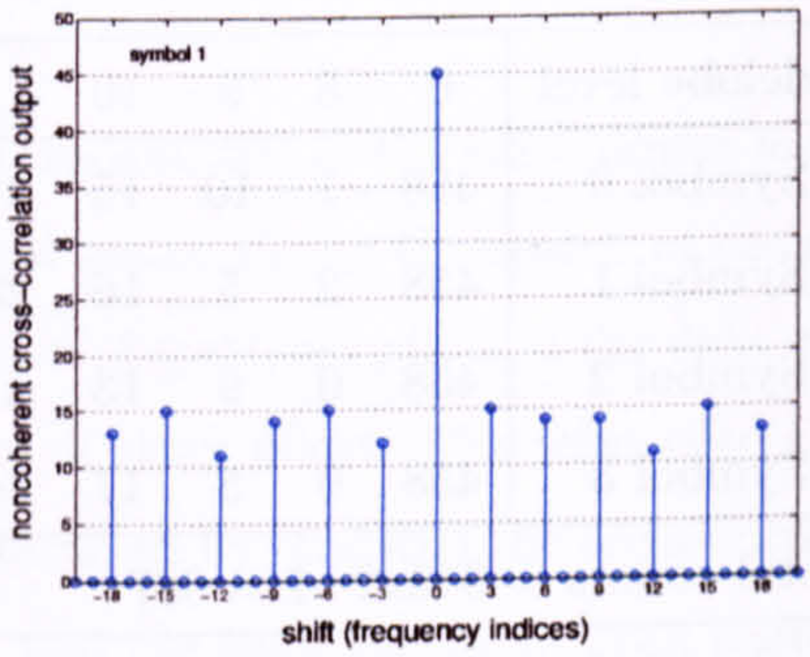

(b) symbol 1

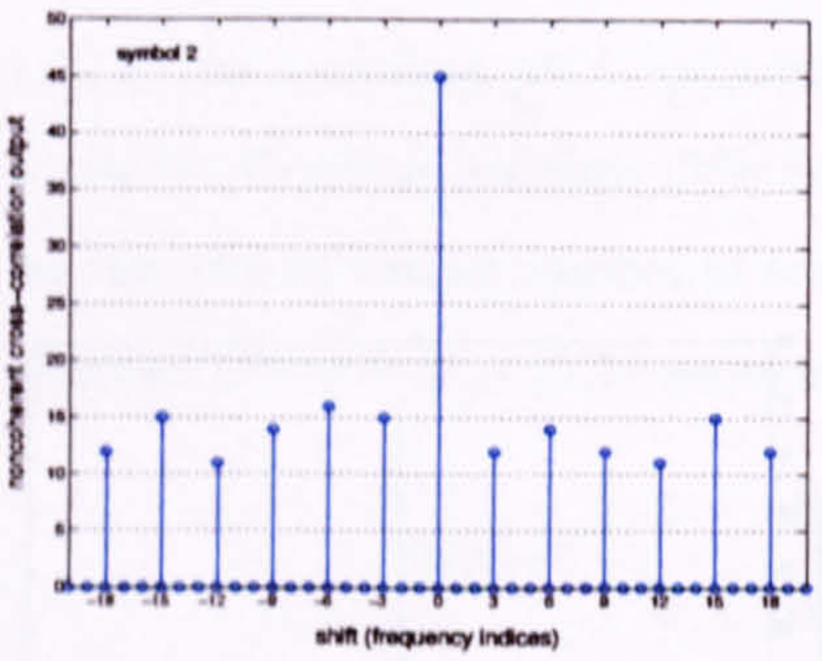

(c) symbol 2

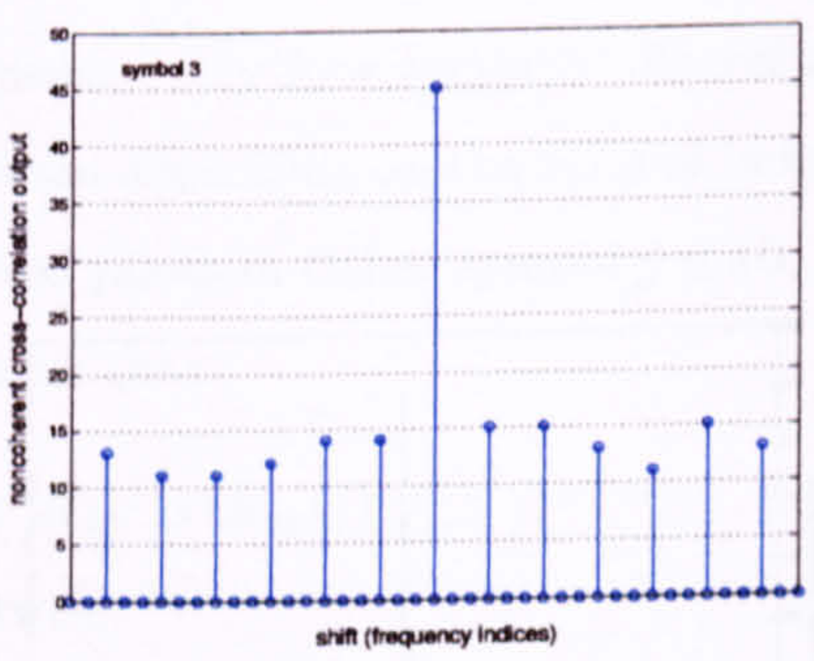

(d) symbol 3

Figure 5.6: Noncoherent cross-correlation functions between the continual pilots and combinations of continual pilots and scattered pilots in (a) symbol 0 (b) symbol 1 (c) symbol 2 and (d)symbol 3 (shift = -20,-19, . . . ,20)

N	Barker Sequence
2	+1 +1
3	+1 +1 -1
4	+1 +1 +1 -1 or +1 +1 -1 +1
5	+1 +1 +1 -1 +1
7	+1 +1 +1 -1 -1 +1 -1
11	+1 +1 +1 -1 -1 -1 +1 -1 -1 +1 -1
13	+1 +1 +1 +1 +1 -1 -1 +1 +1 -1 +1 -1 +1

Table 5.7: Binary Barker sequences with length equal to 2,3,4,5,7,11 and 13

5.5 Binary Sequences

Binary sequences with good autocorrelation properties have found applications in radar, sonar and digital communications. Following the definitions given in [78], binary sequences can be classified into four classes:

- **Coherent Binary Periodic Sequences:** $\{a_i : a_i = a_{i+L} \in (-1, 1)\ ,\ i \in \mathbb{Z}\}$

  - A sequence of binary digits with period L; each digit is either +1 or -1.

  - It is called perfect if its autocorrelation function is equal to

$$\mathcal{R}(k) = \sum_{n=1}^{L} a_n a_{n+k} = \begin{cases} L & k = 0, \pm L, \pm 2L, \cdots \\ -1 & \text{otherwise} \end{cases} \tag{5.7}$$

  Sequences with the period $L = 2^n - 1$, $n \in \mathbb{Z}^+$ are called maximal length sequences and can be generated by a linear shift register [32, 78, 82].

- **Coherent Binary Words (Non-periodic):** $\{a_i : a_i \in (-1, 1), i = 1, \cdots, N\}$

  - A finite sequence of N binary digits; each digit is either -1 or +1.

  - It is called perfect if its autocorrelation function is equal to

$$\mathcal{R}(k) = \sum_{n=1}^{N-k} a_n a_{n+k} = \begin{cases} N & k = 0 \\ 0 \text{ or } \pm 1 & k = 1, 2, \cdots, N-1 \\ 0 & k \geq N \end{cases} \tag{5.8}$$

  Perfect coherent binary words are only known for N=1, 2, 3, 4, 5, 7, 11 and 13. They are all listed in Table. 5.7. These perfect words are often called *Barker Sequence.*

- **Incoherent Binary Periodic Sequences:** $\{a_i : a_i = a_{i+L} \in (0, 1)\ ,\ i \in \mathbb{Z}\}$

  - A sequence of binary digits with period L; each digit is either 0 or +1.

  - It is called perfect if its autocorrelation function is equal to

$$\mathcal{R}(k) = \sum_{n=1}^{L} a_n a_{n+k} = \begin{cases} V & k = 0, \pm L, \pm 2L, \cdots \\ 1 & \text{otherwise} \end{cases} \tag{5.9}$$

  where V is the number of +1 digits per period.

Such sequences exist for $L = p^{2n} + p^n + 1$, where p is a prime number. For a given period L, the maximum number of ones are limited to $V = p^n + 1$. For

example, each codeword of optical orthogonal codes (OOC) [10] belongs to this class of sequences.

- **Incoherent Binary Words (Non-periodic):** $\{a_i : a_i \in (0,1)\ ,\ i = 1, 2, \cdots, N\}$
  - A finite sequence of N binary digits; each digit is either 0 or +1.
  - The number of +1 digits is equal to V.
  - It is called perfect if its autocorrelation function is equal to

$$\mathcal{R}(k) = \sum_{n=1}^{N-k} a_n a_{n+k} = \begin{cases} V & k = 0 \\ 0 \text{ or } \pm 1 & \text{otherwise} \end{cases} \tag{5.10}$$

  where V is the total number +1 digits.

The pilots pattern can be viewed as a non-periodic binary sequence consisting of bits equal to either zero or one. An incoherent binary word can be used as the pattern to assign pilot carriers in an OFDM symbol. For optimum performance, the pattern should be a perfect word in order to minimize the effects of the sidelobes. Examples of generating perfect incoherent binary words can be found in [46, 78, 85], which are based on the theory of perfect difference sets [1, 28, 78] or least residues modulo a prime number [85]. Alternatively, the sequences can also be generated by punctuating optical orthogonal codes [10] or perfect incoherent binary periodic sequences.

A sequence is represented by a series of numbers that define the positions with one in the sequence. For example, a sequence $\{1010010001\ldots\}$ is represented by $\{0, 2, 5, 9, \ldots\}$. When the sequence is used as the pilots pattern, pilots are assigned at the positions with one. We have generated twelve perfect {0,1}-binary incoherent words. They are listed in Table 5.8 in the increasing order of the sequence length. The off-peak autocorrelation outputs of all these sequences are either 0 or 1. At first, we generate twelve periodic sequences using the procedures outlined in [78] that is based on the theory of finite projective planes [78, 97]. The sequences are then truncated to a shorter length. The first six sequences are truncated in such a way that all of them start at 0 and stop at 51. Therefore, these sequences can be used as the pilots pattern for the standard IEEE 802.11a and Hiperlan/2. On the other hand, the last element in the remaining six sequences has to be less than 1705 so that they can be used in the DVB-T 2k system.

Length	p	n	Positions with Ones									
3	3	3	0	8	51							
4	2	4	0	14	23	51						
8	3	2	0	10	13	24	25	29	31	51		
9	2	3	0	16	17	28	36	42	46	49	51	
9	2	3	0	2	5	9	15	23	34	35	51	
9	3	2	0	4	12	14	17	35	36	42	51	
35	7	2	7	2	0	10	15	47	128	190	341	342
			462	487	562	585	598	715	761	810	876	945
			967	1061	1099	1117	1126	1138	1209	1321	1418	1517
			1559	1619	1626	1683	1699					
36	7	2	0	50	102	125	244	284	398	427	436	539
			637	716	736	810	851	882	943	959	973	1008
			1019	1021	1026	1029	1063	1179	1250	1267	1289	1378
			1384	1429	1502	1514	1529	1698				
37	7	2	0	17	19	139	149	178	199	214	227	284
			293	324	380	461	484	487	491	535	618	634
			707	727	739	830	855	863	897	932	1116	1228
			1229	1281	1287	1292	1509	1610	1692			
40	7	2	0	3	24	53	69	95	107	134	170	171
			193	201	365	374	408	486	490	616	668	673
			719	752	796	893	941	954	982	1001	1050	1120
			1138	1193	1200	1210	1225	1352	1354	1410	1573	1688
40	7	2	0	90	114	130	151	159	182	195	248	327
			359	361	381	436	439	469	487	586	642	659
			701	702	729	803	822	885	894	1031	1134	1169
			1180	1218	1265	1304	1387	1562	1568	1572	1666	1691
41	7	2	0	10	56	59	82	97	98	159	216	224
			230	248	252	261	315	368	452	580	597	599
			649	693	766	824	888	928	939	1009	1034	1064
			1069	1241	1319	1331	1352	1399	1513	1542	1618	1625
			1652									

Table 5.8: Perfect binary incoherent words with elements defined over Galois field $GF(p^n)$

5.6 Robustness Improvement

We have shown that the performance of the non-coherent coarse frequency estimator can be increased by using a better pilots pattern. In this section, we will discuss an enhancement of the coarse frequency estimator by employing the technique of one-sided trimming to remove the effect of strong tonal interference, and an error detection method by exploiting the data after coherent demodulation. If the receiver knows that the output of the estimator is incorrect, it can either determine the parameters again using the enhanced method, or discard the current data and ask for retransmission. As a result, the robustness of the system can be improved.

5.6.1 One-sided Trimmed Sum

Recall that the coarse frequency estimator is the summation of instantaneous power of a set of carriers. Therefore, it would be very sensitive to strong tonal interferences that would bring up the outputs of the estimator at incorrect positions leading to wrong synchronization.

If the frequencies of interferences are static and known to the system, the jammed carriers can be switched off for transmission in an OFDM system. However, the number and the power of interferers are usually unknown in practical applications. In addition, dynamic allocation of pilot carriers is not applicable because there is still frequency ambiguity before the frequency offset has been estimated and it will increase the complexity of the receiver. The robustness of the estimator can be improved by one-side trimming to reduce the effect of outliers.

Let the observed power $u_1, u_2, \cdots, u_{44}, u_{45}$ be ordered as follows

$$u_{(1)} < u_{(2)} < \cdots < u_{(44)} < u_{(45)} \tag{5.11}$$

where $u_{(1)}$ is the smallest and $u_{(45)}$ is the largest. Again, we assume that there are total 45 pilots as defined in the DVB-T standard. The sum trimmed at λ is defined by

$$U^{(\lambda)} \equiv u_{(1)} + u_{(2)} + \cdots + u_{(45-\lambda)} \tag{5.12}$$

For example, when trimming level λ is 3, the three largest observations, $u_{(45)}$,$u_{(44)}$ and $u_{(43)}$, are discarded.

Interferers with power much less than the nominal value have a small contribution to the final summation output and hence have little effect on the performance of the estimator. Therefore, one-side trimming, and not the conventional two-side trimming, is recommended [105]. Monte Carol simulations have been carried out to study the effect of trimming and determine the optimal level of trimming by exploiting the distance criterion.

In particular, we measure the distance between the following two cases

$$\begin{aligned} H_1 : U^{(0)} &= \sum^{45} (\text{pilots only}) \\ H_0 : U^{(0)} &= \sum^{9} (\text{pilots}) + \sum^{n_i} (\text{interferers}) + \sum^{36-n_i} (\text{data carriers}) \end{aligned}$$

In case H_0, we arbitrary assume that the contaminated data has 9 stray pilots and $n_i = 1, 2, \cdots, 6$ interferers. The total number of carriers in either case is identical and equal to 45. As in DVB-T 2k mode, the transmission power of the pilot carriers is boosted at a ratio of 1.78. On the other hand, all interferers are assumed to have identical power which is 3 dB larger than those of the pilot carriers. The observed subcarriers are arranged in ascending order of power and the largest λ observations are discarded to form the one-side trimmed sum $U^{(\lambda)}$. The Rayleigh fading channel model is assumed.

Following the definition in Section 3.4.1, the distance $\mathcal{D}(\lambda)$ can be determined by

$$\mathcal{D}(\lambda) = \frac{E[U^{(\lambda)}|H_1] - E[U^{(\lambda)}|H_0]}{\sqrt{var[U^{(\lambda)}|H_1]} + \sqrt{var[U^{(\lambda)}|H_0]}} \tag{5.13}$$

The simulation results are plotted in Figure 5.7. As shown, the distance is bounded by the composition of H_0. The distance achieves the largest value when there is only one interferer and decreases with the number of interferers. While moderate trimming increases the distance, it reaches a plateau and the maximum is rather flat. The range of flatness increases with the number of interferers. Any value of λ between 3 and 8 can be used in this particular example.

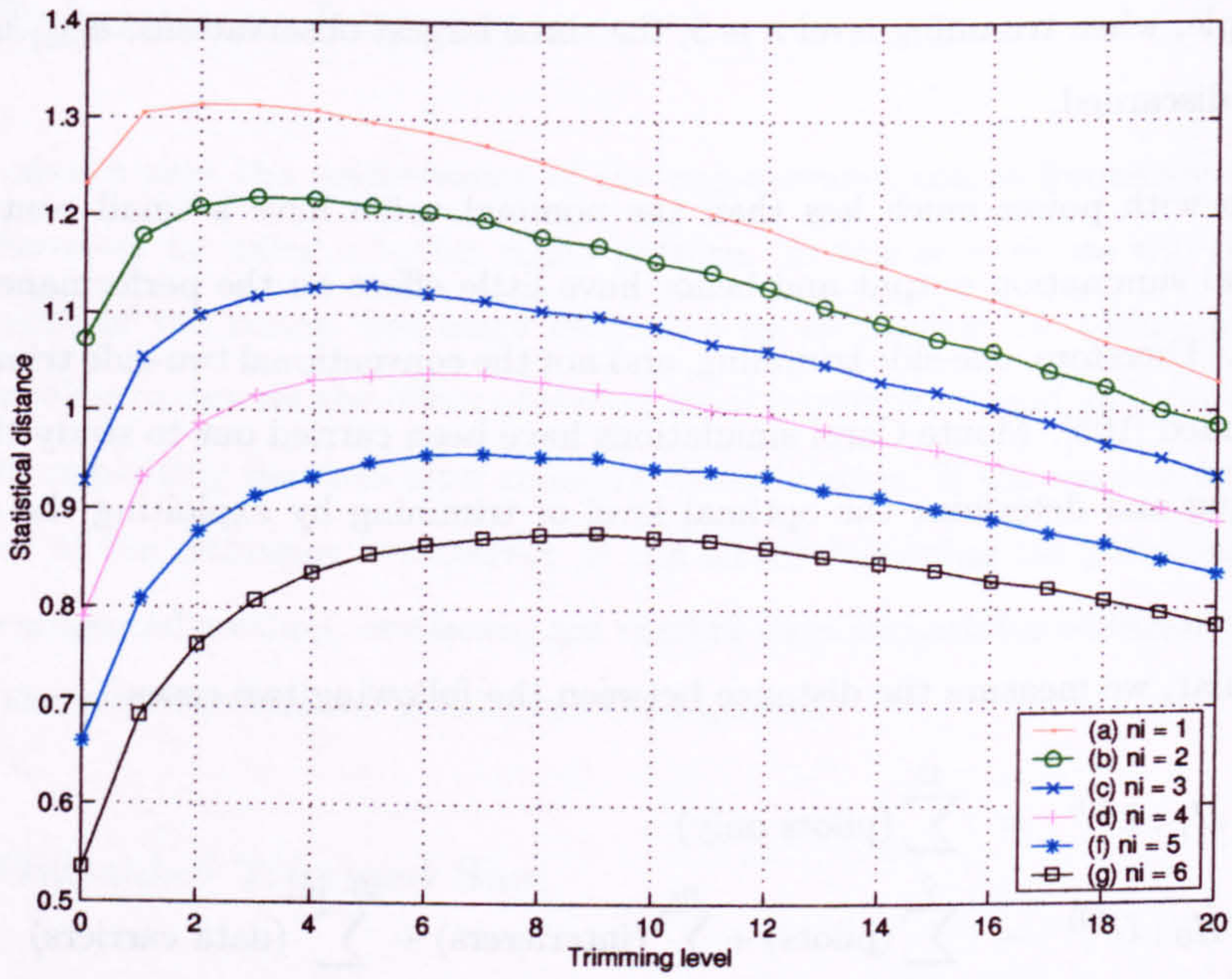

Figure 5.7: Effects of one-sided trimming on the statistics distance; there are 9 pilots, n_i inferes and $36 - n_i$ data carriers; total 45 carriers.

5.6.2 Error Detection (Coherent Demodulation)

In the tracking phase, the receiver has corrected the effects due to the propagation channel and synchronization defects. Therefore, the data transmitted through each carrier can be recovered by coherent demodulation. We can determine the coarse frequency offset again by exploiting the data recovered from the pilot carriers and compare the new result with the one determined in the acquisition phase. An error is detected if they are different.

Pilot carriers are usually modulated with values generated by a fixed sequence which is known to the receiver. For example, the continual pilots in DVB-T system are modulated with values generated by a pseudo-random binary sequence (PRBS), whose generator polynomial is $X^{11} \oplus X^2 \oplus 1$ as shown schematically in Figure 5.8.

Suppose there are total N carriers per OFDM symbol in which L carriers are pilots and the pilots are modulated with values generated by a pseudo-random sequence $g(n)$. The sequence $g(n)$ should be chosen so that its aperiodic autocorrelation function $\mathcal{R}_{gg}(a)$

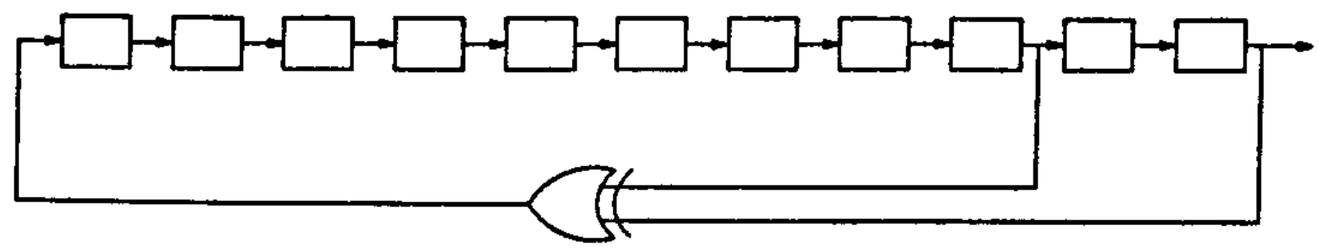

Figure 5.8: Structure of a linear feedback shift register that generate data to modulate pilot carriers in DVB-T 2k mode; all flip-flops are initially set to one and a new value is generated on every used carrier whether it is a pilot or not.

has only one dominant peak at zero shift and very small sidelobes elsewhere. That is

$$\left|\mathcal{R}_{gg}(a)\right| = \left|\sum_{n=0}^{L-a-1} g(n+a)g^*(n)\right| \tag{5.14}$$

$$= \begin{cases} L & a=0 \\ \ll L & \text{otherwise} \end{cases} \tag{5.15}$$

Let $\mathcal{K} = \{k_0{=}0, k_1, k_2, \ldots, k_{L-1}\}$ be the pilots pattern and $\hat{m}$ be the number of shifts in intercarrier spacing due to the coarse frequency offset. Then, the shifted pilot carriers can be found at subcarriers with frequency indices $k \in \{\mathcal{K} + \hat{m}\}$.

Define $\mathcal{R}_{pg}(m)$ as the sum of the products of the recovered data $p(k)$ at the k-th subcarrier and the sequence $g(n)$. That is

$$\mathcal{R}_{pg}(m) = \sum_{n=0}^{L-1} p(k_n + m)g^*(n) \tag{5.16}$$

where $k_n \in \mathcal{K}$ and $m = 0, 1, \ldots, (N-1-k_{L-1})$.

The recovered data $p(k)$ can be modelled as discrete zero-mean random variables and are uniformly distributed among the constellation points defined by the corresponding modulation scheme. Theoretically, if $p(k) = c(k)$, then $\mathcal{R}_{pg}(m) = \mathcal{R}_{gg}(m)$. In general, $|\mathcal{R}_{pg}(m)|$ will achieve a maximum value at $m = \hat{m}$ where $p(k_n + \hat{m})$ and $g(n)$ are closely matched. The starting position of the shifted pilots pattern can be determined by locating the peak of the $\mathcal{R}_{pg}$.

We have verified this statement by computer simulations. Two sequences $g_1(n)$ and $g_2(n)$ with length equal to 45 and 13 respectively are used. The elements in sequence $g_1(n)$ are those used to modulate the continual pilots in DVB-T 2k mode and $g_2(n)$ is a Barker sequence with 13 elements as given in Table. 5.7. The aperiodic autocorrelation

functions of $g_1(n)$ and $g_2(n)$ are shown in Figure 5.9. The data $p(n)$ are assumed to be complex random variables with values defined by the constellation points of various modulation schemes including QPSK,16-QAM and 64-QAM. Two special cases have been also tested in which the data are either zero-mean complex Gaussian random variables or constant amplitude random variables with phases uniformly distributed in the range $[-\pi, \pi]$. In all the cases, the average power of $p(n)$ is normalized so that $E[p \cdot p^*] = 1$.

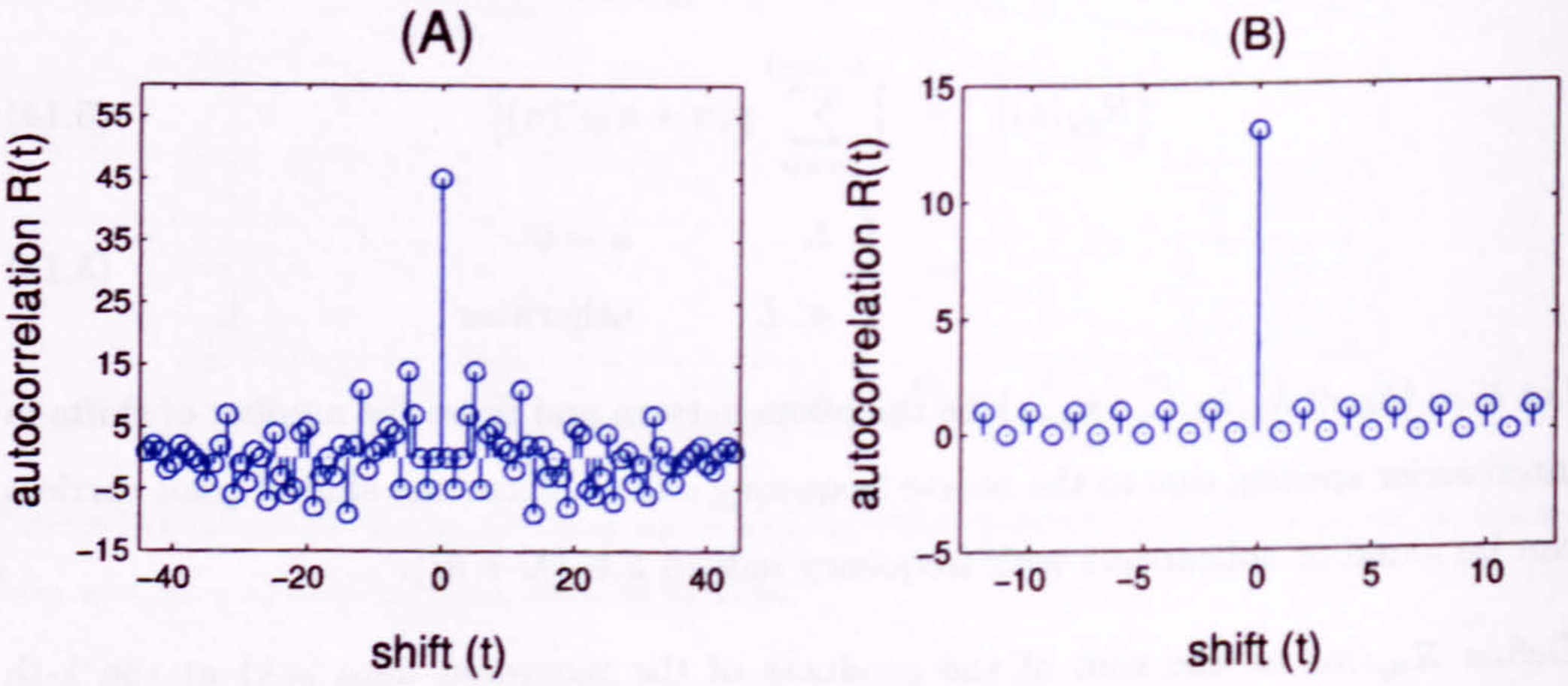

Figure 5.9: Autocorrelation function of (A) $g_1(n)$, sequence to modulate continual pilots in DVB-2k mode and (B) $g_2(n)$, 13-element Baker sequence.

Define the test statistic $U(i,p)$ as

$$U(i,p) = \left| \sum_{n=0}^{L_i-1} p(n) g_i(n) \right| \tag{5.17}$$

where $i = 1, 2$ and L_i is the length of $g_i(n)$. The mean and variance of $U(i,p)$ have been determined and they are given in Table 5.9. The histograms of the distributions of $U(i,p)$ are plotted in Figure 5.10 and Figure 5.11. Total 10^6 trials are used for each case.

The statistical distance $\mathcal{D}(i,p)$, where $i = 1$ or 2, is defined as

$$\mathcal{D}(i,p) \equiv \frac{E[U(i,g_i)] - E[U(i,p)]}{\sqrt{\text{var}[U(i,g_i)]} + \sqrt{\text{var}[U(i,p)]}} \tag{5.18}$$

where $\Big(E[U(1,g_1)], \text{var}[U(1,g_1)]\Big)$ and $\Big(E[U(2,g_2)], \text{var}[U(2,g_2)]\Big)$ are equal to (45,0) and (13,0), respectively.

p(n)	$g_1(n)$ = continual pilots (2k mode)			$g_2(n)$ = Barker sequence (13 elements)		
	E[U(1,p)]	var[U(1,p)]	$\mathcal{D}(1,p)$	E[U(2,p)]	var[U(2,p)]	$\mathcal{D}(2,p)$
$g(n)$	45	0	0	13	0	0
QPSK	5.96	9.54	12.64	3.21	2.65	6.01
16-QAM	5.94	9.62	12.59	3.20	2.73	5.93
64-QAM	5.95	9.61	12.60	3.21	2.73	5.93
Gaussian	5.93	9.65	12.58	3.20	2.78	5.88
uniform phase	5.95	9.56	12.63	3.21	2.69	5.97

Table 5.9: Mean E[U(i,p)] ,variance var[U(i,p)] and distance $\mathcal{D}(i,p)$ of U for different types of $p(n)$, where i=1 or i=2

If $p(n)$ is equal to $g(n)$, the distribution of $U(i,p)$ will be a straight line at the right margin of each graphs in Figure 5.10 and Figure 5.11. As seen, the distributions of all $U(i,p)$ are "far way" from the right margins. The observation agrees with the large distance values as shown in Table. 5.9. In addition, this scheme is also robust to the modulation sequence $g(n)$ and the actual payload data because all distributions have similar profile irrespective to the difference in these two parameters.

Therefore, the test statistic U can differentiate pilots from data and noise easily. In fact, no error has been detected in the simulations. It follows that the position of the shifted pilots can be determined easily by locating the maximum of the cross-correlation between the known sequence $g(n)$ and the recovered data. Then the coarse frequency offset is given by the amount of shifts of the pilots pattern.

In acquisition mode, this algorithm can be used to verify the coarse frequency offset obtained by other methods. An out-of-sync is detected if the receiver is operating in tracking mode and the current estimate $\tilde{m}$ is different from the one obtained before the synchronization errors have been corrected. The receiver may have to abort the tracking mode and restart the whole process of synchronization again.

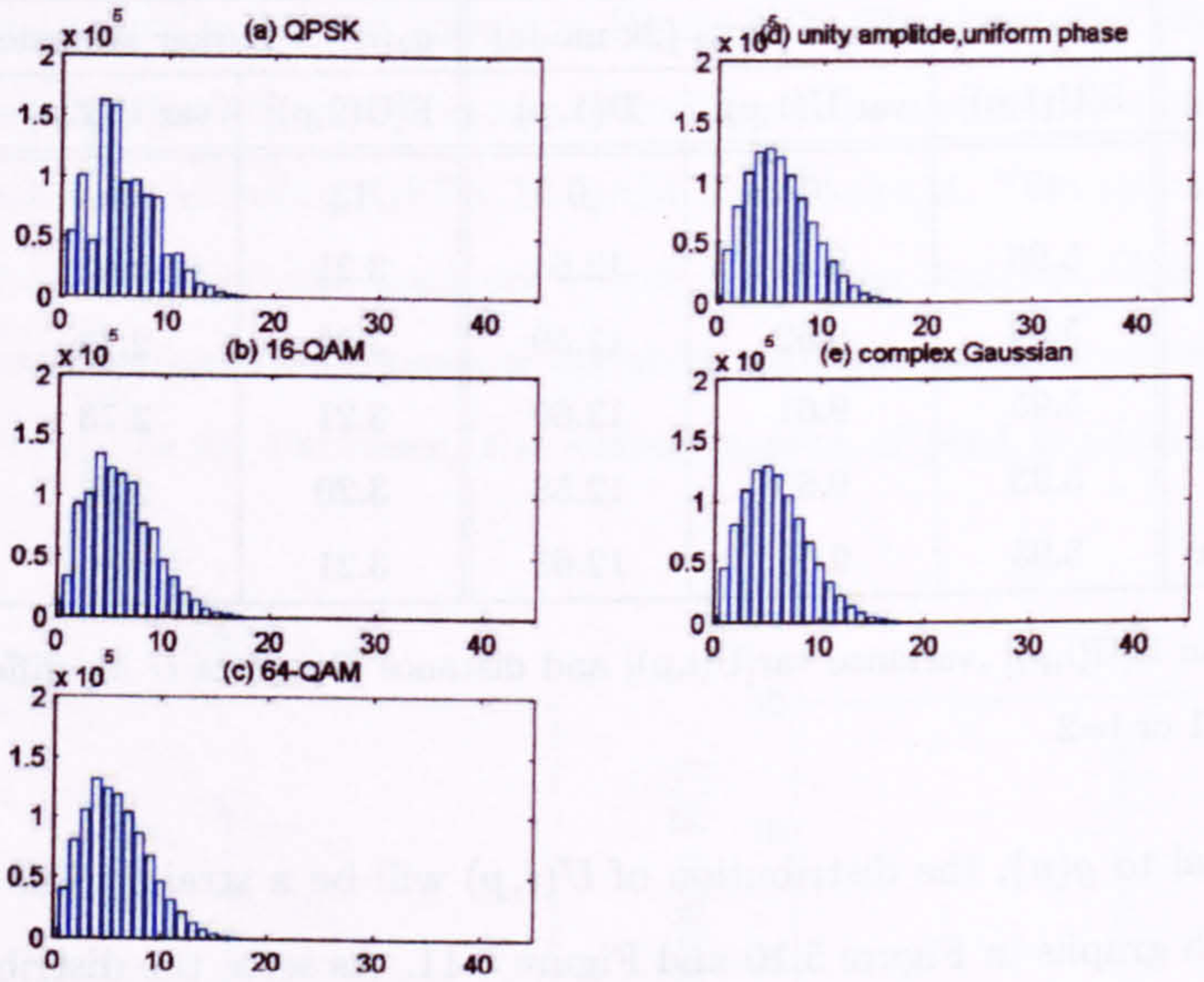

Figure 5.10: Histogram of the distribution of $U(1, g_1)$, where $g_1(n)$ is equal to the values used to modulate continual pilots in DVB-T 2k mode. The x-axis is the output of the estimator $U(1, g_1)$ and y-axis is the corresponding counts. (10^6 runs in each case)

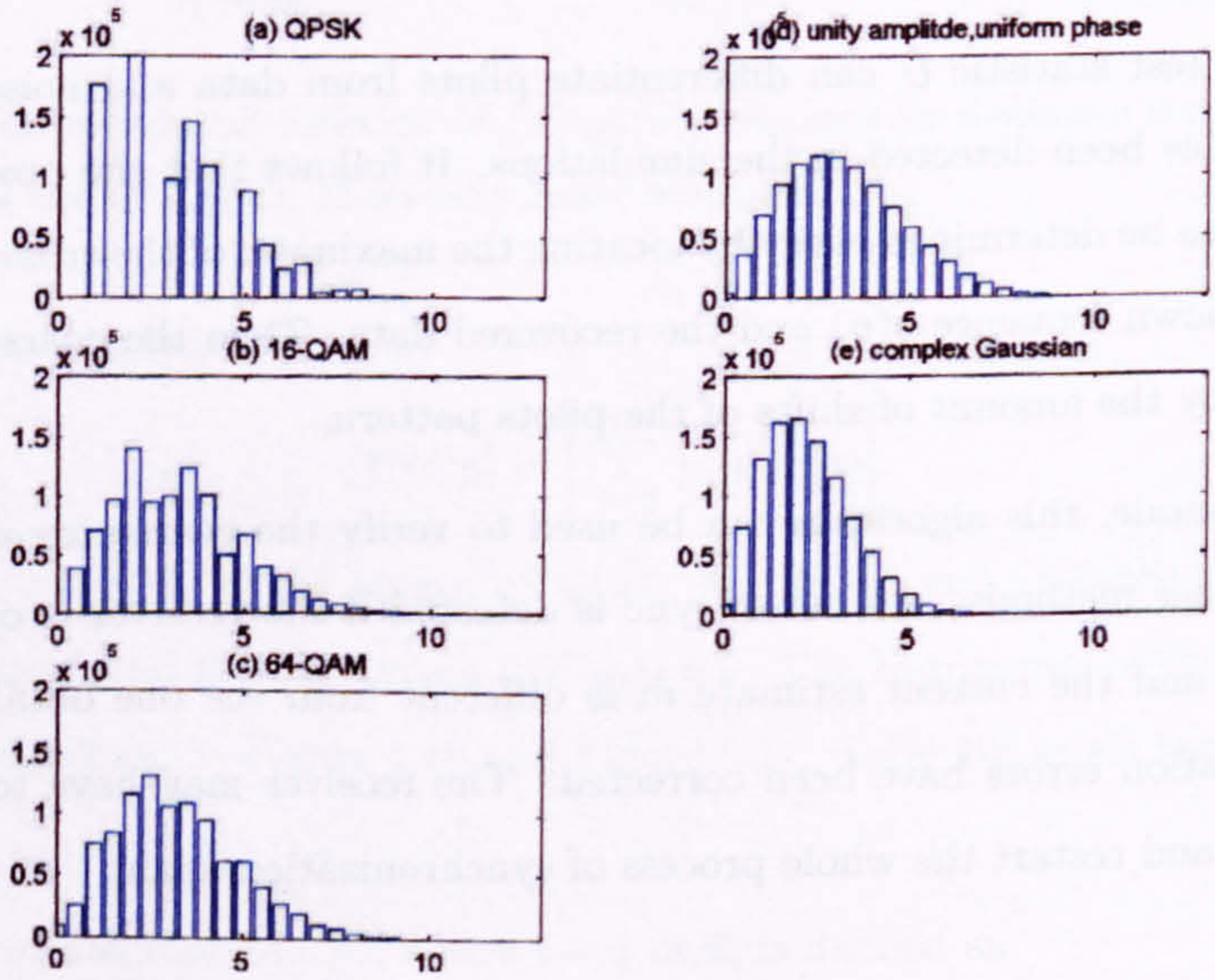

Figure 5.11: Histogram of the distribution of $U(2, g_2)$, where $g_2(n)$ is generated from the 13-element Baker sequence. The x-axis is the output of the estimator $U(2, g_2)$ and y-axis is the corresponding counts. (10^6 runs in each case)

5.7 Simulations and Results

In the previous sections, we have stated that the original continual pilots pattern in the DVB-T standard is not well-designed for the non-coherent estimation of the coarse frequency offset with reference to the received pilots power. In this section, we will verify this by simulations in a multipath environment. The performance of the original continual pilots pattern is compared with the longest binary sequence given in Table 5.8. Apart from the positions of the continual pilots, the system models in both cases are identical and are equal to those specified for the DVB-T 2k-mode standard [25] in order to have a fair comparison.

The performance is simulated in a static Rayleigh channel and a Ricean channel that are defined in the DVB-T standard document [25]. The received signal is given by

$$r(t) = \frac{\rho_0 \cdot s(t) + \sum_{i=1}^{20} \rho_i \cdot e^{-j2\pi\theta_i} s(t-\tau_i)}{\sqrt{\sum_{i=0}^{20} \rho_i^2}} \tag{5.19}$$

where r(t) and s(t) are the output and the input signals respectively. The parameters ρ_i, τ_i and θ_i are the attenuation, relative delay and the phase shift from scattering of the i-th path respectively. The numerical values of these parameters are listed in Table 5.10. In the simulations, a 10 dB Ricean factor [1] and the QPSK modulation scheme are assumed. The first term ρ_0 represents the attenuation of the direct line-of-sight path and is given by

$$\rho_0 = \begin{cases} 0 & \text{Rayleigh channel} \\ \sqrt{10 \sum_{i=1}^{20} \rho_i^2} & \text{Ricean channel} \end{cases} \tag{5.20}$$

Figure 5.12 illustrates the effects of the pilots pattern in the performance of the proposed pilots-power-detection coarse frequency estimator. Here, a simplified OFDM symbol structure is assumed in which only the subcarriers defined in the pilots pattern are transmitted in boosted power and the scattered pilots are replaced with data

[1] The Ricean factor is the ratio of the power of the direct path to the reflected paths.

subcarriers. This simplified model allows us to compare the intrinsic properties of the continual pilots pattern only and avoids any complication in the results due to the scattered pilots. As verified with the simulation results shown in Figure 5.12, the original pilots pattern defined in the DVB-T standard [25] has poorer performance.

In DVB-T system, not only the continual pilots are transmitted in boosted power, but also the scattered pilots. There are four different ways to assigned the scattered pilots in the DVB-T system, namely symbol 0, symbol 1, symbol 2 and symbol 3. The joint effects of the continual pilots and the scattered pilots are illustrated in Figure 5.13 and Figure 5.14. The positions of the scattered pilots are assigned as in the symbol 1.

We can see that the inclusion of the scattered pilots increases the error rate. This is because the additional scattered pilots will increase the sidelobes level. In addition, the new pilots pattern is not always better than the original one. The performance of the simplified system using the original pilots pattern is now better than the "complete" system using the new pilots pattern. Here, we named a system as "complete" if scattered pilots are used in every OFDM symbols as in the DVB-T standard. In other words, the scattered pilots degrade the performance of the new pilots pattern. This suggest that more future works have to be done to design the pilots pattern jointly with the scattered pilots in order to further increase the performance of the coarse frequency offset estimator.

However, if we limit our scope of comparison in the DVB-T system only, the new pilots pattern is always better than the original pilots pattern as shown in Figure 5.15 and Figure 5.16. In conclusion, the original continual pilots pattern in the DVB-T standard is not well-designed for the non-coherent estimation of the coarse frequency offset with reference to the received pilots power.

i	ρ_i	$\tau_i[\mu s]$	θ_i[rad]	i	ρ_i	$\tau_i[\mu s]$	θ_i
1	0.057662	1.003019	4.855121	11	0.295723	0.429948	5.928383
2	0.176809	5.422019	3.419109	12	0.350825	3.228872	3.053023
3	0.407163	0.518650	5.864470	13	0.262909	0.848831	0.628578
4	0.303585	2.751772	2.215894	14	0.225894	0.073883	2.128544
5	0.258782	0.602895	3.758058	15	0.170996	0.203952	1.099463
6	0.061831	1.016585	5.430202	16	0.149723	0.194207	3.462951
7	0.150340	0.143556	3.952093	17	0.240140	0.924450	3.664773
8	0.051534	0.153832	1.093586	18	0.116587	1.381320	2.833799
9	0.185074	3.324866	5.775198	19	0.221155	0.640512	3.334290
10	0.400967	1.935570	0.154459	20	0.259730	1.368671	0.393889

Table 5.10: Attenuation(ρ_i), phase(θ_i) and delay values (τ_i) of the i-th path for the simulation of the multipath fading channels in the DVB-T system [25]

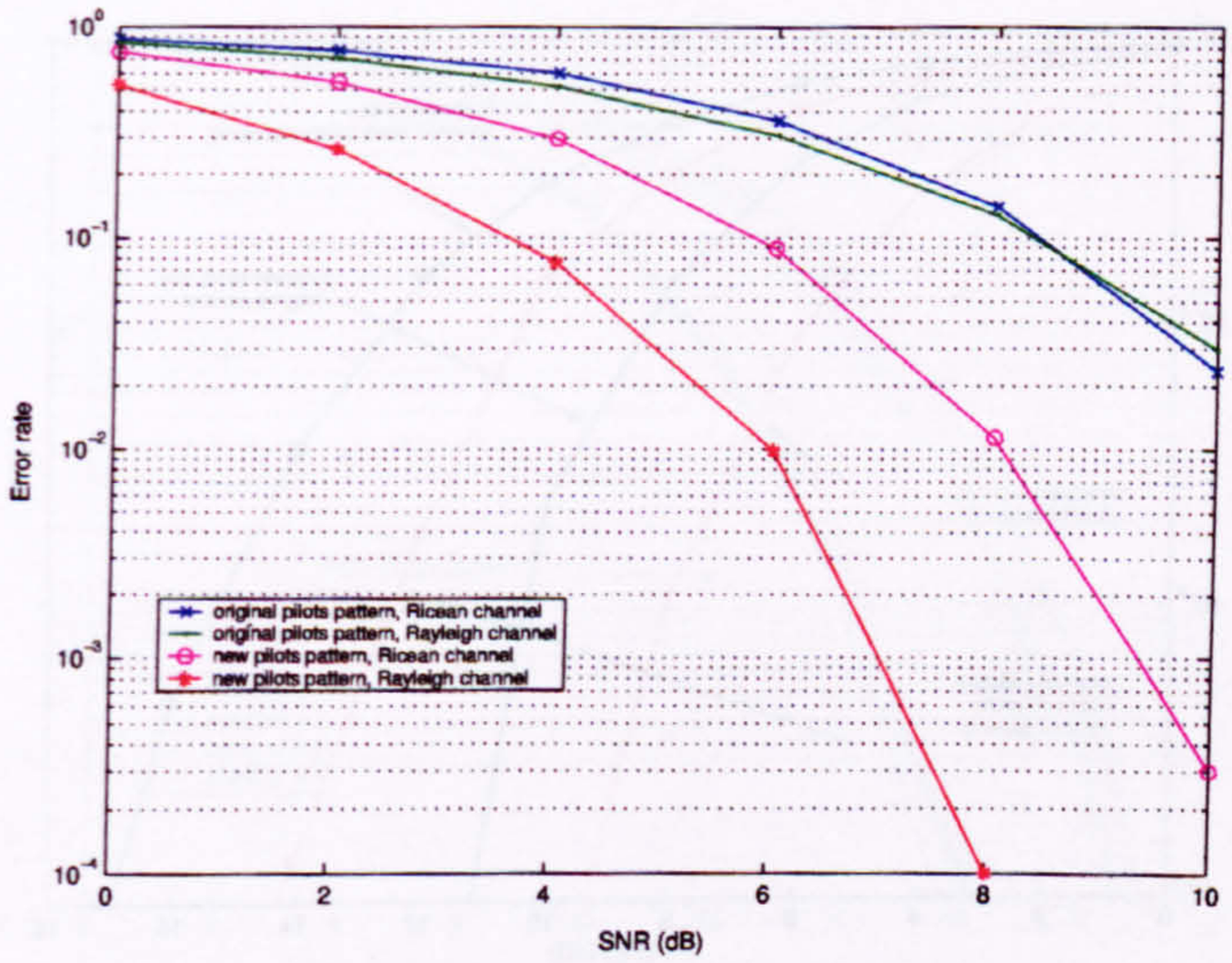

Figure 5.12: Effects of the pilots pattern in the performance of the proposed pilots-power-detection coarse frequency estimator in the DVB-T 2k system

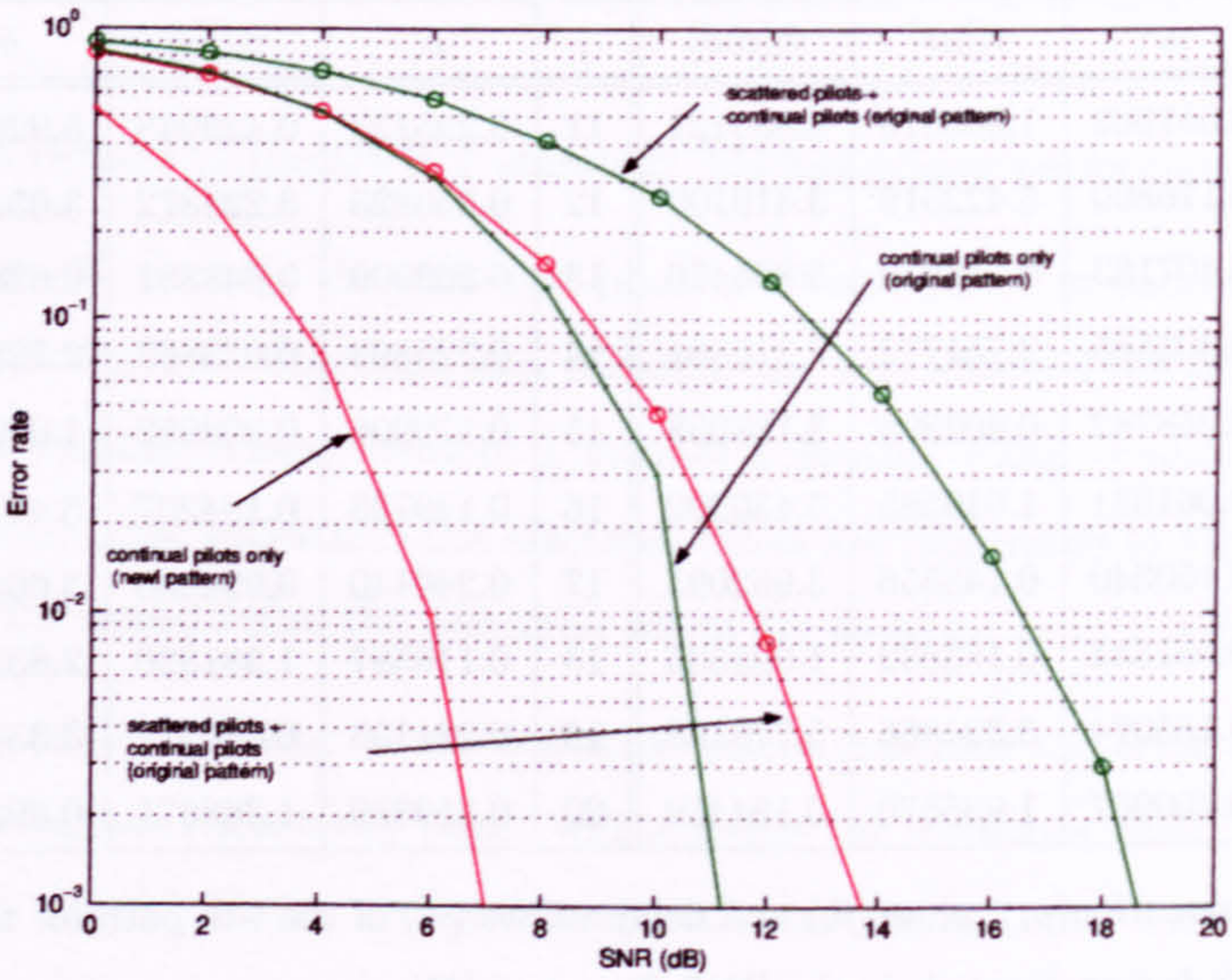

Figure 5.13: Effects of the scattered pilots to the continual pilots pattern in the Rayleigh fading channel with AWGN

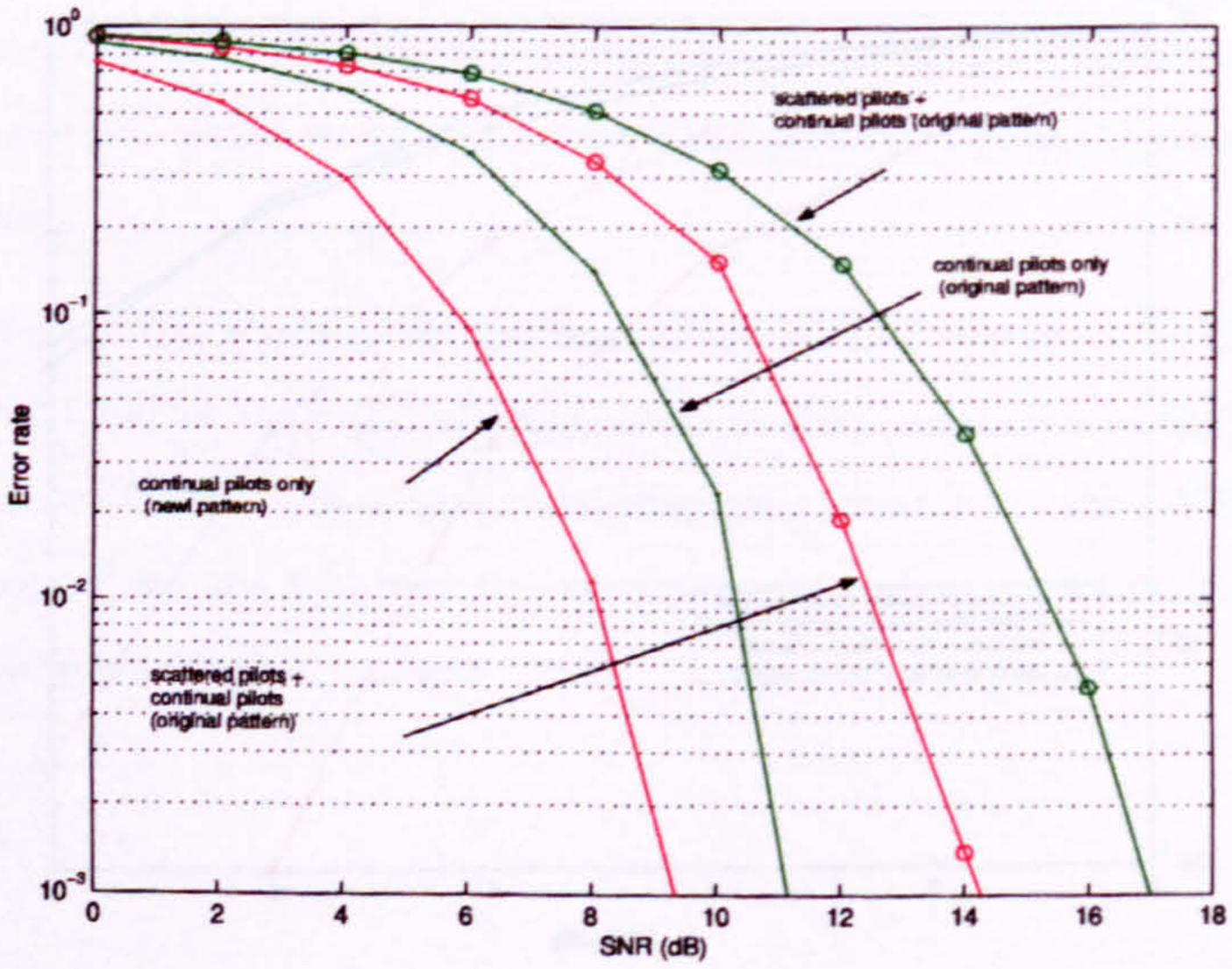

Figure 5.14: Effects of the scattered pilots to the continual pilots pattern in the Ricean fading channel with AWGN

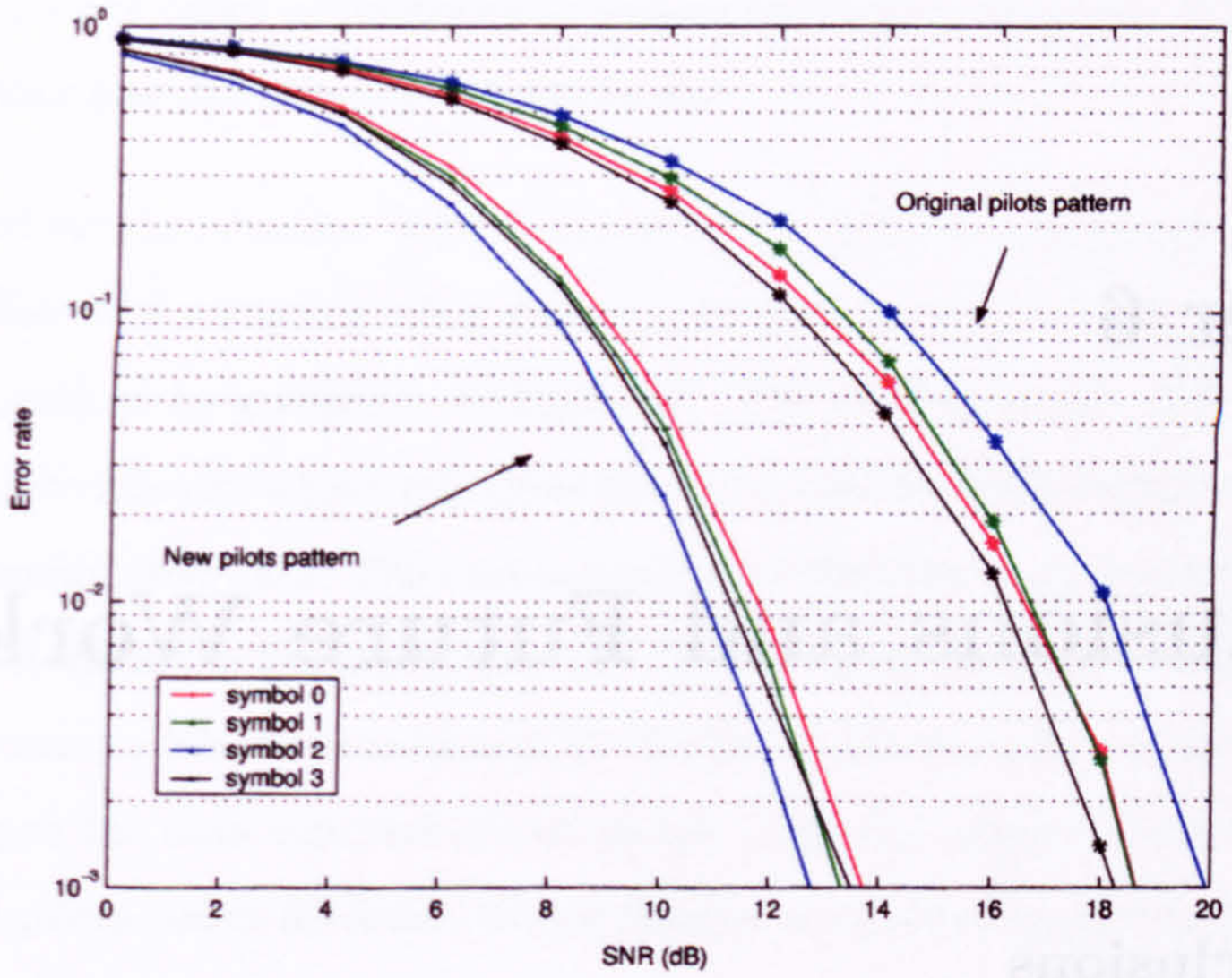

Figure 5.15: Comparison of the performance of the new pilots pattern and the original pilots pattern of the DVB-T 2k system in Rayleigh fading channel

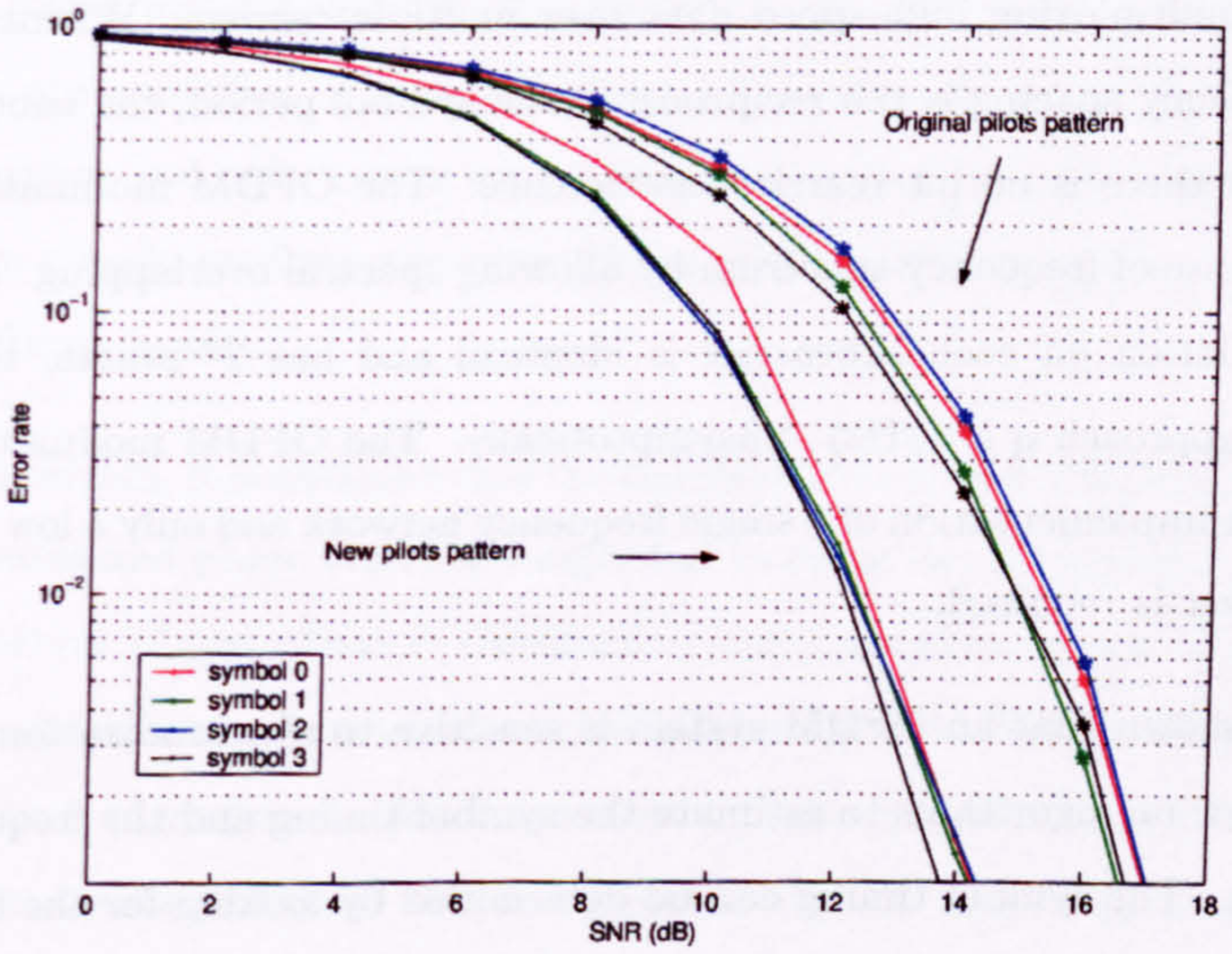

Figure 5.16: Comparison of the performance of the new pilots pattern and the original pilots pattern of the DVB-T 2k system in Ricean fading channel

Chapter 6

Conclusions and Future Works

6.1 Conclusions

The general principles and properties of the OFDM modulation scheme have been discussed. Comparing with the single carrier systems, the symbol rate in OFDM systems is reduced by multiplexing high-speed data over multiple carriers. Whenever the intercarrier frequency spacing is the reciprocal of the symbol period, the subcarriers are orthogonal and there is no intercarrier interference. The OFDM modulation scheme allows efficient use of frequency spectrum by allowing spectral overlapping. If the modulation constellation on each subcarrier is identical and has 2^q points, the spectral efficiency will approach q $bit(s\text{Hz})^{-1}$ asymptotically. The OFDM modulation scheme also enables the implementation of a single frequency network and only a low complexity channel equalizer is required.

We have also shown that an OFDM system is sensitive to synchronization defects. A literature review on algorithms to estimate the symbol timing and the frequency offset has been given. The symbol timing can be determined by looking for the known data structures within the received time-domain signal. The symbol timing estimation algorithms have been discussed in groups with reference to these known data structures including the null symbol, cyclic prefix and training symbols. Similarly, we have categorized the frequency offset estimation algorithms into groups according to the data

sources which include the repeated training symbols, cyclic prefix and virtual subcarriers. The frequency offset estimators can also be classified into either data-aided/blind or time-domain based/frequency-domain based.

The effects of synchronization defects including the symbol timing error, phase offset, frequency offset and sampling clock errors have been studied analytically and the results are supported by computer simulations. The symbol timing error will lead to intersymbol interference, which will affect the performance of the estimators that make use of the demodulated data. The coarse frequency offset does not cause intercarrier interference, but shifts the frequency spectrum of the signal. In addition, we have shown that the intercarrier interference caused by the fine frequency offset decreases the noise margin between the data subcarriers and pilots. This will degrade the performance of the proposed pilots-power-detection coarse frequency offset estimator under very noisy conditions.

Two coarse frequency synchronization algorithms have been proposed. Both of these algorithms are frequency-domain based and some of the subcarriers are required to be assigned as pilots without carrying the payload data. However, different properties of the pilots are exploited in each algorithm. The first algorithm ignores the phase of the subcarriers and only makes use of their instantaneous power, while the second one exploits a pseudo-random sequence differentially modulated across subcarriers in a two-symbol frame header.

In the first algorithm, it is assumed that the effects of fading have not been corrected and hence magnitude and phase errors are expected to occur at all frequencies. Therefore, phase modulation of the pilots is disregarded and only their power is exploited for non-coherent detection. A maximum likelihood estimator for the coarse frequency offset estimation is proposed. We have shown that the test statistic is simply the sum of instantaneous power of subcarriers taken from a shifted pilots pattern, and hence we name it as the 'pilots-power-detection' algorithm in the context. A statistical distance is defined with respect to the two conditional probability density functions of which the selected subcarriers are either all pilots, or a combination of pilots and data subcarriers. It corresponds to the geometric distance between the conditional means

when the conditional standard deviations are used as the units of length. With the help of this statistical distance, we have shown that the performance of the proposed estimator increases with the total number of pilots and the boosted power ratio, and decreases with the sidelobes level of the autocorrelation function of the pilots pattern. As a rule of thumb, the total number of pilots should be more than ten.

We have shown using computer simulations that the performance of the proposed pilots-power-detection algorithm is better than that of the maximum correlation methods and the guard-band power detection algorithm in a highly frequency selective fading channel. On the other hand, the complexity of the proposed algorithm is similar to that of the guard-band power detection algorithm while the maximum correlation algorithm has the highest complexity. The major drawback of the proposed algorithm is a possible degradation of the system throughput because pilots subcarriers are not used for data transmission. However, if boosted pilots have already been used as in the DVB-T system, the application of the algorithm has no effect on the data throughput.

Secondly, a low-complexity coarse frequency offset estimator for a frame-based OFDM system has been proposed. The coarse frequency offset is determined by locating the maximum of the cross-correlation between the known pilots sequence and the recovered data. The data is recovered by taking differential demodulation on pairs of subcarriers between the two adjacent symbols in a two-symbol frame header. A new frame header has been proposed. Compared with the conventional frame header, there is an additional guard interval between the useful parts of the two symbols. Supported with computer simulations in two-path fading channels, the proposed algorithm is robust against the selection of the pseudo-random sequence used to generate the frame header and the performance of the new estimator is similar to those used in the conventional system. With the expenses of minor reduction in the data throughput and slightly increase in the system response time, the additional guard interval improves the performance of the coarse frequency estimator. Since all OFDM symbols have identical structure now, the complexity in hardware implementation is reduced. Another major reduction in the complexity is due to the introduction of the mapping function which convert the phase difference from a real number into a two-level integer, either 1 or -1. Then the correlation can be carried out using a combination of exclusive-nor logic gates

and a simple binary adder without the needs of complex multiplier and accumulator. Finally, an architecture for the implementation of the estimator in hardware has been proposed.

A case study in the DVB-T system reviews that the frequency indices of the existing pilots pattern have a common factor 3 leading to many sidelobes in the autocorrelation function of the pilots pattern. We have shown that by replacing the existing pilots pattern in the DVB-T 2k system with a sequence having better autocorrelation properties, the performance of the proposed pilots-power-detection algorithm can be increased. Total 12 perfect binary {0,1} incoherent words based on the finite projective plain geometry are generated. Half of them can be used as the pilots pattern in the Hiperlan/2 while the other six longer sequences can be used for the DVB-T 2k system. Since DVB-T is in operation now, it is unlikely that the current standard will be changed. However, the proposed schemes can be used as a reference for any new designs that use similar OFDM parameters. On the other hand, we have also shown that the robustness of the system can be improved by using one-sided trimming to remove strong tonal interference and an algorithm to verify the correctness of the coarse frequency offset estimator after all synchronization errors have been corrected.

6.2 Future Works

It has been shown that the number of pilot carriers should be greater than ten. This may limit the use of the proposed pilots-power-detection algorithm in the OFDM systems that have a small total number of subcarriers. Although the pilots are usually modulated with a pseudo-random sequence, this information has not been used in the proposed pilots-power-detection algorithm. Therefore, the estimator could be modified to incorporate both the instantaneous power and the phase of the pilots subcarriers. Thereafter, it may be possible to reduce the required number of pilots and increase the overall estimation accuracy.

Both the guard-band power detection algorithm and the proposed pilots-power detection algorithm work on the sum of the instantaneous power of the received subcarriers.

An ad-hoc estimator could be constructed by sliding a searching window in the frequency spectrum so that the sum of instantaneous power from one set of subcarriers (guard-band) reaches a minimum while the corresponding sum taken from the other set (pilots pattern) reaches the maximum. More research work has to be done to obtain an optimum fusion rule in combining the test statistics from these two different estimation algorithms.

It has been suggested in [17, 30, 57, 99] that using multiple frames of received data can refine the carrier offset. Similarly, the error rate of the proposed estimators may be reduced by averaging the test statistics over multiple frames. More work can be done to determine the optimum number of frames in various conditions.

In the proposed pilots-power-detection algorithm, the spacing between pilots should be all different so that the maximum sidelobe level of the autocorrelation of the pilots pattern will be limited to one. However, it has been proposed in [94] that the pilots subcarriers should be equally spaced if they are used for channel estimation in a frequency-selective time-invariant channel. There is a conflict and hence more future work could be carried out to determine the optimum pilots placing scheme, and the corresponding joint algorithm to estimate both the propagation channel and the coarse frequency offset simultaneously.

On the other hand, the performance of the low-complexity estimator that exploits the phases of the pilots has only been studied using computer simulations. More research work on the theoretical analysis about the characteristics of the quantizer, which converts the phase difference from a real number to a two-level integer, could be done in the future.

Although we have only concentrated in the synchronization problems of the OFDM systems, some future works could also be done to analysis the performance degradation due to the non-linearity of mixers and determine the techniques to minimize the effects. Throughout the discussions, it is assumed that the transmission model is linear and the effects of nonlinear distortion have been ignored. However, in practical implementation, an OFDM system may suffer from nonlinear distortion due to the nonlinearly of components such as power amplifiers and frequency mixers. Although some researchers

have named the component "mixer" in the literatures, their studies are limited to the clipping distortion due to the high peak-to-average power ratio of OFDM at the output power amplifier only. In principle, a mixer is a nonlinear device and generates harmonics of the input signal. In single carrier system, these out-of-band harmonics can be easily removed by filtering with careful selection of the mixing frequency. However, an OFDM signal has a wider bandwidth and it is difficult to ensure wide-band impedance matching between mixers and the following stages of a pre-amplifier. The reflected signal will mixed up again with the input signal causing intermodulation distortion. Since OFDM is a multicarrier system in which difference in frequency between any two carriers is an integer multiple of the subcarrier spacing, the harmonics generated by intermodulation at the mixer will coincide with the original spectrum and cannot be removed by simple filtering. Thus, more future works could be done to develop techniques to minimize these effects.

Appendix A

A.1 Proof of Equation (2.3)

Given that the captured samples $\{r(n) : n \in [-N_g \ldots N_u - 1]\}$ of an OFDM symbol have the following characteristics:

- free from ISI: $\{r(-\tau_{gd}+1), r(-\tau_{gd}+2), \ldots, r(N_u-1)\}$
- corrupted by ISI: $\{r(-\tau_s), r(-\tau_s+1), \ldots, r(-\tau_{gd})\}$

and

$$c(k) = \sum_{n=0}^{N_u-1} r(n) e^{-j\frac{2\pi kn}{N_u}} \tag{A.1}$$

Recall that $\tau_{gd} \equiv N_g - \tau_d + 1$ and τ_s is the offset from the optimum position of the starting position of the data window at position C (Fig. 2.1). Then the fourier transform of the samples taken from the data window is given by

$$\begin{aligned}
& \sum_{n=0}^{N_u-1} r(n-\tau_s) e^{-j\frac{2\pi kn}{N_u}} \\
= & \sum_{n=-\tau_s}^{N_u-\tau_s-1} r(n) e^{-j\frac{2\pi k}{N_u}(n+\tau_s)} \\
= & e^{-j\frac{2\pi k\tau_s}{N_u}} \left\{ \sum_{n=-\tau_s}^{-\tau_{gd}} r(n) e^{-j\frac{2\pi kn}{N_u}} + \sum_{-\tau_{gd}+1}^{N_u-\tau_s-1} r(n) e^{-j\frac{2\pi kn}{N_u}} \right\} \\
= & e^{-j\frac{2\pi k\tau_s}{N_u}} \left\{ \sum_{n=N_u-\tau_s}^{N_u-\tau_{gd}} r(n) e^{-j\frac{2\pi kn}{N_u}} + \sum_{-\tau_{gd}+1}^{N_u-\tau_s-1} r(n) e^{-j\frac{2\pi kn}{N_u}} + \sum_{n=-\tau_s}^{-\tau_{gd}} r(n) e^{-j\frac{2\pi kn}{N_u}} - \sum_{n=N_u-\tau_s}^{N_u-\tau_{gd}} r(n) e^{-j\frac{2\pi kn}{N_u}} \right\} \\
= & e^{-j\frac{2\pi k\tau_s}{N_u}} \left\{ \sum_{n=-\tau_{gd}+1}^{N_u-\tau_{gd}} r(n) e^{-j\frac{2\pi kn}{N_u}} + \sum_{n=-\tau_s}^{-\tau_{gd}} r(n) e^{-j\frac{2\pi kn}{N_u}} - \sum_{n=-\tau_s}^{-\tau_{gd}} r(N_u+n) e^{-j\frac{2\pi kn}{N_u}} \right\}
\end{aligned} \tag{A.2}$$

Notice that by construction, $\forall\, n \in \{-\tau_{gd}+1,\ldots,-1\}, r(n) \equiv r(N_u+n)$ and these values are ISI free. Therefore

$$\begin{aligned}\sum_{n=-\tau_{gd}+1}^{-1} r(n)e^{-j\frac{2\pi kn}{N_u}} &= \sum_{n=-\tau_{gd}+1}^{-1} r(N_u+n)e^{-j\frac{2\pi kn}{N_u}} \\ &= \sum_{n=N_u-\tau_{gd}+1}^{N_u-1} r(n)e^{-j\frac{2\pi k}{N_u}(N_u+n)} \\ &= \sum_{n=N_u-\tau_{gd}+1}^{N_u-1} r(n)e^{-j\frac{2\pi kn}{N_u}}\end{aligned}$$

It follows that the first term in Equation A.2 is equal to

$$\begin{aligned}\sum_{n=-\tau_{gd}+1}^{N_u-\tau_{gd}} r(n)e^{-j\frac{2\pi kn}{N_u}} &= \sum_{n=0}^{N_u-\tau_{gd}} r(n)e^{-j\frac{2\pi kn}{N_u}} + \sum_{n=-\tau_{gd}+1}^{-1} r(n)e^{-j\frac{2\pi kn}{N_u}} \\ &= \sum_{n=0}^{N_u-\tau_{gd}} r(n)e^{-j\frac{2\pi kn}{N_u}} + \sum_{n=N_u-\tau_{gd}+1}^{N_u-1} r(n)e^{-j\frac{2\pi kn}{N_u}} \\ &= \sum_{n=0}^{N_u-1} r(n)e^{-j\frac{2\pi kn}{N_u}} \\ &= c(k) \qquad \text{(A.3)}\end{aligned}$$

Finally, we can get Equation 2.3 by substituting all these values into Equation A.2. That is

$$\sum_{n=0}^{N_u-1} r(n-\tau_s)e^{-j\frac{2\pi kn}{N_u}} = c(k)e^{-j\frac{2\pi k\tau_s}{N_u}} + \mathcal{N}_{\text{ISI}} \qquad \text{(A.4)}$$

where

$$\mathcal{N}_{\text{ISI}} = e^{-j\frac{2\pi k\tau_s}{N_u}} \sum_{n=-\tau_s}^{-(N_g-\tau_d+1)} \Big(r(n) - r(N_u+n)\Big)e^{-j\frac{2\pi kn}{N_u}} \qquad \text{(A.5)}$$

A.2 Proof of Equations (2.15) and (2.16)

From Equation 2.13 and Equation 2.14, we have

$$r(n) = \frac{e^{j\theta}}{N}\sum_{k=0}^{N-1} c_k H(k)\exp\left\{j\frac{2\pi(k+\delta)[n(1-\epsilon)]}{N}\right\} \qquad \text{(A.6)}$$

$$\tilde{c}(l) = \sum_{n=0}^{N-1} r(n)\exp\left\{-j\frac{2\pi ln}{N}\right\} \qquad \text{(A.7)}$$

Substitute Equation A.6 into Equation A.7,

$$\begin{aligned}\tilde{c}(l) &= \frac{e^{j\theta}}{N}\sum_{n=0}^{N-1}\sum_{k=0}^{N-1}c(k)H(k)\exp\left\{j\frac{2\pi(k+\delta)[n(1-\epsilon)]}{N}\right\}\exp\left\{-j\frac{2\pi ln}{N}\right\}\\ &= \frac{e^{j\theta}}{N}\sum_{k=0}^{N=0}c(k)H(k)\sum_{n=0}^{N-1}\exp\left\{j\frac{2\pi[(k+\delta)(1-\epsilon)-l]n}{N}\right\} \qquad \text{(A.8)}\end{aligned}$$

Notice that for a power series $\{1, e^{ja}, e^{j2a}, \ldots, e^{ja(N-1)}\}$, the summation is given by

$$\begin{aligned}\sum_{n=0}^{N-1}e^{jan} &= \frac{1-(e^{ja})^N}{1-e^{ja}}\\ &= \frac{e^{\frac{jaN}{2}}(e^{\frac{-jaN}{2}}-e^{\frac{jaN}{2}})}{e^{\frac{ja}{2}}(e^{\frac{-ja}{2}}-e^{\frac{ja}{2}})}\\ &= e^{\frac{ja}{2}(N-1)}\frac{\sin\frac{aN}{2}}{\sin\frac{a}{2}} \qquad \text{(A.9)}\end{aligned}$$

Putting

$$a = \frac{2\pi[(k+\delta)(1-\epsilon)-l]}{N} \qquad \text{(A.10)}$$

we have

$$\sum_{n=0}^{N-1}\exp\left\{j\frac{2\pi[(k+\delta)(1-\epsilon)-l]n}{N}\right\} = \exp\left\{j\frac{\pi[(k+\delta)(1-\epsilon)-l](N-1)}{N}\right\}\frac{\sin\pi[(k+\delta)(1-\epsilon)-l]}{\sin\left[\frac{\pi[(k+\delta)(1-\epsilon)-l]}{N}\right]} \qquad \text{(A.11)}$$

In addition, if $k = l$,

$$\begin{aligned}(k+\delta)(1-\epsilon)-l &= (l+\delta)(1-\delta)-l\\ &= l-\epsilon l+\delta-\delta\epsilon-l\\ &= \delta-\epsilon(l+\delta) \qquad \text{(A.12)}\end{aligned}$$

Finally, substitute Equation A.11 and Equation A.12 into Equation A.8 and rearrange the term $e^{j\theta}/N$, the received signal $c(l)$ at the l-th carrier can be represented by

$$\tilde{c}(l) = c(l)H(l)e^{j\theta}\exp\left\{j\frac{\pi[\delta-\epsilon(l+\delta)](N-1)}{N}\right\}\frac{\sin\pi[\delta-\epsilon(l+\delta)]}{N\sin\left[\frac{\pi[\delta-\epsilon(l+\delta)]}{N}\right]} + \mathrm{ICI}(l) \qquad \text{(A.13)}$$

where

$$\mathrm{ICI}(l) = \sum_{\substack{k=0\\k\neq l}}^{N-1}c(k)H(k)e^{j\theta}\exp\left\{j\frac{\pi[(k+\delta)(1-\epsilon)-l](N-1)}{N}\right\}\frac{\sin\pi[(k+\delta)(1-\epsilon)-l]}{N\sin\left[\frac{\pi[(k+\delta)(1-\epsilon)-l]}{N}\right]} \qquad \text{(A.14)}$$

A.3 Proof of Equation (2.21)

Given by Equation 2.15

$$\tilde{c}(l) = c(l)H(l)e^{j\theta}\exp\left\{j\frac{\pi[\delta-\epsilon(l+\delta)](N-1)}{N}\right\}\frac{\sin\pi[\delta-\epsilon(l+\delta)]}{N\sin\left[\frac{\pi[\delta-\epsilon(l+\delta)]}{N}\right]} + \mathrm{ICI}(l) \quad \text{(A.15)}$$

By L'Hôspital rule, if $a \in \mathbb{R}$,

$$\begin{aligned}\lim_{a\to 0}\frac{\sin(\pi a)}{N\sin(\frac{\pi a}{N})} &= \lim_{a\to 0}\frac{\pi\cos(\pi a)}{N\cdot\frac{\pi}{N}\cos(\frac{\pi a}{N})}\\ &= 1 \qquad \text{(A.16)}\end{aligned}$$

Putting $a = \delta - \epsilon(l+\delta)$, we have

$$\lim_{\substack{\delta\to 0\\ \epsilon\to 0}}\frac{\sin\pi[\delta-\epsilon(l+\delta)]}{N\sin\left[\frac{\pi[\delta-\epsilon(l+\delta)]}{N}\right]} = 1 \qquad \text{(A.17)}$$

In addition, the ICI term is zero if $\delta = 0$ and $\epsilon = 0$ from Equation 2.20; that is,

$$\mathrm{ICI}(l|\delta=0,\epsilon=0) = 0 \qquad \text{(A.18)}$$

Therefore

$$\begin{aligned}\tilde{c}(l|\delta{=}0,\epsilon{=}0) &\approx \lim_{\substack{\delta\to 0\\ \epsilon\to 0}}\tilde{c}(l)\\ &= c(l)H(l)e^{j\theta}\lim_{\substack{\delta\to 0\\ \epsilon\to 0}}\frac{\sin\pi[\delta-\epsilon(l+\delta)]}{N\sin\left[\frac{\pi[\delta-\epsilon(l+\delta)]}{N}\right]}\\ &= c(l)H(l)e^{j\theta} \qquad \text{(A.19)}\end{aligned}$$

Appendix B

B.1 Calculation of $E[u_k]$ and $var[u_k]$

Suppose x_k and y_k are independent zero-mean Gaussian random variables $\mathcal{N}(0, \frac{1}{2}\sigma_k^2)$. That is

$$E[x_k^2] = E[y_k^2] = \frac{1}{2}\sigma_k^2 \tag{B.1}$$

The even n-th moment $E[g^n]$ of a Gaussian random variable $g \sim \mathcal{N}(0, \sigma_g^2)$ is [79]:

$$E[g^n] = 1 \cdot 3 \cdot 5 \cdots (n-1)\sigma_g^n \tag{B.2}$$

Therefore

$$\begin{aligned} E[x_k^4] &= 3(\frac{1}{\sqrt{2}}\sigma_k)^4 \\ &= \frac{3}{4}\sigma_k^4 \end{aligned} \tag{B.3}$$

and

$$E[y_k^4] = \frac{3}{4}\sigma_k^4 \tag{B.4}$$

Let u_k be the sum of the square of x_k and y_k

$$u_k = x_k^2 + y_k^2 \tag{B.5}$$

B.1.1 Mean

$$\begin{aligned} E[u_k] &= E[x_k^2 + y_k^2] \\ &= E[x_k^2] + E[y_k^2] \qquad (\because x_k \text{ and } y_k \text{ are uncorrelated}) \\ &= \frac{1}{2}\sigma_k^2 + \frac{1}{2}\sigma_k^2 \\ &= \sigma_k^2 \end{aligned} \tag{B.6}$$

B.1.2 Variance

From Eq. B.2 and Eq. B.5

$$\begin{aligned} E[u_k^2] &= E[x_k^2 + y_k^2]^2 \\ &= E[x_k^4 + y_k^4 + 2x_k^2 y_k^2] \\ &= \frac{3}{4}\sigma_k^4 + \frac{3}{4}\sigma_k^4 + 2(\frac{1}{2}\sigma_k^2)(\frac{1}{2}\sigma_k^2) \\ &= 2\sigma_k^4 \end{aligned} \tag{B.7}$$

Therefore

$$\begin{aligned} var[u_k] &= E[u_k^2] - E^2[u_k] \\ &= 2\sigma_k^4 - \sigma_k^4 \\ &= \sigma_k^4 \end{aligned} \tag{B.8}$$

B.2 Calculation of E[u_{nk}] and var[u_{nk}]

Let $x_k \sim \mathcal{N}(0, \frac{1}{2}\sigma_k^2)$, $y_k \sim \mathcal{N}(0, \frac{1}{2}\sigma_k^2)$ and $n_k \sim \mathcal{N}(0, \frac{1}{2}\sigma_n^2)$, where $\mathcal{N}(\mu, \sigma^2)$ denotes Gaussian random variables with mean μ and variance σ^3. Define x_{nk}, y_{nk} and u_{nk} as follows

$$x_{nk} = x_k + n_k \tag{B.9}$$

$$y_{nk} = y_k + n_k \tag{B.10}$$

$$u_{nk} = x_{nk}^2 + y_{nk}^2 \tag{B.11}$$

Then

$$E[x_{nk}] = E[y_{nk}] = 0 \tag{B.12}$$

$$\begin{aligned} var[x_{nk}] &= var[x_k + n_k] \\ &= var[x_k] + var[n_k] \quad (\because x_k \text{ and } n_k \text{ are uncorrelated}) \\ &= \frac{1}{2}(\sigma_k^2 + \sigma_n^2) \end{aligned} \tag{B.13}$$

Therefore

$$\begin{aligned} E[x_{nk}^2] &= var[x_{nk}] - E[x_{nk}]^2 \\ &= \frac{1}{2}(\sigma_k^2 + \sigma_n^2) \end{aligned} \tag{B.14}$$

Similarly

$$E[y_{nk}^2] = \frac{1}{2}(\sigma_k^2 + \sigma_n^2) \tag{B.15}$$

Since x_{nk} is the sum of two independent Gaussian random variables, its distribution is also Gaussian [79]. From Eq. B.2 and Eq. B.14

$$\begin{aligned} E[x_{nk}^4] &= 3\left(\sqrt{var[x_{nk}]}\ \right)^4 \\ &= 3\left(\frac{1}{\sqrt{2}}(\sigma_k^2 + \sigma_n^2)^{1/2}\right)^4 \\ &= \frac{3}{4}\left(\sigma_k^2 + \sigma_n^2\right)^2 \end{aligned} \tag{B.16}$$

Similarly

$$E[y_{nk}^4] = \frac{3}{4}\left(\sigma_k^2 + \sigma_n^2\right)^2 \tag{B.17}$$

B.2.1 Mean

$$\begin{aligned} E[u_{nk}] &= E[x_{nk}^2 + y_{nk}^2] \\ &= E[x_{nk}^2] + E[y_{nk}^2] \qquad (\because x_{nk} \text{ and } y_{nk} \text{ are independent}) \\ &= \sigma_k^2 + \sigma_n^2 \end{aligned} \tag{B.18}$$

B.2.2 Variance

$$\begin{aligned} E[u_{nk}^2] &= E[x_{nk}^2 + y_{nk}^2]^2 \\ &= E[x_{nk}^4] + E[y_{nk}^4] + 2E[x_{nk}^2]E[y_{nk}^2] \\ &= \frac{3}{4}\left(\sigma_k^2 + \sigma_n^2\right)^2 + \frac{3}{4}\left(\sigma_k^2 + \sigma_n^2\right)^2 + 2\left(\frac{1}{2}(\sigma_k^2 + \sigma_n^2)\right)\left(\frac{1}{2}(\sigma_k^2 + \sigma_n^2)\right) \\ &= 2\left(\sigma_k^2 + \sigma_n^2\right)^2 \end{aligned} \tag{B.19}$$

Therefore, the variance of u_{nk} is

$$\begin{aligned} var[u_{nk}] &= E[u_{nk}^2] - E[u_{nk}]^2 \\ &= \left(\sigma_k^2 + \sigma_n^2\right)^2 \end{aligned} \tag{B.20}$$

Bibliography

[1] C. Argon, H.F. Ahmad, "Optimal Optical Orthogonal Code Design using Difference Sets and Projective Geometry", Optics Communications, Vol. 118, pp. 505-508, August 1995

[2] V. Barnett, T. Lewis, "Outliers in Statistical Data", 1994, 3rd Edition, John Wiley & Sons

[3] L.D. Baumert, "Cyclic Difference Sets", Lecture Notes in Mathematics, 182, Springer-Verlag, 1971

[4] S.Barbarossa, M.Pompili, G.B.Giannakis, "Channel-Independent Synchronization of Orthogonal Frequency Division Multiple Access Systems", IEEE Journal on Selected Areas in Communications, Vol. 20, No. 2, pp. 474-486, Feb. 2002

[5] J.J.Van de Beek, M. Sandell, P.O. Borjesson, "ML Estimation of Time and Frequency Offset in OFDM Systems", IEEE Trans. on Signal Processing, Vol. 45, No. 7, pp.1800-1805, July 1997

[6] J.J.Van de Beek, M. Sandell, M. Isaksson, P.O. Börjesson, "Low-Complex Frame Synchronization in OFDM Systems", In Proceedings of International Conference on Universal Personal Communication ICUCP'95, pp. 982-986, Tokyo, Japan, Nov. 1995

[7] J.J.van de Beek, O. Edfors, M. Sandell, S.K. Wilson, and P.O. Borjesson, "On Channel Estimation in OFDM systems", IEEE Vehicular Technology Conference VTC'95, Chicago, July 1995

[8] P.A. Bello, "Selective Fading Limitations of the Kathryn Modem and some System Design Considerations,", IEEE Trans. Commun., Vol. COM-13, pp. 320-333, Sept. 1965

[9] John A.C. Bingham, "Multicarrier Modulation for Data Transmission: An Idea Whose Time Has Come", IEEE Communications Magazine, pp. 5-14, May 1990

[10] C.M. Bird, A.D. Keedwell, "Design and Applications of Optical Orthogonal Codes - a Survey", Bulletin of the Institute of Combinatorics and its Applications, Vol. 11, pp. 21-44, 1994

[11] H. Bolcskei, "Blind Esitmation of Symbol Timing and Carrier Frequency Offset in Wireless OFDM systems", IEEE Transcations on Communications, Vol. 49, No. 6, pp. 988-999, June 2001

[12] Paul G.M De Bot, F. Daffara, "Digital Terrestrial Television Broadcasting", Philips Journal of Research, Vol. 50, No. 1/2, pp. 61-77, 1996

[13] L.J. Cimini, "Analysis and Simulation of A Digital Mobile Channel Using Orgthogonal Frequency Division Mulitplexing," IEEE Trans. Commun., Vol. COM-33, pp. 665-675, July 1985.

[14] Cost 207 Management Committe, "COST 207: Digital Land Mobile Radio Communications", Commission of the European Communities, Luxembourg, 1989

[15] Robert W. Chang, "Synthesis of Band-Limited Orthogonal Signals for Multichannel Data Transmission", The Bell System Technical Journal, pp. 1775-1796, Dec. 1966

[16] S. Chang, E.J. Powers, "A New Estimation Scheme for Frequency and Timing Offsets in OFDM systems", VTC 2000, pp. 1832-835

[17] B. Chen, H. Wang, "Maximum Likelihood Estimation of OFDM Carrier Frequency Offset", IEEE International Conference on Communications, Vol. 1, pp. 49-53, 2002

[18] Fan R.K. Chung, J.A. Salehi, V.K Wei, "Optical Orthogonal Codes: Design, Analysis, and Applications", IEEE Transcations on Information Theory, Vol. 35, No. 3, pp. 595-604, May 1989

[19] T.de Couasnon et al, "OFDM for Digital TV Broadcasting", Signal Processing, Vol. 39, pp.1-32, Sept. 1994

[20] F. Classen, H. Meyr, "Frequency Synchronization Algorithms for OFDM Systems Suitable for Communication over Frequency Selective Fading Channels", IEEE Vehicular Technology Conference VTC'94, pp. 1655-1659, 1994

[21] Radio Broadcasting Systems: Digital Audio Broadcasting (DAB) to mobile, portable and fixed receivers, ETSI-EN-300-401-V1.3.2 (2000-09)

[22] F. Daffara, O. Adami, "A New Frequency Detector for Orthogonal Multicarrier Transmission Techniques", Proc. VTC'95, Vol. 2, pp. 804-809, July 1995

[23] F. Daffara, A. Chouly, "Maximum Likelihood Frequency Detectors for Orthogonal Multicarrier System," in Proc. IEEE Int. Conf. Commum., pp. 766-771, 1993

[24] D. Dardari, V. Tralli, A. Vaccari, "A Theoretical Characterization of Nonlinear Distortion Effects in OFDM Systems", IEEE Transcations on Communications, Vol. 48, No. 10, pp. 1755-1763, Oct. 2000

[25] DVB Document A012, "Framing Structure, Channel Coding and Modulation for Digital Terrestrial Television"

[26] A. Eyadeh, P. Nobles, F. Halsall, T. Davies, "OFDM Fine Time Synchronization for Indoor Wirelcss Data Communications", IEE Colloquium (Digcst), Vol. 7, pp. 1-5, 1996

[27] O. Edfors, M. Sandell, J.J. van de Beek, S.K.Wilson and P.O.Borjesson, "OFDM Channel Estimation by Singular Value Decomposition", IEEE Trans. Commum., Vol .46, pp. 931-939, July 1998

[28] P. Fan, X.G. Xia, "Block Coded Modulation for the Reduction of the Peak-to-Average Power Ratio in OFDM Systems", IEEE Transcations on Consumer Electronics, Vol. 45, No. 4, pp. 1025-1029, Nov. 1999

[29] P. Fan, M. Darnell, "Sequence Design for Communications Applications", 1996, Research Studies Press Ltd.

[30] H. Ge, K. Wang, "Efficient Method for Carrier Offset Correction in OFDM System", ICASSP' 99, Vol. 5, pp. 2467-2470, March 1999

[31] D.A.G. Gillies, Y.J. Guo, S.K. Barton, "Synchronisation Techniques for HIPERLAN", Wireless Personal Communications, Vol. 4, No. 1, pp. 1-10, 1997

[32] Solomon W. Golomb, "Shift Register Sequences", Aegean Park Press, Revised Edition, 1982

[33] M. Grayson, M. Darnell, "Extended Analysis of Word Synchronization Using Sequence Correlation Techniques", IEE Proc. Commun., Vol. 142, No. 6, pp. 357-362, Dec. 1995

[34] M. Grayson, M. Darnell, "Synchronization Preamble Design: New Results", Electronics Letters, Vol. 26, No. 21, pp. 1775-1776, Oct. 1990

[35] J.A. Gansman, M.P. Fitz, J.V. Krogmeier, "Optimum and Suboptimum Frame Synchronization for Pilot-Symbol-Assisted Modulation", IEEE Transcations on Communications, Vol. 45, No. 10, pp. 1327-1337, Oct. 1997

[36] L. Hanzo, W. Webb, T. Keller, "Single- and Multi-carrier Quadrature Amplitude Modulation", 1st Edition, John Wiley & Sons, Ltd

[37] F.R. Hampel, "The Influence Curve and Its Role in Robust Estimation", Journal of the American Statistical Association, Vol. 69, Number 346, pp. 383-393, June 1974

[38] J.F. Hélard, "Time Synchronization Without Specific Symbols for OFDM", Electronics Letters, Vol. 35, No. 2, pp. 130-132, Jan. 1999

[39] M.H. Hsieh, C.H. Wei, "Channel Estimation for OFDM Systems Based On Comb-type Pilot Arrangement in Frequency Selective Fading Channels", IEEE Transcations on Consumer Electronics, Vol. 44, No. 1, pp. 217-225, Feb. 1998

[40] A.T. Huq, E. Panayirci and C.N. Georghiades,"Maximum Likelihood Carrier Frequency Offset Estimation in Orthogoanl Frequency Division Multiplexing (OFDM) System", Proc. Thirty-sixth Annual Allerton Conf. on Communication, Control and Computing, Sept. 23-25, 1998

[41] Y.L. Huang, C.R. Sheu, C.C. Huang, "Joint Synchronization in Eureka 147 DAB System Based on Abrupt Phase Change Detection", IEEE Journal on Selected Areas in Communications, Vol. 17, No. 10, pp. 1770-1780, Oct. 1999

[42] In ho Hwang, Hwang soo Lee, Keon woo Kang, "Frequency and Timing Period Offset Estimation Technique for OFDM systems", Electronics Letters, Vol. 34, No. 6, pp. 520-521, March 1998

[43] ETSI-TS-101-475 v1.1.1(2000-04): Broadband Radio Access Networks(BRAN); HIPERLAN Type 2; Physical(PHY) layer

[44] D. Jungnickel, A. Pott, "Perfect and Almost Perfect Sequences", Discrete Applied Mathematics, Vol. 95, pp. 331-359, 1999

[45] W.C. Jakes, "Microwave Mobile Communications", Wiley-Interscience, 1974

[46] C. Kaiteris, W.L. Rubin, "Pulse Trains with Low Residue Ambiguity Surfaces That Minimize Overlapping Target Echo Suppression in Limiting Receivers", Proceeding of the IEEE, Vol. 54, pp. 438-439, March 1966

[47] T. Keller, L. Hanzo, "Adaptive Multicarrier Modulation: A Convenient Framework for Time-Frequency Processing in Wireless Communications", IEEE Proceedings of the IEEE, Vol. 88, No. 5, pp. 611-640, May 2000,

[48] D.K. Kim, S.H. Do, H.K. Lee, H.J. Choi, "Performance Evaluation of the Frequency Detectors for Orthogonal Frequency Division Multiplexing", IEEE Transcations on Consumer Electronics, Vol. 43, No. 3, pp. 776-782, Aug. 1997

[49] D.K. Kim, S.H. Do, H.B. Cho, H.J. Choi, K.B. Kim, "A New Joint Algorithm of Symbol Timing Recovery and Sampling Clock Adjustment for OFDM Systems", IEEE Transcations on Consumer Electronics, Vol. 44, No. 3, pp. 1142-11491, Aug. 1998

[50] H. Kim, H. Kang, W. Hwang, K. Kim, "An Improved Frequency Synchronization Scheme using a Modified OFDM Burst Frame for Wireless LAN Systems", IEEE Transcations on Consumer Electronics, Vol. 46, No. 4, pp. 1021-1025, Nov. 2000

[51] Y.H. Kim, I.Song, S.Yoon and S.R.Park, "An Efficient Frequency Offset Estimator for OFDM Systems and Its Performance Characteristics", IEEE Transcations on Vehicular Technology, Vol.50, No.5, September 2001, pp.1307-1311

[52] M. Kiviranta, A. Mämmelä, "Coarse Frame Synchronization Structures in OFDM", ACTS Mobile Communications Summit, Vol. 2, pp. 467-470, 1996

[53] Patrick J. Langfeld, K. Dostert, "OFDM System Synchronization for Powerline Communications," Proceedings of the 4th International Symposium on Powerline Communications and its Applications, Ireland, pp. 15-22, April 5th-7th 2000

[54] Y. Li, L.J. Cimini and N.R. Sollenberger, "Robust Channel Estimation for OFDM systems with rapid Dispersive Fading Channels", IEEE Transactions on Communication, Vol. 46, pp. 902-915, July 1998

[55] H. Li, G. Malgren, M. Pauli, "Performance comparison of the radio link protocols of IEEE802.11a and Hiperlan/2", VTC 2000, pp. 2185-2191

[56] Jian Li, Guoqing Liu, Georgios B. Giannakis,"Carrier Frequency Offset Estimation for OFDM-base WLANs", IEEE Signal Processing Letters, Vol. 8, No. 3, pp.80-82, March 2001

[57] H. Lui, U. Tureli, "A High-Efficiency Carrier Estimator for OFDM Communications", IEEE Communications Letters, Vol. 2, No. 4, pp. 104-106, April 1998

[58] X. Li, J.A. Ritcey, "M-sequences for OFDM Peak-to-Average Power Ratio Reduction and Error Correction", Electronics Letters, 27 March 1997, Vol. 33, No. 7, pp. 554-555, March 1997

[59] D. Lee, K. Cheun, "A New Symbol Timing Recovery Algorithm for OFDM Systems", IEEE Transactions on Consumer Electronics, Vol. 43, No. 3, pp. 767-774, Aug. 1997

[60] Marco Luise, "Carrier Frequency Acquisition and Tracking for OFDM Systems", IEEE Transactions on Communications, Vol. 44, No. 11, pp. 1590-1598, Nov. 1995

[61] X. Ma, C. Tepedelenlioglu, G.B. Giannakis, S. Barbarossa, "Non-data-aided Carrier Offset Estimators for OFDM with Null Subcarriers: Identifiability, Algorithms, and Performance", IEEE Journal on Selected Areas in Communications, Vol.19, No.12, December 2001

[62] M.C.D. Maddocks, "An Introduction to Digital Modulation and OFDM Techniques," BBC Research Department Report No. BBC RD 1993/10

[63] James L. Massey, "Optimum Frame Synchronization", IEEE Transcations on Communicaitons, Vol. COM-20, No. 2, pp.115-119, April 1972

[64] A.C. McCormick, P.M. Grant, J.S. Thompson and E.A. Ai-susa, "A Carrier Frequency Offset Correction Scheme for MC-CDMA", IEEE VTC'01, pp.1689-1692

[65] M. Mizoguchi, T. Onizawa, T. Kumagai, "A Fast Burst Synchronization Scheme for OFDM", IEEE International Conference on Universal Personal Communications, Vol. 2, pp. 125-130, 1998

[66] L.G. Møller, "Digital Terrestrial Television - the 8k system," EBU Technical Review Winter 1995, pp. 40-50

[67] M. Morelli, U. Mengali, "An Improved Frequency Offset Estimator for OFDM Applications", IEEE Communications Letters, Vol. 3, No. 3, pp. 75-77, March 1999

[68] P.H. Moose, "A Technique for Orthogonal Frequency Division Multiplexing Frequency Offset Correction", IEEE Transcations on Communications, Vol. 42, No. 10, pp. 2908-2914, Oct. 1994,

[69] Stefan H. Müller, R.W. Bäuml, R.F.H. Fischer, J.B. Huber, "OFDM with Reduced Peak-to-Average Power Ratio by Mulitple Signal Representation", In Annuals of Telecommunications, Vol. 52, No. 1-2, pp. 58-67, Feb. 1997

[70] Stefan H. Müller, "On the Optimality of Metrics for Coarse Frame Synchronization in OFDM: A Comparison", PIMRC'98, pp. 533-537, Sept. 1998

[71] B. Muquet and M.de Courville, "Blind and Semi-blind Channel Identification Methods using Second Order Statistics for OFDM systems", ICASSP'01, pp. 2745-2748

[72] R.v. Nee and R. Prasad, "OFDM for Wireless Multimedia Communications", Artech House, 2000

[73] F. Neuman, L. Hofman, "New Pulse Sequence with Desirable Correlation Properties", Proc. Nat. Telemetry Conf, pp. 272-282, 1971

[74] P.T. Nielsen, "Some Optimum and Suboptimum Frame Synchronizers for Binary Data in Gaussian Noise", IEEE Transcations on Communications, pp. 770-772, June 1973

[75] Hiroshi Nogami, Toshio Nagashima, "A Frequency and Timing Period Acquisition Technique for OFDM Systems", IEICE Trans. Commun., Vol. E79-B, No. 8, pp. 1135-1146, Aug. 1996

[76] Seamus O'Leary, "Hierarchical Transmission and COFDM Systems"', IEEE Transcations on Broadcasting, Vol. 43, No. 2, pp. 1135-1146, June 1997

[77] Alan V. Oppenheium, R.W. Schafer, "Discrete-Time Signal Processing", 2nd edition, Prentice-Hall Internaltional

[78] E. Paaske, "Note on Incoherent Binary Sequences", IEEE Transactions on Aerospace and Electronic Systems, pp. 128-130, Jan. 1968

[79] A. Papoulis , "Probability, Random Variables, and Stochastic Processes", 3rd edition, 1991, McGraw-Hill Book Co.

[80] "Orthogonal Frequency Division Multiplexing", U.S. Patent 3,488,445, filed Nov. 14 1966, issued Jan. 6, 1970

[81] A. Peled, A. Ruiz, "Frequency Domain Data Transmission using Reduced Computational Complexity Algorithms", Proc. IEEE ICASSP'80, pp. 964-967, 1980

[82] Ray H. Pettit, "Pulse Sequences with Good Autocorrelation Properties", Microwave Journal, pp.63-67, Feb. 1967

[83] B.Y. Prasetyo, A.H. Aghvami, "Simplified Frame Structure for MMSE-based Fast Burst Synchronization in OFDM Systems", Electronics Letters, Vol. 35, No. 8, pp. 617-618, April 1999

[84] E. Panayirci, C.N. Georghiades, "Carrier Phases Synchronization of OFDM Systems over Frequency-Selective Channels via the EM Algorithm", IEEE 1999, pp. 675-679

[85] J.B. Resnick, "High Resolution Waveforms Suitable for A Multiple Target Environment", M.S. Thesis, M.I.T, Cambridge, Mass., 1962

[86] M. Russell, G. Stüber, "Terrestrial Digital Video Broadcasting for Mobile Reception Using OFDM", Wireless Personal Communications, Vol. 2, pp. 45-66, 1995

[87] T.S. Rappaport, "Wireless Communications Principles and Practice", Prentice-Hall, 1996

[88] J.A. Salehi, "Code Division Multiple-Access Techniques in Optical Fiber Networks - Part I: Fundamental Principles", IEEE Transcations on Communications, Vol. 37, No. 8, pp. 824-833, August 1989

[89] Timothy M. Schmidl, Donald C. Cox, "Robust Frequency and Timing Synchronization for OFDM", IEEE Transcations on Communications, Vol. 45, No. 12, pp. 1613-1621, Dec. 1997

[90] M.R. Schroeder, "Synthesis of Low-Peak-Factor Signals and Binary Sequences with Low Autocorrelation", IEEE Transcations on Information Theory, pp. 85-89, Jan. 1970

[91] T. Seki, M. Itami, H. Ohta, K. Itoh, "The Channel Estimation Technique based on the Propagation Path Model of an OFDM System", IEEE, 2001

[92] M. Speth, F. Classen, H. Meyr, "Frame Synchronization of OFDM Systems in Frequency Selective Fading Channels", IEEE 47th Vehicular Technology Conference, Vol. 3, pp. 1807-1811, 1997

[93] M. Speth, S. Fechtel, G. Fock, H. Meyr, "Optimum Receiver Design for OFDM-Based Broadband Transmission - Part II: A Case Study", IEEE Transcations on Communications, Vol. 49, No. 4, pp. 571-578, April 2001

[94] A.Stamoulis, Suhas N.Diggavi, Naofal Al-Dhahir, "Estimation of fast fading channels in OFDM", IEEE Wireless Communication and Networking Conference, Florida, pp.465-470, March 2002

[95] M. Evans, N. Hastings, B. Peacock, "Statistical Distributions", 3rd edition, John Wiley & Sons, Inc.

[96] P. Shelswell, "The COFDM modulation system: The Heart of Digital Audio Broadcasting," IEE Electronics & Communication Engineering Journal, pp. 127-136, June 1995

[97] J. Singer, "A Theorem in Finite Projective Geometry and Some Applications to Number Theory", Transcations of the American Mathematical Society, Vol. 43, Issue 3, pp. 377-385, May 1938

[98] L. Thibault, M.T. Le, "Performance Evaluation of COFDM for Digital Audio Broadcasting Part I: Parametric Study", IEEE Transcations on Broadcasting, Vol. 43, No. 1, pp.64-74, March 1997

[99] U. Tureli, H. Liu, "Blind Carrier Synchronization and Channel Identification for OFDM Communications", ICASSP'98, pp. 3509-3512, May 1998

[100] U. Tureli, H. Liu, M.D. Zoltowski, "OFDM Blind Carrier Offset Estimation: ESPRIT", IEEE Trans. Commun., Vol 48, No. 9, pp. 1613-1621, Dec. 2000

[101] X. Wang, T.T. Tjhung, C.S. Ng, "Reduction of Peak-to-Average Power Ratio of OFDM System Using a Companding Technique", IEEE Transcations on Broadcasting, Vol. 45, No. 3, pp. 303-422, Sep. 1999

[102] S.B. Weinstein, P.M. Ebert, "Data Transmission by Frequency Division Multiplexing Using the Discrete Fourier Transform", IEEE Trans. Comm. Techno., Vol. COM-19, No. 15, pp. 628-634, Oct. 1971

[103] K. Witrisal, Y.H. Kim, R. Prasad, L.P. Ligthart, "Experimental Study and Comparison of OFDM Transmission Techniques", 5th International OFDM-Workshop in Hamburg, pp. 1-5, Sept. 2000

[104] K. Witrisal, R. Prasad, L.P. Ligthart, "OFDM Technology for Realizing Broadband Wireless Multimedia Communications", Proc. Korea Telecom International Symposium (KTIS'99), Seoul, pp. 307-312, Oct. 1999

[105] W.J. Szajnowski, "A Multicarrier Receiver using a Weighted Sum of Pilot Powers to Detect Mistuning", UK Patent Application, GB-2343311-A, 3 May 2000

[106] F. Yanzeng, Z.Hailin, W.Yumin, "Frequency Synchronization in OFDM Systems", 3G Mobile Communication Technologies, 26-28 March 2001, Conference Publicaion No. 477, IEE 2001

[107] B. Yang, K.B. Letaief, R.S. Cheng, Z. Cao, "An Improved Combined Symbol and Sampling Clock Synchronization Method for OFDM Systems", IEEE Wireless Communications and Networking Conference, Sept. 1999

[108] C.S. Yeh, Y. Lin, "Channel Estimation Using Pilot Tones in OFDM Systems", IEEE Transcations on Broadcasting, Vol. 45, No. 4, p. 400-409, Dec. 1999

[109] C.S. Yeh, Y. Lin, Y. Wu, "OFDM System Channel Estimation Using Time-Domain Training Sequence for Mobile Reception of Digital Terrestrial Broadcasting", IEEE Transcations on Broadcasting, Vol. 46, No. 3, pp. 215-220, Sep. 2000

[110] X. Zhuang, Z.Ding and A. Swindlehurtst, "A Statistical Subspace Method for Blind Channel Identification in OFDM Communications", ICASSP'01, pp. 2493-2496

[111] M.S. Zimmerman, A.L. Kirsch, "The AN/GSC-10 (Kathryn) Variable Rate Data

Modem for HF Radio,", IEEE Trnas. Commun. Techno., Vol. COM-15, pp. 197-205, April 1967

[112] William Y. Zou, Y. Wu, "COFDM: An Overview", IEEE Transcations on Broadcasting, Vol. 41, No. 1, pp. 1-8, March 1995